eman ta zabal zazu

Universidad del País Vasco
Euskal Herriko Unibertsitatea

Polymeric Materials with Multiple Crystalline Phases: Structure, Morphology and Crystallization

Eider Matxinandiarena Almandoz

PhD Thesis

Department of Polymers and Advanced Materials: Physics, Chemistry and Technology, University of the Basque Country UPV/EHU

Donostia-San Sebastian, 2021

eman ta zabal zazu

Universidad del País Vasco
Euskal Herriko Unibertsitatea

Polymeric Materials with Multiple Crystalline Phases: Structure, Morphology and Crystallization

by

Eider Matxinandiarena Almandoz

Advisors

Prof. Alejandro Jesús Müller Sánchez

Prof. Agurtzane Múgica Iztueta

Department of Polymers and Advanced Materials: Physics, Chemistry and Technology, University of the Basque Country UPV/EHU

Donostia-San Sebastian, 2021

Index

Chapter 4. Neat/Recycled Polymer Blend and Nanocomposites (PBNANOs) with Titanium Dioxide Nanoparticles and Compatibilizer Agents: Morphology, Crystallization and Mechanical Properties

List of Abbreviations

AFM	Atomic Force Microscopy
Cp	Heat capacity
D	Particle size distribution
d_n	Number average diameter
d_v	Volume average diameter
DSC	Differential Scanning Calorimetry
G	Isothermal spherulitic growth rate
G_0	Isothermal growth rate constant
K	Overall crystallization rate constant
K_g	Nucleation parameter
MA	Maleic anhydride
M_n	Number average molecular weight
M_w	Weight average molecular weight
N	Polymerization degree
n	Avrami index
N_i	Average droplet number
NP	Nanoparticles
PBNANO	Polymer blend nanocomposite
PCL	Poly (ε-caprolactone)
PDI	Polydispersity index
PE	Polyethylene
PEO	Poly (ethylene oxide)
PET	Poly (ethylene terephthalate)
PLLA	Poly (L-lactide)
PLOM	Polarized Light Optical Microscopy

PP	Polypropylene
PPgMA	Polypropylene grafted with maleic anhydride
R	Universal gas constant
SAXS	Small-angle X-ray Scattering
SEM	Scanning Electron Microscopy
t_0	Induction time for the beginning of the crystallization
T_c	Crystallization temperature
T_{cc}	Cold crystallization temperature
TEM	Transmission Electron Microscopy
T_g	Glass transition temperature
TGA	Thermogravimetric Analysis
T_m	Melting temperature
U^*	Activation energy
WAXS	Wide-angle X-ray Scattering
Wt %	Weight percentage
$1/\tau_{50\%}$	Inverse of the half of the crystallization time
ΔG	Free energy barrier
ΔH_c	Crystallization enthalpy
ΔH_m	Melting enthalpy
ΔT	Supercooling
$\tau_{1/2}$	Time needed to achieve 50% of the overall crystallization
X_c	Degree of crystallinity
δ	Solubility parameter
χ	Flory-Huggins interaction parameter
X_c	Crystallinity degree

Chapter 1

General Introduction and Objectives

1.1. Introduction

Extensive research has been performed during the past decades in order to develop high-performance multiphase polymeric materials, such as polymer blends, composites, nanocomposites, interpenetrating polymer networks, block copolymers, and polymer gels. Since crystallization is the main physical characteristic that allows the control of the final properties of a crystallizable material, understanding its crystalline behaviour is vital to tailor properties and obtain new materials with enhanced properties[1].

The first part of this PhD project studies the structure and properties relationship of PET/HDPE polymer blends, employing a compatibilizer agent and titanium dioxide nanoparticles to create PBNANOs (polymer blend nanocomposites). Generally, immiscible polymer blends show sea-island morphologies with large droplet sizes and lack of adhesion between the two phases, exhibiting poor mechanical properties. Thus, compatibilization strategies need to be designed and applied, and the most commonly employed techniques are the addition of block copolymers, compatibilizing agents and nanoparticles. The use of such techniques improves the final performance of materials[2-6].

In addition, a study with recycled polymer blends containing titanium dioxide nanoparticles has also been performed. Due to the high demand and manufacturing of polymers, for instance, in the packaging area, recycling has become vital to save manufacturing resources, lower energy consumption, and minimize the impact of plastic on the environment[7]. Nowadays, PET is the most widely employed polymer in packaging because of its good properties[8]. However, it is common to find polyethylene or polypropylene among PET waste, and during the last years, titanium dioxide nanoparticles have also been introduced in the production of opaque white milk bottles. Since the treatment of plastic waste is becoming a global problem, the analysis of such materials is very interesting.

After the analysis of polymer blends with two crystallizable phases in the first part, the next part of the thesis continues with the analysis of multicrystalline polymeric systems, focusing on the crystalline behaviour of block copolymers:

tricrystalline PE-*b*-PEO-*b*-PLLA and PE-*b*-PCL-*b*-PLLA triblock terpolymers, and tetracrystalline PE-*b*-PEO-*b*-PCL-*b*-PLLA tetrablock quarterpolymers. Their precursor diblock copolymers and PE homopolymers have also been studied for comparison purposes. The aim of this part is to carry out a comprehensive study of tri- and tetracrystalline block copolymers, since as in the case of polymer blends, the relationship between structure and properties plays a key role in the final behavior of the materials.

Many works have been published about AB-type diblock copolymers with one or two crystallizable blocks, and particularly, biodegradable and biocompatible polymers, such as poly (ethylene oxide) (PEO), poly (ε-caprolactone) (PCL), and poly (L-lactide) (PLLA) have attracted attention due to their biodegradable nature[9-17]. However, the addition of a third and fourth potentially crystallizable block to diblock copolymers makes the analysis more challenging. Some authors reported results for ABC-type triblock terpolymers[18-22]. Sun et al[23]. reported the triple crystalline nature of triblock and pentablock terpolymers with PCL, PEO, and PLLA blocks using DSC and WAXS. Palacios et al. studied PEO-*b*-PCL-*b*-PLLA triblock terpolymers, and they found three types of crystals, identifying a trilamellar self-assembly with lamellae of the three blocks at room temperature[20, 21]. In addition, they followed the evolution of this tri-lamellar morphology on the subsequent melting of the triblock terpolymer by in situ hot-stage AFM[22]. Regarding tetracrystalline quarterpolymers, to our knowledge, only one report about the synthesis of tetracrystalline tetrablock quarterpolymers has been published[24]. The quarterpolymers under study in this thesis have been synthesized using a new synthesis strategy developed by Prof. Nikos Hadjichristidis, which is explained in the Experimental Part.

Therefore, the aim of this research is to understand the crystalline behaviour of these complex triblock terpolymers and tetrablock quarterpolymers. Different morphologies can be obtained controlling the crystallization conditions, and thus, properties can be tuned to obtain new materials for applications in the biomedical field, drug delivery or nanotechnology[25-27], for instance [28].

Therefore, in Chapter 1, a general introduction and objectives of this doctoral research are presented. Chapter 2 explains the general basics of polymer crystallization, focusing on crystal structure and morphology, crystallization kinetics, and the most relevant crystallization theories. All the experimental techniques and conditions employed in this work are presented in Chapter 3. Chapter 4 firstly provides a general introduction to binary blends and nanocomposites, and then the results of the materials under study are presented. Chapters 5 and 6 are focused on multicrystalline triblock terpolymers and tetrablock quarterpolymers. A background on previously reported similar materials is provided, and then, results of the analysis of our tricrystalline and tetracrystalline materials are presented. To finish, the Chapter 7 summarizes the global conclusions of this doctoral research in multiphasic polymer systems.

1.2. Objectives

1.2.1. General objectives

The main objective of the present work is to study the morphology and crystallization behavior of multiphasic polymeric systems with at least two crystallizable phases: binary polymer blends, on the one hand, and block copolymers with three and four crystallizable blocks, on the other hand. Different experimental techniques are employed to obtain comparable results and thus determine the most relevant characteristics of the materials to gain knowledge on essential physical aspects of the systems.

Two main systems are analyzed:

a) **Polymer blends:** Neat/recycled polymer blend and nanocomposites (PBNANOs) with titanium dioxide nanoparticles and compatibilizer agents:

    i. PET/HDPE polymer blends with and without the compatibilizer agent PEgMA.

ii. PET/HDPE polymer blends with and without TiO_2 nanoparticles.

iii. PET/HDPE polymer blends with TiO_2 nanoparticles and the compatibilizer agent PEgMA.

iv. Recycled PP/PET/TiO_2 blends : rPP/rPET/TiO_2 PBNANOs.

b) Block copolymers:

i. Tricrystalline PE-*b*-PEO-*b*-PLLA and PE-*b*-PCL-*b*-PLLA triblock terpolymers and their corresponding PE-*b*-PEO and PE-*b*-PCL diblock copolymer and PE homopolymer precursors.

ii. Tetracrystalline PE-*b*-PEO-*b*-PCL-*b*-PLLA tetrablock quarterpolymers and their precursors: PE-*b*-PEO-*b*-PCL triblock terpolymers, PE-*b*-PEO diblock copolymers and PE homopolymers.

1.2.2. Specific objectives

a) Polymer blends: Neat/Recycled Polymer Blend and Nanocomposites (PBNANOs) with Titanium Dioxide Nanoparticles and Compatibilizer Agents

- Analysis of the effect of the compatibilizer agent PEgMA or/and TiO_2 nanoparticles in PET/PE blends to study the relationship between matrix-droplet morphology by SEM and TEM.
- Optimization of the blend morphology by changing the TiO_2 nanoparticles content.
- Analysis of non-isothermal crystallization behaviour of the PET and HDPE phases by DSC.
- Analysis of the combined effect of both the compatibilizer agent PEgMA and TiO_2 nanoparticles in the morphology and non-isothermal crystalline behavior.

- Study the effect of TiO_2 nanoparticles content and nature (hydrophilic (hphi), hydrophobic (hpho), and hydrophobically modified (hphoM) nanoparticles) in morphology by analyzing the preferential location of the nanoparticles in recycled PP/PET PBNANOs by SEM and TEM.
- Analysis of non-isothermal crystallization behavior of the recycled PP and PET phases in the PBNANOs by DSC.
- Analysis of isothermal crystallization kinetics of the recycled PP and PET phases in the PBNANOs by DSC.
- Evaluation of the mechanical properties by tensile testing experiments.

b) Block copolymers: Tricrystalline PE-*b*-PEO-*b*-PLLA and PE-*b*-PCL-*b*-PLLA triblock terpolymers and tetracrystalline PE-*b*-PEO-*b*-PCL-*b*-PLLA tetrablock quarterpolymers along with their diblock copolymer and homopolymer precursors

- Analysis of the miscibility by SAXS.
- Study of the non-isothermal sequential crystallization behavior by DSC and WAXS.
- Analysis of the microscale morphology by PLOM.
- Analysis of the nanoscale morphology of the tetrablock quarterpolymers by AFM.
- Analysis of the mechanical properties by nanoindentation of the tetrablock quarterpolymers.

1.3. References

1. Arif P., M.; Kalarikkal, N.; Thomas, S., Introduction on crystallization in multiphase polymer systems. *In Crystallization in multiphase polymer systems*, Thomas, S.; Arif P., M.; Gowd, E. B.; K., K., Eds. Elsevier: **2018**; pp 1-13.

2. Koning, C.; Van Duin, M.; Pagnoulle, C.; Jerome, R., Strategies for compatibilization of polymer blends. *Progress in Polymer Science* **1998**, *23*, 707-757.

3. Paul, D. R.; Robeson, L. M., Polymer nanotechnology: Nanocomposites. *Polymer* **2008**, *49*, 3187-3204.

4. Ajji, A., Interphase and compatibilization by addition of a compatibilizer. *In Polymer blends handbook*, Second Edition ed.; Utracki, L. A.; Wilkie, C. A., Eds. Springer: Dordrecht, **2014**; pp 447-516.

5. Taguet, A.; Cassagnau, P.; Lopez-Cuesta, J. M., Structuration, selective dispersion and compatibilizing effect of (nano)fillers in polymer blends. *Progress in Polymer Science* **2014**, *39*, 1526-1563.

6. Agwuncha, S. C.; Owonubi, S. J.; Sadiku, E. R.; Varaprasad, K.; Ray, S. S.; Selvam, S. P.; Shittu, T. A.; Shanavas, A.; Mukwevho, E., Crystallization and morphological changes in nanostructured polymer blends. *In Design and applications of nanostructured polymer blends and nanocomposite system*s, Shanks, R.; Chandrasekharakrup, S., Eds. Wiliam Andrew Publishing: Boston, **2016**; pp 287-312.

7. Zhang, Z.; Wang, C.; Mai, K., Reinforcement of recycled PET for mechanical properties of isotactic polypropylene. *Advanced industrial and engineering polymer research* **2019**, *2*, 69-76.

8. Sangroniz, L.; Ruiz, J. L.; Sangroniz, A.; Fernández, M.; Etxeberria, A.; Müller, A. J.; Santamaría, A., Polyethylene terephthalate/low density polyethylene/titanium dioxide blend nanocomposites: Morphology, crystallinity, rheology, and transport properties. *Journal of Applied Polymer Science* **2019**, *2*, 46986.

9. Castillo, R. V.; Müller, A. J., Crystallization and morphology of biodegradable or biostable single and double crystalline block copolymers. *Progress in Polymer Science* **2009**, *34*, 516-560.

10. Hamley, I. W.; Castelletto, V.; Castillo, R. W.; Müller, A. J.; Martin, C. M.; Pollet, E.; Dubois, P., Crystallization in poly(L-lactide)-*b*-poly(ε-caprolactone) double crystalline diblock copolymers: a study using X-ray scattering, differential scanning calorimetry and polarized optical microscopy. *Macromolecules* **2005**, *38*, 463-472.

11. Müller, A. J.; Arnal, M. L.; Balsamo, V., Crystallization in block copolymers with more than one crystallizable block. *In Progress in understanding of polymer crystallization*, Reiter, G.; Strobl, G. R., Eds. Lecture Notes in Physics: Springer, Berlin, Heidelberg, **2007**; Vol. 714, pp 229-259.

12. Sakurai, T.; Ohguma, Y.; Nojima, S., Morphological evolution during isothermal crystallization observed in a crystalline-crystalline diblock copolymer. *Polymer Journal* **2008**, *40*, 971-978.

13. Müller, A. J.; Albuerne, J.; Esteves, L. M.; Marquez, L.; Raquez, J.-M.; Degée, P.; Dubois, P.; Collins, S.; Hamley, I. W., Confinement effects on the crystallization kinetics and self-nucleation of double crystalline poly(p-dioxanone)-*b*-poly(ε-caprolactone) diblock copolymers. *Macromolecular Symposia* **2004**, *215*, 369-382.

14. He, C.; Sun, J.; Deng, C.; Zhao, T.; Deng, M.; Chen, X.; Jing, X., Study of the synthesis, crystallization, and morphology of poly(ethylene glycol)-poly(ε-caprolactone) diblock copolymers. *Biomacromolecules* **2004**, *5*, 2040-2047.

15. Arnal, M. L.; Boissé, S.; Müller, A. J.; Meyer, F.; Raquez, J. M.; Dubois, P.; Prud`homme, R. E., Interplay between poly(ethylene oxide) and poly(L-lactide) blocks during diblock copolymer crystallization. *CrystEngComm* **2016**, *18*, 3635-3649.

16. Liénard, R.; Zaldua, N.; Josse, T.; Winter, J. D.; Zubitur, M.; Mugica, A.; Iturrospe, A.; Arbe, A.; Coulembier, O.; Müller, A. J., Synthesis and characterization of double crystalline cyclic diblock copolymers of poly(ε-caprolactone) and poly(L(D)-lactide) (c(PCL-b-PL(D)LA)). *Macromolecular Rapid Communications* **2016**, *37*, 1676-1681.

17. Wang, J. L.; Dong, C. M., Synthesis, sequential crystallization and morphological evolution of well-defined star-shaped poly(ε-caprolactone)-*b*-poly(L-lactide) block copolymer. *Macromolecular Chemistry and Physics* **2006**, *207*, 554-562.

18. Palacios, J. K.; Mugica, A.; Zubitur, M.; Iturrospe, A.; Arbe, A.; Liu, G.; Wang, D.; Zhao, J.; Hadjichristidis, N.; Müller, A. J., Sequential crystallization and morphology of triple crystalline biodegradable PEO-*b*-PCL-*b*-PLLA triblock terpolymers. *Royal Society of Chemistry Adv*. **2016**, *6*, 4739.

19. Palacios, J. K.; Zhao, J.; Hadjicrhistidis, N.; Müller, A. J., How the complex interplay between different blocks determines the isothermal crystallization kinetics of triple-crystalline PEO-*b*-PCL-*b*-PLLA triblock terpolymers. *Macromolecules* **2017**, *50*, 9683-9695.

20. Palacios, J. K.; Tercjak, A.; Liu, G.; Wang, D.; Zhao, J.; Hadjicrhistidis, N.; Müller, A. J., Trilayered morphology of an ABC triple crystalline triblock terpolymer. *Macromolecules* **2017**, *50*, 7261-7281.

21. Palacios, J. K.; Liu, G.; Wang, D.; Hadjichristidis, N.; Müller, A. J., Generating triple crystalline superstructures in melt-miscible PEO-*b*-PCL-*b*-PLLA triblock terpolymers by controlling thermal history and sequential crystallization. *Macromolecular Chemistry and Physics* **2019**, *220*, 1900292.

22. Palacios, J. K.; Zhang, H.; Zhang, B.; Hadjichristidis, N.; Müller, A. J., Direct identification of three crystalline phases in PEO-*b*-PCL-*b*-PLLA tribock terpolymer by in situ hot-stage atomic force microscopy. *Polymer* **2020**, *205*, 122863.

23. Sun, L.; Shen, L. J.; Zhu, M. Q.; Dong, C. M.; Wei, Y., Synthesis, self-assembly, drug-release behavior, and cytotoxicity of triblock and pentablock copolymers composed of poly(ε-caprolactone), poly(L-lactide), and poly(ethylene glycol). *Journal of Polymer Science Part A: Polymer Chemistry* **2010**, *48*, 4583-4593.

24. Ladelta, V.; Zapsas, G.; Abou-Hamad, E.; Gnanou, Y.; Hadjichristidis, N., Tetracrystalline tetrablock quarterpolymers: Four different crystallites under the same roof. *Angewandte Chemie International Edition* **2019**, *58*, 16267-16274.

25. Huang, S.; Jiang, S., Structures and morphologies of biocompatible and biodegradable block copolymers. *RSC Advances* **2014**, *4*, 24566-24583.

26. Barthel, M. J.; Schacher, F. H.; Schubert, U. S., Poly(ethylene oxide)(PEO)-based ABC triblock terpolymers - synthetic complexity vs. application benefits. *Polymer Chemistry* **2014**, *5*, 2647.

27. Guo, X.; Wang, L.; Wei, X.; Zhou, S., Polymer-based drug delivery systems for cancer treatment. *Journal of Polymer Science, Part A: Polymer Chemistry* **2016**, *54*, 3525-3530.

28. Danafar, H., Applications of copolymeric nanoparticles in drug delivery systems. *Drug Research* **2016**, *66 (10)*, 506-519.

Chapter 2

Introduction to Polymer Crystallization

2.1. Introduction

Crystallization of polymers has become very important in polymer science because crystallization conditions determine the final structure and physical properties of materials. In the past few decades, many scientists have performed extensive research to develop high-performance macro/micro and nanostructured multiphase polymeric materials. These systems commonly consist of polymer blends, composites, nanocomposites, interpenetrating polymer networks, block copolymers, and polymer gels[1, 2].

2.1.1. Polymer Blends

Blending two or more polymers is an effective way to produce materials with enhanced properties. The crystallization behavior and the superstructure are influenced by miscibility, composition, mixing conditions, and interfacial characteristics of the phases. Crystallization in polymer blends occurs between the glass transition temperature (T_g) and the equilibrium melting temperature (T_m^0) of the crystallizable polymer. In binary miscible blends, the crystallization behavior depends on the glass transition of the amorphous component since it is intermediate to those of the blend components. If both components can crystallize, morphology is mainly controlled by phase separation that occurs when crystals grow in the presence of an amorphous component. The first crystallizable component forms spherulites at the liquid crystal interface, increasing its concentration in the amorphous phase.

Many works have been published about the crystalline behavior of polymer blends. For instance, the PP/PA6 blend is a well-studied system due to the versatility of the pure materials[3-7].

2.1.2. Composites and Nanocomposites

These polymer-based matrixes have some materials as reinforcements, such as glass fibers, carbon materials (carbon black, fibers, graphite, nanotubes), calcium carbonate, metal oxides, silica, talc, montmorillonite, etc. in small

percentages in order to improve mechanical, thermal, electrical, optical, magnetic, barrier, and flame retardant properties. They are classified depending on the size of filler particles. In general trends, acceleration/retardation of crystallization, changes in spherulitic morphologies, and in few cases, changes in the crystal structure can be observed. The size of the polymer chain and the nanofiller is usually close to each other, and nanofillers can act as nucleating agents[1].

Crystallization on polymer blend nanocomposites is very important to study from the point of view of product manufacturing since processing of polymers (extrusion, injection molding and film blowing) generally involve non-isothermal crystallization conditions. Thus, knowledge of the parameters affecting crystallization is vital for optimizing processing conditions and properties of the final products. Usually, studies on crystallization behavior of polymers include crystallization temperature, crystal shapes, and isothermal and non-isothermal kinetics. Particularly, crystallization kinetics give important information about crystallization behavior of polymeric nanocomposites[8] such as polymer nanolayered[9-24], metal-polymer[25-31], carbon-nanotube based[32-40], calcium carbonate[41-47], silica[48-60] and nanocellulose-based nanoparticles[61-66] in polymer nanocomposites in order to predict the material's behaviour[1].

Many works have been published about the effectiveness of nanoparticles as nucleating agents[30, 67-73] since they act as heterogeneous nucleation sites for crystallization. In general, the overall crystallization process is expected to be accelerated. Nevertheless, it was found that some fillers delay the crystallization rate by hindering chain mobility, so the effect of nanofillers as nucleating agents is still controversial since there is a competition between the nucleating and chain retardation effects that determine the final overall crystallization kinetics of a system[74].

In the present work, the effect of titanium dioxide nanoparticles (TiO_2) and/or the compatibilizer agent PEgMA in PET/PE blends is studied. In addition, three different types of TiO_2 nanoparticles are employed in recycled PET/PP blends in order to determine their preferential location and thus study the effect on morphology, crystallization kinetics, and mechanical properties.

2.1.3. Block Copolymers

Microstructure and composition influence the crystallization behavior of block copolymers, and in consequence, determine morphology and final properties. In addition, transition temperatures (order-disorder transition temperature or T_{ODT}, crystallization temperature or T_c, and glass transition temperature or T_g of the block[75]) and block miscibility are two factors that need to be taken into account. Block miscibility is related to segregation strength in the melt, and can be estimated as the product of the Flory-Huggins interaction parameter between blocks (χ) and the block copolymer polymerization degree (N)[76-78].

If the system is weakly segregated ($\chi N \sim 10$), breakout crystallization occurs, overwriting the previously formed melt structure with a new crystalline one, usually lamellar[79]. Two scenarios are possible in medium segregated systems ($\chi N \sim 10$-100): the melt morphology can be preserved after quenching the sample, or breakout crystallization can destroy it[75, 80-85]. If the system is strongly segregated ($\chi N > 100$), however, the morphology of the molten state is preserved, and confined crystallization occurs inside the microdomains of each phase forming well-organized microdomain structures[78].

The crystallization process in semicrystalline block copolymers with one or more crystallizable blocks is a complicated phenomenon. The final morphology depends on the competition between two transitions: phase separation between incompatible blocks and crystallization of the blocks. The process with a stronger driving force will determine the final morphology. However, depending on whether phase separation or crystallization occurs first,

the final structure will also be influenced, since different scenarios may be possible: confined crystallization in preformed microdomains, break out of the firstly formed structure in the melt due to crystallization of one block, or phase separation due to crystallization[78].

So, the addition of a potentially crystallizable block to diblock copolymers, forming triblock terpolymers and tetrablock quarterpolymers make the analysis of the crystalline behavior more complex. Several factors will affect crystallization kinetics and morphology and hence, final properties[75-77, 86-90].

Many works have studied the crystallization behavior of miscible or weakly segregated block copolymer systems during the last years[87, 91-98]. However, some medium or strongly segregated systems such as poly(ethylene oxide)-*b*-poly(ε-caprolactone) (PEO-*b*-PCL)[99-107], poly(ethylene oxide)-*b*-poly(L-lactide) (PEO-*b*-PLLA)[108-115] and poly(ε-caprolactone)-*b*-poly(lactide)s (PCL-*b*-PLA)[92-94, 116-118] have also been a matter of interest due to their biodegradable and biocompatible nature which can be very useful for applications in the biomedical field.

Furthermore, the addition of a polar PE block into these type of copolymers have also been studied, and some reports have been published regarding such systems as polyethylene-*b*-poly(L-lactide) (PE-*b*-PLLA)[75, 87, 119-122], polyethylene-*b*-poly(ethylene-oxide) (PE-*b*-PEO)[75, 87, 123-129] and polyethylene-*b*-poly(ε-caprolactone) (PE-*b*-PCL)[130-133].

However, there are few reports about ABC-type block terpolymers and ABCD-type quarterpolymers with three or four potentially crystallizable blocks, since the crystallization behaviour becomes very complex[103, 134-140]. In this work, novel ABC-type triple crystalline triblock terpolymers and ABCD-type tetracrystalline tetrablock quarterpolymers are studied, as well as their precursor diblock copolymers and homopolymers.

2.1. Crystal Structure and Morphology

Crystallization is the main physical characteristic that allows the control of the final properties since it has a significant effect on the mechanical, optical and thermal properties. Crystallizable polymers are semicrystalline, which means that they are partly crystalline and partly amorphous, usually with a crystallinity degree in the range of 10-80%. The crystal structure is often formed during cooling from the melt, although mechanical stretching and solvent evaporation can also be employed. Crystal structure and degree of crystallinity depend on the molecular structure, growth conditions, presence of impurities, crystallization temperature, cooling rate, tacticity, etc[1, 141].

Crystal morphology determines the final practical applications, so that is why morphology control is a good way to tune properties for several applications. Morphology is determined by crystallization mechanisms, kinetics, crystallization models, and depends on the components and crystallization conditions. That is why several crystal morphologies can be obtained, such as lamellae[142-146], cylinder[147-151], ribbons[152], capsules[153] and flowers[154-158], although lamellar morphologies are the most common.

Crystallization is a thermal process in polymers. During crystallization from the melt, long macromolecular chains disentangle from each other, and an ordered chain region called lamellae (Figure 2.1) with a thickness of approximately 10 nm is formed because polymer chains are aligned and folded together[1].

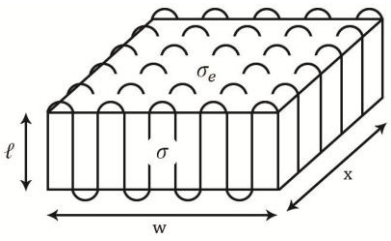

Figure 2.1. Schematic representation of a lamellar crystal with chain folds (*l*, *w*, *x*: lamellar thickness, length, and width; σ and σ_e: lateral and fold surface free energies of the lamellae, respectively)[159]

In crystalline/amorphous block copolymers, the crystalline component crystallizes, first forming lamellar crystals. Amorphous components are excluded from crystals, and depending on the composition of the AB-type diblock copolymer, different morphologies such as spheres, cylinders or lamellae can be obtained due to micro-phase segregation even in completely amorphous block copolymers (Figure 2.2) [78, 160-165].

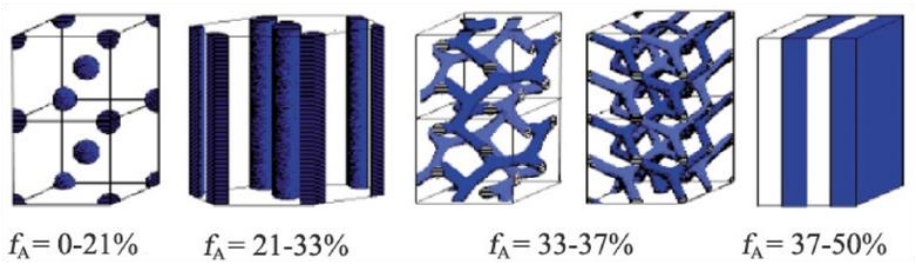

Figure 2.2. Possible morphologies in strongly segregated AB-type diblock copolymers. The blue component represents the minority phase A, and f_A determines the block volume fraction of block A[78].

In crystalline/crystalline diblock copolymers, competition between phase separation and crystallization also occurs, and which process takes place firstly will also affect the final morphology. However, if the two blocks crystallize at different temperatures, two different scenarios are possible: the crystallization of the first block determines the final morphology because the second block has to crystallize into the structure previously formed, or the subsequent crystallization of the second block may modify or redefine the firstly formed microstructure[78, 87, 88, 95, 106, 119, 166-168]. In addition, lower crystallinity and melting temperatures could be obtained, even if the two blocks are miscible in the melt, due to confined crystallization of one block into the lamellar crystals of the other block. This decrease comparing to the homopolymer is frequently a signal of confined crystallization[87, 169, 170].

So, several morphologies can finally be obtained by changing the crystallization sequence with the same polymers[78, 102, 171]. Furthermore, adding a third or fourth potentially crystallizable block to obtain triblock terpolymers or tetrablock quarterpolymers makes the analysis of the crystalline structure much more difficult due to interactions among all blocks, and new and complex morphologies could be obtained. Some of the possible morphologies for strongly segregated ABC-type triblock terpolymers are shown in Figure 2.3. The analogous of diblock copolymers (Figure 2.3a-c) are the most common ones and the rest are theoretical predictions which are experimentally undiscovered yet[172-176].

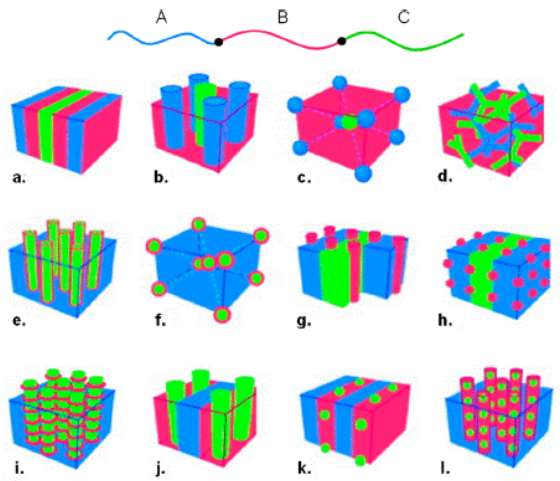

Figure 2.3. Possible morphologies of ABC type triblock terpolymers[172]

Lamellae with folded chains are the fundamental unit of polymer morphologies, as reported by Keller, and they grow to form supramolecular structures such as spherulites, axialites, and hedrites. Spherulites are spherical symmetric aggregates of radial lamellae. They can be observed by Polarized Light Optical Microscope (PLOM) and generally show characteristic extinction patterns called Maltese cross, which are formed parallel and perpendicular to the direction of polarization[177-179].

Transmission Electron Microscopy (TEM) demonstrates how spherulites are constituted by radially growing lamellae, which are separated by amorphous interlamellar regions. Chains are arranged perpendicularly to the flat horizontal surface of the lamellae, they are tangential to the spherulite and to the growth direction (Figure 2.4)[180].

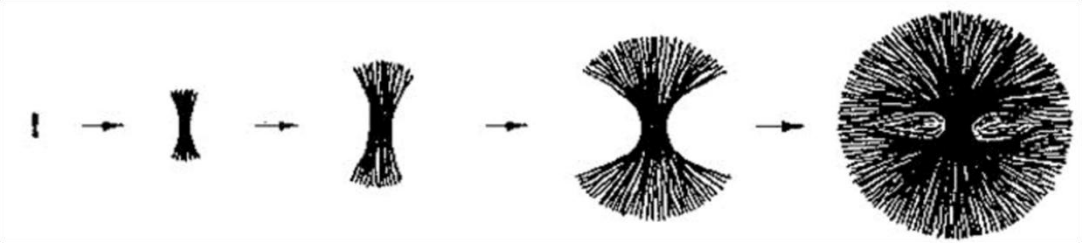

Figure 2.4. Schematic representation of the development of a spherulite[180]

The model proposed by Mandelkern[178] in 1964 is currently accepted for spherulitic morphology. Three regions are defined (Figure 2.5): the crystalline region formed by lamellae; the totally disordered amorphous region; and the interfacial region formed by chains that are part of the lamellae. Differences in size and morphology of different polymer spherulites depend on the chemical structure, molecular weight and distribution, crystallization conditions, and the density of active nuclei of the materials.

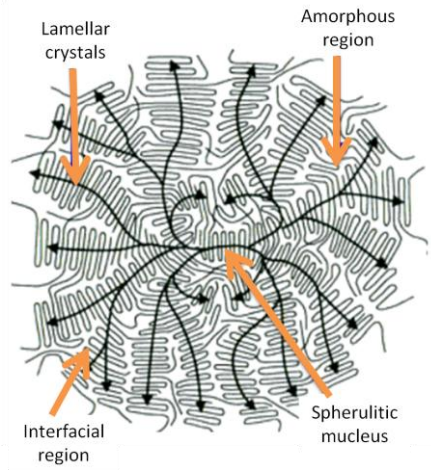

Figure 2.5. Two dimensional spherulite with amorphous, crystalline, and interfacial regions and a homogeneous nucleus (adapted from ref.[181]).

2.3. Crystallization Kinetics

2.3.1. Introduction

Crystallization of polymers is a first-order phase transformation of a supercooled liquid[179]. Polymers are able to crystallize at higher supercoolings than low molecular weight compounds. Polymer crystallization takes place at temperatures between the melting temperature (T_m) and the glass transition temperature (T_g). The crystallization rate increases as temperature is decreased upon cooling from the melt since the energy barrier needed for phase transformation decreases. However, as the temperature is further decreased, the crystallization rate is decreased due to the decrease in the diffusion of molecular segments. In addition, this effect is more significant at temperatures near the glass transition[182]. When polymers crystallize from the melt, crystallization starts slowly, then more rapidly with a maximum crystallization rate, and finally crystallization rate decreases. That is why crystallization follows a bell shape trend. On the contrary, when crystallization occurs from the vitreous state, the same phenomenon happens but as temperature increases. Hence the high temperature limit is controlled by the thermodynamic forces and the low temperature limit by diffusion limitations of chain segments[178, 179].

Primary and secondary crystallization are the main phenomenon taking place during polymer crystallization, although crystal reorganization may occur after secondary crystallization. Primary crystallization involves two mechanisms: nucleation and crystal growth.

2.3.2. Primary Crystallization

a) Nucleation

Crystal formation starts with nucleation. Firstly, a nuclei of supercritical size is formed. Then, the enthalpy barrier required to allow the nuclei to grow is

surpassed, and chain addition occurs irreversibly, starting the crystal growth process.

Nucleation can be homogeneous or heterogeneous. Homogeneous nucleation refers to the mechanism by which the formation of nuclei occurs in the bulk phase. It starts randomly due to of the spontaneous aggregation of a few parallel polymer chains. These seeds grow if the size of the grains exceeds a certain critical value, because if not, they disappear again. This is due to the fact that the nucleation step is an active process associated with a free energy barrier that has to be overcome. There is a critical size separating small particles whose free energy of formation increases during growth from those whose energy decreases. If this critical size is overcome, kinetically stable nuclei are formed[183, 184].

The critical radius of the sphere (r^*) associated with the free energy barrier is obtained by the following equation (Eq. 2.1):

$$r^* = \frac{2\sigma T_m^\circ}{\Delta H^\circ \Delta T} \qquad \text{Eq. 2.1}$$

where ΔH^o is the enthalpy of fusion, $T_m{}^o$ is the melting temperature at the thermodynamic equilibrium, σ is the specific free surface energy of the nucleus at the surface, and ΔT represents supercooling defined as ($T_m{}^o$- T_c). In addition, the free energy barrier which must be overcome in order to form stable aggregates is expressed by the following equation:

$$\Delta G^* = \frac{16\pi\sigma^3 T_m^{\circ\,2}}{3\Delta H^{\circ 2}\Delta T^2} \qquad \text{Eq. 2.2}$$

According to Eq. 2.1 and Eq. 2.2 nucleation occurs more easily at lower crystallization temperatures since the free energy barrier associated with the process is smaller because the critical size of the nuclei is also smaller[185].

Turnbull and Fisher.[186] proposed the following equation in which nucleation rate ($\dot{N}$) and temperature are related in order to obtain the formation rate of crystalline nuclei which overcome the critical size and are able to grow:

$$\dot{N} = N_0 e^{(\frac{E_D}{kT} - \frac{\Delta G^*}{kT})} \qquad \text{Eq. 2.3}$$

where $\dot{N}$ is the nucleation rate, N_0 is the number of chain segments, E_D is the activation energy for the diffusion process and ΔG^* represents the free energy for the formation of an aggregate with critical dimensions.

According to Eq. 2.2 and Eq. 2.3, ΔG^* progressively decreases during cooling from the melt, so nucleation rate increases until it reaches a maximum value, from which it starts to decrease approximating to the glass transition. Temperature decrease means increase of viscosity, preventing chain diffusion.

As previously mentioned, nucleation can also be heterogeneous, which occurs due to randomly dispersed insoluble particles in the melt, such as impurities, fillers or other components. It is thermodynamically favoured since the presence of these particles allows nucleation to take place at smaller supercooling temperatures because the free energy barrier to be overcome is smaller than forming new nuclei[187].

b) Crystal Growth

Crystal growth occurs by secondary and tertiary nucleation. A secondary nucleus is formed, and then several tertiary nucleation events take place[185]. Many lamellae grow radially forming quasispherical spherulites (1-100 μm)[188].

The trend of the spherulitic growth rate (G) with temperature is similar to the one of the primary nucleation. Two factors are involved: the transport term (diffusion) and the secondary nucleation term. The growth rate shows a maximum and has a bell shape curve form as a function of crystallization temperature or supercooling, since both terms have opposite behaviors with

temperature. On the left side of the bell shape curve (high supercoolings) the dominant term is molecular transport or diffusion. As the temperature reaches the glass transition, the diffusion of the macromolecules to the growing front becomes difficult, and the growth rate is decreased to zero. On the right side of the bell shape curve (high crystallization temperatures), however, the growth rate is driven by thermodynamic forces of the secondary nucleation (Figure 2.6)[189].

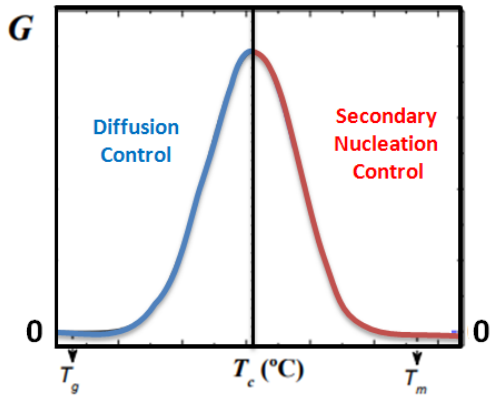

Figure 2.6. Crystal growth rate (*G*) as a function of the isothermal crystallization temperature[189].

2.3.3. Secondary Crystallization

Although the initial fast crystallization is dominated by primary crystallization, when crystal growth is completed by the impingement of spherulites, secondary crystallization takes place by the thickening of lamellae, or the growth of defective spherulites. In addition, crystal reorganization or perfection may also occur by employing particular conditions, for instance, long crystallization times[190].

2.4. Crystallization Theories

In 1957, several groups almost simultaneously obtained polyethylene single crystals[191-193], and Keller[194] proposed the "folded chain model" based on the experimental observations. It was assumed that a polymer chain should fold back and forth on itself in an adjacently re-entered manner. There was some controversy because chain folding was thought to be energetically unfavourable due to the chain torsion chain folding brings itself. However, arguments demonstrate that chain folding is a natural action during polymer crystallization due to kinetic effects.

Lauritzen and Hoffman proposed the first theory to explain the experimental crystallization results of polymer chains in 1960[195]. Due to the complex nature of polymer crystallization, there are different opinions and discussions still continue because oversimplifications are critically argued by several authors. However, the Lauritzen and Hoffman theory is the most successful and widely accepted theory, since it provides a simple and analytical approach to deal with polymer crystallization.

The first studies of polymer crystallization were mainly based on X-ray diffraction techniques because it provides evidence of unit cell parameters, the degree of crystallinity, and crystal dimensions[2].

Overall crystallization kinetics can be described by many crystallization theories, including primary nucleation and crystal growth contributions or the exclusively contribution of crystal growth (secondary nucleation). The most common theories explaining polymer crystallization are the Lauritzen and Hoffman (LH) theory[178, 180, 185, 188], the Sadler and Gilmer theory[185], the Strobl mesomorphic precursors thesis[188], and the "free growth" theory formulated by Göler and Sachs[178, 196]. According to the "free growth" theory, once a nuclei is created it grows without the influence of others that may have also been created and could be growing at the same time. The Avrami equation is one of the

possible solutions to this theory. The LH theory was developed to provide analytical expressions to quantify the free energy barrier associated to the crystal growth[178, 189, 197].

2.4.1. Lauritzen and Hoffman Theory

The Lauritzen and Hoffman (LH) theory is based on secondary nucleation, since crystal growth occurs in a pre-existing crystalline structure. There is a competition between the rate of deposition of secondary nuclei (i) and the rate of lateral surface spreading (g), which leads to three different regimes (regime behavior varies depending on the supercooling)[185, 198]:

- Regime I ($i << g$): each new nucleation site grows and terminates growing before a new nuclei is created[185], and occurs at very low supercoolings (high T_c)[198].
- Regime II (the same order of magnitude for i and g): more than a single nuclei grows at the same time (nucleation rate is higher), creating different layers[185]. It occurs at moderate supercoolings[198].
- Regime III ($i > g$): multiple nucleation events take place at the same layer[185]. This happens at very high supercoolings[198].

The secondary nucleation rate is directly proportional to the spherulitic growth rate (G), provided by the LH theory by equation 2.4[198, 199]:

$$G\ (T) = G_0\ exp\left(\frac{-U^*}{R(T_c - T_\infty)}\right) \exp\left(\frac{-k_g}{T_c \Delta T f}\right) \qquad \text{Eq. 2.4}$$

where G is the spherulitic growth rate, G_0 is the growth rate constant, U^* is the activation energy for the transport of macromolecular segments to the crystallization site (a typical constant value is assumed, i.e., 6280 J/mol), R is the universal gas constant, T_c is the crystallization temperature, T_∞ is the hypothetical temperature at which all motion associated with viscous flow ceases (expressed as T_g – 30K), K_g is the nucleation parameter, ΔT is the supercooling ($T_m^{\,0} - T_c$) and f is a temperature dependant correction factor ($f = 2T/(T_m^{\,0} - T)$).

G_0 is the growth rate constant, defined as:

$$G_0 = \frac{c_i}{n_u} \qquad \text{Eq. 2.5}$$

where C_i is a value dependent on the growth regime, and n_u represents the number of repetitive units of the macromolecular chain in the lineal interval. Therefore, following equation 2.4, higher the molecular weight, lower the crystal growth rate.

The nucleation parameter K_g is defined as:

$$K_g = \frac{jb\sigma\sigma_e T_m^0}{k\Delta H} \qquad \text{Eq. 2.6}$$

where k is the Boltzmann constant (1.38 x 10^{-23} J/K), ΔH is the heat of fusion per unit volume (2.80 x 10^8 J/m^3), $T_m{}^0$ is the equilibrium melting temperature, b is the layer thickness, σ is the specific free energy of lateral surfaces, σ_e is the specific free energy of the folding surface, and j depends on the regime (4 for regime I and II, 2 for regime II)[91, 141, 185].

2.4.2. The Avrami Equation

Evans, Kolmogoroff, Johnson and Mehl, and Avrami developed the Avrami equation in the 1930s and 1940s to describe the crystallization phenomenon in polymers. The model assumed that crystallization starts randomly at different locations and propagates from the nucleation sites[185]. Although there are some limitations and considerations, the simplest form of the Avrami equation can be expressed as the following equation[189, 200]:

$$1 - V_c = \exp(-k\mathrm{t}^n) \qquad \text{Eq. 2.7}$$

where V_c is the relative volumetric transformed fraction, n is the Avrami index, k the overall crystallization rate constant which includes contributions from both nucleation and growth and t is the experimental time.

The Avrami index value depends on the mechanism of nucleation and on the dimensionality of crystal growth and it consist in two terms[189]:

$$n = n_d + n_n \qquad \text{Eq. 2.8}$$

where n_n represents the time dependence of the nucleation and n_d the dimensionality of the growing crystals.

The values of the term n_n range from 0 to 1, where 0 corresponds to instantaneous nucleation (n_n=0) and 1 to sporadic nucleation (n_n=1). The possible dimensions of the growing crystal (n_d) are 2 or 3 in polymers; and they represent two dimensional lamellar aggregates (axialites) or superstructural three dimensional aggregates (spherulites), respectively. However, nucleation may not be completely instantaneous or sporadic and values between 0 and 1 are obtained. Hence, there are different combinations, shown in Table 2.1[178, 189, 197, 200, 201].

Table 2.1. Avrami Index *n* for various types of nucleation and crystal dimensionality

Avrami Index (*n*)	Crystal Dimensionality (n_d)	Nucleation Dependence (n_n)	Description
1	1	0	Instantaneous needle
2	1	1	Sporadic needle
2	2	0	Instantaneous axialite
3	2	1	Sporadic axialite
3	3	0	Instantaneous spherulite
4	3	1	Sporadic spherulite

The constant k provides a quantitative evaluation of the crystallization evolution, since it includes the contribution of both nucleation and crystal growth. It is directly related to the overall crystallization rate ${t_{1/2}}^{-1}$ and follows next equation[200]:

$$K = \left({t_{1/2}}^{-1}\right)^{n} ln2 \approx 0.7 \left({t_{1/2}}^{-1}\right)^{n} \qquad \text{Eq. 2.9}$$

where ${t_{1/2}}^{-1}$ is the inverse of the half of the crystallization time, and $t_{1/2}$ corresponds to the time needed to achieve 50 % of the overall crystallization.

The Avrami equation is useful to analyze isothermal crystallization data, which gives information about the variation of the crystalline content as a function of time at a constant crystallization temperature (T_c). Many experimental methods measure the overall crystallization rate by following a change in a property sensitive to crystallinity, such as small-angle x-ray scattering, nuclear magnetic resonance or differential scanning calorimetry (DSC) among others[178]. However, the most popular technique to follow crystallization kinetics is the DSC due to its simplicity to fit the experimental data to the Avrami equation, although two factors are of vital importance in order to get a good fitting: the relative volumetric conversion range and the correction of the induction time[189, 197].

The Avrami equation describes the overall transformation rate until the impingement of the crystals, which occurs when primary crystallization ends (at V_c<40~50 %), and that is why a conversion range within primary crystallization data should be chosen for the fitting. It can also be defined as the time needed to achieve 50 % of the overall crystallization. Lorenzo et al.[197] determined that a range between 3 and 20% is recommended (it ensures that no impingment between spherulites has occurred and therefore the free growth approximation of the Avrami theory is satisfied), omitting the initial data points due to experimental errors, and beyond 50 % because the secondary crystallization produces some deviations due to a reorganization process.

In addition, mathematically, the Avrami equation is defined when crystallization starts, so the induction time t_0 (or incubation time before crystallization starts) has to be subtracted, modifying the classical Avrami Equation 2.7 into Equation 2.10. Applying logarithmic to both sides, Equation 2.11 is obtained:

$$1 - V_c = \exp(-k(t - t_0)^n) \qquad \text{Eq. 2.10}$$

$$\log(-\ln[1 - \mathrm{V_c}(\mathrm{t} - \mathrm{t_o})]) = \log k + \mathrm{n}\log(\mathrm{t} - \mathrm{t_0}) \qquad \text{Eq. 2.11}$$

This way, the Avrami fit can be properly applied to isothermal crystallization data. The relative volumetric fraction (V_c) is calculated as:

$$V_\mathrm{c} = \frac{W_c}{W_c + \left(\frac{\rho_c}{\rho_a}\right)(1 - W_c)} \qquad \text{Eq. 2.12}$$

where W_c is the mass fraction of the sample, ρ_c the density of a 100% crystalline sample, and ρ_a is the density of 100% amorphous sample. W_c is calculated from Equation 2.13, from the integration of the DSC experimental data measured during the isothermal crystallization[87]:

$$W_c = \frac{\Delta H\ (t)}{\Delta H_{total}} \qquad \text{Eq. 2.13}$$

where ΔH(t) is the enthalpy variation as a function of the time spent at a given crystallization temperature and ΔH_total is the maximum enthalpy value reached at the end of the isothermal crystallization process[189].

Following Equation 2.11 the Avrami plot can be constructed (Figure 2.7a) by applying a linear fit in the adequate range (as mentioned before between 3 and 20 %). This way, the Avrami index (n) can be obtained from the slope, and the overall crystallization rate constant (k) from the intercept. Correlation data (R^2) value close to 0.9999 is recommended in order to obtain a good fit.

Then, the predicted exotherm of crystallization and the theoretical relative untransformed fraction (i.e. 1-V_c) as a function of time is constructed and compared to experimental data. Figure 2.7b-c shows the comparison between some theoretical and experimental data obtained by the Origin plug-in developed by Lorenzo et al.[197].

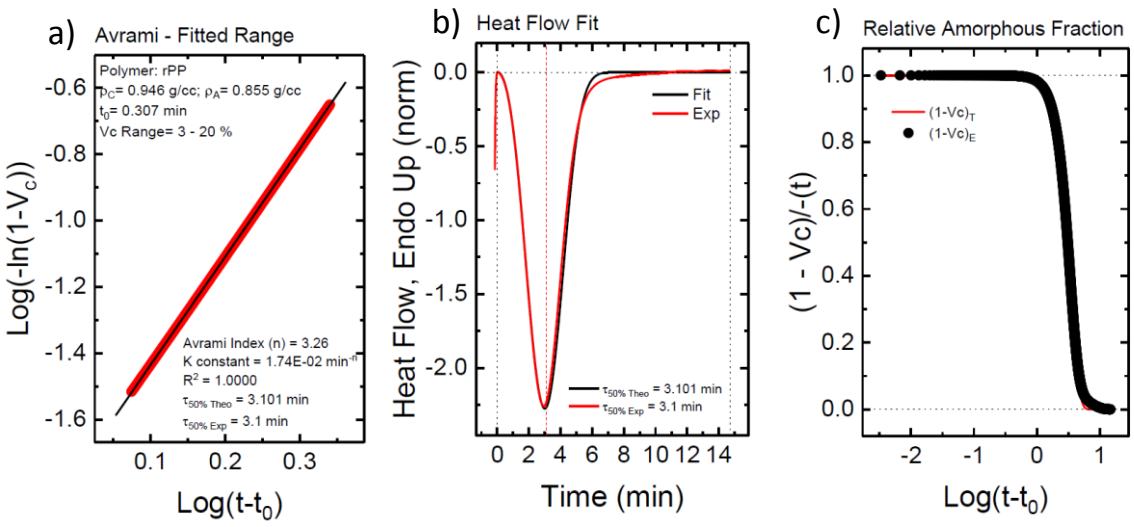

Figure 2.7. Avrami fits obtained by Origin: a) Representation of the Avrami equation, b) Isothermal curve fit, and c) Untransformed relative amorphous fraction (1- V_c) as a function of time

2.5. References

1. Arif P., M.; Kalarikkal, N.; Thomas, S., Introduction on crystallization in multiphase polymer systems. In *Crystallization in multiphase polymer systems*, Thomas, S.; Arif P., M.; Gowd, E. B.; K., K., Eds. Elsevier: **2018**; pp 1-13.

2. Zhang, M. C.; Guo, B. H.; Xu, J., A review on polymer crystallization theories. *Crystals* **2017,** *7(1)*, 1-37.

3. Zeng, N.; Bai, S. L.; G'Sell, C.; Hiver, J. M.; Mai, Y. W., Study on the microstructures and mechanical behavior of compatibilized polypropylene/polyamide-6 blends. *Polymer International* **2002,** *51*, 1439-1447.

4. Liu, H.; Xie, T.; Zhang, Y.; Ou, Y.; Yang, G., Phase morphology development in PP/PA6 blends induced by a maleated thermoplastic elastomer. *Journal of Polymer Science Part B: Polymer Physics* **2006,** *44*, 1050-1061.

5. Moon, H. S.; Ryoo, B. K.; Park, J. K., Concurrent crystallization in polypropylene/nylon-6 blends using maleic anhydride grafted polypropyene as a compatibilizing agent. *Journal of Polymer Science Part B: Polymer Physics* **1994,** *32*, 1427-1435.

6. Tang, T.; Huang, B., Fractionated crystallization in polyolefins-nylon 6 blends. *Journal of Applied Polymer Science* **1994,** *53*, 355-360.

7. Ikkala, O. T.; Holsti-Miettinen, R. M.; Seppälä, J., Effects of compatibilization on fractionated crystallization of PA6/PP blends. *Journal of Applied Polymer Science* **1993,** *49*, 1165-1174.

8. Cyras, V. P.; D'Amico, D. A.; Manfredi, L. B., Crystallization behavior of polymer nanocomposites. In *Crystallization in multiphase polymer systems*, Thomas, S.; Arif P., M.; Gowd, E. B.; Kalarikkal, N., Eds. Elsevier: **2018**; pp 269-306.

9. D'Amico, D. A.; Cyras, V. P.; Manfredi, L. B., Non-isothermal crystallization kinetics from the melt of nanocomposites based on poly(3-hydroxybutyrate) and modified clays. *Thermochim Acta* **2014,** *594*, 80-88.

10. D'Amico, D. A.; Manfredi, L. B.; Cyras, V. P., Crystallization behavior of poly(3-hydroxybutyrate) nanocomposites based on modified clays: effect of organic modifiers. *Thermochim Acta* **2012,** *544*, 47-53.

11. Lai, S. M.; Wu, S. H.; Lin, G. G.; Don, T. M., Unusual mechanical properties of melt-blended poly(lactid acid) (PLA)/clay nanocomposites. *European Polymer Journal* **2014,** *52*, 193-206.

12. Krikorian, V.; Pochan, D., Unusual crystallization behavior of organoclay reinforced poly(L-lactid acid)nanocomposites. *Macromolecules* **2004,** *37*, 6480-6491.

13. Smith, L.; Vasanthan, N., Effect of clay on melt crystallization, crystallization kinetics and spherulitic morphology of poly(trimethyleneterephthalate) nanocomposites. *Thermochim Acta* **2015,** *617*, 152-162.

14. Papageorgiou, G. Z.; Karandrea, E.; Giliopoulos, D.; Papageorgiou, D. G.; Ladavos, A.; Katerinopoulou, A.; Achilias, D. S.; Triantafyllidis, K. S.; Bikiaris, D. N., Effect of clay structure and type of organomodifier on the thermal properties of poly(ethylene terephthalate) based nanocomposites. *Thermochim Acta* **2014,** *576*, 84-96.

15. Perez, C. J.; Alvarez, V. A., Overall crystallization behavior of polypropylene-clay nanocomposites; effect of clay content and polymer/clay compatibility on the bulk crystallization and sphrulitic growth. *Journal of Applied Polymer Science* **2009,** *114*, 3248-3260.

16. Yuan, Q.; Awate, S.; Misra, R. D. K., Nonisothermal crystallization behavior of melt-intercalated polyethylene-clay nanocomposites. *Journal of Applied Polymer Science* **2006,** *102*, 3809-3818.

17. Maiti, P.; Okamoto, M., Crystallization controled by silicate surfaces in nylon 6-clay nanocomposites. *Macromolecular Materials and Engineering* **2003,** *288*, 440-445.

18. Aubry, T., An overview on clay-mediated compatibilization of polyethylene/polyamide blends with droplet morphology. *Applied Clay Science* **2019,** *175*, 184-189.

19. Huitric, J.; Ville, J.; Mederic, P.; Aubry, T., Solid-state morphology, structure, and tensile properties of polyethylene/polyamide/nanoclay blends: Effect of clay fraction. *Polymer Testing* **2017,** *58*, 96-103.

20. Nuzzo, A.; Bilotti, E.; Peijs, T.; Acierno, D.; Filoppone, G., Nanoparticle-induced co-continuity in immiscible polymer blends - A comparative study on bio-based PLA-PA11 blends filled with organoclay, sepiolite, and carbon nanotubes. *Polymer* **2014,** *55*, 4908-4919.

21. Filippone, G.; Causa, A.; Luna, M. S.; Sanguigno, L.; Acierno, D., Assembly of plate-lie nanoparticles in immiscible polymer blends - effect of the presence of a preferred liquid-liquid interface. *Soft Matter* **2014,** *10*, 3183-3191.

22. Sinha Ray, S.; Bousmina, M., Effect of organic modification on the compatibilization efficiency of clay in an immiscible polymer blend. *Macromolecular Rapid Communications* **2005,** *26*, 1639-1646.

23. Sinha Ray, S.; Pouliot, S.; Bousmina, M.; Utracki, L. A., Role of organically modified layered silicate as an active interfacial modifier in immiscible polystyrene/polypropylene blends. *Polymer* **2004,** *45*, 8403-8413.

24. Chen, B.; Evans, J. R. G., Mechanical properties of polymer-blend nanocomposites with organoclays: Polystyrene/ABS and high impact polystyrene/ABS. *Journal of Polymer Science Part B: Polymer Physics* **2011,** *49*, 443-454.

25. Ma, D.; Akpalu, Y. A.; Li, Y.; Siegel, R. W.; Schadler, L. S., Effect of titania nanoparticles on the morphology of low density polyethylene. *Journal of Polymer Science: Polymer Physics* **2005,** *43*, 488-497.

26. Xia, X.; Cai, S.; Xie, C., Preparation, structure and thermal stability of Cu/LDPE nanocomposites. *Materials Chemistry and Physics* **2006,** *95*, 122-129.

27. Huang, Z.; Wang, S.; Kota, S.; Pan, Q.; Barsoum, M. W.; Li, C. Y., Structure and crystallization behavior of poly(ethylene oxide)/$Ti_3C_2T_x$ MXene nanocomposites. *Polymer* **2016,** *102*, 119-126.

28. Olmos, D.; Domínguez, C.; Castrillo, P. D.; Gonzalez-Benito, J., Crystallization and final morphology of HDPE: effect of the high energy ball milling and the presence of TiO_2 nanoparticles. *Polymer* **2009,** *50*, 1732-1742.

29. Sangroniz, L.; Moncerrate, M. A.; De Amicis, V. A.; Palacios, J. P.; Fernández, M.; Santamaría, A.; Sánchez, J. J.; Laoutid, F.; Dubois, P.; Müller, A. J., The outstanding ability of nanosilica to stabilize dispersions of nylon 6 droplets in a polypropylene matrix. *Polymer Physics* **2015,** *53*, 1567-1579.

30. Sangroniz, L.; Ruiz, J. L.; Sangroniz, A.; Fernández, M.; Etxeberria, A.; Müller, A. J.; Santamaría, A., Polyethylene terephthalate/low density polyethylene/titanium dioxide blend nanocomposites: Morphology, crystallinity, rheology, and transport properties. *Journal of Applied Polymer Science* **2019,** *2*, 46986.

31. Palacios, J. K.; Sangroniz, A.; Eguiazabal, J. I.; Etxeberria, A.; Müller, A. J., Tailoring the properties of PP/PA6 nanostructured blends by the addition of nanosilica and compatibilizer agents *European Polymer Journal* **2016,** *85*, 532-552.

32. Chen, E. C. H.; Wu, T. M., Isothermal and nonisothermal crystallization kinetics of nylon 6/functionalized multi-walled carbon nanotube composites. *Journal of Polymer Science: Polymer Physics* **2008,** *46*, 158-169.

33. Zeng, R. T.; Hu, W.; Wang, M.; Zhang, S. D.; Zeng, J. B., Morphology, rheological and crystallization behavior in nonovalently functionalized carbon nanotube reinforced poly(butylenesuccinate) nanocomposites with low percolation threshold. *Polymer Testing* **2016,** *50*, 182-190.

34. Li, J.; Fang, Z.; Tong, L.; Gu, A.; Liu, F., Effect of multi-walled carbon nanotubes on nonisothermal crystallization kinetics of polyamide 6. *European Polymer Journal* **2006,** *42*, 3230-3235.

35. Lin, S. Y.; Chen, E. C.; Liu, K. Y.; Wu, T. M., Isothermal crystallization behavior of polyamide 6,6/multiwalled carbon nanotube nanocomposites. *Polymer Engineering and Science* **2009,** *49 (12)*, 2447-2453.

36. Haggenmueller, R.; Fischer, J. E.; Wine, K. I., Single wall carbon nanotube/polyethylene nanocomposites: nucleating and templating polyethylene crystallites. *Macromolecules* **2006,** *39*, 2964-2971.

37. Lim, J. Y.; Kim, J.; Kim, S.; Kwak, S.; Lee, Y.; Seo, Y., Nonisothermal crystallization behaviors of nanocomposites of poly(vinylidene fluoride) and multiwalled carbon nanotubes. *Polymer* **2015,** *62*, 11-18.

38. Papageorgiou, D. G.; Zhuravev, E.; Papageorgiou, G. Z.; Bikiaris, D.; Chrissafis, K.; Schick, C., Kinetics of nucleation and crystallization in poly(butylene succinate) nanocomposites. *Polymer* **2014,** *55*, 6725-6734.

39. Baudouin, A. C.; Auhl, D.; Tao, F.; Devaux, J.; Bailly, C., Polymer blend emulsion stabilization using carbon nanotubes interfacial confinement. *Polymer* **2011,** *52*, 149-156.

40. Baudouin, A. C.; Bailly, C.; Devaux, J., Interface localization of carbon nanotubes in blends of two copolymers. *Polymer Degradation and Stability* **2010,** *95*, 389-398.

41. Deshmukh, G. S.; Peshwe, D. R.; Pathak, S. U.; Ekhe, J. D., Nonisothermal crystallization kinetics and melting behavior of poly(butylene terephthalate) and calcium carbonate nanocomposites. *Thermochim Acta* **2015,** *606*, 66-76.

42. Avella, M.; Cosco, S.; Di Lorenzo, M. L.; Di Pace, E.; M.E., E., Influence of $CaCO_3$ nanoparticles shape on thermal and crystallization behavior of isotactic polypropylene based nanocomposites. *Journal of Thermal Analysis and Calorimetry* **2005,** *80*, 131-136.

43. Supaphol, P.; Harnsiri, W.; Junkasem, J., Effects of calcium carbonate and its purity on crystallization and the melting behavior, mechanical properties, and processability of syndiotactic polypropylene. *Journal of Applied Polymer Science* **2004,** *2004*, 201-212.

44. Avella, M.; Cosco, S.; Di Lorenzo, M. L.; Di Pace, E.; Errico, M. E.; Gentile, G., Nucleation activity of nanosized $CaCO_3$ on crystallization of isotactic polypropylene, in dependence on crystal modification, particle shape, and coating. *European Polymer Journal* **2006,** *42*, 1548-1557.

45. Wan, W.; Yu, D.; Guo, X.; Xie, Y., Effect of nanoparticle surface treatment on nonisothermal crystallization behavior of polypropylene/calcium carbonate nanocomposites. *Polymer Plastics Technology and Engineering* **2008,** *47*, 433-442.

46. Huang, J. W.; Wen, Y. L.; Kang, C. C.; Tseng, W. J.; Yeh, M. Y., Nonisothermal crystallization of high density polyethylene and nanoscale calcium carbonate composites. *Polymer Engineering and Science* **2008,** *48*, 1268-1278.

47. Run, M.; Yao, C.; Wang, Y.; Song, H., Nonisothermal crystallization behavior and crystals morphology of poly(trimethylene terephthalate)/nano-calcium carbonate composites. *Polymer Composites* **2008,** *29*, 1235-1243.

48. Rong, M. Z.; Zhang, M. Q.; Zheng, Y. X.; Zeng, H. M.; Walter, R.; Friedrich, K., Structure-property relationships of irradiation grafted nano-inorganic particle filled polypropylene composites. *Polymer* **2001,** *42*, 167-183.

49. Papageorgiou, G. Z.; Achilias, D. S.; Bikiaris, D. N.; Karayannidis, G. P., Crystallization kinetics and nucleation activity of filler in polypropylene/surface-treated SiO_2 nanocomposites. *Thermochim Acta* **2005,** *427*, 117-128.

50. Yang, F.; Ou, Y.; Yu, Z., Polyamide 6/silica nanocomposites prepared by in situ polymerization. *Journal of Applied Polymer Science* **1998,** *69*, 355-361.

51. Li, Y.; Yu, J.; Guo, Z. X., The influence of interphase in nylon-6/nano-SiO_2 composite materials obtained from in situ polymerization. *Polymer International* **2003,** *52(6)*, 981-986.

52. Ke, Y.-C.; Wu, T. B.; Xia, Y. F., The nucleation, crystallization and dispersion behavior of PET-monodisperse SiO_2 composites. *Polymer* **2007,** *48*, 3324-3336.

53. Zhang, Q.; Yang, H.; Fu, Q., Kinetics-controlled compatibilization of immiscible polypropylene/polystyrene blends using nano-SiO_2 particles. *Polymer* **2004,** *45*, 1913-1922.

54. Laoutid, F.; Estrada, E.; Michell, R. M.; Bonnaud, L.; Müller, A. J., The influence of nanosilica on the nucleation, crystallization and tensile properties of PP-PC and PP-PA blends. *Polymer* **2013,** *54*, 3982-3993.

55. Laoutid, F.; Francois, D.; Paint, Y.; Bonnaud, L.; Dubois, P., Using nanosilica to fine-tune morphology and properties of polyamide 6/poly(propylene) blends. *Macromolecular Materials and Engineering* **2013,** *298*, 328-338.

56. Laoutid, F.; Francois, D.; Paint, Y.; Bonnaud, L.; Dubois, P., Morphology and properties of polyamide 6/poly(propylene) blends fine-tuned with nanosilica. *Macromolecular Symposia* **2012,** *321-322*, 90-94.

57. Elias, L.; Fenouillot, F.; Majeste, J. C.; Martin, G.; Cassagnau, P., Migration of silica nanoparticles in polymer blends. *Polmyer Science, Part B: Polymer Physics* **2008,** *46*, 1976-1983.

58. Elias, L.; Fenouillot, F.; Majesté, J. C.; Alcouffe, P.; Cassagnau, P., Immiscible polymer blends stabilized by nano-silica particles:rheology and effective interfacial tension. *Polymer* **2008,** *49*, 4379-4385.

59. Elias, L.; Fenouillot, F.; Majeste, J. C.; Cassagnau, P., Morphology and rheology of immiscible polymer blends filled with silica nanoparticles. *Polymer* **2007,** *48*, 6029.

60. Vermant, J.; Cioccolo, G.; Golapan Nair, K.; Moldenaers, P., Coalescence suppression in model immiscible polymer blends by nano-sized colloidal particles. *Rheological Acta* **2004,** *43*, 529-538.

61. Dhar, P.; Bashney, S. D.; Kumar, A.; Katiyar, V., Acid functionalized cellulose nanocrystals and its effect on mechanical, thermal, crystallization and surfaces properties of poly (lactid acid) bionanocomposites films: a comprehensive study. *Polymer* **2016,** *101*, 75-92.

62. Lizundia, E.; Vilas, J. L.; León, L. M., Crystallization, structural relaxation and thermal degradation in poly(L-lactide)/cellulose nanocrystal renewable nanocomposites. *Carbohydrate Polymers* **2015,** *123*, 256-265.

63. Han, J.; Zhu, Y.; Hu, J.; Luo, H.; Yeung, L. Y.; Li, W., Morphology, reversible phase crystallization, and thermal sensitive shape memory effect of cellulose whiskers/SMPU nanocomposites. *Journal of Applied Polymer Science* **2012,** *123(2)*, 749-762.

64. Nasseri, R.; Mohammadi, N., Starch-based nanocomposites: a comparative performance study of cellulose whiskers and starch nanoparticles. *Carbohydrate Polymers* **2014,** *106*, 432-439.

65. Arrieta, M. P.; Fortunati, E.; Dominici, F.; Rayón, E.; López, J.; Kenny, J. M., Multifunctional PLA-PHB/cellulose nanocrystal films: processing, structural and thermal properties. *Carbohydrate Polymers* **2014,** *107*, 16-24.

66. Rahimi, S. K.; Otaigbe, J. U., The role of particle surface functionality and microstructure development in isothermal and non-isothermal crystallization behavior of polyamide 6/cellulose nanocrystals nanocomposites. *Polymer* **2016,** *107*, 316-331.

67. Matxinandiarena, E.; Múgica, A.; Zubitur, M.; Yus, C.; Sebastián, V.; Irusta, S.; Loaeza, A. D.; Santana, O.; Maspoch, M. L.; Puig, C.; Müller, A. J., The effect of titanium dioxide surface modification on the dispersion, morphology and mechanical properties of recycled PP/PET/TiO_2 PBNANOs. *Polymers* **2019,** *11* (10), 1692.

68. Selvin, T. P.; Kuruvilla, J.; Sabu, T., Mechanical properties of titanium dioxide-filled polystyrene microcomposites *Materials Letters* **2004,** *58*, 281-289.

69. Xiu, H.; ai, H. W.; Huang, C. M.; Xu, C. L.; Li, X. Y.; Fu, Q., Selective localization of titanium dioxide nanoparticles at the interface and its effect on the impact toughness of poly(L-lactide)/poly(ether)urethane blends. *Polymer Letters* **2013,** *7*, 261-271.

70. Canto, L. B., Aspects regarding the efficiency of nanosilica as an interfacial compatibilizer of a polypropylene/ethylene vinyl-acetate immiscible blend. *Polymer Testing* **2019,** *73*, 135-142.

71. Fenouillot, F.; Cassagnau, P.; Majesté, J. C., Uneven distribution of nanoparticles in immiscible fluids: Morphology development in polymer blends. *Polymer* **2009,** *50*, 1333-1350.

72. Salzano de Luna, M.; Filippone, G., Effects of nanoparticles on the morphology of immiscible polymer blends-Challenges and opportunities. *European Polymer Journal* **2016,** *83*, 10-21.

73. Palacios, J. K.; Sangroniz, A.; Eguiazabal, J. I.; Etxeberria, A.; Müller, A. J., Tailoring the properties of PP/PA6 nanostructured blends by the addition of nanosilica and compatibilizer agents. *European Polymer Journal* **2016,** *85*, 532-552.

74. Nitta, K. H.; Asuka, K.; Liu, B.; Terano, M., The effect of the addition of silica particles on linear spherulite growth rate of isotactic polypropylene and its explanation by lamellar cluster model. *Polymer* **2006,** *47(18)*, 6457-6463.

75. Müller, A. J.; Arnal, M. L.; Lorenzo, A. T., Crystallization in nano-confined polymeric systems. In *Handbook of polymer crystallization*, Piorkowska, E.; Rutledge, G. C., Eds. John Wiley and Sons: Hoboken, New Jersey (USA), **2013**; pp 347-372.

76. Hamley, I. W., *The Physics of Block Copolymers*. Oxford University Press: Oxford, **1998**.

77. Abetz, V.; Simon, P. F. W., Phase behaviour and morphologies of block copolymers. *Advances in Polymer Science* **2005,** *189*, 125-212.

78. De Rosa, C.; Di Girolamo, R.; Malafronte, A.; Scoti, M.; Talarico, G.; Auriemma, F.; Ruiz de Ballesteros, O., Polyolefins based crystalline block copolymers: ordered nanostructures from control of crystallization. *Polymer* **2020,** *196*, 122423.

79. Li, S.; Register, A., Crystallization in Copolymers. In *Handbook of Polymer Crystallization*, Piorkowska, E.; Rutledge, G. C., Eds. John Wiley and Sons: Hoboken, NJ, **2013**; p 327.

80. Ryan, A. J.; Hamley, I. W.; Bras, W.; Bates, F. S., Structure development in semicrystalline diblock copolymers crystallizing from the ordered melt. *Macromolecules* **1995,** *28*, 3860-3868.

81. Douzinas, K. C.; Cohen, R. E.; Halasa, A. F., Evaluation of domain spacing scaling laws for semicrystalline diblock copolymers. *Macromolecules* **1991,** *24*, 4457-4459.

82. Rangarajan, P.; Register, R. A.; Adamson, D. H.; Fetters, L. J.; Bras, W.; Naylor, S.; Ryan, A. J., Dynamics of structure formation in crystallizable block copolymers. *Macromolecules* **1995,** *28*, 1422-1428.

83. Rangarajan, P.; Register, R. A.; Fetters, L. J.; Bras, W.; Naylor, S.; Ryan, A. J., Crystallization of a weakly segregated polyolefin diblock copolymer. *Macromolecules* **1995,** *28*, 4932-4938.

84. Rohadi, A.; Endo, R.; Tanimoto, S.; Sasaki, S.; Nojima, S., Effects of molecular weight and crystallization temperature on the morphology formation in asymmetric diblock copolymers with a highly crystalline block. *Polymer Journal* **2000,** *32*, 602-609.

85. Quiram, D. J.; Register, R. A.; Marchand, G. R., Crystallization of asymmetric diblock copolymers from microphase-separated melts. *Macromolecules* **1997,** *30*, 4551-4558.

86. Palacios, J. P.; Mugica, A.; Zubitur, M.; Müller, A. J., Crystallization and morphology of block copolymers and terpolymers with more than one crystallizable block. In *Crystallization in multiphase polymer systems*, Thomas, S.; Arif P., M.; Gowd, E. B.; Kalarikkal, N., Eds. Elsevier: **2018**; pp 123-171.

87. Castillo, R. V.; Müller, A. J., Crystallization and morphology of biodegradable or biostable single and double crystalline block copolymers. *Progress in Polymer Science* **2009,** *34*, 516-560.

88. Müller, A. J.; Arnal, M. L.; Balsamo, V., Crystallization in block copolymers with more than one crystallizable block. In *Progress in understanding of polymer crystallization*, Reiter, G.; Strobl, G. R., Eds. Lecture Notes in Physics: Springer, Berlin, Heidelberg, **2007**; Vol. 714, pp 229-259.

89. Müller, A. J.; Balsamo, V.; Arnal, M. L., Nucleation and crystallization in diblock and triblock copolymers. In *Block copolymers II*, Abetz, V., Ed. Springer, Berlin, Heidelberg: Advances in Polymer Science, **2005**; Vol. 190, pp 1-63.

90. Michell, R. M.; Müller, A. J., Confined crystallization of polymeric materials. *Progress in Polymer Science* **2016,** *54-55*, 183-216.

91. Müller, A. J.; Albuerne, J.; Marquez, L.; Raquez, J. M.; Degée, P.; Dubois, P.; Hobbs, J.; Hamley, I. W., Self-nucleation and crystallization kinetics of double crystalline poly(p-dioxanone)-*b*-poly(ε-caprolactone) diblock copolymers. *Faraday Discuss* **2005,** *128*, 231-252.

92. Castillo, R. V.; Müller, A. J.; Raquez, J. M.; Dubois, P., Crystallization kinetics and morphology of biodegradable double crystalline PLLA-*b*-PCL diblock copolymers. *Macromolecules* **2010,** *43*, 4149-4160.

93. Hamley, I. W.; Parras, P.; Castelletto, V.; Castillo, R. V.; Müller, A. J.; Pollet, E.; Dubois, P.; Martin, C. M., Melt structure and its transformation by sequential crystallization of the two blocks within poly(L-lactide)-*block*- poly(ε-caprolactone) double crystalline diblock copolymers. *Macromolecular Chemistry and Physics* **2006,** *207*, 941-953.

94. Hamley, I. W.; Castelletto, V.; Castillo, R. W.; Müller, A. J.; Martin, C. M.; Pollet, E.; Dubois, P., Crystallization in poly(L-lactide)-*b*-poly(ε-caprolactone) double crystalline diblock copolymers: a study using X-ray scattering, differential scanning calorimetry and polarized optical microscopy. *Macromolecules* **2005,** *38*, 463-472.

95. Myers, S. B.; Register, R. A., Crystalline-crystalline diblock copolymers of linear polyethylene and hydrogenated polynorbornene. *Macromolecules* **2008,** *41*, 6773-6779.

96. Müller, A. J.; Albuerne, J.; Esteves, L. M.; Marquez, L.; Raquez, J.-M.; Degée, P.; Dubois, P.; Collins, S.; Hamley, I. W., Confinement effects on the crystallization kinetics and self-nucleation of double crystalline poly(p-dioxanone)-*b*-poly(ε-caprolactone) diblock copolymers. *Macromolecular Symposia* **2004,** *215*, 369-382.

97. Albuerne, J.; Máquez, L.; Müller, A. J.; Raquez, J. M.; Degée, P.; Dubois, P.; Castelleto, V.; Hamley, I. W., Nucleation and crystallization in double crystalline

poly(p-dioxanone)-*b*-poly(ε-caprolactone) diblock copolymers. *Macromolecules* **2003,** *36*, 1633-1644.

98. Laredo, E.; Prutsky, N.; Bello, A.; Grimau, M.; Castillo, R. V.; Müller, A. J.; Dubois, P., Miscibility in poly(ʟ-lactide)-*b*-poly(ε-caprolactone) double crystalline diblock copolymers. *European Physical Journal E* **2007,** *23*, 295-303.

99. Ponjavic, M.; Nikolic, M. S.; Jevtic, S.; Roga, J.; Stevanovic, S.; Djonlagic, J., Influence of a low content of PEO segment on the thermal, surface and morphological properties of triblock and diblock PCL copolymers. *Macromolecular research* **2016,** *24*, 323-335.

100. Li, Y.; Huang, H.; Wang, Z.; He, T., Tuning radial lamellar packing and orientation into diverse ring-banded spherulites: effects of structural feature and crystallization condition. *Macromolecules* **2014,** *47*, 1783-1792.

101. Li, L.; Meng, F.; Zhong, Z.; Byelov, D.; De Jeu, W. H.; Feijen, J., Morphology of a highly asymmetric double crystallizable poly(ε-caprolactone-*b*-ethylene oxide) block copolymer. *The Journal of Chemical Physics* **2007,** *126*, 024904.

102. Van Horn, R. M.; Zheng, J. X.; Sun, H. J.; Hsiao, M. S.; Zhang, W. B.; Dong, X. H.; Xu, J.; Thomas, E. L.; Lotz, B.; Chen, S. Z. D., Solution crystallization behavior of crystalline-crystalline diblock copolymers of poly(ethylene oxide)-*block*-poly(ε-caprolactone). *Maromolecules* **2010,** *43*, 6113-6119.

103. Vivas, M.; Contreras, J.; López-Carrasquero, F.; Lorenzo, A. T.; Arnal, M. L.; Balsamo, V.; Müller, A. J.; Laredo, E.; Schmalz, H.; Abetz, V., Synthesis and characterization of triblock terpolymers with three potentially crystallizable blocks: polyethylene-*b*-poly(ethylene oxide)-*b*-poly(ε-caprolactone). *Macrolecular Symposia* **2006,** *239*, 58-67.

104. Jiang, S.; He, C.; An, L.; Chen, X.; Jiang, B., Crystallization and ring-banded spherulite morphology of poly(ethylene oxide)-*block*-poly(ε-caprolactone) diblock copolymer. *Macromolecular Chemistry and Physics* **2004,** *205*, 2229-2234.

105. Arnal, M. L.; López-Carrasquero, F.; Laredo, E.; Müller, A. J., Coincident or sequential crystallization of PCL and PEO blocks within polystyrene-*b*-poly(ethylene oxide)-*b*-poly(ε-caprolactone) linear triblock copolymers. *European Polymer Journal* **2004,** *40*, 1461-1476.

106. Nojima, S.; Ono, M.; Ashida, T., Crystallization of block copolymers II. Morphological study of poly (ethylene glycol)-poly (ε-caprolactone) block copolymers. *Polymer Journal* **1992,** *24*, 1271-1280.

107. Wei, Z.; Liu, L.; Yu, F.; Wang, P.; Qi, M., Synthesis and characterization of poly(ε-caprolactone)-*b*-poly(ethylene glycol)-*b*-poly(ε-caprolactone) triblock copolymers with dibutylmagnesium as catalyst. *Journal of applied polymer science* **2009,** *111*, 429-436.

108. Arnal, M. L.; Boissé, S.; Müller, A. J.; Meyer, F.; Raquez, J. M.; Dubois, P.; Prud`homme, R. E., Interplay between poly(ethylene oxide) and poly(L-lactide) blocks during diblock copolymer crystallization. *CrystEngComm* **2016,** *18*, 3635-3649.

109. Zhou, D.; Sun, J.; Shao, J.; Bian, X.; Huang, S.; Li, G.; Chen, X., Unusual crystallization and melting behaviour induced by microphase separation in MPEG-*b*-PLLA diblock copolymer. *Polymer* **2015,** *80*, 123-129.

110. Yang, J.; Liang, Y.; Han, C. C., Effect of crystallization temperature on the interactive crystallization behavior of poly(L-lactide)-*block*-poly (ethylene glycol) copolymer. *Polymer* **2015,** *79*, 56-64.

111. Huang, S.; Li, H.; Jiang, S.; Chen, X.; An, L., Morphologies and structures in poly(L-lactide-*b*-ethylene oxide) copolymers determined by crystallization, microphase separation and vitrification. *Polymer Bulletin* **2011,** *67*, 885-902.

112. Huang, S.; Jiang, S.; An, L.; Chen, X., Crystallization and morphology of poly(ethylene oxide-*b*-lactide) crystalline-crystalline diblock copolymers. *Journal of Polymer Science, Part B: Polymer Physics* **2008,** *46*, 1400-1411.

113. Huang, C. I.; Tsai, S. H.; Chen, C. M., Isothermal crystallization behaviour of poly(L-lactide) in poly(L-lactide)-*block*-poly(ethylene glycol) diblock copolymers. *Journal of Polymer Science: Part B: Polymer Physics* **2006,** *44*, 2438-2448.

114. Sun, J.; Hong, Z.; Yang, L.; Tang, Z.; Chen, X.; Jing, X., Study on crystalline morphology of poly(L-lactide)-poly(ethylene glycol) diblock copolymer. *Polymer* **2004,** *45*, 5969-5977.

115. Shin, D.; Shin, K.; Aamer, K. A.; Tew, G. N.; Russell, T. P.; Lee, J. H.; Jho, J. Y., A morphological study of a semicrystalline poly(L-lactic acid-*b*-ethylene oxide-*b*-L-lactic acid) triblock copolymer. *Macromolecules* **2005** *38*, 104-109.

116. Wang, J. L.; Dong, C. M., Synthesis, sequential crystallization and morphological evolution of well-defined star-shaped poly(ε-caprolactone)-*b*-poly(L-lactide) block copolymer. *Macromolecular Chemistry and Physics* **2006,** *207*, 554-562.

117. Liénard, R.; Zaldua, N.; Josse, T.; Winter, J. D.; Zubitur, M.; Mugica, A.; Iturrospe, A.; Arbe, A.; Coulembier, O.; Müller, A. J., Synthesis and characterization of double crystalline cyclic diblock copolymers of poly(ε-caprolactone) and poly(L(D)-lactide) (c(PCL-*b*-PL(D)LA)). *Macromolecular Rapid Communications* **2016,** *37*, 1676-1681.

118. Navarro-Baena, I.; Marcos-Fernández, A.; Fernández-Torres, A.; Kenny, J. M.; Peponi, L., Synthesis of PLLA-*b*-PCL-*b*-PLLA linear tri-block copolymers and their corresponding poly(ester-urethane)s: Effect of the molecular weight on their crystallization and mechanical properties. *RSC Advances* **2014,** *4*, 8510-8524.

119. Castillo, R. V.; Müller, A. J.; Lin, M. C.; Chen, H. L.; Jeng, U. S.; Hillmyer, M. A., Confined crystallization and morphology of melt segregated PLLA-*b*-PE and PLDA-*b*-PE diblock copolymers. *Macromolecules* **2012,** *45*, 4254-4261.

120. Müller, A. J.; Castillo, R. V.; Hillmyer, M., Nucleation and crystallization of PLDA-*b*-PE and PLLA-*b*-PE diblock copolymers. *Macromolecular Symposia* **2006,** *242*, 174-181.

121. Müller, A. J.; Lorenzo, A. T.; Castillo, R. V.; Arnal, M. L.; Boschetti-de-Fierro, A.; Abetz, V., Crystallization kinetics of homogeneous and melt segregated PE containing diblock copolymers. *Macromolecular Symposia* **2006,** *245-246*, 154-160.

122. Lin, M. C.; Wang, Y. C.; Chen, J. H.; Chen, H. L.; Müller, A. J.; Su, C. J.; Jeng, U. S., Orthogonal crystal orientation in double-crystalline block copolymer. *Macromolecules* **2011,** *44*, 6875-6884.

123. Boschetti-De-Fierro, A.; Fierro, D.; Albuerne, J.; Funari, S. S.; Abetz, V., Thermal monitoring of morphology in triblock terpolymers with crystallizable blocks. *Journal of Polymer Science B: Polymer Physics* **2007,** *45*, 3197-3206.

124. Sun, L.; Liu, Y.; Zhu, L.; Hsiao, B. S.; Avila-Orta, C. A., Pathway-dependent melting in a low-molecular weight polyethylene-*block*-poly(ethylene oxide) diblock copolymer. *Macromolecular rapid communications* **2004,** *25*, 853-857.

125. Boschetti-de-Fierro, A.; Müller, A. J.; Abetz, V., Synthesis and characterization of novel linear PB-*b*-PS-*b*-PEO and PE-*b*-PS-*b*-PEO triblock terpolymers. *Macromolecules* **2007,** *40*, 1290-1298.

126. Boschetti-de-Fierro, A.; Lorenzo, A. T.; Müller, A. J.; Schmalz, H.; Abetz, V., Crystallization kinetics of PEO and PE in different terpolymers: effect of microdomain geometry and confinement. *Macromolecular Chemistry and Physics* **2008,** *209*, 476-487.

127. Schmalz, H.; Knoll, A.; Müller, A. J.; Abetz, V., Synthesis and characterization of ABC triblock copolymers with two different crystalline end blocks: influence of confinement on crystallization behavior and morphology. *Macromolecules* **2002,** *35*, 10004-10013.

128. Castillo, R. V.; Arnal, M. L.; Müller, A. J.; Hamley, I. W.; Castelleto, V.; Schmalz, H.; Abetz, V., Fractionated crystallization and fractionated melting of confined PEO microdomains in PB-*b*-PEO and PE-*b*-PEO diblock copolymers. *Macromolecules* **2008,** *41*, 879-889.

129. Weiyu, C.; Tashiro, K.; Hanesaka, M.; Takeda, S.; Masunaga, H.; Sasaki, S.; Takata, M., Relationship between morphological change and crystalline phase transitions of polyethylene-poly(ethylene oxide) diblock copolymers, revealed by the temperature-dependent synchrotron WAXD/SAXS and infrared/Raman spectral measurements. *Journal of Physical Chemistry B* **2009,** *113*, 2338-2346.

130. Nojima, S.; Akutsu, Y.; Washino, A.; Tanimoto, S., Morphology of melt-quenched poly (ε-caprolactone)-*block*-polyethylene copolymers. *Polymer* **2004,** *45*, 7317-7324.

131. Nojima, S.; Ito, K.; Ikeda, H., Composition dependence of crystallized lamellar morphology formed in crystalline-crystalline diblock copolymers. *Polymer* **2007,** *48*, 3607-3611.

132. Sakurai, T.; Ohguma, Y.; Nojima, S., Morphological evolution during isothermal crystallization observed in a crystalline-crystalline diblock copolymer. *Polymer Journal* **2008,** *40*, 971-978.

133. Sakurai, T.; Nagakura, H.; Gondo, S.; Nojima, S., Crystallization of poly(ε-caprolactone) blocks confined in crystallized lamellar morphology of poly(ε-caprolactone)-*block*-polyethylene copolymers:effects of polyethylene crystallinity and confinement size. *Polymer Journal* **2013,** *45*, 436-443.

134. Palacios, J. K.; Mugica, A.; Zubitur, M.; Iturrospe, A.; Arbe, A.; Liu, G.; Wang, D.; Zhao, J.; Hadjichristidis, N.; Müller, A. J., Sequential crystallization and morphology of triple crystalline biodegradable PEO-*b*-PCL-*b*-PLLA triblock terpolymers. *Royal Society of Chemistry Adv.* **2016,** *6*, 4739.

135. Palacios, J. K.; Tercjak, A.; Liu, G.; Wang, D.; Zhao, J.; Hadjicrhistidis, N.; Müller, A. J., Trilayered morphology of an ABC triple crystalline triblock terpolymer. *Macromolecules* **2017,** *50*, 7261-7281.

136. Palacios, J. K.; Liu, G.; Wang, D.; Hadjichristidis, N.; Müller, A. J., Generating triple crystalline superstructures in melt-miscible PEO-*b*-PCL-*b*-PLLA triblock terpolymers by controlling thermal history and sequential crystallization. *Macromolecular Chemistry and Physics* **2019,** *220*, 1900292.

137. Chiang, Y. W.; Hu, Y. Y.; Li, J. N.; Huang, S. H.; Kuo, S. W., Trilayered single crystals with epitaxial growth in poly(ethylene oxide)-*block*-poly(ε-caprolactone)-*block*-poly(L-lactide)thin films. *Macromolecules* **2015,** *48*, 8526-8533.

138. Matxinandiarena, E.; Múgica, A.; Zubitur, M.; Zhang, B.; Ladelta, V.; Zapsas, G.; Hadjichristidis, N.; Müller, A. j., The effect of the cooling rate on the morphology and crystallization of triple crystalline PE-*b*-PEO-*b*-PLLA and PE-*b*-PCL-*b*-PLLA triblock terpolymers. *ACS Applied Polymer Materials* **2020,** *2*, 4952-4963.

139. Palacios, J. K.; Zhang, H.; Zhang, B.; Hadjichristidis, N.; Müller, A. J., Direct identification of three crystalline phases in PEO-*b*-PCL-*b*-PLLA tribock terpolymer by in situ hot-stage atomic force microscopy. *Polymer* **2020,** *205*, 122863.

140. Sun, L.; Shen, L. J.; Zhu, M. Q.; Dong, C. M.; Wei, Y., Synthesis, self-assembly, drug-release behavior, and cytotoxicity of triblock and pentablock copolymers composed of poly(ε-caprolactone), poly(L-lactide), and poly(ethylene glycol). *Journal of Polymer Science Part A: Polymer Chemistry* **2010,** *48*, 4583-4593.

141. Liang, G.; Bao, S.; Zhu, F., Theoretical aspects of polymer crystallization in multiphase systems. In *Crystallization in multiphase polymer systems*, Thomas, S.; Arif P., M.; Gowd, E. B.; Kalarikkal, N., Eds. Elsevier: **2018**; pp 17-48.

142. Zhang, B.; Chen, J. B.; Baier, M. C.; Mecking, S.; Reiter, R.; Mulhaupt, R.; Reiter, G., Molecular weight-dependent changes in morphology of solution-grown polyethylene single crystals. *Macromolecular Rapid Communications* **2015,** *36*, 181-189.

143. Scheinhardt, B.; Trzaskowski, J.; Baier, M. C.; Stempfle, B.; Oppermann, A.; Woll, D.; Mecking, S., Anisotropic polyethylene nanocrystals labeled with a single fluorescent dye molecule: toward monitoring of nanoparticle orientation. *Macromolecules* **2013,** *46*, 7902-7910.

144. Rochette, C. N.; Rosenfeldt, S.; Henzler, K.; Polzer, F.; Ballauf, M.; Q., T.; Mecking, S.; Drechsler, M.; Narayanan, T.; Harnau, L., Annealing of single lamella nanoparticles of polyethylene. *Macromolecules* **2011,** *44*, 4845-4851.

145. Barenwald, R.; Goerlitz, S.; Godehardt, R.; Osichow, A.; Tong, Q.; Krumova, M.; Mecking, S.; Saalwächter, K., Local flips and chain motion in polyethylene crystallites: a comparison of melt-crystallized samples, reactor powders, and nanocrystals. *Macromolecules* **2014,** *47*, 5163-5173.

146. Ortmann, P.; Trzaskowski, J.; Krumova, M.; Mecking, S., Precise microstructure self-stabilized polymer nanocrystals. *ACS Macro Letters* **2013,** *2*, 125-127.

147. Zhou, H.; Lu, Y. J.; Zhang, M.; Guerin, G.; Manners, I.; Winnik, M. A., PFS-b-pnipan: a first step toward polymeric nanofibrillar hydrogels based on uniform fiber-like micelles. *Macromolecules* **2016,** *49*, 4265-4276.

148. Nazemi, A.; Boott, C. E.; Lunn, D. J.; Gwyther, J.; Hayward, D. W.; Richardson, R. M.; Winnik, M. A.; Manners, I., Monodisperse cylindrical micelles and block comicelles of controlled length in aqueous media. *Journal of the American Chemical Society* **2016,** *138*, 4484-4493.

149. Li, X. Y.; Jin, B. X.; Gao, Y.; Hayward, D. W.; Winnik, M. A.; Luo, Y. J.; Manners, I., Monodisperse cylindrical micelles of controlled length with a liquid-crystalline perfluorinated core by 1D "Self-Seeding". *Angewandte Chemie International Edition* **2016,** *55*, 11392-11396.

150. Zhang, J. J.; Li, C. W.; Zhang, R.; Zhang, F. Y.; Liu, W.; Liu, X. Y.; Lee, S. M.-Y.; Zhang, H., A phosphinate-based near-infrared fluoescence probe for imaging the superoxide radical anion in vitro and in vivo. *Chemical Comunications* **2016,** *52*, 2679-2682.

151. Guerin, G.; Rupar, P.; Molev, G.; Manners, I.; Jinnai, H.; Winnik, M. A., Lateral growth of 1D core-crystalline micelles upon annealing in solution. *Macromolecules* **2016,** *49*, 7004-7014.

152. Wu, J. L.; Weng, L. T.; Qin, W.; Liang, G. D.; Tang, B. Z., Crystallization-induced redox-active nanoribbons of organometallic polymers. *ACS Macro Letters* **2015,** *4*, 593-597.

153. Wang, W. D.; Qi, H.; Zhou, T.; Mei, S.; Han, L.; Higuchi, T.; Jinnai, H.; Li, C. Y., Highly robust crystalsome via directed polymer crystallization at curved liquid/liquid interface. *Nature Communications* **2016,** *7*, 10599.

154. Bao, S. P.; Liu, T. T.; Liang, G. D.; Gao, H. Y.; Zhu, F. M.; Wu, Q., The synthesis of organometallic coordination polymer flowers of Prussian blue with ultrathin petals by using crystallization-assisted interface coordination polymerization (CAICP). *Chemistry European Journal* **2012,** *18*, 15272-15276.

155. Liang, G. D.; Zheng, L. M.; Bao, S. P.; Gao, H. Y.; Zhu, F. M.; Wu, Q., Graphene-induced tiny flowers of organometallic polymers with ultrathin petals for hydrogen peroxide sensing. *Carbon* **2015,** *93*, 719-730.

156. Liang, G. D.; Li, X. D.; Bao, S. P.; Gao, H. Y.; Zhu, F. M.; Wu, Q., Large-scale synthesis of organometallic polymer flowers with ultrathin petals for hydrogen peroxide sensing. *Polymer Chemistry* **2015,** *6*, 4447-4454.

157. Liang, G. D.; Zheng, L. M.; Bao, S. P.; Fei, B.; Gao, H. Y.; Zhu, F. M.; Wu, Q., Growing tiny flowers of organometallic polymers along carbon nanotubes. *Macromolecules* **2015,** *48*, 4115-4121.

158. Zhang, K.; Geissler, A.; Chen, X. L.; Rosenfeldt, S.; Yang, Y. B.; Förster, S.; Müller-Plathe, S., Polymeric flower-like microparticles from self-assembled cellulose stearoyl esters. *ACS Macro Letters* **2015**.

159. Mohammadi, H. On the melting and crystallization of linear polyethylene, poly(ethylene oxide) and metallocene linear low-density polyethylene, Virginia Polytechnic Institute and State University, Blacksburg, Virginia, **2018**.

160. Kalloudis, M.; Glynos, E.; Pispas, S.; Walker, J.; Koutsos, V., Thin films of poly(isoprene-*b*-ethylene oxide) diblock copolymers on mica: an atomic force microscopy study. *Langmuir* **2013,** *29*, 2339-2349.

161. Liang, G. D.; Xu, J. T.; Fan, Z. Q., Structure of crystalline domains in semicrystalline block copolymer thin films. *Chinese Journal of Polymer Science* **2006,** *24*, 341-344.

162. Liang, G. D.; Xu, J. T.; Fan, Z. Q.; Mai, S. M.; Ryan, A. J., Effect of substrate surface on dewetting behavior and chain orientation of semicrystalline block copolymer thin films. *The Journal of Physical Chemistry B* **2006,** *110*, 24384-24389.

163. Liang, G. D.; Xu, J. T.; Fan, Z. Q.; Mai, S. M.; Ryan, A. J., Thin film morphology of symmetric semicrystalline oxyethylene/oxybutylene diblock copolymers on silicon. *Macromolecules* **2006,** *39*, 5471-5478.

164. Liang, G. D.; Xu, J. T.; Fan, Z. Q., Lamellar orientation in thin films of symmetric semicrystalline polystyrene-*b*-poly(ethylene-*co*-butene) block copolymers: effects of molar mass, temperature of solvent evaporation, and annealing. *The Journal of Physical Chemistry B* **2007,** *111*, 11921-11928.

165. Liang, G. D.; Xu, J. T.; Fan, Z. Q.; Mai, S. M.; Ryan, A. J., Effect of substrate and molecular weight on the stability of thin films of semicrystalline block copolymers. *Langmuir* **2007,** *23*, 3673-3679.

166. Loo, Y. L.; Register, R. A.; Ryan, A. J., Modes of crystallization in block copolymer microdomains: breakout, templated and confined. *Macromolecules* **2002,** *35*, 2365-2374.

167. Sun, L.; Liu, Y.; Zhu, L.; Hsiao, B. S.; Avila-Orta, C. A., Self-assembly and crystallization behavior of a double-crystalline polyethylene-*block*-poly(ethylene oxide) diblock copolymer. *Polymer* **2004,** *45*, 8181-8193.

168. Sakurai, T.; Nojima, S., Significant increase in melting temperature of poly(ε-caprolactone) blocks confined in crystallized lamellar morphology of poly(ε-caprolactone)-*block*-polyethylene copolymers. *Polymer Journal* **2011,** *43*, 370-377.

169. He, W. N.; Xu, J. T., Crystallization assisted self-assembly of semicrystalline block copolymers. *Progress in Polymer Science* **2012,** *37*, 1350-1400.

170. Hamley, I., *Crystallization in block copolymers*. Advances in Polymer Science: **1999**; Vol. 148.

171. Liang, G. D.; Weng, L. T.; Lam, J. W. Y.; Qin, W.; Tang, B., Crystallization induced hybrid nanosheets of fluorescent polymers with aggregation-induced emission characteristics for sensitive explosive detection. *ACS Macro Letters* **2014,** *3*, 21-25.

172. The ABCs of block polymers. *Macromolecules* **2020,** *53*, 2765-2768.

173. Zheng, W.; Wang, Z.-G., Morphology of ABC triblock copolymers. *Macromolecules* **1995,** *28*, 7215-7223.

174. Mogi, Y.; Nomura, M.; Kotsuji, H.; Ohnishi, K.; Matsushita, Y.; Noda, I., Superlattice structures in morphologies of the ABC triblock copolymers. *Macromolecules* **1994,** *27*, 6755-6760.

175. Stadler, R.; Auschra, C.; Beckmann, J.; Krappe, U.; Voight-Martin, I.; Leibler, L., Morphology and thermodynamics of symmetric poly(A-*block*-B-*block*-C) triblock copolymers. *Macromolecules* **1995,** *28*, 3080-3097.

176. Park, C.; Yoon, J.; Thomas, E. L., Enabling nanotechnology with self assembled block copolymer patterns. *Polymer* **2003,** *44*, 6725-6760.

177. Gedde, U. W.; Mattzzi, A., Polyethylene morphology. *Advanced polymer science* **2004,** *169*, 29-73.

178. Mandelkern, L., *Crystallization of Polymers. Volume 2: Kinetics and Mechanisms*. Second Edition ed.; Cambridge University Press: **2004**.

179. Schultz, J. M., *Polymer Crystallization: The Development of Crystalline Order in Thermoplastic Polymers*. Oxford University Press: **2001**.

180. Sperling, L. H., *Introduction to Physical Polymer Science*. Fourth Edition ed.; John Wiley and Sons: **2005**.

181. Arandia, I. Crystallization and morphology of poly(butylene succinate-*ran*-butylene azelate) random isodimorphic copolymers. University of the Basque Country (UPV/EHU), Donostia-San Sebastián, **2018**.

182. Sbirrazzuoli, N.; Guigo, N.; Vyazovkin, S., Isoconversional kinetics by fast scanning calorimetry. In *Fast Scanning Calorimetry*, Schick, C.; Mathot, V., Eds. Springer International Publishing: **2016**; pp 237-257.

183. Reiter, G.; Strobl, R. L., *Progress in Understanding of Polymer Crystallization*. Springer: Berlin, **2007**.

184. Van Krevelen, D. W.; Te Nikenhuis, K., *Calorimetric Properties*. **2009**.

185. Gedde, U. W., *Polymer Physics*. Chapman and Hall: London: New York, **1995**.

186. Turnbull, D.; Fischer, J. C., Rate of nucleation in condensed systems. *The Journal of Chemical Physics* **1949,** *17*, 71-73.

187. Gedde, U. W.; Hedenqvist, M. S., Morphology of semicrystalline polymers. In *Fundamental Polymer Science*, Second Edition ed.; Springer: **2019**; pp 251-372.

188. Strobl, G., The Physics of Polymers: Concepts for understanding their structures and behavior. Third Edition ed.; Springer: **2007**; pp 1-518.

189. Müller, A. J.; Michell, R. M.; Lorenzo, A. T., Isothermal crystallization kinetics of polymers. In *Polymer Morphology: Principles, Characterization, and Processing*, Guo, Q., Ed. John Wiley and Sons: Hoboken, NJ, **2016**; pp 181-203.

190. Wang, Z. G.; Hsiao, B. S.; Sauer, B. B.; Kampert, W. G., The nature of secondary crystallization in poly(ethylene terephthalate). *Polymer* **1999,** *40*, 4615-4627.

191. Keller, A., A note on single crystals in polymers - Evidence for a folded chain configuration. *Philosophical Magazine* **1957**, 1171-1175.

192. Till, P. H., The growth of single crystals of linear polyethylene. *Journal of Polymer Science* **1957,** *24*, 301-306.

193. Jaccodine, R., Observations of spiral growth steps in ethylene polymer. *Nature* **1955,** *176*, 305-306.

194. Keller, A.; O'Connor, A., Large periods in polyethylene: The origin of low-angle X-ray scattering. *Nature* **1957,** *180*, 1289-1290.

195. Lauritzen, J.; Hoffman, J. D., Theory of formation of polymer crystals with folded chains in dilute solution. *Journal Research of the National Bureau of Standards. Section A: Physics and Chemistry* **1960,** *64*, 73-102.

196. Ergoz, E.; Fatou, J. G.; Mandelkern, L., Molecular weight dependence of the crystallization kinetics of linear polyethylene. I. Experimental results. *Macromolecules* **1972,** *5*, 147-157.

197. Lorenzo, A. T.; Arnal, M. L.; Albuerne, J.; Müller, A. J., DSC isothermal polymer crystallization kinetics measurements and the use of the Avrami equation to fit the data: Guidelines to avoid common problems. *Polymer Testing* **2007,** *26*, 222-231.

198. Mark, J. E., *Physical Properties of Polymers Handbook*. Springer-Verlag: New York, **2007**.

199. Lauritzen Jr, J. I.; Hoffman, J.D., Formation of polymer crystals with folded chains from dilute solutions. *The Journal of Chemical Physics* **1959,** *31*, 1959.

200. Van Krevelen, D. W.; Te Nijenhuis, K., *Properties of Polymers*. Fourth Edition ed.; Elsevier: Amsterdam, **2009**.

201. Hiemenz, P. C.; Lodge, T. P., *Polymer Chemistry*. CRC Press: **2007**.

Chapter 3

Experimental Part

3.1 Nanocomposites and Neat/Recycled Polymer Blend Nanocomposites (PBNANO)s

3.1.1 Materials

High-density polyethylene (HDPE) from INEOS (Rigidex HD6070EA, MFI (190 °C/2.16 kg) = 7.6 g 10^{-1} min) and neat PET from Brilen (Novapet CR, Barbastro, Spain) with an intrinsic viscosity of 0.80 dlg $^{-1}$ in m_cresol were used. The primary phenolic antioxidant from BASF (IRGANOX 1010) was employed for processing and long-term thermal stabilization. A polyethylene grafted with maleic anhydride (PEgMA) (DuPont, Fusabond E226) was employed as a compatibilizer agent. The titanium dioxide nanoparticles used was a hydrophilic TiO_2 (hphi) 99%, provided by io-li-tec nanomaterials (Heilbronn, Germany).

Regarding recycled materials, recycled PET flakes (rPET) and recycled PP pellets (rPP) provided by *Suez* (a waste treatment French company) were employed. It is important to note that the recycled PET material already contains 2% of a commercial hydrophobic TiO_2. Three different titanium dioxide nanoparticles were used: (a) A hydrophilic titanium dioxide (hphi) 99%, provided by io-li-tec nanomaterials (a German company that sells ionic liquids and nanoparticles in Heilbronn, Germany) with rutile crystalline form; (b) a hydrophobic titanium dioxide (hpho) 92%, coated with silicone oil from US Research Nanomaterials, Inc. (Houston, TX, USA), with rutile crystalline form; and (c) hydrophilic titanium dioxide (AEROXIDE TiO_2 P25 99.5% from Evonik Industries, Essen, Germany) modified by a sol-gel reaction with octadecyltrimethoxysilane (97% Apollo Scientific, Manchester, UK) to turn it hydrophobic, which is denoted hydrophobically modified TiO_2 (hphoM).

3.1.2 TiO_2 Nanoparticles Modification

The hydrophobization process of TiO_2 nanoparticles was carried out following the procedure reported by Pazokifard et al.[1]. Briefly, 1 g of particles were dispersed in 25 mL ethanol, and then a 1 mmol octadecyltrimethoxysilane (TMOS) solution in ethanol was added. The pH was adjusted to 12 using NH_4OH. The mixture was kept for 18 h under stirring. Then the particles were washed by centrifugation (8000 rpm, 10 min) and dried at 60 °C for 24 h (Figure 3.1).

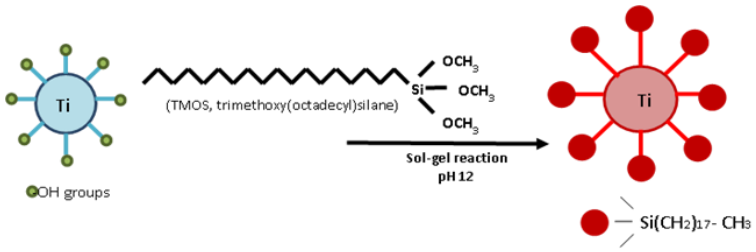

Figure 3.1. Scheme of hydrophilic nanoparticles functionalization

3.1.3 PBNANOs Preparation

Melt compounding by extrusion is the most common technique to prepare PBNANOs. A typical extrusion process consists of feeding and flow of the solid material, melting, mixing, melt flow, and solidification. Many parameters such as temperature profile or screw speed are determined in order to obtain the desired materials[2].

Melt compounding of all blends was performed in a Collins ZK 25T co-rotating twin-screw extruder (L/D ratio 18 and screw diameter 25 mm). Extrudates were cooled in a water bath and cut into pellets by a pelletizer. Prior to extrusion, HDPE, PET, and PEgMA were dried for 24 h at 80 °C under vacuum. Blends were prepared in two steps. Firstly, HDPE was mixed with the antioxidant IRGANOX 1010 (0.2%) with a temperature profile 160-170-180-190 °C in the extrusion zone. For PET/HDPE blends, a second extrusion process was performed, adding neat PET with a temperature profile 215-215-215-270 °C. For PET/HDPE/PEgMA blends, besides adding neat PET, the compatibilizer PEgMA was added, and its content was fixed at 10% with respect to the dispersed phase. For the

PET/HDPE/TiO_2 and PET/HDPE/TiO_2/PEgMA blends, the chosen PET/HDPE ratio was 70:30. Adequate quantities of TiO_2 nanoparticles were used in order to finally have 5 and 10% weight content, and PEgMA content was also fixed at 10% with respect to the dispersed phase. In both extrusion steps the screw rotation rate was 40 rpm. All the prepared samples are the following:

- PET/HDPE: 0/100, 10/90, 20/80, 30/70, 40/60, 50/50, 60/40, 70/30, 80/20, 90/10, 100/0 (all compositions)
- PET7HDPE/PEgMA: : 0/100, 10/90, 20/80, 30/70, 40/60, 50/50, 60/40, 70/30, 80/20, 90/10, 100/0 (all compositions)
- 70PET/30HDPE/TiO_2: 70PET/30HDPE/5 % TiO_2 and 70PET/30HDPE/10 % TiO_2
- 70PET/30HDPE/TiO_2/PEgMA: 70PET/30HDPE/5 % TiO_2/10 % PEgMA and 70PET/30HDPE/10 % TiO_2/10 % PEgMA

Regarding recycled blends, rPP and rPET were also dried for 48 h at 80 °C under vacuum before extrusion. Firstly, rPP/10%TiO_2 and rPP/20%TiO_2 masterbatches were prepared. Then, adequate quantities of the masterbatch were used to increase the amount of TiO_2 by 1, 3, 5, 7.5, and 10 % with respect to the total amount of material, so that polymer blends with the same polymer ratio of 80rPP/20rPET could be prepared. As the 80rPP/20rPET blend has approximately 2% TiO_2 nanoparticles (as a residue in the rPET employed), the final concentrations of TiO_2 are 3, 5, 7, 9.5, and 12% TiO_2. Note that three different types of TiO_2 nanoparticles (as described above) were used to prepare each of the compositions. All PBNANOs prepared are listed in Table 3.1.

Samples for morphological and mechanical characterization were prepared by compression molding using a P200E Collin hot press at 270 °C and under 150 bar for 3 minutes, and then they were quenched in a water bath. Square plates of 100 x 100 mm and 1 mm in thickness were prepared. Specimens of 1 mm were obtained for SEM observation.

Table 3.1. Compositions of the prepared recycled PBNANOs in w/w

Samples	Added TiO_2	Total amount of TiO_2
80rPP/20rPET/TiO_2	0	2
80rPP/20rPET/TiO_2	1	3
80rPP/20rPET/TiO_2	3	5
80rPP/20rPET/TiO_2	5	7
80rPP/20rPET/TiO_2	7.5	9.5
80rPP/20rPET/TiO_2	10	12

3.1.4 TiO_2 Nanoparticles Characterization

Water contact angle measurements were carried out to determine the hydrophobicity of the TiO_2 nanoparticles in a Dataphysics OCA-Series equipment (*Dataphysics Instruments GmbH*, Germany) at room temperature. The equilibrium contact angle is the angle of a liquid formed on a solid surface at the solid-liquid-vapor contact line, i.e., the three-phase contact line. The angle is governed by the interfacial tensions between those three phases, and since it is unique for each system, it can be used to quantitatively describe the wettability of a solid by a liquid, which will determine the hydrophobicity of the solid TiO_2 nanoparticles[3].

To do so, particle films were deposited on a slide, and the contact angles were calculated from water drop images. The hydrodynamic nanoparticle size and ζ-potential in water were determined by dynamic light scattering (DLS) using a *Brookhaven Instruments* 90Plus. The presence of organic compounds on NPs surface was confirmed by Fourier-transform infrared (FTIR) spectra obtained with a Vertex 70 from Bruker, equipped with an ATR Golden Gate accessory. Hydrophobic and hydrophobically modified nanoparticles were characterized with a thermogravimetric analyzer (TGA) from Mettler Toledo (TGA/SDTA 851e) to measure the organic content. The TGA experiments were performed in an air atmosphere at 10 ºC/min in a temperature range from 30 to 800 ºC.

3.1.5 Thermogravimetric Analysis (TGA)

TGA is a technique in which the weight of a sample is measured as a function of temperature or time. The sample is placed in a very accurate balance, and this is introduced in a furnace. During the measurement, the sample is under nitrogen or air atmosphere. Different types of experiments can be performed, being the most common dynamic or isothermal experiments. In a non-isothermal experiment, the sample is heated from room temperature to high temperatures (typically 800 ºC). In isothermal experiments, the sample is kept at a certain temperature, and the weight loss during time is measured in order to check the thermal stability. Results as the loss of mass due to degradation, the loss of solvent or water, the loss of a plasticizer or the quantity of a filler can be obtained.

The TiO_2 nanoparticle content in all blends was determined in a Q500 *TA Instruments* TGA analyzer under oxidative atmosphere. The sample mass was approximately 5 mg. Before the measurements, samples were dried overnight. A heating run was carried out from 40 to 700 °C at 10 °C/min. The unburnt residue left at 700 °C was measured to determine the final TiO_2 content.

3.1.6 Scanning Electron Microscopy (SEM) and Transmission Electron Microscopy (TEM)

Structure and morphology of materials are studied by SEM since this technique is able to distinguish between differences in topology and composition. An electron beam is focused on the surface of the sample, and the beam interacts with the surface of the specimen and generates signal electrons which are used to form an image. An electronic device collects the signals. Electrons are scattered when the primary beam penetrates the surface of the sample. The intensity of the emissions depends on the angle formed between the electron beam and the surface, that is, it depends on the morphology of the material[4, 5]

Morphology of the blends and nanoparticles was firstly observed by SEM using a *Hitachi* S-2700 electron microscope under high vacuum and with accelerating voltage of 20 kV, at different magnifications. Before observation, the samples were cryogenically fractured in liquid $N_{2,}$ and the fracture surfaces were coated with gold in a *Bio-Rad* SC500 sputter coater before being exposed to the electron beam. The diameter of the droplets was measured on around 100 particles. Number (d_n) and volume (d_v) average diameters and particle size polydispersity (D) were calculated using the following equations (Equation 3.1)[6], in which n_i is the number of particles "i" of diameter d_i:

$$d_n = \frac{\sum n_i d_i^2}{\sum n_i d_i} \qquad d_v = \frac{\sum n_i d_i^4}{\sum n_i d_i^3} \qquad D = \frac{d_v}{d_n} \qquad \text{Eq. 3.1}$$

Morphology, composition and crystallographic information of the samples are studied by TEM. Electrons are generated in a similar way to that of SEM, however, electrons in this technique are used as a light source. The electron beam is focused in the sample, and some of the electrons are absorbed or deflected when they are trying to pass through the sample. Depending on the material, some areas will allow more electrons to go through than other more dense areas. The areas in which more electrons go through will be brighter in the final image[7]. The density of the material should be different in order to see differences, because if not, the sample should be stained with different solutions. These substances are accumulated in the amorphous zone of the polymers, and differences between crystalline and amorphous regions are detected. This is very advantageous to observe crystal morphology, i.e. if there are lamellas or shish kebab structures.

In this work, the location of TiO_2 nanoparticles was determined by TEM analysis. The samples were first cut at room temperature with a diamond knife on a Leica EMFC 6 ultramicrotome device. The ultra-thin sections of 90 nm thick were mounted on 200 mesh copper grids. Finally, they were examined using a *TECNAI* G2 20 TWIN TEM equipped with LaB6 filament operating at an accelerating voltage of 120 kV. To image the lamellar morphology, a RuO_4

solution was employed for staining. Thin strips of samples were immersed in this solution for 16 h and ultra-thin sections were cut at room temperature for analysis.

3.1.7 Thermal Analysis by Differential Scanning Calorimetry (DSC)

Differential Scanning Calorimetry (DSC) is a thermoanalytical technique in which the difference in heat capacity (C_p) of a sample and a reference is recorded as a function of temperature. A power compensation DSC is composed by two cells: in one of them, the sample is in a suitable pan, and in the other, the reference pan is placed. Two heating circuits control the temperature average and the difference between the two ovens. The first circuit changes the temperature of the two ovens, both the sample and the reference, at a constant speed as indicated in the program. The second circuit compensates for the temperature difference between the two ovens when an exothermic or endothermic process occurs in the sample, maintaining the temperature of the sample and the reference constant. This instrument uses a feedback loop to maintain the sample at a set temperature while measuring the power needed to do this against a reference furnace.

In polymers, this technique allows determining the changes that polymers suffer when the temperature varies, such as the melting temperature (T_m), the glass transition temperature (T_g), the crystallization temperature (T_c) or cold crystallization temperature (T_{cc}), transitions between crystalline phases, the percentage of crystallinity of a material as well as the enthalpies corresponding to the aforementioned thermal transitions. In addition, from the corresponding enthalpies the degree of crystallinity of the samples is calculated following Equation 3.2:

$$X_c = \frac{\Delta H_m}{\Delta H_{(100\%)}} \qquad \text{Eq. 3.2}$$

where ΔH_m is the value of the melting enthalpy, and $\Delta H_{(100\%)}$ is the heat of fusion of a 100 % crystalline polymer.

The thermal properties of the samples were studied by Differential Scanning Calorimetry (DSC) using a *Perkin Elmer* DSC Pyris 1 equipped with a refrigerated cooling system (Intracooler 2P), under ultra-high purity nitrogen atmosphere. The instrument was previously calibrated with indium and tin standards. All samples were dried before testing for 24 h at 80 °C under vacuum. Aluminum pans were used to encapsulate samples of approximately 5 mg. Different thermal protocols used to study the crystallization behavior of the samples are described below.

Non-isothermal DSC experiments

All samples were firstly measured by standard non-isothermal DSC experiments. The thermal program applied was the following: an initial heating run to erase previous thermal history by heating the samples to 30 °C above their peak melting temperature for 3 min. Then, cool the molten sample to -20 °C at a controlled cooling rate of 20 °C/min and hold the sample 1 minute for stabilization at -20 °C. Finally, a heating scan from -20 °C to 30 °C above their peak melting temperature at 20 °C/min. By these measurements, the crystallization temperature (T_c) or the cold crystallization temperature (T_{cc}), the melting temperature (T_m) and the corresponding enthalpies of each one have been obtained.

Isothermal DSC experiments

Isothermal measurements were performed using the procedure recommended by Lorenzo et al.[8]. The thermal program applied was the following: erasure of thermal history by heating the samples to 30 °C above their peak melting temperature for 3 min; rapid cooling to a chosen isothermal crystallization temperature (T_c) at a controlled rate of 60 °C/min; isothermal crystallization (measurements of heat flow versus time) at T_c until saturation (typically, the peak time x 3); and a final heating run from T_c to 30 °C above their peak melting temperature at 20 ºC/min.

Before starting with the isothermal procedure, the minimum isothermal crystallization temperature was first determined. This was done by heating the sample directly from the chosen T_c temperature, after being quenched from the melt. The lowest temperature which did not show any melting enthalpy during

immediate subsequent heating was the minimum isothermal crystallization temperature employed.

3.1.8 Mechanical Properties by Tensile Experiments

Tensile tests are commonly used to study the mechanical behavior of the samples. A sample is subjected to a controlled tension until it is fractured. Some properties such as tensile strength, breaking strength, or the maximum elongation are directly measured, and Young modulus or yield stress are obtained, for instance. Specimens are prepared depending on the test method employed[9].

So the mechanical behavior was studied by tensile tests, according to ISO-527-2 standard, on 80rPP/20rPET PBNANOs without and with 10% w/w of additional TiO_2 (hydrophobic (hpho), hydrophobically modified (hphoM) and hydrophilic (hphi)). A *GALDABINI* 2500 universal testing machine equipped with a *MINTRON* OS-65D video extensometer and a 1kN load cell was used. The specimens were stamped from the compression molded plates according to the type 1BA dumbbell geometry. The tests were carried out at 22 ± 1 ºC and a crosshead speed of 5 mm min^{-1}. The engineering stress-strain curves for every sample were recorded, and elastic modulus (E), yield strength (σ_y), yield strain (ε_y) and strain at break (ε_b) were determined. The average values and corresponding standard deviation were determined from 10 valid tests.

After testing, the fractured surfaces of all samples were inspected by Scanning Electron Microscopy (SEM) (*JEOL*, JSM-7001F, Tokyo, Japan). Experiments were performed under vacuum with an accelerating voltage of 2 kV. Samples were previously coated with platinum vapor.

3.2 Multicrystalline Block Copolymers: Tricrystalline and Tetracrystalline Block Copolymers and their Precursors containing PE, PEO, PCL and PLLA blocks

3.2.1 Materials

The homopolymers, diblock copolymers, triblock terpolymers and tetrablock quarterpolymers under study were kindly provided by Prof. Nikos Hadjichristidis, head of the Polymer Synthesis Laboratory from King Abdullah University of Science and Technology in KAUST (Saudi Arabia).

Many samples are employed in this work. Tables 3.2 and 3.3 show the materials divided into two blocks. In all cases, subscripts indicate composition in wt% and superscripts represent M_n values in kg/mol. M_n of the blocks was determined by 600 MHz ^{1}H NMR spectroscopy (toluene-*d*8, 80 °C).

Table 3.2 shows molecular characteristics of the triblock terpolymers of poly (ethylene)-*b*-poly (ethylene oxide)-*b*-poly (L-Lactide) and poly (ethylene)-*b*-poly (ε-caprolactone)-*b*-poly (L-Lactide): $PE_{21}^{2.6}$-*b*-$PEO_{32}^{4.0}$-*b*-$PLLA_{47}^{5.9}$ and $PE_{21}^{7.1}$-*b*-$PCL_{12}^{4.2}$-*b*-$PLLA_{67}^{23.0}$, with their corresponding precursors. In addition, the synthesis of these materials is provided in Scheme 3.1.

PE-*b*-PEO-*b*-PLLA is a new type of triple-crystalline triblock terpolymer, synthesized following the newly established organic/metal "catalyst-switch" strategy, which consists on combining polyhomologation with ring-opening polymerization (ROP). Firstly, a perfectly linear PE-OH is obtained by polyhomologation, and it is used as macroinitiator for the ROP of CL or LLA, employing $Sn(Oct)_2$ as catalyst. Each of the blocks is assigned with a colour through the whole work in order to identify easily the blocks (violet for PE, green for PLLA, blue for PCL and red for PEO). More details on the synthesis of these materials can be found in a previous publication[10].

Table 3.2. Number-average molecular weight (M_n) of the homopolymers, diblock copolymers and triblock terpolymers. Subscripts indicate composition in wt %, and superscripts represent M_n values of each block in kg/mol

Sample	M_n PE (g/mol)	M_n PEO (g/mol)	M_n PCL (g/mol)	M_n PLLA (g/mol)
$PE^{2.6}$	2600	-	-	-
$PE_{39}{}^{2.6}$-*b*-$PEO_{61}{}^{4.0}$	2600	4000	-	-
$PE_{21}{}^{2.6}$-*b*-$PEO_{32}{}^{4.0}$-*b*-$PLLA_{47}{}^{5.9}$	2600	4000	-	5900
$PE^{7.1}$	7100	-		-
$PE_{63}{}^{7.1}$-*b*-$PCL_{37}{}^{4.2}$	7100	-	4200	-
$PE_{21}{}^{7.1}$-*b*-$PCL_{12}{}^{4.2}$-*b*-$PLLA_{67}{}^{23.0}$	7100	-	4200	23000

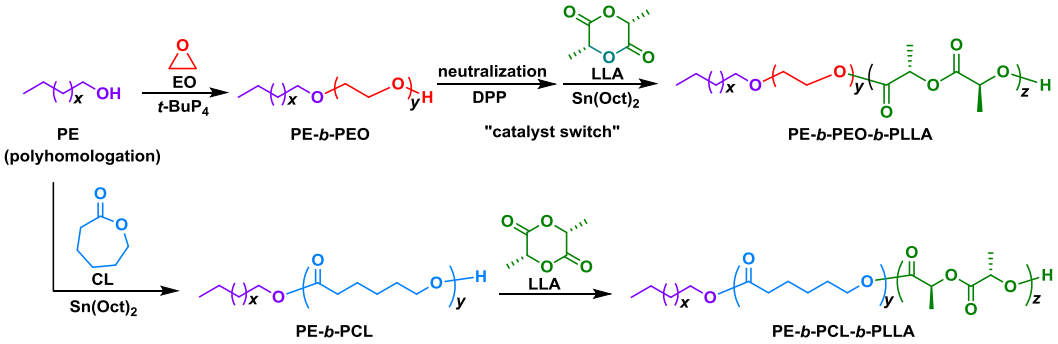

Scheme 3.1. Synthesis of the triblock terpolymers $PE_{21}{}^{2.6}$-b-$PEO_{32}{}^{4.0}$-b-$PLLA_{47}{}^{5.9}$ and $PE_{21}{}^{7.1}$-b-$PCL_{12}{}^{4.2}$-b-$PLLA_{67}{}^{23.0}$, with colors indicating each of the blocks

The other set of samples are presented in Table 3.3. In this case, two novel tetracrystalline tetrablock quarterpolymers of poly (ethylene)-*b*-poly (ethylene oxide)-*b*-poly (ε-caprolactone)-*b*-poly (L-Lactide) were synthesized: $PE_{18}{}^{7.1}$-*b*-$PEO_{37}{}^{15.1}$-*b*-$PCL_{26}{}^{10.4}$-*b*-$PLLA_{19}{}^{7.6}$ (Q1) and $PE_{29}{}^{9.5}$-*b*-$PEO_{26}{}^{8.8}$-*b*-$PCL_{23}{}^{7.6}$-*b*-$PLLA_{22}{}^{7.3}$ (Q2). Note that the molecular weight and block content varies from one another. In addition, their precursor triblock terpolymers $PE_{22}{}^{7.1}$-*b*-$PEO_{46}{}^{15.1}$-*b*-$PCL_{32}{}^{10.4}$ (T1) and $PE_{37}{}^{9.5}$-*b*-$PEO_{34}{}^{8.8}$-*b*-$PCL_{29}{}^{7.6}$ (T2), the diblock copolymers $PE_{32}{}^{7.1}$-*b*-$PEO_{68}{}^{15.1}$ and $PE_{52}{}^{9.5}$-*b*-$PEO_{48}{}^{8.8}$, and the $PE^{7.1}$ and $PE^{9.5}$ homopolymers have also been studied.

Synthesis is provided in Scheme 3.2. A linear hydroxyl-terminated polyethylene (PE-OH) was firstly synthesized by polyhomologation of dimethylsulfoxonium methylide with triethyl borane as initiator/catalyst[11] and used with t-BuP4 (catalyst) to promote ring-opening polymerization (ROP) of ethylene oxide (EO) towards PE-*b*-PEO. Then, neutralization of t-BuP_4 was carried out with diphenyl phosphate (DPP). For the ROP of ε-caprolactone (CL), two different catalysts were used, $Sn(Oct)_2$ for T1 (organic/metal catalyst-switch), and phosphazene base *t*-BuP_2 for T2 (organic/organic catalyst-switch). The ROP of L-lactide (LLA) was catalyzed by the weaker base t-BuP_2. The catalyst-switch strategies were applied to avoid as much as possible side reactions during the ROP of CL and LLA in toluene at 80 ºC, although they are not completely suppressed. However, under these conditions, *S*,*R*-lactide monomeric units are formed because of racemization, which leads to a decrease of PLLA crystallinity.

Therefore, an organic/metal *t*-BuP_4/DPP/$Sn(Oct)_2$ (isotactic tetrads 98%) "catalyst switch" strategy was applied for the synthesis of Q1, which consists of using tin(II) 2-ethylhexanoate [$Sn(Oct)_2$] in order to obtain *S*,*S*-lactide monomeric units. On the other hand, Q2 was synthesized by organic/organic "catalyst-switch"(*t*-BuP_4/DPP/*t*-BuP_2) strategy (isotactic tetrads 84%)[12].

Table 3.3 shows the molecular weights of each of the blocks of the synthesized materials. The polyethylene block precursors are not 100 % linear because of possible side reactions and monomer purity issues. According to NMR measurements, the PE block of T1 and Q1 contains 0.32 % propyl side groups and 3 % methyl groups, and that of T2 and Q2 contains 0.45 % propyl side-groups and 2 % methyl groups[10, 12]. This difference may have consequences in the crystalline behavior of the materials, which will be discussed in the discussion and results section. The formation of tetracrystalline quarterpolymers was confirmed by ^{1}H NMR spectroscopy and gel-permeation chromatography[12]. Furthermore, Differential Scanning Calorimetry (DSC), X-ray diffraction (SAXS/WAXS) and Polarized Light Optical Microscopy (PLOM) proved the existence of different crystalline domains depending on the sample analyzed.

Table 3.3. Number-average molecular weight (M_n) of the homopolymers, diblock copolymers, triblock terpolymers, and tetrablock quarterpolymers. Subscripts indicate composition in wt %, and superscripts represent M_n values of each block in kg/mol

Sample	M_n PE (g/mol)	M_n PEO (g/mol)	M_n PCL (g/mol)	M_n PLLA (g/mol)
$PE^{7.1}$	7100	-	-	-
$PE_{32}^{7.1}$-*b*-$PEO_{68}^{15.1}$	7100	15100	-	-
$PE_{22}^{7.1}$-*b*-$PEO_{46}^{15.1}$-*b*-$PCL_{32}^{10.4}$ (T1)	7100	15100	10400	-
$PE_{18}^{7.1}$-*b*-$PEO_{37}^{15.1}$-*b*-$PCL_{26}^{10.4}$-*b*-$PLLA_{19}^{7.6}$ (Q1)	7100	15100	10400	7600
$PE^{9.5}$	9500	-	-	-
$PE_{52}^{9.5}$-*b*-$PEO_{48}^{8.8}$	9500	8800	-	-
$PE_{37}^{9.5}$-*b*-$PEO_{34}^{8.8}$-*b*-$PCL_{29}^{7.6}$ (T2)	9500	8800	7600	-
$PE_{29}^{9.5}$-*b*-$PEO_{26}^{8.8}$-*b*-$PCL_{23}^{7.6}$-*b*-$PLLA_{22}^{7.3}$ (Q2)	9500	8800	7600	7300

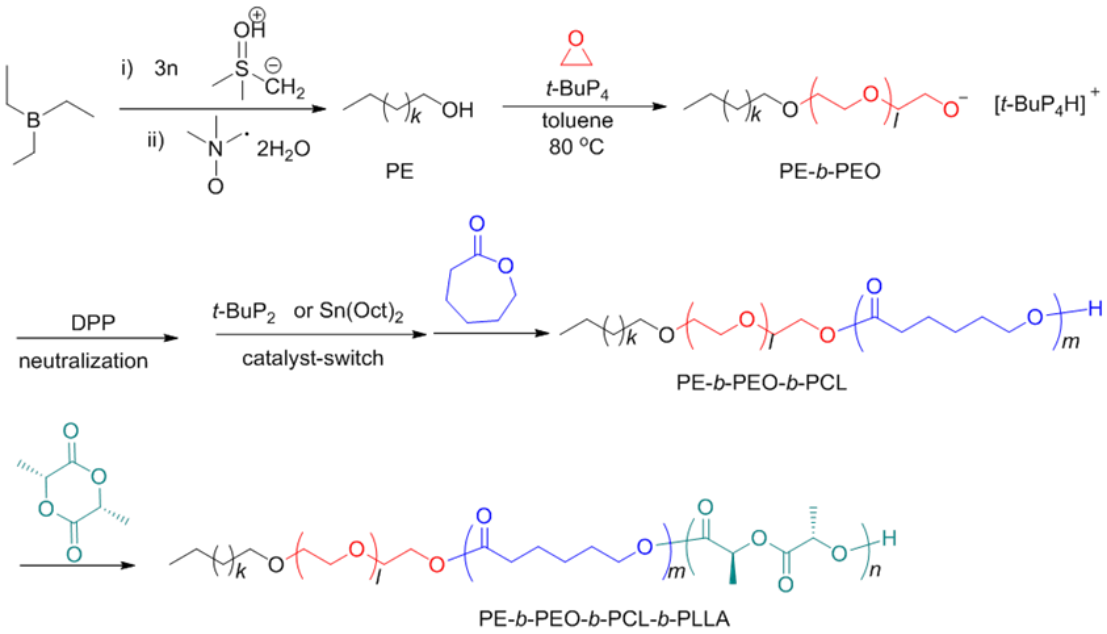

Scheme 3.2. Synthesis of the triblock terpolymer PE-*b*-PEO-*b*-PCL and tetracrystalline quarterpolymer PE-*b*-PEO-*b*-PCL-*b*-PLLA by a combination of polyhomologation and catalyst-switch strategy[12], with colours indicating each of the blocks

3.2.2 Differential Scanning Calorimetry (DSC)

In this work, a *Perkin Elmer* DSC Pyris 1 calorimeter with an Intracooler 2P (cooling device) was employed in order to perform non-isothermal DSC experiments. Indium and tin standards were used for calibration. About 3 mg of sample was used after encapsulation in standard aluminum pans. An ultra-high purity nitrogen atmosphere was employed.

Non-isothermal experiments were run in a temperature range between 0-180 °C and 0-160 °C, depending on the samples under study to avoid degradation. Cooling and heating rates of 20 ºC/min were employed in most of the cases, but 1 ºC/min was also used in some cases in order to study the effect of the cooling rate in the crystallization sequence of the blocks in triblock terpolymers. Thermal history is erased by keeping the samples for 3 minutes at 30 °C above the peak melting temperature of the highest temperature melting block; samples are then cooled down, keeping them 1 minute at low temperatures for stabilizing the system and then heated up at a constant rate of 20 °C/min.

3.2.3 Small Angle and Wide Angle X-ray Scattering (SAXS/WAXS)

Small Angle and Wide Angle X-Ray Scattering (SAXS/WAXS) are X-Ray diffraction techniques are very often employed to examine the crystalline features of polymers. They are very useful and non-destructive techniques to characterize solid materials.

SAXS allows quantifying nanoscale density differences in a sample by analyzing the elastic scattering behavior of X-rays. It is called “Small Angle” because usually, the X-ray passes through the samples at small angles, typically ranging from 0.1 to 10 º. SAXS may be able to provide structural information (1-100 nm) depending on the angular range in which a scattering signal can be recorded[13].

On the contrary, WAXS refers to “Wide Angle” and samples are scanned in a wide-angle goniometer. Crystalline structures are composed of atomic planes,

and the ordered packing of the polymer chains generate sharp diffraction peaks at certain scattering angles (2θ), sometimes indicated by the scattering vector *q*, where $q=2\pi/d=4\pi\sin\theta/\lambda$. Predictable patterns are obtained, and thus, the chemical composition or phase composition of a film, the alignment of crystallites, the crystallite size, or the presence of film stress can be determined[13]. In addition, crystallinity of a material can be calculated by analyzing the ratio of the area under the crystalline peaks[14].

In the present work, Small-Angle (SAXS) and Wide-Angle (WAXS) X-ray scattering experiments were measured simultaneously at beamline BL11-NCD in the ALBA Synchrotron (Barcelona, Spain). Capillaries were employed to place samples in the beam path. A THMS600 Linkam hot stage together with a liquid nitrogen cooling device was employed for temperature control and to heat and cool the samples. SAXS/WAXS diffractograms were periodically recorded while copolymers crystallized and melted, using the same cooling and heating conditions employed in the non-isothermal DSC experiments, and thus, having comparable results.

The X-ray energy source was 12.4 keV (λ=1.03 Å). For SAXS, used to probe the lamellar structure within the spherulites, a sample-detector distance of 6463 mm was used, with 0 ° tilt angle, and silver behenate was used for calibration (ADSC Q315r, Poway, CA, USA, with a resolution of 3070 x 3070 pixels, pixel size of 102 μm^2). For WAXS, the sample-detector distance was 132.6 mm with a 21.2 ° tilt angle, and chromium (III) oxide was employed to do the calibration (Rayonix LX255-HS detector, Evanston, IL, USA, with a resolution of 1920 x 5760 pixels, pixel size of 44 μm^2). The intensity profiles plot the scattering intensity as a function of scattering vector, $q=4\pi\sin\theta\lambda^{-1}$, where λ is the X-ray wavelength (λ=1.03 Å) and 2θ is the scattering vector.

In the case of the $PE_{21}^{7.1}$-*b*-$PCL_{12}^{4.2}$-*b*-$PLLA_{67}^{23.0}$ triblock terpolymer, SAXS/WAXS patterns taken during cooling from the melt at 1 °C/min were measured in a laboratory set-up instead of at the Alba synchrotron. The equipment was capable of performing *in situ* measurements at such a slow cooling rate. *In situ*

WAXS/SAXS measurements were performed with a Nano-inXider vertical system (λ=0.154 nm, Xenocs, Sassenage, France), equipped with two two-dimensional Dectris Platius3 hybrid pixel detectors and operated at 50 kV and 0.6 mA. The distances between the sample and the detector are 79 and 936 mm for WAXS and SAXS measurements, respectively. A Linkam HFSX350 hot stage (Linkam Scientific Instruments, Tadworth, U.K.) was used for temperature control. The heating and cooling rates were 1 °C/min, and the data acquisition time for each scattering profile was 60 s.

3.2.4 Polarized Light Optical Microscopy (PLOM)

Microscopy can be used to determine if a sample has any crystalline features or not, specifically to analyze the microstructure of the polymers obtained from the arrangement of the crystallites. Lamellae are the smallest organized units of polymer chains, and they form spherulites. Lamellae (nanometers) can only be detected by TEM, but the larger spherulites (micrometers) can be observed by optical microscopy[14].

The Polarized Light Optical Microscope (PLOM) is an optical microscope with two polarizers located above and below the sample. One of them is located in the light path before the sample, and the other one is between the rear aperture and the observation tube (or camera port). If the polarizers are crossed, there is no light transmission when there is no sample, or when the sample has an isotropic disordered structure (amorphous polymers or semicrystalline polymers in the melt). When observing a semicrystalline polymer (a birefringent sample), the light beam passes through the microscope due to an interference phenomenon. In consequence, the ordered anisotropic regions of the sample are bright and the background dark, which corresponds to the amorphous or molten fraction of the material[15].

The morphological study was performed with an Olympus BX51 Polarized Light Optical Microscope (PLOM). A THMS600 Linkam hot stage with a liquid

N_2 cooling device was used for temperature control. Images, as well as videos, were recorded with an SC50 (Olympus) camera. Samples were melted on a glass slide with a thin glass coverslip on top, and 20 °C/min or 1 ºC/min was used as cooling and heating rates to record all morphological changes. Furthermore, an isothermal experiment was also performed for the $PE_{18}^{7.1}$ -*b* -$PEO_{37}^{15.1}$ -*b*- $PCL_{26}^{10.4}$ -*b*- $PLLA_{19}^{7.6}$ (Q1) quarterpolymer keeping it at 88 ºC until the whole microscope field was covered with spherulites before applying a cooling scan at 20 ºC/min.

In addition, the obtained micrographs were analyzed with ImageJ, an image processing software[16]. The light intensity that passes through the cross polarizers in a sample is recorded, and an increase in that intensity means that the crystal content in the sample is increasing. The whole micrographs at different temperatures are considered as a "region of interest" in order to record intensity changes caused by all the superstructures that can be formed in the whole microscope field. This allows us to determine the temperature at which crystallization of a particular polymer block starts, and the whole crystallization process can be followed by means of intensity changes.

3.2.5 Atomic Force Microscopy (AFM)

Atomic Force Microscopy (AFM) is a technique by which the nanoscale morphology can be observed. Three are the main components: the microscope stage, control electronics, and the computer. The microscope stage contains the scanner for moving the AFM tip to the sample, the sample holder, and a force sensor to monitor the AFM tip. Control electronics are needed to generate the signals used to move the scanner and other components, as well as to digitize the signals to record them. The computer acquires and displays images. When the AFM tip is located on the sample, it "feels" the surface with a sharp probe and records information by building a map of the height of the surface. Data is collected to analyze with specific software. Lamellar thickness can be measured, and the growth of crystals can also be followed, for instance[17].

The morphology of some samples was explored by AFM. The observations were performed with a Bruker ICON scanning probe microscope equipped with a Nanoscope V controller. The micrographs were acquired in tapping mode using TESP-V2 tip with 127 um cantilever (cantilever spring constant, k = 42 N/m, and resonance frequency, f_o = 320 kHz, Bruker). The AFM phase images of the investigated samples were subjected to a first-order plane-fitting procedure to compensate for sample tilt.

Homogeneous thin film samples were spin-coated on mica substrates (SCC-200, Novocontrol technologies, Germany) from tetrahydrofuran solutions (4 mg/mL) after determining the best sample preparation conditions. Then, two different thermal protocols were applied on each sample before observing the samples at room temperature:

a) Cooling from the melt at 50 ºC/min to room temperature
b) Cooling from the melt at 20 ºC/min to room temperature

3.2.6 Nanoindentation

This non-destructive technique consists in the application of a force in the surface of a material with a known geometry indenter or tip (usually pyramidal or spherical), in which the force and the depth of the tip into the surface is always monitored. It is mainly employed to measure mechanical properties such as hardness and elastic modulus. However, due to its versatility, other information can also be obtained: fracture resistance, mechanical mapping, dislocation behaviors, yield strength, and residual stresses, plastic/elastic deformation, viscoelastic behavior, etc. In addition, the measurement is local, and this allows the characterization of different phases of the samples. It is an efficient tool to evaluate mechanical properties at micro and nanolevel scales[18].

In our case, some of the most interesting samples were analyzed by nanoindentation. They were prepared on a Linkam hot plate by cooling (at 20 ºC/min) from the melt to the crystallization temperature (T_c) of each of the blocks (determined by DSC and WAXS) to perform isothermal steps of 5 minutes in

order to crystallize each block until saturation before finally cooling down at 20 ºC/min to room temperature. The coverslip was removed after the sample reached room temperature, and the glass slide was glued onto a cylindrical metal holder that was placed in the platform of a G200 nanoindenter (KLA Tencor, USA). A low load resolution head (dynamic contact module, DCM) with a Berkovich indenter was employed. The tip area was calibrated against a fused silica standard[19].

During the loading ramp a constant strain rate was employed (0.05 s^{-1}) and at the same time, a small oscillating force at a frequency of 75 Hz was superimposed. Such dynamic testing allowed a continuous measure of the contact stiffness and damping during the loading cycle based on the phase lag between the oscillation force and the harmonic displacement[20]. In the end, storage modulus, E', loss modulus, E'', and hardness, H, were calculated[19, 20]. Poisson's ratio was taken as 0.4.

The advantage of dynamic testing with respect to quasi-static loading is two-fold. On the one hand, time-dependent behavior can be examined. On the other, a profile of the mechanical properties as a continuous function of indentation depth can be obtained instead of a single reading at one indentation depth. As an example, Figure 3.2 illustrates the E' and H behavior with indentation depth, h, for Q1 and Q2 and one can see that both mechanical properties are constant beyond $h \approx 300$ nm and up to the maximum penetration depth $h \approx 1$ μm. The fact that E' and H remain constant with h suggests that mechanical properties are independent across the sample thickness and that substrate effects can be disregarded. Each E' and H value of Figure 3.2 represents the average of at least 50 different indentations tests and the error bars are associated to the standard deviation over the mean values.

Indents were evenly distributed along the sample surface to make the average E' and H values representative of the whole material. This is especially important in those samples in which the spherulite dimension was similar to the size of the volume of deformation (which approximately covers a hemisphere with

a radius of 20 μm for an indentation depth of 1 μm[21]. For the case of PEO, the radii of the spherulites approached the millimeter scale, and average *E´* and *H* values were meaningless. Instead, a range of experimentally measured *E´* and *H* values was reported.

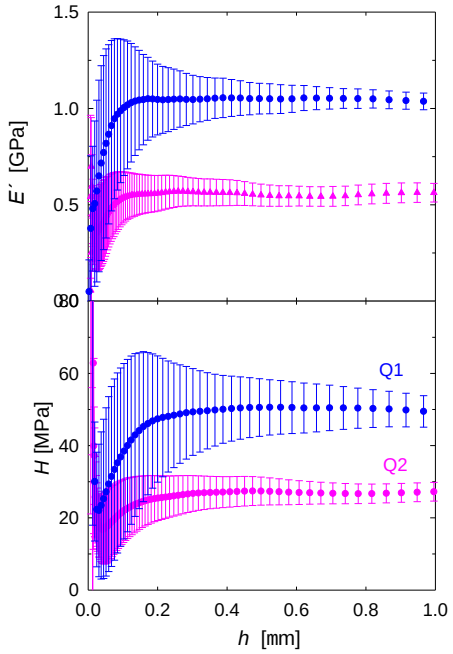

Figure 3.2. Variation of *E´* and *H* with indentation depth, *h*, for the tetrablock quarterpolymers Q1 and Q2. *E´* and *H* values represent the average of 70 and 50 indentation tests for Q1 and Q2, respectively. Data at small penetration depths below *h* = 300 nm can be disregarded because they are affected by surface roughness and material independent effects such as tip area miscalibrations[22]

3.3 References

1. Pazokifard, S.; Farrokhpay, S.; Mirabedini, M.; Esfandeh, M., Surface treatment of TiO_2 nanoparticles via sol-gel method: Effect of silane type on hydrophobicity of the nanoparticles. *Progress in Organic Coatings* **2015,** *87*, 36-44.

2. *Polymer Blends and Alloys*. Springer: Dordrecht, **1993**.

3. Alghunaim, A.; Kirdponpattara, S.; Newby, B. Z., Techniques for determining contact angle and wettability of powders. *Powder Technology* **2016,** *287*, 201-215.

4. Egerton, R. F., *Physical principles of electron microscopy: an introduction to TEM, SEM and AFM*. Springer: New York, **2006**.

5. Khursheed, A., *Scanning Electron Microscope Optics and Spectrometers*. World Scientific: Hackensack, USA, 2011.

6. Arnal, M. L.; Matos, M. E.; Morales, R. A.; Santana, O. O.; Müller, A. J., Evaluation of the fractionated crystallization of dispersed polyolefins in a polystyrene matrix. *Macromolecular Chemistry and Physics* **1998,** *199*, 2275-2298.

7. Reimer, L.; Kohl, H., *Transmission Electron Microscopy Physics of Image Formation*. Springer: New York, 2008.

8. Lorenzo, A. T.; Arnal, M. L.; Albuerne, J.; Müller, A. J., DSC isothermal polymer crystallization kinetics measurements and the use of the Avrami equation to fit the data: Guidelines to avoid common problems. *Polymer Testing* **2007,** *26*, 222-231.

9. *Tensile Testing*. Second Edition ed.; ASM International: Ohio, 2004.

10. Ladelta, V.; Zapsas, G.; Gnanou, Y.; Hadjichristidis, N., A new tricrystalline triblock terpolymer by combining polyhomologation and ring-opening polymerization. Synthesis and thermal properties. *Journal of Polymer Science, Part A: Polymer Chemistry* **2019,** *57*, 2450-2456.

11. Wang, D.; Zhang, Z.; Hadjichristidis, N., C1 polymerization: a unique tool towards polyethylene-based complex macromolecular architectures. *Polymer Chemistry* **2017,** *8*, 4062-4073.

12. Ladelta, V.; Zapsas, G.; Abou-Hamad, E.; Gnanou, Y.; Hadjichristidis, N., Tetracrystalline tetrablock quarterpolymers: Four different crystallites under the same roof. *Angewandte Chemie International Edition* **2019,** *58*, 16267-16274.

13. De Jeu, W. H., *Basic X-ray scattering for soft matter*. 1st ed.; Oxford: 2016.

14. Murthy, N. S., Experimental techniques for understanding polymer crystallization. In *Crystallization in multiphase polymer systems*, Thomas, S.; Arif, M.; Gowd, E. B.; Kalarikkal, N., Eds. Elsevier: **2018**; pp 49-72.

15. Carlton, R. A., Polarized Light Microscopy. In *Pharmaceutical Microscopy*, Springer: New York, **2011**; pp 7-64.

16. Carmeli, E.; Wang, B.; Moretti, P.; Tranchida, D.; Cavallo, D., Estimating the nucleation ability of various surfaces towards isotactic polypropylene via light intensity induction time measurements. *Entropy* **2019,** *21*, 1068.

17. Eaton, P.; West, P., Introduction. In *Atomic Force Microscopy*, Oxford University Press: **2010**; pp 1-6.

18. Arzate-Vázquez, I.; Chanona-Pérez, J.; Rodríguez-Castro, G.; Fuerte-Hernández, A.; Méndez-Méndez, J.V.; Gutiérrez-López, G.F., Indentation Technique: Overview and applications in food science. In *Food Nanoscience and Nanotechnology*, Hernández-Sánchez, H.; Gutíerrez-López, G.F., Eds. Springer: Cham, **2015**; pp 81-98.

19. Oliver, W. C.; Pharr, G. M., An improved technique for determining hardness and elastic modulus using load and displacement sensing indentation experiments. *Journal of Materials Research* **1992,** *7*, 1564-1586.

20. Herbert, E. G.; Oliver, W. C.; Pharr, G. M., Nanoindentation and the dynamic characterization of viscoelastic solids. *Journal of Physics D: Applied Physics* **2008,** *41*, 74021.

21. Hay, J.; Crawford, B., Measuring substrate-independent modulus on thin-films. *Journal of Materials Research* **2011,** *26* (6), 727-738.

22. Díez-Pascual, A. M.; Gómez-Fatou, M. A.; Ania, F.; Flores, A., Nanoindentation in polymer nanocomposites. *Progress in Materials Science* **2015,** *67*, 1-94.

Chapter 4

Neat/Recycled Polymer Blend and Nanocomposites (PBNANOs) with Titanium Dioxide Nanoparticles and Compatibilizer Agents: Morphology, Crystallization and Mechanical Properties

4.1 General Concepts

4.1.1 Polymer Recycling

Plastic consumption in packaging and many other applications is increasingly growing. In 2018, 359 million tonnes of plastics were produced worldwide, from which 61.8 million tonnes (17 %) were produced in Europe. The European plastic converters demand was 51.2 Mt, and Germany was the country with the highest plastic demand (24.6 %), followed by Italy (13.9 %), France (9.4 %) and Spain (7.6 %). Regarding the plastics demand by segment, packaging (39.9 %) and building and construction (19.8 %) by far represents the largest end-use markets, followed by the automotive industry 9.9 %).

In addition, the most demanded polymers are polyolefins: polypropylene (PP) for food packaging, sweet and snack wrappers, hinged caps, microwave containers, pipes, automotive parts, etc. (19.3 %); low and linear low-density polyethylene (PE-LD/PE-LLD) for reusable bags, trays, and containers, agricultural films, food packaging films, etc. (17.5 %); and high/medium density polyethylene (PE-HD/PE-MD) for toys, milk bottles, pipes, housewares, etc. (12.2 %). Other polymers such as polyvinyl chloride (PVC), polyurethane (PUR) and polyethylene terephthalate (PET) are also in demand for many other applications.

As a consequence of the high demand and manufacturing of plastic products, a large amount of waste is generated at the end of their service life, which goes from less than a year to 50 years or more. 29.1 Mt of post-consumer plastic waste was collected in the year 2018, from which 42.6 % was used for energy recovery, 32.5 % for recycling, and 24.9 % was sent to landfills.

Since 2006, the quantity of plastic post-consumer packaging waste sent to recycling has increased by 92%. From the 17.8 million tones of plastic post-consumer packaging waste collected, 42 % was recycled, 39.5 % was employed for energy recovery, and 18.5 % was sent to landfills. This positive trend is confirmed by the fact that more than half of the European countries have plastic packaging recycling rates above 40 %. However, although recycling is the first

option for plastic packaging waste, recycling rates are still low and more efficient reprocessing techniques are needed to make the recycling process more sustainable[1].

It is well known the need for recycling because of several benefits like saving manufacturing resources, lowering energy consumption, and minimizing the impact of plastics on the environment[2]. Many methods are used to recycle plastic waste: primary (a re-extrusion process), mechanical or secondary (plastics are separated based on their density in a tank and extruded after waste is reduced into pellets or powder), chemical or tertiary (which includes glycolysis, methanolysis, and hydrolysis to obtain the highest percentages of monomer) and incineration or quaternary recycling (for energy recovery). Each method has its own pros and cons, and depending on the polymer and the method employed in the production process, recycling processes are going to differ[3-5]. The efficient treatment of plastic waste is still challenging.

Polyethylene terephthalate (PET) is one of the most widely used polymers in packaging because of its good tensile strength, barrier properties, chemical resistance, elasticity, and the wide temperature range that it can support[6]. PET shows a greater tendency to replace traditional glass bottles in drink packaging due to its lighter weight and lower energy consumption during its production. That is why it is widely used for bottles to package mineral waters, milk, non-alcoholic beverages, fruit juices, carbonated soft drinks, etc[7].

However, it is very common to find more than one type of plastic in packaging products, such as water or milk bottles with PET bodies and polypropylene (PP) or polyethylene (PE) caps[8]. This implies removing the caps from the bottles before recycling or recycling PET/PP or PET/PE immiscible blends. Mechanical recycling is the most popular method to recycle PET waste because it is easy, economically affordable, and materials with relatively good mechanical properties can be obtained[2].

In addition, opaque PET bottles that have been introduced in the past few years in the market contain titanium dioxide (TiO_2) nanoparticles to provide better barrier and mechanical properties, and nanoparticle quantities vary depending on the application[9]. The TiO_2 is used because it protects the fluids in the PET bottles from ultraviolet radiation[10]. However, the white color of the bottles (promoted by TiO_2) limits the recycling feasibility of the bottles considerably, since transparent sheets and fibers are highly demanded[6].

Nevertheless, the addition of nanofillers (such as TiO_2 nanoparticles) is an alternative way to surpass the inherent incompatibility in polymer blends, as compatibilization is one of the main requirements to obtain new materials with good properties in PET/PP or PET/PE immiscible blends. In this section, a brief description of polyethylene terephthalate (PET), polypropylene (PP), polyethylene (PE), and titanium dioxide nanoparticles (TiO_2) will be presented. Then, general concepts of polymer blending and compatibilization will be described, with special attention to PP/PET/TiO_2 immiscible blend.

4.1.2 Polyethylene Terephthalate (PET)

Polyethylene terephthalate (PET) is a semicrystalline polyester. It is one of the most important engineering polymers because of its desirable properties: lightweight, high tensile and impact strength, stiffness, high chemical resistance, favorable creep characteristics, low flavor absorption, good barrier properties, reasonable thermal stability, and low flexibility (due to the presence of the short ethylene group and the *p*-phenylene group)[11, 12].

PET is produced by two different starting reactions: an esterification reaction between terephthalic acid (TPA) and ethylene glycol (EG) and a *trans*-esterification reaction with dimethyl terephthalate (DMT) and ethylene glycol (EG). The *trans*-esterification reaction is the preferred one because of its easier purification (Figure 4.1a). The output of these processes is bis(hydroxyethyl)

terephthalate (BHET), which is polymerized to a polymerization degree of up to 30 (Figure 4.1b). In the next polycondensation process the degree of polymerization is increased to 100. This low molecular PET is suitable for some applications such as fibres and sheets. In order to obtain higher molecular weight PET solid state polymerization (SSP) can be performed. Bottle grade PET is usually produced by SSP at 210 °C for around 15-20 h[12].

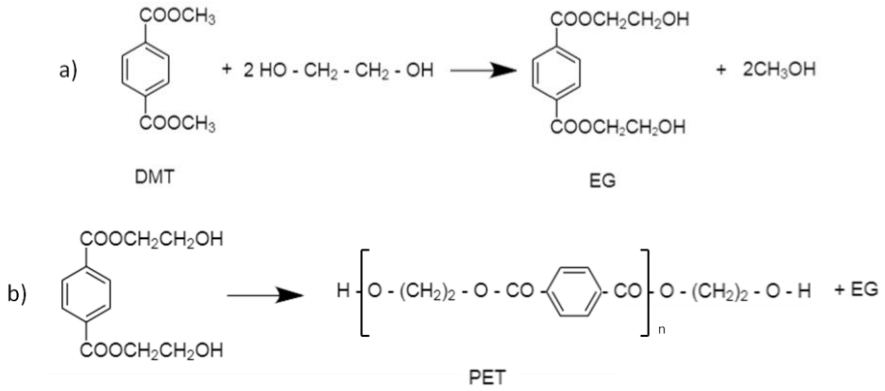

Figure 4.1. PET synthesis reactions: a) *trans*-esterification; b) condensation

Table 4.1 shows the physical and chemical properties of PET. Due to these good properties, PET is widely used in many applications such as food packaging, photographic applications, electrical and electronic instruments, house-wares, lighting products, power tools, material handling equipment, sporting goods, films, and fibers, etc.

Table 4.1. Physical and chemical properties of PET

Property	**Test method**	**Value (unit)**
Molecular weight (repeating unit)	-	192 (g/mol)
Mark-Houwink parameters	-	$K=3.72\cdot10^{-2}$ (ml/g) a=0.73
Weight-average MW	-	30000-80000 (g/mol)
Density	-	1.41 (g/cm^3)
Glass transition temperature	DSC	69-115 (°C)
Melting temperature	DSC	265 (°C)

Heat of fusion	DSC	166 (J/g)
Breaking strength	Tensile	50 (MPa)
Tensile strength (Young's modulus)		1700 (MPa)
Yield strain	Tensile	4 (%)
Impact strength	ASTM D256-86	90 (J/m)
Water absorption (after 24 h)	-	0.5 (%)

There are different ways of processing PET. Extrusion is the oldest and simplest one, and it can be either extrusion molding or extrusion to produce foam. Injection molding is not that satisfactory due to the poor mechanical properties of injection-molded PET. Blow molding is extensively used to produce bottles[12].

PET crystallizes in a triclinic crystal structure with these unit cell dimensions: a=4.56, b=5.94 and c=10.75 Å; and α=98.5 º, β=118 º and γ=112 º. However, slight variations in unit cell parameters are reported for PET since they vary with crystallization temperature, draw ratio, and subsequent annealing temperature and time[13]. Virgin PET shows a slow crystallization rate, and it depends on molecular weight, the presence of nucleating agents, the degree of chain orientation, the nature of the polymerization catalyst used in the original production of PET, and the thermal history[12].

4.1.3 Polyolefins: Polypropylene (PP) and Polyethylene (PE)

a) Polypropylene (PP)

Polypropylene (PP) is a semicrystalline thermoplastic polyolefin with good physical, mechanical and thermal properties: it is relatively stiff and has a high melting point, low density, and relatively good resistance to impact. Its main features make PP a highly versatile polymer for many applications in packaging, fibers, fabrics, strapping, films, sheets/thermoforming, injection or blow molded pieces, or in the automotive industry[14]. The main physical properties are listed in Table 4.2.

Table 4.2. Physical properties of a PP homopolymer[15]

Property	Test method (ASTM)	Value
Melt flow index	D1238	12 (g/10min)
Tensile yield strength	D638	34 (MPa)
Elongation at yield	D638	10 (%)
Flexural modulus	D790	1400 (MP)
Izod impact strength	D256	35 (J/mg)
Rockwell hardness	D785	88 (R scale)
Deflection temperature under laod	D648	92 (at 455 kPa)

Commercial polypropylene grades include homopolymers, block copolymers, random copolymers, rubber modified blends, and grafted PP. According to tacticity, homopolymer PP can be isotactic, syndiotactic, or atactic, but the isotactic polypropylene (iPP) is the most widely used one, in which all the methyl groups have the same configuration with respect to the polymer backbone. It is the most commercially significant due to its desirable properties: high melting temperature (≈160-170 °C under normal analysis conditions), softening point, rigidity, hardness, modulus, and tensile strength. Properties depend on molecular weight, crystal structure, lamellar size and crystallinity (a semicrystalline polymer contains amorphous and crystalline regions), additives, and processing conditions[15]. One of the disadvantages of PP is that it may suffer oxidation and thermal degradation at high temperatures because of the reactivity of the tertiary carbons in the main chain. That is why antioxidants are commonly added to PP[16].

The structure of PP consists of saturated aliphatic chains and, propylene is the repetitive unit. iPP was firstly discovered by Giulio Natta and co-workers in the early 50s. The heterogeneous Ziegler-Natta catalyst is identified as the best catalytic cycle to produce iPP, although the first-generation titanium trichloride catalysts used in the late 60s have been replaced by the high activity magnesium chloride catalysts[17].

The crystallization behavior of iPP shows polymorphism. Polymorphism is the ability of a material to crystallize in more than one crystallographic form or crystal structure. Three crystalline forms are known for iPP (α, β, and γ forms) and the mesomorphic form. The dominant crystalline form is the α-form, with a monoclinic unit cell with parameters a=6.65, b=20.96, c=6.50 Å and β=99.3º. It is the most stable thermodynamically, and it is formed under conventional industrial conditions. Typically, the β-form crystallizes in mixture with the α-form, showing a pseudohexagonal system, but specific nucleating agents are needed to obtain higher contents of the β-form in the iPP, since spontaneous nucleation occurs more easily for the α-form. In addition, the β-form is less stable and shows a melting temperature (≈155°C) lower than the α-form (≈170°C). The triclinic γ-form can only be obtained under specific conditions. And the mesomorphic form of iPP can be obtained through fast cooling procedures (higher than 100 K/s)[18, 19].

iPP can crystallize in different shapes. Spherulitic structures are the most common as a result of nucleation and growth phenomena. The size of the spherulites depends on the crystallization conditions (can vary between 5-100 μm), and it affects the mechanical and optical properties. The decrease of the spherulite size means a general increase in impact strength and transparency. Regarding morphology development, cooling rates, deformation fields, and pressure levels play a role during processing. Injection molding is the most employed technique in iPP processing because it presents the best set of conditions under which morphology development takes place[20].

In addition, nucleating agents are usually added to iPP because a larger number of smaller spherulites are created. The size reduction of the spherulites affects optical properties, reducing haze, and may improve flexural modulus and rigidity. To achieve an optimal efficiency of the nucleating agents, good dispersion is vital, and thus dispersion techniques during processing are very important[20].

b) Polyethylene (PE)

Polyethylene (PE) is a semicrystalline thermoplastic polyolefin, essentially a long-chain aliphatic hydrocarbon. Branching variations that the main carbon backbone may show leads to different types of PE (Figure 4.2):

a. High-density polyethylene (HDPE): it is chemically the most similar in structure to pure PE with almost no branches. Generally, high degree of crystallinity is achieved, resulting in high density (0.94-0.97 g/cm^3).
b. Low-density polyethylene (LDPE): the branching level is substantially higher and, generally, these branches consist of ethyl and butyl groups with some long-chain branches. As the crystallization process is hindered, lower crystallinity values are obtained, resulting in relatively low densities (0.90-0.94 g/cm^3) comparing to HDPE.
c. Linear low-density polyethylene (LLDPE): short alkyl groups at random intervals are attached to molecules with linear PE backbones. The most common branches are ethyl, butyl, or hexyl groups and, the average separation of branches along the main chain is typically 25-100 carbon atoms. Crystallization is inhibited to some extent, thus reducing density (0.90-0.94 g/cm^3) comparing to HDPE.
d. Very low/ultra low density polyethylene (VLDPE/ULDPE): this is a form of LLDPE with a much higher concentration of short-chain branches. The branches are usually separated by 7-25 backbone carbon atoms. Crystallinity degree is very effectively reduced, thus obtaining very low densities (0.86-0.90 g/cm^3)[21].

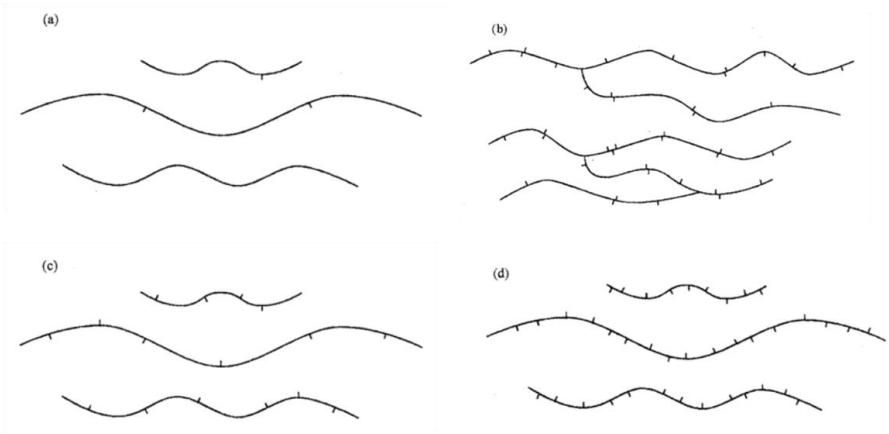

Figure 4.2. Schematic representations of different types of polyethylenes: (a) High density polyethylene (HDPE); (b) Low density polyethylene (LDPE); (c) Linear low density polyethylene (LLDPE); (d) Very low/ultra low density polyethylene (VLDPE/ULDPE)

Although these are the main PE types, there are hundreds of grades of PE available. Differences arise from many variables such as variations in the degree of short-chain or long-chain branching, variation in the average molar mass, the presence of small amounts of comonomer or polymerization residues or other impurities. Although these factors will affect the properties of the different PEs available, packaging is the most important application field.

However, PE is widely employed in many other applications due to its low cost, easy processability, excellent electrical insulation properties, excellent chemical resistance, toughness, and flexibility even at low temperatures, reasonable clarity of thin films, lack of odor and toxicity, and low water vapour permeability for packaging, building and agricultural applications[22].

It is a very versatile polymer and, properties can be tunned manipulating molecular and processing variables. In addition, antioxidants and stabilizers are usually employed to avoid oxidation reactions and other phenomena such as photodegradation or degradation by micro-organisms[23]. Fillers, pigments, flame

retardants, slip agents, blowing agents, rubbers or cross-linking agents are other widely used additives[22].

Table 4.3 shows some properties of different types of PE. However, this data should not be considered absolute since preparation conditions and testing configurations may show values outside the indicated ranges.

Table 4.3. Main properties of different types of PE

Property	**HDPE**	**LDPE**	**LLDPE**	**VLDPE**
Density (g/cm^3)	0.94-097	0.91-0.94	0.90-0.94	0.86-0.90
Crystallinity degree (%) (from calorimetry)	55-77	30-54	22-55	0-2
Flexural modulus (psi)	$1,45\text{-}2.25\cdot10^5$	$3.5\text{-}4.8\cdot10^4$	$0.4\text{-}1.6\cdot10^5$	$<4\cdot10^4$
Tensile modulus (psi)	$1,55\text{-}2.0\cdot10^5$	$2.5\text{-}5.0\cdot10^4$	$0.38\text{-}1.3\cdot10^5$	$<3.8\cdot10^4$
Tensile yield stress (psi)	$2.6\text{-}4.5\cdot10^3$	$1.3\text{-}2.8\cdot10^3$	$1.1\text{-}2.8\cdot10^3$	$<1.1\cdot10^3$
Tensile strength at break (psi)	$3.2\text{-}4.5\cdot10^3$	$1.2\text{-}4.5\cdot10^3$	$1.9\text{-}6.5\cdot10^3$	$2.5\text{-}5.0\cdot10^3$
Tensile elongation at break (%)	10-1500	100-650	100-950	100-600
Shore hardness type D	66-73	44-50	55-70	25-55
Izod impact strength (ft-lb/in)	0.4-4.0	No break	0.35-No break	No break
Melting temperature (ºC)	125-132	98-115	100-125	60-100
Heat distortion temperature (ºC)	80-90	40-44	55-80	-
Heat of fusion (cal/g)	38-53	21-37	15-43	0-15
Thermal expansivity (10^{-6} in/in/ºC)	60-110	100-220	70-150	150-270

PE was firstly synthesized in the 1930s by the hand of Eric Fawcett and Reginald Gibbon but, it was not until 1935 that Michael Perrin established the conditions to polymerize ethylene consistently. However, it was a highly branched low-density PE. It was not till the 1950s that Ziegler and coworkers developed linear PE employing low pressure polymerization techniques. In addition, the copolymerization of ethylene with small amounts of other alkenes in the 1960s extended the availability of PE-based products in the market[21].

Regarding the crystal structure, three structures are known for PE: the stable orthorhombic phase, a metastable monoclinic phase and, a hexagonal phase. The parameters for the orthorhombic cell are a=7.42; b=4.95, c=2.55 Å and α=β=γ=90 º. The monoclinic phase of PE (a=8.09; b=2.53, c=4.79 Å and β=107.90 º) is obtained applying stress to the orthorhombic one, but this metastable form transforms below the melting point to orthorhombic PE on the heating. The hexagonal PE phase (a=8.42; b=4.56, c=not determined Å) appears at high pressures but, it is also transformed into the orthorhombic phase[24].

Crystallization of PE may lead to the formation of spherulites or axialites. Morphology depends on the molecular mass, crystallization conditions (isothermal crystallization temperature or cooling rate), molecular constitution, and polydispersity. In general words, axialites are formed at low molecular weights (<17.000 g/mol), axialites or spherulites depending on crystallization temperatures (18.000-115.000 g/mol), spherulites at higher molecular weights (116.000-800.000), and not clear structures can be detected for molecular weights greater than 2.000.000 g/mol[25]. The size and distribution of spherulites will affect the final properties of the material, thus two techniques can be employed in order to increase the number of spherulites with a reduced size: control the method and rate of cooling or incorporation of nucleating agents. Optimization of PE morphology can improve physical properties such as water vapor transmission, optical clarity, shrinkage, and some electrical properties[26].

4.1.4 Binary Polymer Blends

Polymer blending is one of the most rapidly growing areas in polymer science because some of the drawbacks that single polymers show for specific applications can be improved by blending or adding fillers. In addition, in the last years the addition of nanofillers (particles are of the nanoscale order) has attracted great interest since small amounts of these nanofillers can bring a significant improvement of the properties[27].

The combinations of the following factors contribute to the continued commercial interest of polymer blends:

- It is more cost-effective the blending of commercially available polymers than developing a new product with the desired properties (which generally involves high research, development, and capital costs).
- Polymer blends can fit the cost-performance gaps in the existing commercial polymers. Properties that a single resin cannot provide are only achieved by blending polymers.
- Polymer blends can be produced at a relatively low cost and in a wide range of production volumes using an extruder. Production of new polymers usually requires new plants and reactors operating at large scales.
- Blends can be formulated, optimized, and commercialized generally at a much faster rate than new polymers.
- Blends offer economic means of upgrading recycled polymers[28].

Melt blending is the most employed technique to produce polymer blends. As the viscosity of polymers is high, the best option to ensure dispersion of one polymer into the other one is the use of intense mechanical mixing at high temperatures, in which all the components are at the molten state[29].

The most effective blending machines are co-rotating twin-screw extruders, but other factors such as blending temperature, screw speed, or residence time

have to be taken into account as they are important in the development of phase morphology[30]. In addition, blend composition also plays a key role. At low contents of the minor phase, the breakup mechanism is favored and will determine the final particle size, whereas, at higher contents of the minor phase, both breakup and coalescence mechanisms will compete. Interfacial properties (miscibility and compatibility) of the components will also affect the final morphology of the blends.

At the beginning of mixing, the droplets of the dispersed phase are big. The dispersed droplets are deformed and stretched into long thin threads because the shear stresses are larger than the interfacial ones. If the radius of the thread is small enough, interfacial disturbances grow on the thread, and small droplets are formed because the breakup of such threads occurs. These small droplets can be broken again or may coalesce due to collisions against each other. The smaller the final droplet size, the better the dispersion of the dispersed phase, preventing coalescence and thus, enhancing mechanical properties because stress transfer between phases is promoted and because of the higher contact surface between the two polymers[29, 30]. So, the final morphology is determined by breakup and coalescence (Figure 4.3).

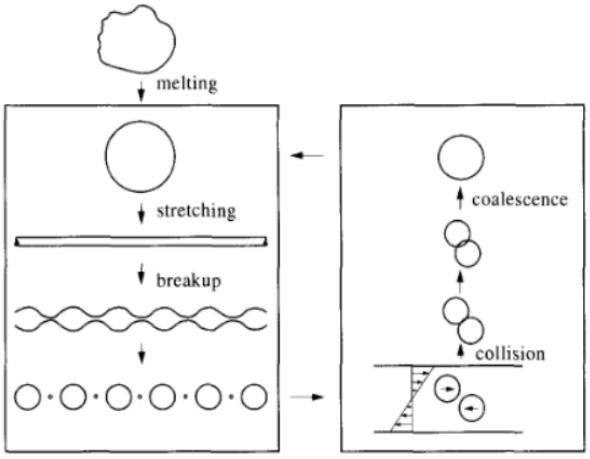

Figure 4.3. Schematic representation of breakup and coalescence mechanism

There are three different types of blends: miscible, partially miscible or compatible and, immiscible or incompatible. In a miscible blend, there is a unique glass transition temperature (T_g), which is between the T_g values of each of the components of the blend. They exhibit a homogeneous phase, and the final mechanical performance is in between the ones shown by the neat polymers. In a partially miscible blend, two phases can be distinguished, one phase is rich in one component and the other phase rich in the other one. Each phase shows a T_g, whose value is between the values of the pure components. There is a wide interphase and usually interfacial adhesion is good enough to show good properties[31, 32]. Finally, immiscible blends are the most common type of blends. They exhibit a sharp interphase with poor adhesion between phases that may conduct the material to fracture due to the relatively low entropy of mixing between phases, and they show two T_g values corresponding to each of the pure components[30].

Poor mechanical properties are commonly observed in immiscible blends. Due to the poor adhesion between phases, mechanical properties such as yield stress, stress at break, maximum elongation at break and impact strength can be decreased[33].

Since the final physical properties and mechanical performance will depend on the miscibility or compatibility of the components, compatibilization of blends is usually required[30]. There are several strategies to do so, as the use of block copolymers, reactive compatibilizing agents and nanoparticles.

In the case of block copolymers, one block is miscible with one component and the other block with the second component of the blend. Interfacial adhesion is improved if enough chain entanglements take place, and coalescence of the droplets is hindered by steric hindrance (Figure 4.4a). In addition, grafted polymers can also be employed because, besides the miscibility with one component of the blend, they usually contain attached functional groups to react with the functional groups of the dispersed phase creating chemical bonds between

both phases. This is called reactive compatibilization, and it is usually employed during melt mixing in order to obtain well-dispersed and stabilized morphologies. Some of the most employed functional groups are maleic anhydride (MA), primary and secondary amines, carboxylic acid, or acrylic acid, among others. Polyethylene and polypropylene modified with MA are widely employed as polymeric compatibilizers (PEgMA and PPgMA)[29, 30, 34-37].

Recently, the use of rigid nanoparticles as compatibilizers or stabilizers has increased, since they can ensure strong interfacial adhesion between two incompatible polymers. Many studies have been published about the use of nanoparticles such as clays[38-50] or nanosilica (NS)[51-65]; fewer studies have been reported for carbon nanotubes (CNT)[9, 66-80], graphene and its derivatives[81-83], and TiO_2 nanoparticles[6, 37, 84-89].

Nanofillers can act as Pickering emulsion promoters[34, 75, 90, 91]. This means that if the nanofiller is located at the interface between the two immiscible phases, then a reduction of the surface tension can be achieved with a concomitant reduction in particle sizes for blends with sea-island morphologies (typically with more that 60% of one of the components in the blends). Furthermore, the new interphase constituted by the surrounding nanofiller shell can act as a physical barrier that prevents coalescence during processing or post-processing procedures (Figure 4.4b). However, other mechanisms such as modification of viscosities of the polymers (due to the presence of nanofillers), reduction of the mobility of the droplets or some steric hindrance may occur. That is why it is complex to determine the mechanisms that take place in the reduction of the dispersed phase[34, 92, 93].

The blends with added nanofillers have been denominated PBNANOs, i.e., *polymer blend nanocomposites*. The changes in morphology caused by the addition of nanofillers can produce significant effects on the mechanical, thermal, barrier, and electrical properties[45-48, 54, 57-61, 66, 67, 76, 92-97]. In addition, low nanofiller content is enough to obtain enhanced properties (<5 wt % or <2-3 vol %), although

the dispersion and specific location of nanofillers play a key role in the compatibilizing effect[31, 98].

Nanofillers can be located in one of the phases, at the interface between the matrix and the dispersed phase, or in both places at the same time. The nanofiller location will be determined by the affinity of the nanofillers to each phase, and this affinity will be determined by the surface chemistry of the particles and the polarity of the polymers. Therefore, the migration of nanoparticles may occur from the less affine phase to the interface, or to the second more affine phase[6, 34, 92].

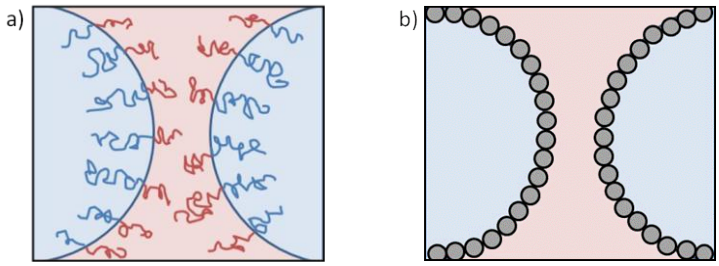

Figure 4.4. Schematic representation of mechanisms to avoid coalescence by a) the addition of a compatibilizer and b) rigid nanoparticles

Another strategy to improve compatibilization of polymer blends is the combination of compatibilizing agents and different types of nanofillers. However, significant improvements were not detected regarding mechanical properties[41, 84, 92, 99-102].

There are three main strategies to produce PBNANOs: in situ polymerization, solvent-assisted techniques and, melt compounding. Melt compounding is the most employed technique to produce commercial PBNANOs due to: fast dispersion of the nanoparticles in the melt by mechanical mixing, available industrial melt compounding capacities, and environmentally friendly preparation[98].

Polymer blends and PBNANOs are very interesting because the combination of two or more polymers with different properties is an effective way to obtain new materials with innovative properties[31]. Generally, they show improved heat resistance, toughness, solvent resistance, moisture resistance, dimensional stability, processability, flame resistance, and appearance[28]. They are very useful for automotive, electrical, and electronic applications. Other applications such as packaging, sports, and recreation equipment and, medical device industries can also take advantage of these materials[29]. Regarding packaging, PP/PET binary blends are widely used since the combination of the properties of PP and PET make these blends very interesting: PET has a lower permeability to gases and a higher permeability to water than PP, and they are also complementary in their resistance to solvent and chemical attack[31].

4.1.5 Crystallization in Immiscible Polymer Blends

The crystallization behavior of both the polymeric matrix at the dispersed phase of a polymer blend can be affected in comparison to the neat polymer. Many factors influence the crystallization process, causing changes in nucleation density, the spherulitic growth rate and overall crystallization kinetics, crystallinity degree, and crystalline morphology:

- Molecular structure and molecular mass of the components
- Composition of the blend
- Type and degree of dispersion of the phases
- Phase interactions, such as nature of the interface, migration of nuclei, etc.
- Crystallization conditions (e.g., T_c, cooling rate, etc.)
- Physical crystallization environment that is, if it's surrounded by melt or solidified material.

However, the physical state of the second phase when crystallization occurs will play a key role in the crystalline behavior[103-105]. It is important to note that the

crystallization order of the phases will affect the crystallization behavior in double crystalline immiscible polymer blends, if the first component to crystallize is the polymer matrix or the dispersed phase.

When the polymer matrix is the first component to crystallize at high temperature while the dispersed droplets remain in the molten state, nucleation density of the components may change due to migration of nuclei/ impurities from one phase to the other in the melt-mixing process. This can shift T_c to higher temperatures because heterogeneous nucleation of the matrix may increase, although the crystal growth rate, *G*, is generally not affected. The crystallization behavior of the matrix is only governed by nucleation.

When the dispersed droplets crystallize firstly, they will do it surrounded by the molten polymer matrix; then, the matrix will crystallize in the presence of semi-crystalline droplets. These solid droplets can act as nucleating agents shifting the T_c to higher temperatures. The size of the firstly crystallized dispersed droplets affects the crystallization behavior.

Additionally, coincident and fractionated crystallization may occur. The crystallization temperature of the matrix can increase due to the nucleating effect of the dispersed phase. If at the same time, the crystallization temperature of the dispersed phase is decreased due to its good dispersion, both crystallization events can overlap, and coincident crystallization occurs[103].

Moreover, the dispersed phase can also crystallize in a fractionated way. This means that crystallization can occur at different temperatures, always at temperatures lower than that of the bulk polymer, when it is well dispersed into sufficiently small droplets. This occurs due to the lack of heterogeneities, which are responsible for the nucleation at a certain temperature. When the droplet size is reduced beyond a certain value, it may no longer have a nucleus for heterogeneous nucleation, and the dispersed droplet crystallize at lower temperatures by a surface or homogeneous mechanism[103, 105-107].

4.1.6 PET/PP and PET/PE Polymer Blends with TiO_2 Nanoparticles

Some works have already been reported for PET/polyolefin/TiO_2 polymer blends. Sangroniz et al. studied the relationship between morphology, thermal properties, and rheology in PET/LDPE and PET/LDPE/TiO_2 PBNANOs rich in PET. They reported a reduction of droplet size with the addition of TiO_2 because of its location at the interphase, and a moderate nucleation effect[6]. Several works have been published dealing with the preferential location of nanofillers in immiscible blends[30, 34, 37, 75, 84, 90, 92-96, 108-111].

Nanofillers are usually functionalized at their surface so that they can have more affinity to one phase. Elias et al. studied the location of hydrophilic and hydrophobic silica in a polypropylene/polystyrene blend. The hydrophilic silica was mostly located within the PS phase, whereas the hydrophobic one was located within the PP phase. They attributed the preferential location to the lower interfacial tension between the nanoparticles and the specific phase where it was located[56]. Majesté et al. reported the confinement of hydrophilic silica in the EVA phase for PP/EVA immiscible blends, whereas hydrophobic nanosilica treated with trimethoxyoctylsilane located at the PP/EVA interphase[55].

However, other authors reported that surface tension is not always the key factor responsible for the preferential location of nanofillers in a blend of two chemically different polymers. The flexibility of polymer chains also has to be considered, as the entropy penalty may be decisive in the absorption of polymers on the surfaces of many nanofillers[112].

In addition to the above-mentioned thermodynamic factors, the blending sequence could also be investigated to determine the preferential location of nanofillers. There are two main methods to incorporate nanofillers into blends: mixing the three components at the same time or, blending one polymer with the nanofiller and adding the second polymer in another extrusion process. Some investigations have shown that the blending sequence does not affect the preferential location of the nanofillers, as they will stay or migrate to the preferred

phase[75, 113]. Fu et al. studied the kinetic-controlled compatibilization of PP/PS blends with nanosilica. According to them, the mixing time affects the dispersed droplet size, as shorter times lead to a reduction of the dispersed PS droplet size[114].

Many reports discuss the mechanical properties of filled polymer systems. Fillers have been used to modify many properties of polymers, such as strength, toughness, processability, dimensional stability, or lubrication. The interaction with the polymer matrix and the filler concentration and particle size are important factors to improve the mechanical properties. Modification of the surface of fillers is becoming more important because of its improvement on adhesion, and hence, on the stress transfer between polymer and filler, which leads to an increase in the dispersion degree[115]. For instance, organically modified montmorillonite is widely used as filler in many systems. Aubry et al. studied the effect o adding modified montmorillonite to an 80% PE/20% PA blend. Because of the location of nanoclays at the interface, break up was promoted, and coalescence inhibited stabilizing the system. Mechanical properties such as stress and elongation at break were improved, as energy dissipation was favored, making these organo-nanoclays good compatibilizers[97, 116].

4.2 Results and Discussion

4.2.1 PET/HDPE and PET/HDPE/PEgMA Blends. Compatibilizer Effect

4.2.1.1 Blends Morphology by SEM

Figure 4.5 shows the SEM micrographs of the binary blends PET/HDPE. All compositions were analyzed (starting with higher content of PET) and the sea-island or droplet-matrix morphology expected for these immiscible binary blends was detected. In Figures 4.5a-d the main component is PET, which corresponds to the polymer matrix with HDPE droplets dispersed in it, whereas in Figures 4.5e-i, the droplets correspond to PET due to the phase inversion that occurs at 60 wt%

PET (Figure 4.5d). HDPE droplet size increases as the content of PET decreases up to the phase inversion, and from now on, PET droplet size is reduced as the content of HDPE increases. In these cases, PET droplets are smaller in size than the droplets of HDPE in their mirror compositions (Figure 4.5). Adhesion between phases is poor, as many holes through the samples can be noticed, which is characteristic of immiscible polymer blends. The average diameters in volume (d_v) and number (d_n) are given in Table 4.4.

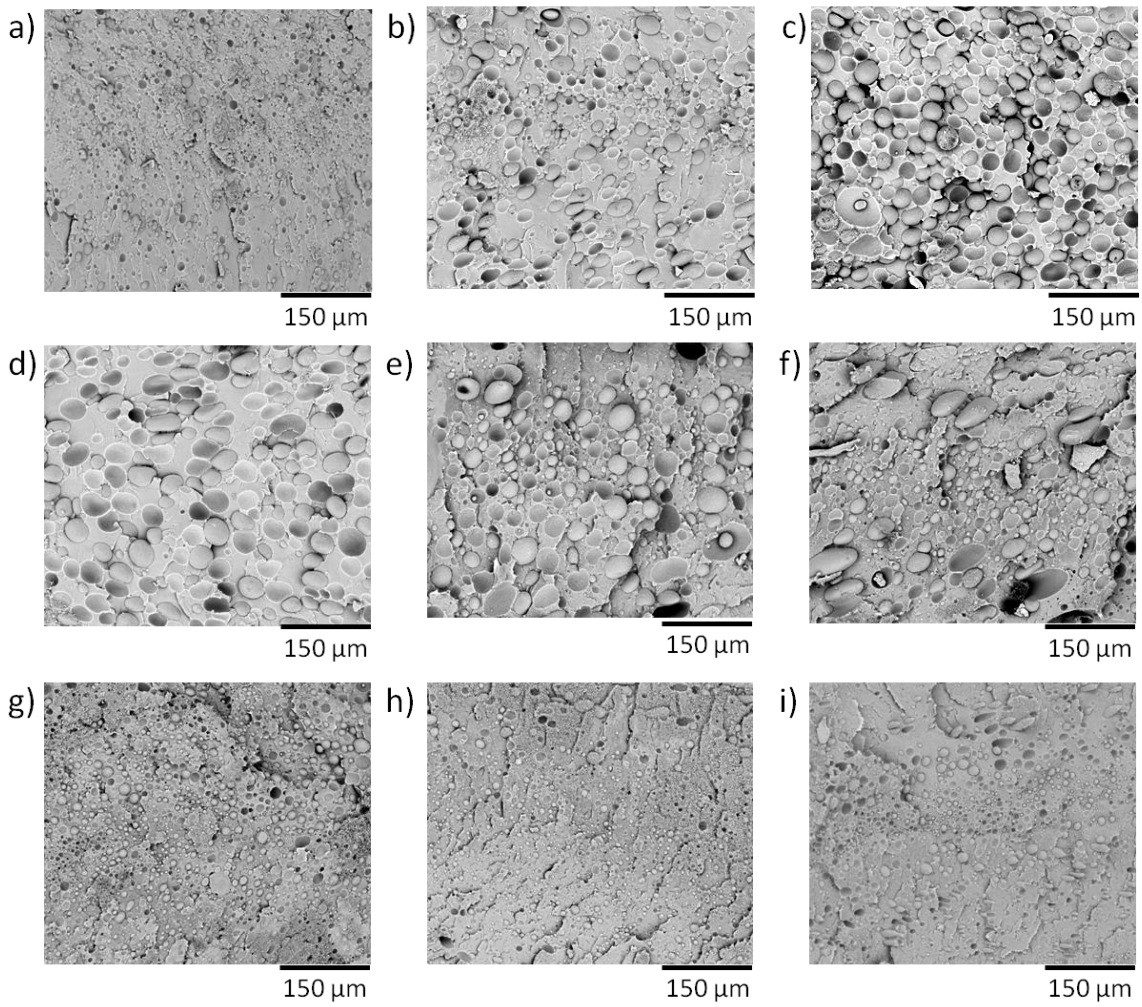

Figure 4.5. SEM images of PET/HDPE binary blends: a) 90/10, b) 80/20, c) 70/30, d) 60/40, e) 50/50, f) 40/60, g) 30/70, h) 20/80, and i) 10/90

Figure 4.6 show the SEM micrographs of the PET/HDPE/PEgMA blends. The compatibilizing agent PEgMA is added to improve morphology, and it always added so that it remains 10 % of the dispersed phase. In these cases, the reduction of droplet size is considerable in comparison with the uncompatibilized PET/HDPE blends (Figure 4.5). Droplet size remains almost unchanged (Figure 4.7) and, although adhesion is better, still some holes can be detected (mostly in the 50/50/5 blend). The average diameters in volume (d_v) and number (d_n) are given in Table 4.4.

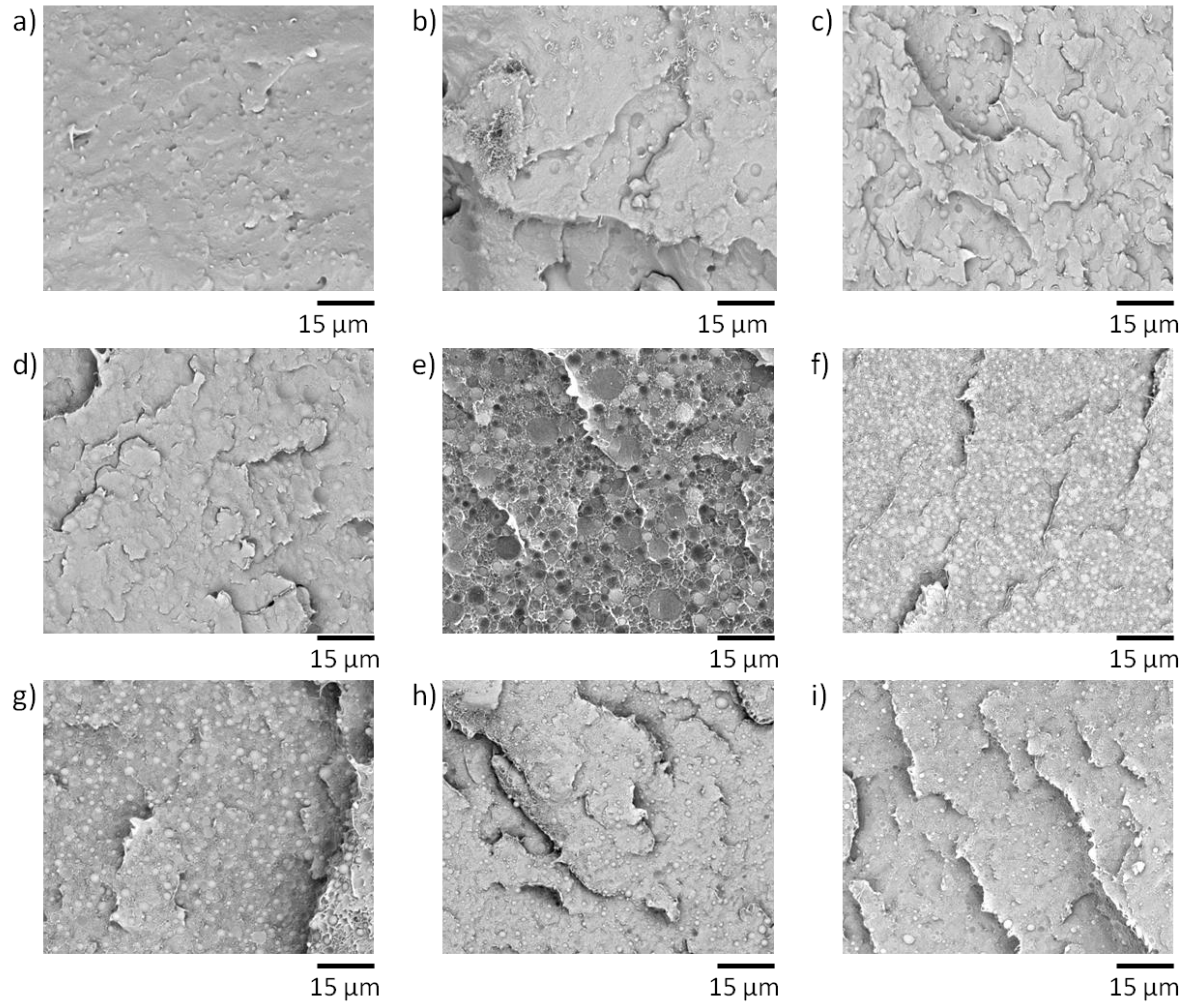

Figure 4.6. SEM images of PET/HDPE/PEgMA blends: a) 90/10/1, b) 80/20/2, c) 70/30/3, d) 60/40/4, e) 50/50/5, f) 40/60/4, g) 30/70/3, h) 20/80/2, and i) 10/90/1

Table 4.4. Number-average (d_n) and volume-average (d_v) diameters and particle size distributions (D) of PET/HDPE and PET/HDPE/PEgMA blends

PET/HDPE	**d_n (µm)**		**d_v (µm)**		**D**	
wt %	No comp.	PEgMA	No comp.	PEgMA	No comp.	PEgMA
90/10	5.44	1.29	10.20	1.60	1.88	1.24
80/20	13.62	2.89	23.41	3.23	1.72	3.23
70/30	18.23	2.12	27.83	2.56	1.53	1.12
60/40	25.59	1.47	32.44	1.81	1.27	1.23
50/50	13.79	2.19	26.39	3.39	1.91	1.55
40/60	5.42	1.11	11.96	1.45	2.21	1.30
30/70	6.85	1.74	10.32	2.03	1.51	1.23
20/80	5.74	3.63	7.85	8.47	1.37	2.33
10/90	4.34	2.71	7.06	3.95	1.63	1.46

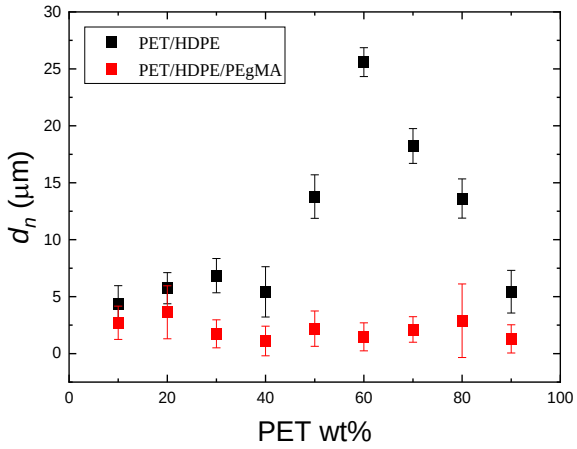

Figure 4.7. Number-average diameter (d_n) as a function of PET weight % for uncompatibilized (PET/HDPE) and compatibilized (PET/HDPE/PEgMA) blends

4.2.1.2 Non-isothermal Crystallization Behavior by DSC

Since the analyzed morphology affects the physical properties of the blends, the effect of droplet size on the crystallization behavior is studied in this section. However, there are no significant changes in the crystalline behavior of these blends. Separate crystallization (T_c) and melting (T_m) peaks are obtained for each of the components, as expected in these immiscible blends. Figure A.4.1 in the

Appendix show all the thermal transitions, and the characteristic thermal properties obtained during the scans are presented in Tables A.4.1.-A.4.4 in the Appendix.

4.2.2 70PET/30HDPE/TiO_2 and 70PET/30HDPE/TiO_2/PEgMA Blends. Effect of the TiO_2 Nanoparticles and the Compatibilizer Agent

The chosen blend for the following study was the 70PET/30HDPE blend, a composition prior to the phase inversion. This blend shows sea-island morphology, where the matrix corresponds to PET (70%) and the dispersed droplets are HDPE (30%).

TiO_2 nanoparticles were added to the uncompatibilized 70PET/30HDPE blend in order to compare the effect of adding the TiO_2 nanoparticles and the compatibilizer agent PEgMA. Therefore, TiO_2 nanoparticles were also added to the compatibilized 70PET/30HDPE/PEgMA blend to study the combined effect of adding both components.

4.2.2.1 Blends Morphology by SEM

The morphology of these samples is shown in the SEM micrographs in Figure 4.8. Figure 4.8a shows the binary PET/HDPE blend, whereas Figures 4.8b and 4.8c show the blends with 5% and 10% of TiO_2, respectively. The very small particles that can be observed in the figures correspond to the TiO_2 nanoparticles. It is clear that the addition of 5% TiO_2 nanoparticles is not enough to reduce the particle size since it remains almost the same as in the PET/HDPE blend (Figure 4.8a). However, the addition of 10% TiO_2 nanoparticles is very effective because the particle size of the dispersed HDPE droplets decreases significantly, although there are some holes which mean adhesion between phases could still be enhanced (Figure 4.8c).

Figure 4.8d shows the compatibilized PET/HDPE/10% PEgMA blend. Adhesion between phases is quite poor, but a significant reduction of droplet size occurs comparing it to the binary PET/HDPE blend (Figure 4.8a), as expected for a good compatibilizer[65, 119-121]. Then, Figures 4.8e and 4.8f show the SEM micrographs of the compatibilized blends with 5% and 10% of TiO_2 nanoparticles, respectively. In both cases, some holes can still be appreciated, and the reduction of droplet size remains almost constant, comparing it to the 70PET/30HDPE/10%PEgMA blend (Figure 4.8d). There is not a combined effect that improves significantly particle size of the dispersed HDPE phase using both the compatibilizer agent and the TiO_2 nanoparticles, they show a similar efficiency reducing particle size on their own. The number (d_n) and volume (d_v) average diameters and particle size distributions (D) calculated according to Equation 4.1 are listed in Table 4.5.

$$d_n = \frac{\sum n_i d_i^2}{\sum n_i d_i} \qquad d_v = \frac{\sum n_i d_i^4}{\sum n_i d_i^3} \qquad D = \frac{d_v}{d_n} \qquad \text{Eq.4.1}$$

Similar morphologies have been previously reported in PET/PE (80/20 wt%) blends compatibilized by nanoclays[121]. They analyzed the thermal stability, morphology, and mechanical properties of PET/PE blends containing a surfactant as a compatibilizing agent alone in the absence of clay to study the effects of both components in these blends separately. The finest morphology was obtained in the absence of clay, although reduction of particle size of the dispersed phase was also obtained by the addition of clays. More studies have been reported for similar immiscible polymer blends[51, 54-56, 59].

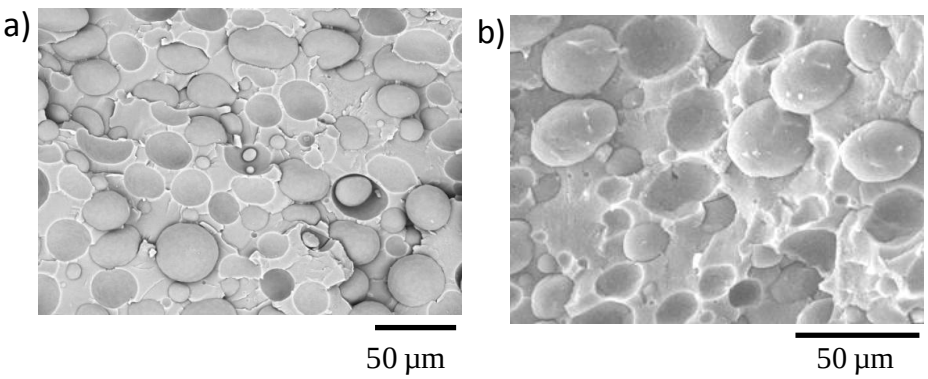

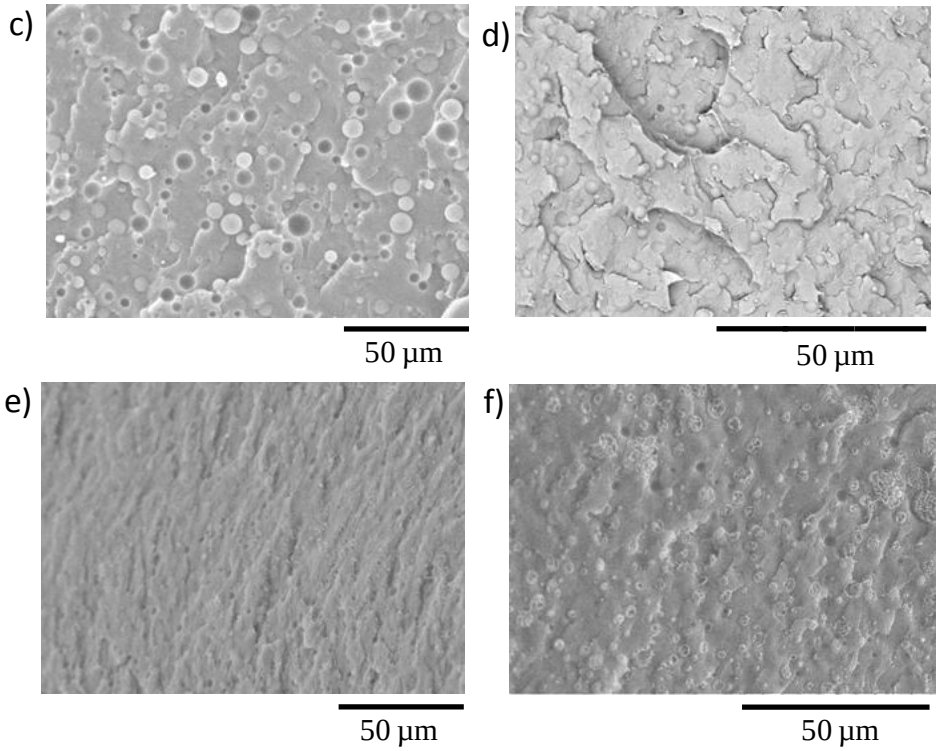

Figure 4.8. SEM micrographs of a) 70PET/30HDPE, b)70PET/30HDPE/5% TiO_2, c) 70PET/30HDPE/10% TiO_2, d) 70PET/30HDPE/10% PEgMA, e) 70PET/30HDPE/5% TiO_2/10% PEgMA, and f) 70PET/30HDPE/10% TiO_2/10% PEgMA

Table 4.5. Number-average (d_n) and volume-average (d_v) diameters and particle size distributions (D) of the indicated samples

Samples	d_n **(µm)**	d_v **(µm)**	**D**
70PET/30HDPE	18.2	27.8	1.5
70PET/30HDPE/5%TiO_2	20.8	24.9	1.2
70PET/30HDPE/10%TiO_2	4.6	6.9	1.5
70PET/30HDPE/10%PEgMA	2.1	2.6	1.1
70PET/30HDPE 5%TiO_2/10%PEgMA	1.9	2.5	1.3
70PET/30HDPE 10%TiO_2/10%PEgMA	2.5	3.1	1.6

4.2.2.2 Blends Morphology by TEM

Although several theories explain the reduction of droplet size, one of the main factors is the location of TiO2 nanoparticles34, 52, 92, 96, so to analyze the location and distribution of the nanoparticles TEM micrographs are shown in Figure 4.9. In Figures 4.9a and 4.9b (5% and 10% TiO_2) nanoparticles are mainly located in the PET matrix, whereas in Figures 4.9c and 4.9d (5% and 10% TiO_2 along with PEgMA) nanoparticles are mostly located inside the dispersed HDPE droplets.

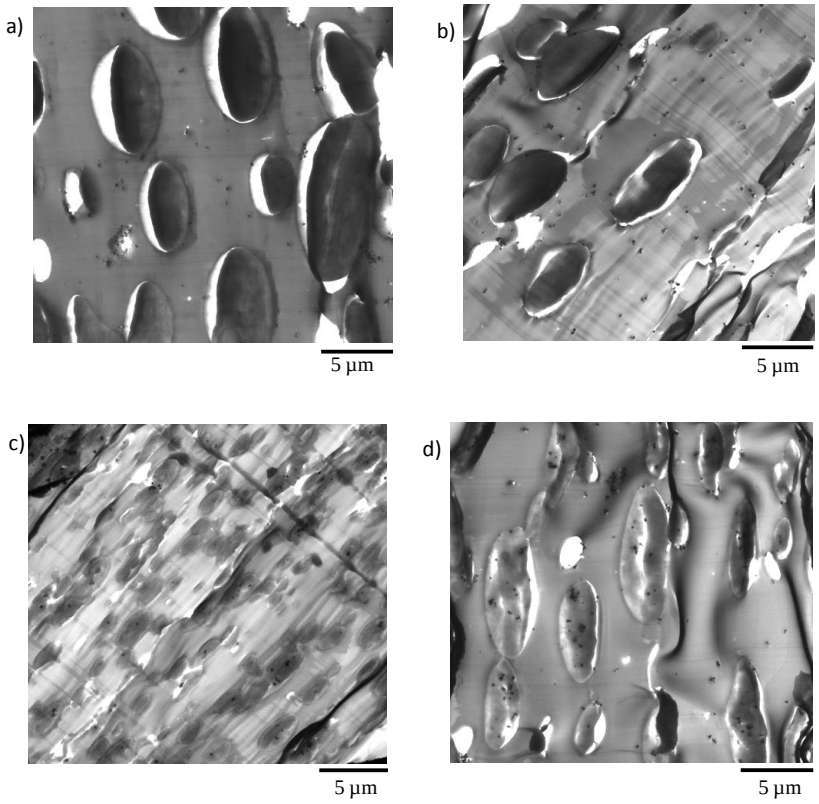

Figure 4.9. TEM micrographs of a) 70PET/30HDPE/5% TiO_2, b) 70PET/30HDPE/10% TiO_2, c) 70PET/30HDPE/5% TiO_2/10%PEgMA and d) 70PET/30HDPE/10% TiO_2/10% PEgMA

A change in the localization of TiO_2 nanoparticles occurs from the PET matrix to the HDPE droplets when both TiO_2 nanoparticles and the compatibilizing agent PEgMA are present in the samples. This could be due to the affinity of the TiO_2 nanoparticles with the PEgMA compatibilizing agent.

Although in the case of PET/PP blends rich in PP, as reported by Li et al., particles locate in the PET droplets, some results in the localization of nanoparticles have been reported[37, 84, 88, 109].

4.2.2.3 Non-isothermal Crystallization Behavior by DSC

Morphology affects the physical properties of the blends, that is why we will study the effect of droplet size reduction on the crystallization behavior of the samples.

The cooling from the melt and heating scans of the samples at 20 °C/min are shown in Figure 4.10, and the characteristic thermal properties obtained during the scans are presented in Tables 4.6-4.7. The blends show separate crystallization (T_c) (Figure 4.10a) and melting (T_m) peaks (Figure 4.10b) that belong to each of the phases, as expected in immiscible blends.

Figure 4.10a shows the cooling scans after erasing the thermal history of the samples. Applying non-isothermal conditions, homopolymers PET and HDPE crystallize with well defined exotherms at 189 °C and 120 °C, respectively. In the blends, the high temperature peak corresponds to the crystallization of the PET matrix, whereas the crystallization of the HDPE droplets occurs at lower temperatures showing a clear exothermic peak.

The crystallization temperature of the HDPE droplets remains almost unchanged in all blends. However, the PET matrix exhibits an increase of 7-11 °C in its crystallization temperature with the addition of 5% and 10% of TiO_2 nanoparticles. As we have previously seen in Figures 4.9a and 4.9b, TiO_2 nanoparticles are mainly located at the PET matrix, and the nucleating effect of these nanoparticles increases its crystallization temperature.

Regarding the 70PET/30HDPE/10% PEgMA blend, a close-up let us determine that PET starts to crystallize at 175 °C, a temperature lower than that of the neat PET. That is why when we have both TiO_2 nanoparticles and the

compatibilizing agent, the crystallization temperature of PET is similar to the neat PET because the nucleating effect of the nanoparticles is suppressed by the antinucleating effect of the compatibilizer.

Analyzing the normalized crystallization enthalpies (i.e., values are normalized with respect to the amount of crystallizing phase considering), all of them exhibit similar values, within the experimental error of the measurements. However, in the case of the 70PET/30HDPE/10% PEgMA blend, the crystallization enthalpy of the PET phase is much lower, but PET crystallization occurs in the heating scan, as the cold crystallization peak (T_{cc}) at 143 °C shows (Figure 4.10b blue curve).

Figure 4.10b shows the heating DSC scans of all samples. Two separate melting peaks are observed for the blends, which do not significantly vary from the melting point of the PET (245 °C) and HDPE (136 °C) homopolymers. Crystallinity values are also reported in Table 4.7, with no variation among them.

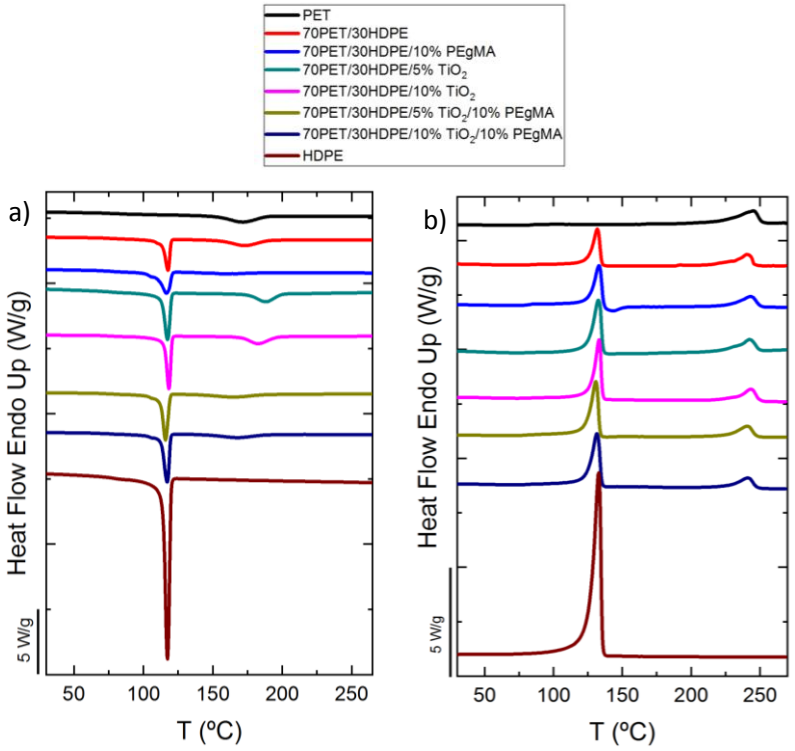

Figure 4.10. DSC scans at 20 °C/min of the indicated blend compositions, a) cooling and b) heating

Table 4.6. Thermal properties during cooling from the melt at 20 ºC/min, enthalpies are normalized

Samples	$T_{c,\ onset,\ PET}$ (ºC)	$\Delta H_{c,PET}$ (J/g)	$T_{c,\ onset,\ HDPE}$ (ºC)	$\Delta H_{c,HDPE}$ (J/g)
PET	189	33.3	-	-
70PET/30HDPE	190	38.8	120	125.8
70PET/30HDPE/10% PEgMA	175	12.5	121	165.8
70PET/30HDPE/5% TiO_2	200	40.0	120	209.2
70PET/30HDPE/10% TiO_2	196	37.0	121	178.0
70PET/30HDPE/5% TiO_2/10% PEgMA	187	22.5	119	193.7
70PET/30HDPE/10% TiO_2/10% PEgMA	188	24.5	120	200.5
HDPE	-	-	120	187.5

Table 4.7. Thermal properties during heating at 20 ºC/min, enthalpies are normalized

Samples	$T_{m,\ peak,\ PET}$ (ºC)	$\Delta H_{m,PET}$ (J/g)	$X_{c,PET}$ (%)	$T_{m,\ peak,\ HDPE}$ (ºC)	$\Delta H_{m,HDPE}$ (J/g)	$X_{c,HDPE}$ (%)
PET	245	31.3	22	-	-	-
70PET/30HDPE	242	31.8	23	136	121.2	41
70PET/30HDPE/10% PEgMA[1]	245	29.1	12	135	123.2	42
70PET/30HDPE/5% TiO_2	243	31.6	23	138	207.6	71
70PET/30HDPE/10% TiO_2	245	30.0	21	-	176.3	60
70PET/30HDPE/5% TiO_2/10% PEgMA	241	26.8	19	135	193.6	66
70PET/30HDPE/10% TiO_2/10% PEgMA	243	26.1	18	135	195.9	67
HDPE	-	-	-	136	188.8	64

[1] $T_{cc,PET}$ = 143 °C and $\Delta H_{cc,\ PET}$ = 12.3 J/g

4.2.3 Recycled rPET/rPP PBNANOs

4.2.3.1 rPET, rPP and rPP/rPET Blends Characterization by TGA

Characterization of all recycled materials was done by TGA. Figure 4.11a shows the weight loss as a function of temperature for the indicated samples. The weight loss indicates the beginning of the degradation process. Thermally, the rPET is the most stable sample, since its thermal degradation starts at high temperature (approximately 375 ºC). As the rPP content of the samples increases, the thermal stability decreases, and rPP is the least stable sample. Phase inversion in the sea-island morphology occurs at 70rPET/30rPP. In addition, this measurement allows determining the TiO_2 residue of the samples, which is 1.89% on average (Figure 4.11b).

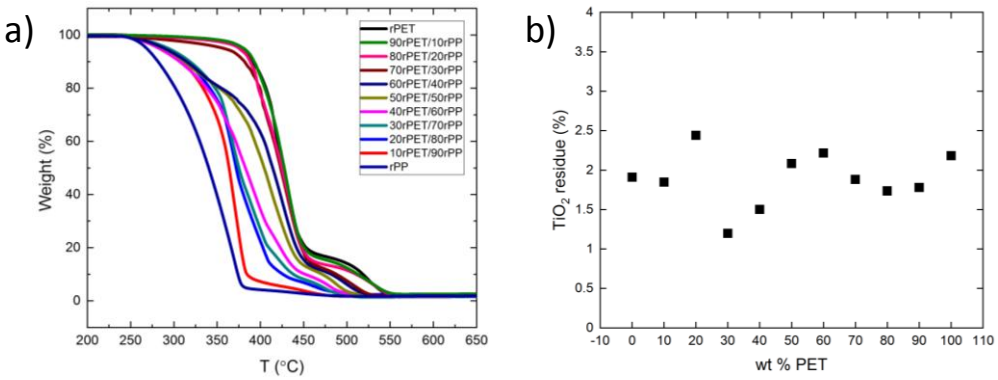

Figure 4.11. a) Weight loss as a function of temperature and b) TiO_2 residue as a function of PET weight content

4.2.3.2 TiO_2 Nanoparticle Characterization

SEM and TEM images of the three different types of nanoparticles added to the blends show that the hydrophilic nanoparticles have larger diameters than the hydrophobic nanoparticles (Figure 4.12).

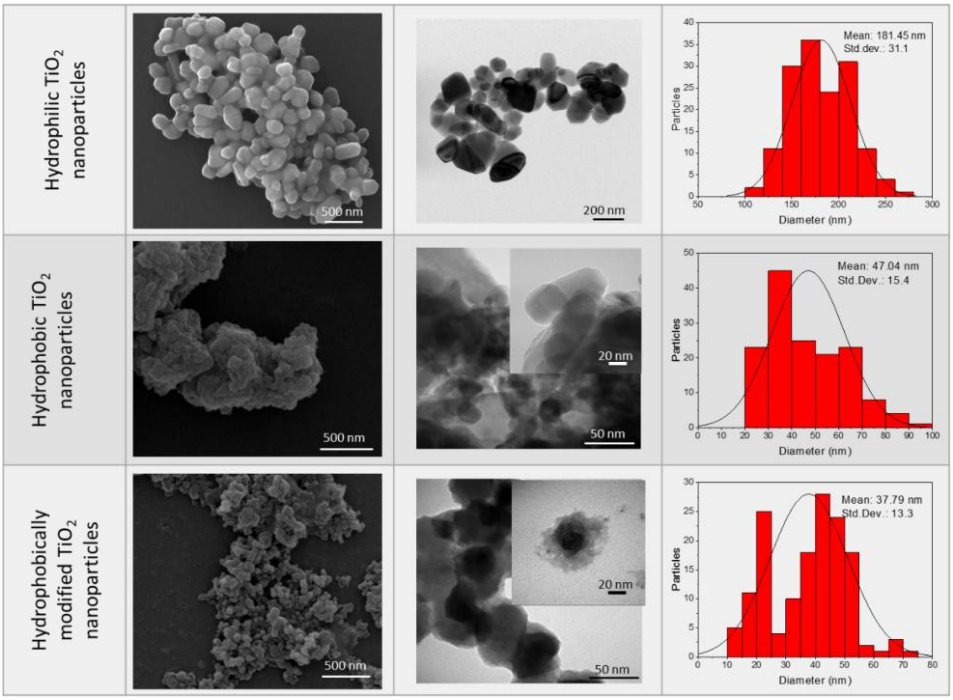

Figure 4.12. SEM and TEM images and size histograms of the three different types of TiO_2 nanoparticles. Hydrophobic samples were negatively stained with Phosphotungstic acid for TEM analysis

However, the commercial hydrophobic NPs present a high degree of agglomeration that was confirmed by DLS analysis, resulting in a hydrodynamic diameter of 541 ± 13 nm (Table 4.8) and a low ζ-potential (-9.1 ± 1.9mV). On the other hand, the dimensions of hydrophobically modified nanoparticles were increased by about 42%, whereas the ζ-potential decreased to -31 mV with respect to the pristine P25 nanoparticles. These results point to a successful functionalization process (Table 4.8). The presence of the octadecyltrimethoxysilane (TMOS) around the hydrophobically modified nanoparticles can be clearly observed in TEM images using a negative staining agent (Figure 4.12).

The degree of hydrophilicity was determined by contact angle measurements. A water drop was immediately absorbed by the film with a water contact angle (WCA) of almost 0º for the un-modified particles, while the

hydrophilic ones showed a WCA of around 36º. This behavior was expected because of the presence of a large number of hydroxyl groups on the surface of the particles[122]. After modification with (TMOS), a completely different behavior was observed, the water contact angle increased to 144º because of the replacement of OH groups by hydrophobic molecules. The commercial hydrophobic nanoparticles showed a WCA lower than the modified ones, but they can still be considered as hydrophobic nanoparticles[123].

Table 4.8. Hydrodynamic size and ζ-potential of TiO_2 nanoparticles

Nanoparticle	Hydrodynamic diameter (nm)	ζ-potential (mV)	Contact angle (º)
Hydrophilic (hphi)[1]	170 ±116	7.2 ± 1.1	36 ± 4
Un-modified[2]	73 ± 21	10.1 ± 0.4	0
Hydrophobically modified (hphoM)[3]	104 ± 54	-31.1 ± 0.6	144 ± 5
Hydrophobic (hpho)[4]	541 ± 13	-9.1 ± 1.9	106 ± 1

[1] Hphi was provided by "io-li-tec" nanomaterials with rutile crystalline form.

[2] Supplied by AEROXIDE TiO_2 P25, from *Evonik Industries*.

[3]AEROXIDE TiO_2 P25, from *Evonik Industries* modified by a sol-gel reaction with octadecyltrimethoxysilane to turn it hydrophobic (hphoM).

[4] Hydrophobic titanium dioxide (hpho) coated with silicone oil from *US Research Nanomaterials, Inc.,* with rutile crystalline form.

The presence of the organic compounds on the surface of the particles was also confirmed by FTIR. Figure 4.13b shows the spectra of non-modified and modified particles together with TMOS spectrum. The band at 1100 cm^{-1}, characteristic of Si-O-CH_3 stretching, indicates the presence of the methyl-silane groups. Bands at 1200 and 1467 cm^{-1} could be assigned to CH_3 rocking and CH_2 stretching, respectively, and bands in the range 3000-2780 cm^{-1} are due to C-H bonds stretching. It is important to notice the presence of a wide band around 3250 cm^{-1} that would be related to O-H stretching of silanol groups derived from the

partial hydrolysis of Si-O-CH_3[124]. On the other hand, the commercial hydrophobic particles spectrum shows only the presence of organic groups (1100-1000 cm^{-1}), but no bands related to O-H groups could be observed (Figure 4.13b).

The load of organic compound in the hydrophobic (hpho) and functionalized nanoparticles (hphoM), obtained from TGA results, was 1.6 ± 1.2% and 16 ± 3% % respectively (Figure 4.13a).

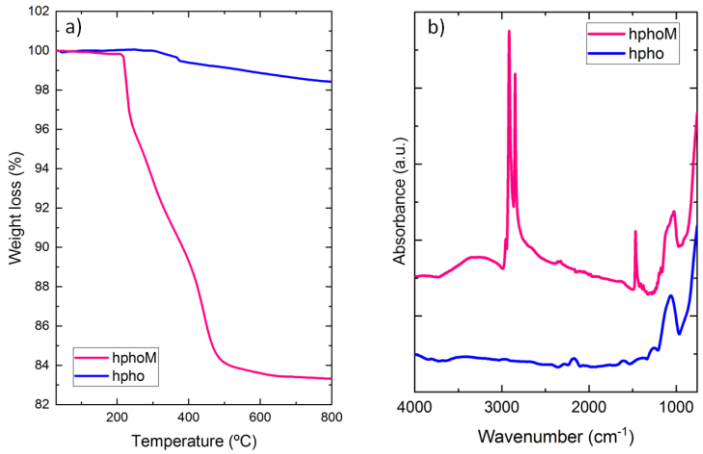

Figure 4.13. a) TGA curves and b) FTIR spectra of commercial hydrophobic (hpho) and TMOS modified nanoparticles (hphoM)

4.2.3.3 Blends Morphology by SEM and TEM

All PBNANOs prepared in this work exhibit sea-island or droplet-matrix morphology, as expected for immiscible blends, with rPP as the matrix (80%) and rPET (20%) as dispersed droplets. Figure 4.14 shows a SEM micrograph of the extruded 80rPP/20rPET/2%TiO_2 blend. TiO_2 nanoparticles were not added in the preparation of this blend, as the recycled PET (rPET) already included 2% TiO_2 nanoparticles. The TiO_2 nanoparticles content was determined by TGA (Figure 4.13a). A lack of adhesion between rPP matrix and rPET droplets can be observed, indicated by the presence of holes where particles were detached. Both in the holes and on some of the particle surfaces, very small white particles can be observed, which are the TiO_2 nanoparticles[59]. In some cases, TiO_2 aggregates can also be

observed. The location of TiO_2 nanoparticles are better observed by TEM, and the results will be presented below.

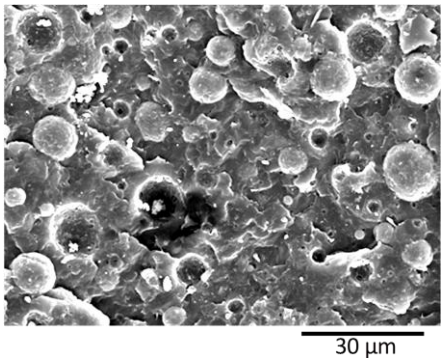

Figure 4.14. SEM image of PBNANO-2% TiO_2

The number average diameter (d_n) was measured for all the blends with the three different types of added TiO_2 nanoparticles: hydrophilic (hphi), hydrophobic (hpho), and hydrophobically modified (hphoM) TiO_2. The values of the average sizes of the rPET droplets are shown in Table 4.9, and the average number diameters are plotted in Figure 4.17 as a function of composition. The average size dispersion of the particles (D) was also calculated according to Equation 4.1 and reported in Table 4.9.

Table 4.9. Number-average diameter *(d_n)* and particle size distribution *(D)* of 80rPP/20rPET/TiO_2 nanocomposite blends

Total TiO_2 %	**Hydrophilic (hphi)**		**Hydrophobic (hpho)**		**Hydrophobically Modified (hphoM)**	
	dn (µm)	*D*	*dn* (µm)	*D*	*dn* (µm)	*D*
2	-	-	4.99	2.63	-	-
3	4.27	1.21	5.25	1.55	4.96	1.39
5	4.22	1.49	4.87	1.64	3.97	1.27
7	3.68	1.17	4.03	1.74	3.45	1.22
9.5	3.89	1.36	4.09	1.19	3.08	0.69
12	3.56	0.93	4.49	1.31	2.67	0.61

As can be appreciated in Figures 4.15 and 4.16, PET particle size is reduced as TiO_2 content increases. Additionally, Table 4.9 reports that particle size dispersion becomes narrower as TiO_2 content increases. The hphoM TiO_2 induces the highest reduction in rPET droplet size (see Figure 4.15), having a final particle size of about 2.7 μm with 12% TiO_2, in comparison with the original PBNANO with 2% TiO_2 with an average number diameter of 4.99 μm. In the case of hphi and hpho nanoparticles, the reduction in droplet size seems to saturate beyond 7% TiO_2 (see Figures 4.15 through 4.17). So, the chemical modification of the nanoparticles is promoting the creation of a physical barrier which avoids coalescence and reduces both particle size and size dispersity.

The functionalization of the nanoparticles could, in principle, also affect the interfacial adhesion. However, for the PBNANOs prepared here, the adhesion between phases does not seem to be significantly modified, as in all samples, characteristic holes can be observed (see Figures 4.15 and 4.16) that are formed during cryogenic fracture interfacial failure (i.e., adhesive failure is seen instead of cohesive failure). Figures A.4.2 - A.4.3 in the Appendix show SEM micrographs with hphi and hpho 3%, 7% and 12% TiO_2 nanoparticles.

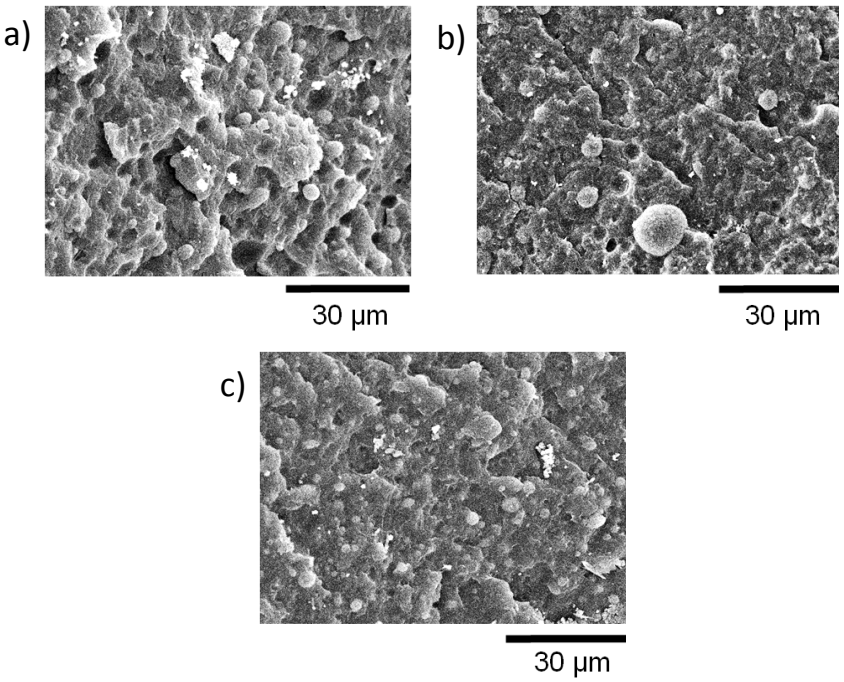

Figure 4.15. SEM images of PBNANO-12% containing: a) hydrophilic (hphi), b) hydrophobic (hpho) and c) hydrophobically modified (hphoM) TiO_2

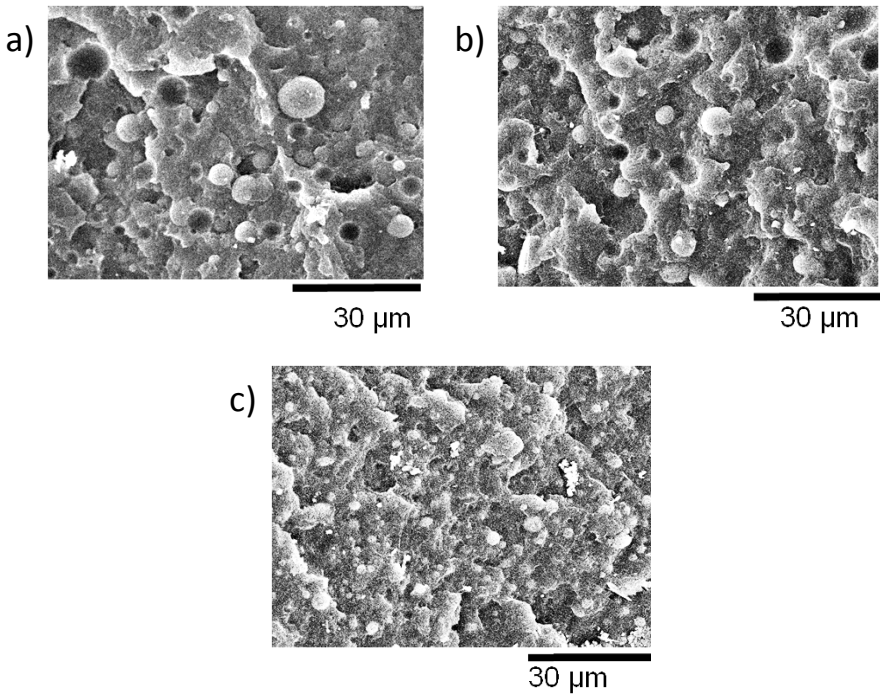

Figure 4.16. SEM images of PBNANO-hphoM with a) 3%, b) 7% and c) 12% TiO_2

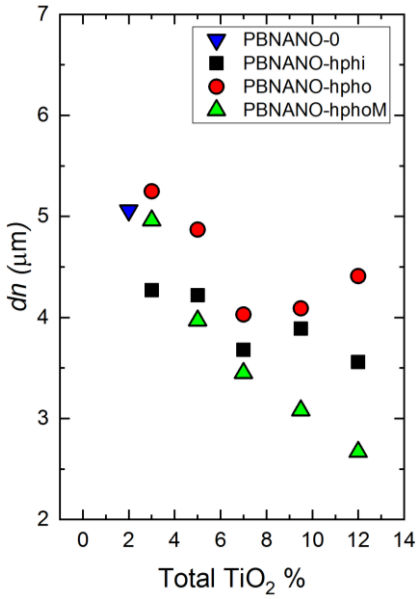

Figure 4.17. Number Average Diameter *(d_n)* plotted as a function of total TiO_2 content for the PBNANOs prepared in this work with the three types of TiO_2 indicated in the legend. PBNANO-0 is the sample without additional TiO_2, which contains 2% TiO_2, as the rPET employed in this work already had 2% TiO_2. So, PBNANO-0 is the 80/20 blend of rPP and rPET without any additional TiO_2

Although several theories have been proposed to explain the reduction of droplet size[96], the significant reduction of droplet diameters when 12% hydrophobically modified TiO_2 nanoparticles are added, is due to the preferred location of such nanoparticles at the polymer-polymer interface, as evidenced by TEM below. Similar results have been previously reported for different PP binary blends. Fenouillot et al. studied the location of hydrophilic pyrogenic silica nanoparticles in PP/EVA blends. The particles migrated from the PP matrix to the EVA dispersed droplets. The authors proposed that collisions between silica particles and the dispersed EVA droplets were the predominant mechanism leading to the location of the final nanoparticles. They also performed hydrophobic surface treatments to the silica and then found that the hydrophobically modified nanoparticles were located in the PP matrix and at the interface[54]. Dubois et al. also demonstrated a reduction in the droplet size of the dispersed phase in 80 PP/20 PA and 80 PP/20 PC blends adding 5% of nanosilica[51].

TEM micrographs of the PBNANO-hphoM are shown in Figure 4.18, as the highest reduction of droplet size is seen by SEM with this type of TiO_2. The nanoparticles are located inside the rPET droplets and the interface. As the content of TiO_2 increases, the interface is progressively coated with nanoparticles. When 12% of hphoM TiO_2 is used, the interface is almost completely covered by nanoparticles. Figures A.4.4 - A.4.5 in the Appendix show TEM micrographs with hydrophilic (hphi) and hydrophobic (hpho) 3%, 7% and 12% TiO_2 nanoparticles.

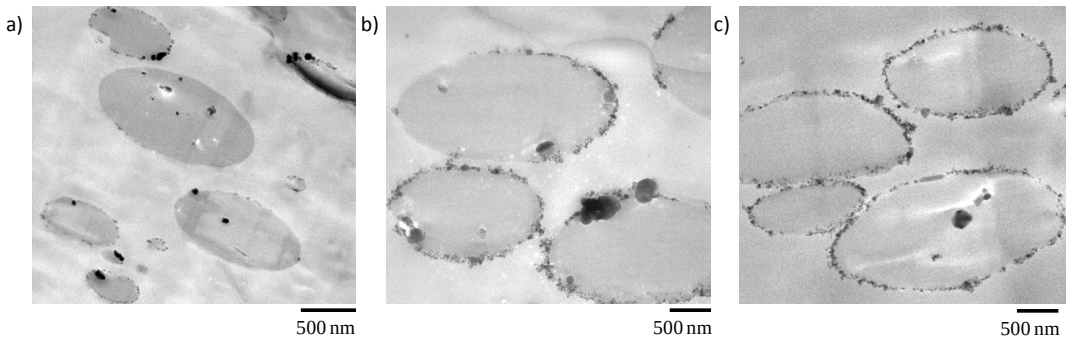

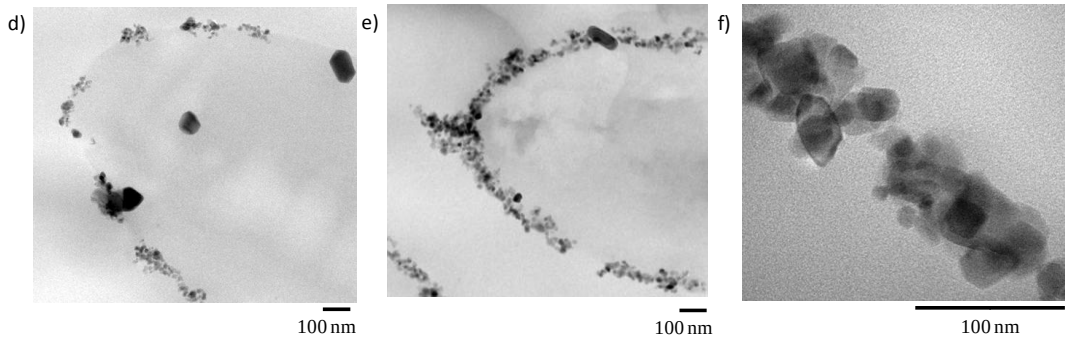

Figure 4.18. TEM images of PBNANO-hphoM: a,d) 3%, b,e) 7%, c,f) 12% TiO_2

Figure 4.19 shows the difference in nanoparticle location using different types of TiO_2 nanoparticles. In the case of hphi nanoparticles, they are located inside the rPET droplets because of their polar nature. The hpho nanoparticles are mostly located in the rPP matrix, although some of the nanoparticles can also be appreciated inside the rPET droplets and at the interface. More interestingly, in the case of the hphoM nanoparticles, the nanoparticles are preferentially located at the interface, as already mentioned above.

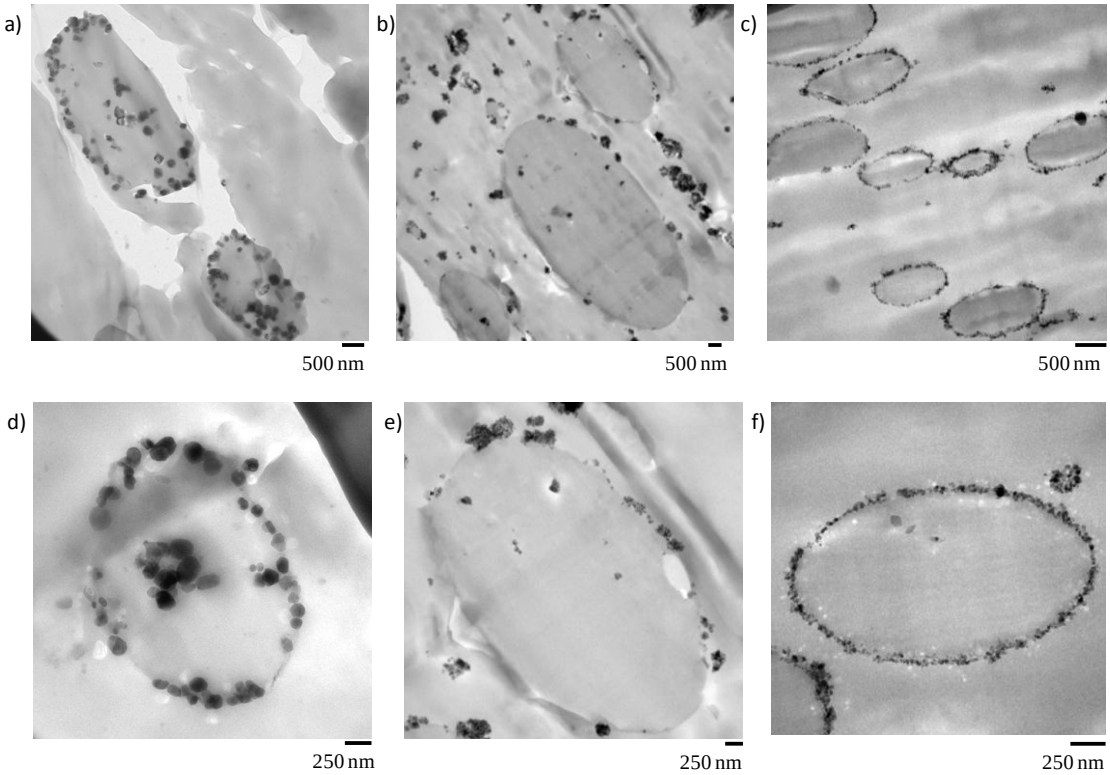

Figure 4.19. TEM images of PBNANO-12% containing: a,d) hydrophilic (hphi); b,e) hydrophobic (hpho) and c,f) hydrophobically modified (hphoM) TiO_2

Several factors affect the final location of nanoparticles in PBNANOS, such as polymer-filler interactions, thermodynamic, and kinetic factors. Most of the time, it is difficult to determine which is the main factor. However, chemical modifications of the nanoparticles could explain their location. Such modifications promote interactions with one of the phases inducing thermodynamic stability. That is why the hydrophilic (hphi) nanoparticles are mostly located inside the rPET polar phase, whereas the hydrophobic (hpho) ones are preferably inside the rPP apolar matrix. However, the hydrophobically modified (hphoM) nanoparticles are located at the interface, probably due to kinetic factors. A balance between thermodynamics and kinetics is to be considered in the final location of nanoparticles[96].

It must be remembered that additional TiO_2 nanoparticles were added by first preparing a masterbatch in rPP. Therefore, during extrusion, the TiO_2 nanoparticles can migrate to the interface or to the PET droplets, depending on a balance between thermodynamics and kinetics. In the case of hydrophilic TiO_2, the nanoparticles were able to migrate to the PET droplets (as shown in Figure 4.19a and Figure 4.19d), as they were probably rejected from the apolar rPP matrix to the interface during extrusion and once at the interface, they were able to easily penetrate the hydrophilic PET droplets. On the other hand, commercial hydrophobic TiO_2 nanoparticles are more affine to the rPP matrix and are expected to remain within the matrix due to the organic groups present on the surface of the particles. The existence of silanols, as well as methyl silane groups, on the surface of the hydrophobically modified TiO_2, revealed by FTIR analysis, would contribute to their location at the interface.

Figure 4.20 shows TEM micrographs of the PBNANOs containing 12% hydrophilic (a, b), hydrophobic (c, d) and modified hydrophobic (e, f) TiO_2. These micrographs were obtained after the sample was stained using a ruthenium tetroxide (RuO_4) solution. The heavy RuO_4 atoms can penetrate and preferentially stain the amorphous regions of the sample, while the denser crystalline regions will remain almost unstained. As a consequence, the lamellae inside the spherulites

or axialites can be observed as the contrast between amorphous and crystalline regions of the sample make the crystalline lamellae easily visible. Interlamellar amorphous regions are seen as dark bands (which absorb more electrons) while the crystalline lamellae are preferentially white (as they are more transparent to the electron beam since they only contain the original atoms present in the polymer crystals, which are light atoms, C, H, and O). Dark regions at the interfaces between matrix and droplets are produced by interfacial staining and also by the presence of TiO_2 nanoparticles at the interface.

However, as these micrographs were obtained to highlight the lamellar morphology, the focus of the microscope was centered at the lamellae and not at the nanoparticles (so the nanoparticles are out of focus), as the TiO_2 nanoparticles were already identified in unstained TEM observations (Figures 4.18 and 4.19). Other dark spots in some of the images are the result of staining artefacts[125]. Figure 4.20 shows that crystalline lamellae and interlamellar amorphous regions can be clearly appreciated inside rPET droplets.

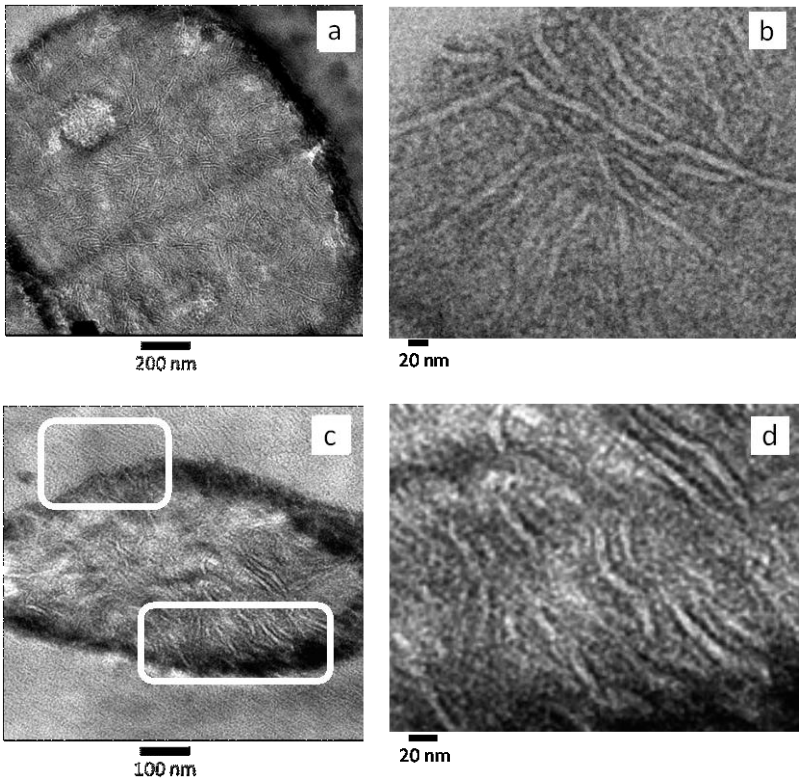

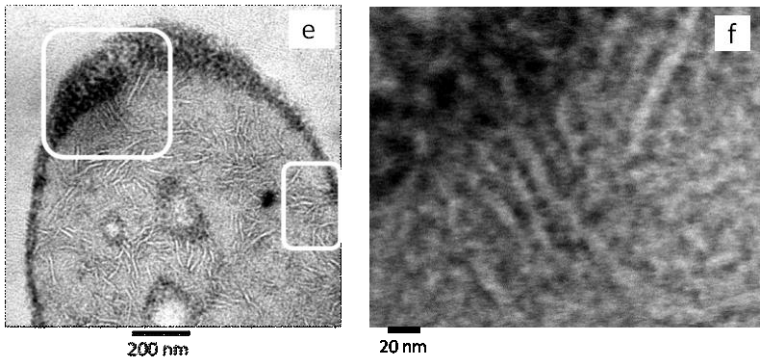

Figure 4.20. TEM images of 80rPP/20rPET/12% TiO_2 PBNANOs containing: a) and b) hydrophilic TiO_2 (hphi); c) and d) hydrophobic TiO_2 (hpho) e) and f) hydrophobically modified TiO_2 (hphoM)

Figure 4.20a and 4.20b correspond to a PBNANO droplet (i.e., rPET) with 12% hydrophilic TiO_2 (hphi). In this case, TiO_2 nanoparticles are randomly dispersed within the rPET droplets (which cannot be seen in this micrograph but previously shown in Figure 4.19a). As a consequence, many edge-on lamellae are clearly visible inside the droplet with a random orientation within the droplet, as they have been nucleated inside the volume of the droplet by the TiO_2 nanoparticles (see Figure 4.20b for a close-up showing in-volume nucleation of the lamellae), as in this case, the nanoparticles do not preferentially sit at the interface with rPP matrix.

On the contrary, Figure 4.20c shows a PBNANO droplet with 12% hydrophobic TiO_2 (hpho). In this case, unstained TEM images showed that most of the nanoparticles concentrate inside the rPP matrix and at the interface between the phases (Figure 4.19b). Figure 4.20c shows some of the rPP lamellar texture within the matrix of the PBNANO, at the top of the micrograph, in the zone signaled by a white rectangle. In fact, a closer examination shows some cross-hatched lamellar morphology, which is typical of isotactic polypropylene[126]. We can also observe in Figure 4.20c the lamellar morphology of rPET (i.e., inside the droplet). In this case, a clear orientation can be observed in some lamellar stacks signaled by the bottom white rectangle. The lamellae are pointing towards the interface, where

they were probably nucleated by TiO_2 nanoparticles sitting at the interface. A close-up is shown in Figure 4.20d, with a higher magnification micrograph, notice the parallel orientation of the lamellae pointing towards the particle interface.

Finally, Figure 4.20e corresponds to the PBNANO with 12% hydrophobically modified TiO_2, where the nanoparticles are accumulated preferentially at the interface (Figure 4.19c). The morphology resembles that of Figure 4.20c. We have identified, by signaling with white rectangles, areas where oriented lamellar stacks seem to have nucleated at the interface and are oriented perpendicular to it (see Figures 4.20e and 4.20f).

4.2.3.4 Blends Thermal Characterization by DSC

a) Non-isothermal DSC Experiments

DSC cooling scans were performed after erasing thermal history, and then the samples were subsequently heated to record the heating DSC scans. The most relevant calorimetric parameters are listed in Table A.4.5 - A.4.6 reported in the Appendix, together with the DSC scans, which are reported in Figure A.4.6. Experiments were performed at 20 °C/min. Enthalpies of crystallization (ΔH_c) and melting (ΔH_m) and the values of crystallinity degree (X_c) were normalized by the weight fraction of the phase under consideration. The enthalpy of crystallization and fusion of 100% crystalline PP and PET were taken as 207[44] and 140 J/g[127].

The results obtained by non-isothermal DSC corroborate the immiscibility of the blends. The two phases, rPP and rPET, crystallize and melt separately, and no significant changes in their melting points were observed. In the case of the crystallization, rPP is not affected by TiO_2 or PET addition, indicating that these PBNANOs components are not able to nucleate rPP. On the other hand, increases in peak crystallization temperature (of up to 10 ºC) of the PET phase were obtained as a result of the nucleating action of TiO_2 on the PET droplets.

b) Isothermal DSC Experiments

Isothermal DSC experiments were performed to quantitatively measure the overall isothermal crystallization kinetics of both crystallizable phases, i.e., rPP and rPET. The inverse of the half-crystallization time is an experimental quantity proportional to the overall crystallization rate, in which both nucleation and growth contributions are included. Figure 4.21 shows the overall crystallization rate (expressed as $1/\tau_{50\%}$) as a function of temperature for neat rPP, and for the rPP matrix phase within all PBNANOs with 12% TiO_2. In consonance with the non-isothermal results, the overall isothermal crystallization rate does not show any significant difference between neat rPP or the rPP phase within the PBNANOs. We can, therefore, conclude that neither the TiO_2 nanoparticles nor the PET droplets can nucleate rPP.

The isothermal crystallization of the dispersed PET droplets within the PBNANOs was also studied. Figure 4.22 shows the results obtained together with representative TEM micrographs of the PET droplets. Both neat rPET and the rPET dispersed droplets within the PBNANOs with 2% of titanium dioxide crystallize at the same rate. This 2% TiO_2 which was already included in rPET is not capable of nucleating PET droplets. According to TEM images, this 2% TiO_2 is mostly located in the rPP phase, so the results are consistent with the lack of nucleation of the rPET droplets.

On the other hand, the nucleation effect on the rPET phase when additional TiO_2 nanoparticles are added is evident. The overall crystallization rate increases with TiO_2 content, and the magnitude of the effect is related to the preferential location of the nanoparticles. Hydrophilic TiO_2 nanoparticles are mostly located inside the rPET droplets, and this causes a nucleation effect on rPET that accelerates its overall crystallization rate, as can be clearly seen in Figure 4.22. The maximum overall crystallization rate among all rPET droplets at low crystallization temperatures is obtained for the PBNANO containing 12% hydrophilic TiO_2, as expected from the nanoparticles privileged location, i.e., well-

dispersed inside the rPET droplets, thereby maximizing possible nucleation effects.

The rPET droplets within PBNANOs with 12% hydrophobic and hydrophobically modified TiO_2 can also crystallize faster than neat rPET. Nevertheless, no large differences can be observed between them, as most of the nanoparticles in both cases stay in the rPP matrix or at the interface. For nucleation to occur, contact between the TiO_2 nanoparticles and the rPET droplets is necessary. A higher overall crystallization rate is therefore correlated with the number of TiO_2 nanoparticles in contact with rPET droplets. The results of Figure 4.22 are remarkably consistent with the morphology and location of the nanoparticles within the PBNANOs employed here.

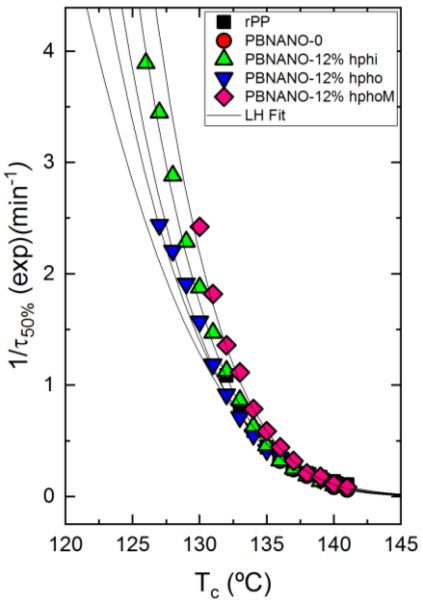

Figure 4.21. Overall crystallization rate of rPP and the rPP phase within the indicated PBNANOs as a function of crystallization temperature. Solid lines correspond to mathematical fits to the Lauritzen and Hoffman theory[128]

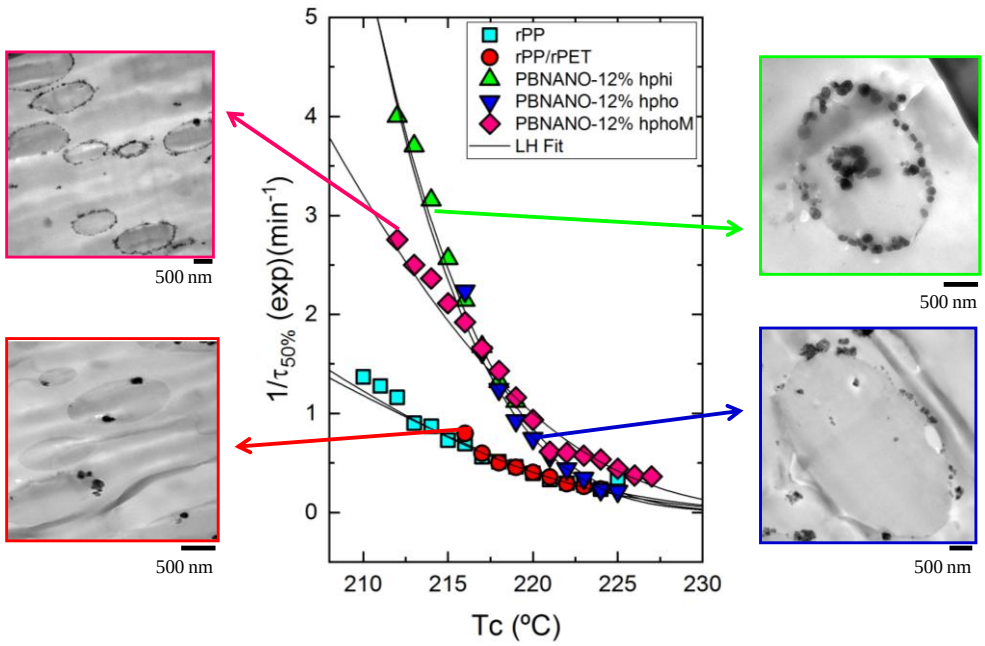

Figure 4.22. Overall crystallization rate of rPET and the rPET phase within the indicated PBNANOs as a function of crystallization temperature. Solid lines correspond to mathematical fits to the Lauritzen and Hoffman theory[128]

The overall crystallization rate behavior can be usually described in the primary crystallization stage (i.e., the free growth stage, before spherulite impingement) with the well known Avrami equation, which can be expressed, according to Lorenzo et al. as[129]:

$$1 - V_c\ (t - t_0) = \exp(-k(t - t_0)^n) \qquad \text{Eq. 4.2}$$

where t is the measurement time, t_0 is the incubation time, V_c is the relative volumetric transformed fraction, n is the Avrami index, and k is the overall crystallization rate constant. The fits to the Avrami equation were performed with the free Origin plug-in developed by Lorenzo et al.[118].

Figure 4.23 shows one example of the good agreement between the Avrami model and the experimental data obtained for neat rPP. Figure 4.23a compares the experimental and the predicted DSC isothermal scan.

In this particular example, the agreement between the experiment and the Avrami theory goes beyond the peak value, i.e., beyond the primary crystallization regime. The predicted half crystallization time is practically the same as that experimentally measured, and the fitting of the theory is very good up to about 80% conversion (see Figures 4.23a and 4.23b). Figure 4.23c shows the typical Avrami plot for a limited conversion range. The Avrami equation can perfectly describe the overall crystallization kinetics within the first part of the primary crystallization range (with a correlation coefficient of 1.0000), during free superstructural growth, in a conversion range up to 20%.

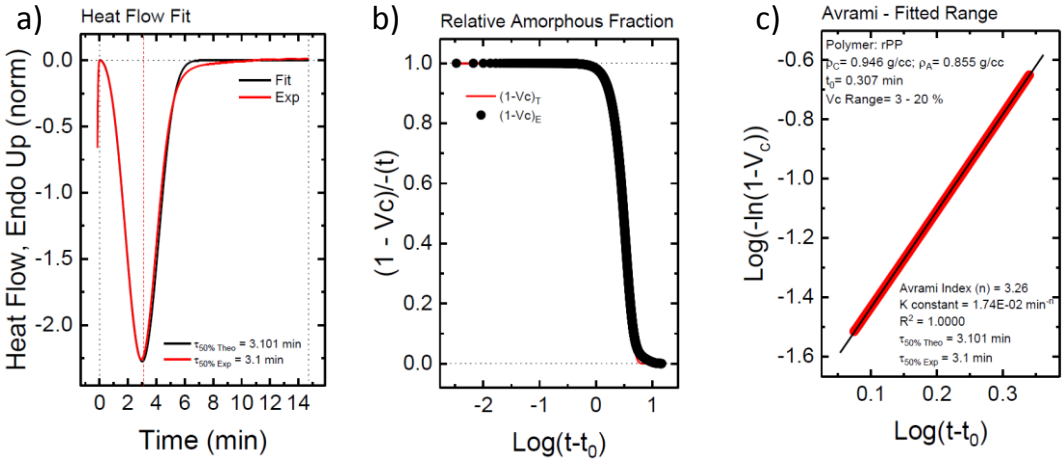

Figure 4.23. a, b, c) Comparison between experimental data and the fits to the Avrami equation using the Origin plug-in developed by Lorenzo et al.[118]

Figure 4.24 shows the results obtained from the application of the Avrami equation for the isothermal crystallization of rPP and rPET phases within PBNANOs. The Avrami index value oscillates from 2.5 to 3.4 for rPP. This range can be approximated to n=3, which is a value that suggests that rPP forms instantaneously nucleated spherulites[118]. The Avrami index obtained in the case of rPET is in the range 2.25 to 3.75. Below n=2.5, the formation of axialites is predominant in some of the PBNANO samples with hydrophobically modified TiO_2 nanoparticles. However, most of the other PBNANOs have Avrami indexes close to 3, once again indicating the presence of instantaneously nucleated spherulites.

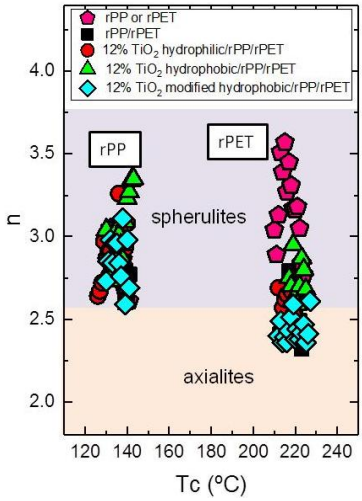

Figure 4.24. Avrami index (n) as a function of crystallization temperature

4.2.3.5 Mechanical Behavior

Figure 4.25a shows representative engineering stress-strain curves of PBNANOs, while in Figure 4.25b the appearance of the material after being tested is presented. PBNANO-0 is the sample without additional TiO_2, which contains 2% TiO_2, as the rPET employed in this work already had 2% TiO_2. So, PBNANO-0 is the 80/20 blend of rPP and rPET without any additional TiO_2, which was first extruded and then compression molded into sheets, from which tensile testing bars were obtained by stamping.

Two of the samples shown in Figure 4.25a exhibit a ductile behavior with cold drawing. This means that after reaching a local maximum in the engineering tension, associated with the yield point, there is a decrease in tension. After the maximum in the stress-strain curve, at higher strains, the tension stabilizes. This phenomenon can be associated with the formation of a neck and its subsequent stable propagation. In the case of the PBNANO-0 and PBNANO-hphoM, although a yield point is reached, the neck stabilization stage does not occur.

Figure 4.25b shows that only two of the PBNANOs (without and with hydrophilic TiO_2) exhibit neck propagation accompanied by stress whitening. In

the case of systems with hydrophobic TiO_2 (without and with modification), the necking and the degree of stress whitening is negligible (hpho) and even non-existent (hphoM). In polymeric systems with dispersed phases with different stiffness than the matrix containing it, stress whitening is usually associated with a de-cohesion/cavitation process of the dispersed particles.

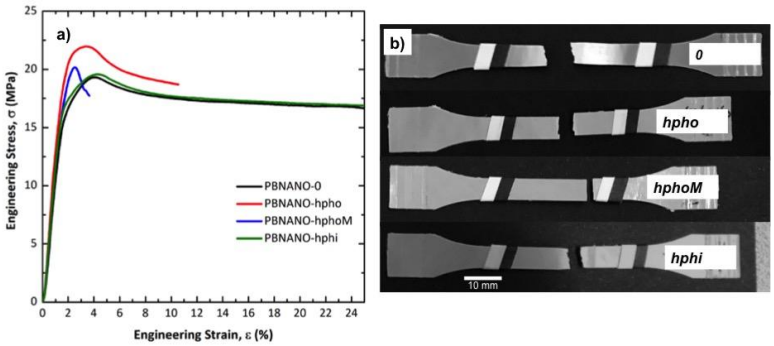

Figure 4.25. a) Representative engineering stress-strain curves of PBNANOs tested and b) appearance of the deformation process zone after tensile tests

Figure 4.26 presents SEM micrographs of the fracture zone of the tensile specimens of the different materials. The observation by SEM of the fracture surfaces after the test (Figure 4.26) reveals that for both PBNANO-0 (Figure 4.26a) and the PBNANO-hphi (Figure 4.26d), the ratio of de-cohesion and cavitation is high (not for PBNANO-hpho and PBNANO-hphoM in Figures 4.26b and 4.26c, respectively), and even the rPP matrix has a high degree of tearing, which decreases with increases in the added quantities of additional TiO_2. It should be noted, that the dispersed phase (rPET-O) shows no significant deformation, indicating that this phase has not reached its yield process, acting as a stiff inclusion in the blend. All these situations indicate that precisely this process of cavitation is helping to alleviate the degree of local triaxiality, promoting the yielding of the matrix. On the contrary, in the case of the PBNANO-hpho and PBNANO-hphoM, the degree of de-cohesion of the dispersed phase is appreciably lower, and even with evidence of extensive tearing of the matrix.

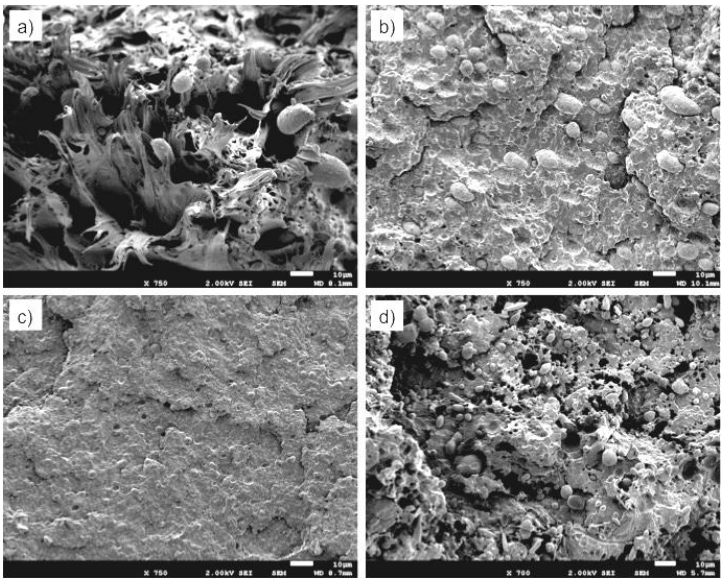

Figure 4.26. SEM micrographs of the fracture process zone after tensile tests of a) PBNANO-0, b) PBNANO-hpho, c) PBNANO-hphoM and d) PBNANO-hphi

Figure 4.27 shows the tensile mechanical parameters obtained. Also, the predictions of the parameters have been represented considering the additive mixing law (AML) at its upper limit (i.e., assuming that the adhesion is good, and therefore both phases are deformed equally) and its lower limit (i.e., both phases bear the same tension, but as a consequence of a moderate adhesion and/or disposition of the dispersed phase, each one is deformed independently).

Considering the elastic range of the material, through the elastic modulus, *E*, (Figure 4.27a), it can be seen that PBNANO-0 complies with the AML prediction at its upper limit, suggesting that the degree of adhesion achieved is sufficient to offer an effective reinforcement in the elastic range of the mechanical behavior of the material. When adding TiO_2, independently of its hydrophobic nature, there is a positive deviation in the trend, registering an increase, with respect to PBNANO-0, of up to 13% in the presence of hydrophobic TiO_2 and of 6% in the other cases. This increase could be expected given the addition of a stiffer phase (TiO_2) at a relatively high content.

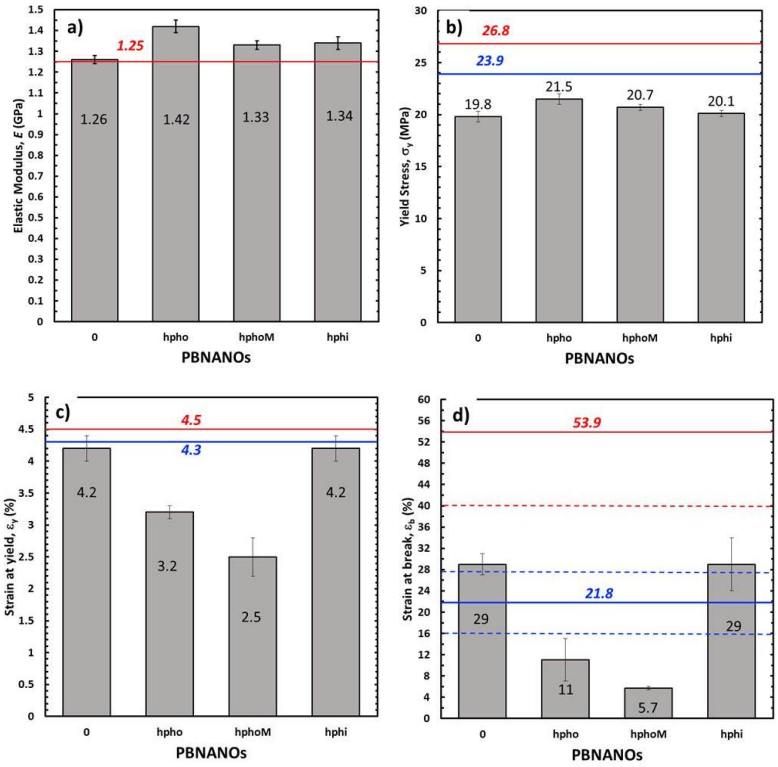

Figure 4.27. Mechanical tensile parameters obtained for the materials under study. a) Elastic modulus (E); b) Yielding stress (σ_y); c) deformation at yield (ε_y) and d) elongation at break (ε_b). Horizontal solid lines represent the upper (red) and the lower (blue) limits of the additive mixing law. The dashed lines in d), represent their respective error bands

Regarding the yield stress (σ_y), associated with the onset of plastic behavior (Figure 4.27b), a negative deviation of the AML at its lower limit is observed for all cases, and without a significant dependence of the type of TiO_2 added. This observation confirms the triaxiality relief effect exerted by the de-cohesion of the dispersed phase, promoting the yield of the matrix (rPP). When considering the deformation registered at this point for each material (ε_y), it is observed how the PBNANOs with TiO_2 of hydrophobic character show a marked negative deviation of AML in its lower limit, while the PBNANO and the PBNANO-hphi practically comply with this prediction.

It is well known that in multiphasic systems, the de-cohesion between phases, during a tensile test, involves loss of stress transfer, so that the matrix begins to bear the entire load from that moment onwards. So the nature and strength of the interface that is generated between the phases acquire an important role.

As discussed in previous sections, the preferential location of TiO_2 in the rPP-rPET-O interface is dictated by the degree of hydrophobicity that the particle presents. In the case of hydrophilic TiO_2, the nanoparticles are located preferentially within the PET phase, while those of a hydrophobic character in the outer zone of the PET phase (Figure 4.19).

Figure 4.28 shows micrographs of the fracture zone of tensile specimens where this situation is once again evident. It can be seen that in the case of PBNANO-hphoM (Figure 4.28a), the particle of rPET-O is coated by TiO_2 on its outer face, and even after cavitation, a "bed" of TiO_2 particles prevails (see the yellow circle in Figure 4.28a). A similar situation has been observed for the PBNANO-hpho (not shown). In the case of the PBNANO-hphi (Figure 4.28b), the rPET-O seems to have some nanoparticles on the surface, but after de-cohesion, no nanoparticles are left on the "bed".

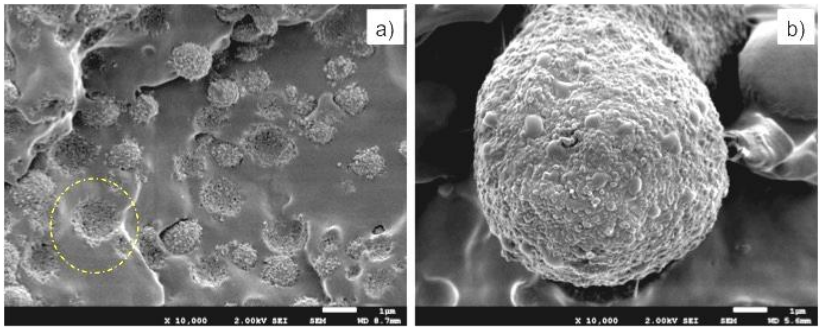

Figure 4.28. SEM micrographs from fracture surface of a) PBNANO-hphoM and b) PBNANO-hphi. The yellow circle highlights the TiO_2 nanoparticles that are left attached to the rPP matrix ("bed") after extraction of a PET droplet

The results presented above show, that for the case of PBNANO-hpho and PBNANO-hphoM, the interface acts as a third phase with very low shear resistance. Perhaps the surface treatment applied promotes a lubrication effect between particles, facilitating the de-cohesion at relatively low global deformation levels, which limits the stress transfer between the phases. The latter, combined with the emulsifying effect exerted on the rPET-O behavior, could cause this phase to act as stress concentrator, accelerating the collapse and rupture of the material.

In the case of the PBNANO-hphi, all seems to indicate that this "third phase" of lower resistance (with lubricating effect) does not exist (as most nanoparticles are inside the PET droplets), so that the relative adhesion is higher through a merely mechanical anchoring mechanism between rough surfaces, which would allow a slight improvement in the stress transfer between phases. This effect is evidenced at the moment of fracture (Figure 4.27d). As it can be observed, the rupture deformation (ε_b) of the PBNANO-0 and PBNANO-hphi systems are within the prediction of the lower limit of the AML, while the systems with hydrophobic load are located far below of this limit, being much smaller in the material with additional hydrophobic treatment. The tensile properties for all materials are also reported in Table A.4.7 in the Appendix.

4.3 Conclusions

The analysis of the crystalline behavior of PET/HDPE blends suggests that one of the most interesting blends to study the effect of titanium dioxide nanoparticles and compatibilizing agents is the 70PET/30HDPE blend, a composition prior to the phase inversion, in which the matrix corresponds to PET (70%) and the dispersed droplets are HDPE (30%).

The strategy of using TiO_2 nanoparticles or the compatibilizing agent PEgMA in order to reduce particle size and tune morphology in 70PET/30HDPE blends is effective, although the combination of both components does not have any synergistic effect so that particle size of the dispersed phase could be more decreased.

The degree of hydrophilicity of the three types of TiO_2 employed in recycled 80rPP/20rPET blends decreases in the order hphi>hpho>hphoM. A general reduction of rPET droplet size and droplet size dispersion occurs with the addition of TiO_2 nanoparticles. A hydrophilic/hydrophobic balance controls nanoparticles location. TEM shows that hphi TiO_2 preferentially locates inside the PET droplets, and hpho is found at the interface and within the PP matrix. HphoM TiO_2 also locates within the PP matrix and at the interface, but at large loadings (12%) it can completely cover the surfaces of the droplets forming a physical barrier that avoids coalescence during blending, leading to the formation of smaller droplets.

While TiO_2 does not nucleate PP and therefore does not significantly influence its crystallization rate, the added TiO_2 nanoparticles do nucleate the PET droplets, and the nucleation effect increases with particle loading. A good correlation is found between the crystallization rate of PET (determined by DSC) and nanoparticles location, where hphi TiO_2 induces the highest PET crystallization rate, as it is preferentially located inside the PET droplets. PET lamellar morphology (revealed by TEM) is also dependent on particle location.

In the case of the PBNANO with hphi TiO_2, edge-on lamellae with random orientation were visualized by TEM inside rPET droplets, because TiO_2 nanoparticles (that are preferentially located inside the droplet volume) randomly nucleate rPET droplet. For the case of the hydrophobic TiO_2 nanoparticles, we were able to see PET lamellae nucleating at the interface of the droplets, where hydrophobic nanoparticles preferentially locate.

The surface treatment of TiO_2 particles that confers the hydrophobic character generates a low resistance interface that promotes a greater de-cohesion of the dispersed phase. This causes a decrease in the tensile strength and accelerates the collapse and subsequent rupture of the system. However, it shows a clear efficiency as mechanical reinforcement in the elastic range of the mechanical behavior of the system.

As PET and other polyolefins such as PP and PE are commonly used in packaging, very high amounts of these materials have to be recycled in order to decrease waste accumulation. Due to the presence of titanium dioxide nanoparticles, recycling is more complicated, and that is why it is interesting to find new applications for these materials, as they could be upcycled, for instance into automotive parts.

4.4 References

1. Plastics-The Facts 2019: an analysis of European plastics production, demand and waste data. Available online: https://www.plasticseurope.org/application/files/9715/7129/9584/FINAL_web_version_Plastics_the_facts2019_14102019.pdf (accessed on 28 May 2020)

2. Zhang, Z.; Wang, C.; Mai, K., Reinforcement of recycled PET for mechanical properties of isotactic polypropylene. *Advanced Industrial and Engineering Polymer Research* **2019**, *2*, 69-76.

3. Tshifularo, C. A.; Patnaik, A., Recycling of plastics into textile raw materials and products. In *Sustainable Technologies for Fashion and Textiles*, **2020**; pp 311-326.

4. Al-Salem, S. M.; Lettieri, P.; Baeyens, J., Recycling and recovery routes of plastic solid waste (PSW): a review. *Waste Managment* **2009**, *29*, 2625-2643.

5. Bartolome, L.; Imran, M.; Cho, B. G.; Al-Masry, W. A.; Kim, D. H., Recent developments in the chemical recycling of the PET. In *Material Recycling: Trends and Perspectives*, Achilias, D. S., Ed. InTech: Rijeka, Croatia, **2012**; pp 65-84.

6. Sangroniz, L.; Ruiz, J. L.; Sangroniz, A.; Fernández, M.; Etxeberria, A.; Müller, A. J.; Santamaría, A., Polyethylene terephthalate/low density polyethylene/titanium dioxide blend nanocomposites: Morphology, crystallinity, rheology, and transport properties. *Journal of Applied Polymer Science* **2019**, *2*, 46986.

7. Stoica, M., Polymer nanocomposites for drink bottles. In *Nanotechnology in the Beverage Industry: Fundamentals and Applications*, Amrane, A.; Rajendran, S.; Nguyen, T. A.; Assadi, A. A.; Sharoba, A. M., Eds. Deans, M.: **2020**; pp 633-655.

8. Zander, N. E.; Gillan, M.; Burckhard, Z.; Gardea, F., Recycled polypropylene blends as novel 3D printing materials. *Additive Manufacturing* **2019**, *25*, 122-130.

9. Sangroniz, L.; Drongelen, M. V.; Cardinaels, R.; Santamaria, A.; Peters, G. W. M.; Müller, A. J., Effect of shear rate and pressure on the crystallization of PP nanocomposites and PP/PET polymer blend nanocomposites. *Polymer* **2020**, *186*, 121950.

10. Echiegu, E. A., Nanotechnology applications in the food industry. In *Nanotechnology: Food and Environmental Paradigm*, Prasad, R.; Kumar, V.; Kumar, M., Eds. **2017**; pp 153-172.

11. Demirel, B.; Yaras, A.; Elcicek, H., Crystallization behavior of PET materials. *Journal of Balikesir University* **2011**, *13* (1), 26-35.

12. Awaja, F.; Pavel, D., Recycling of PET. *European Polymer Journal* **2005**, *41*, 1453-1477.

13. Liu, J.; Geil, P. H., Crystal structure and morphology of poly(ethylene terephthalate) single crystals prepared by melt polymerization. *Journal of Macromolecular Science: Part B: Physics* **1997**, *36* (1), 61-85.

14. Kissel, W. J.; Han, J. H.; Meyer, J. A., Polypropylene: structure, properties, manufacturing processes, and applications. In *Handbook of Polypropylene and Polypropylene Nanocomposites*, Second ed.; Karian, H. G., Ed. RheTech, Inc: Whitmore Lake, Michigan, USA, **2009**; pp 10-27.

15. Lieberman, R.; Stewart, C., Propylene polymers. In *Encyclopedia of Polymer Science and Technology*, John Wiley and Sons, Inc: **2002**.

16. Brydson, J. A., Aliphatic polyolefins other than polyethylene, and diene rubbers. In *Plastics Materials*, 7 ed.; Oxford, Butterworth-Heinemann, **1999**; pp 247-310.

17. Talarico, G.; De Rosa, C.; Auriemma, F., Tacticity, regio and stereoregularity. In *Polypropylene Handbook: Morphology, Blends and Composites*, Karger-Kocsis, J.; Bárány, T., Eds. Springer: **2019**; pp 1-35.

18. Auriemma, F.; De Rosa, C.; Malafronte, A.; Scoti, M.; Girolamo, R. D., Solid state polymorphism of isotactic and syndiotactic polypropylene. In *Polypropylene Handbook: Morphology, Blends and Composites*, Karger-Kocsis, J.; Bárány, T., Eds. Springer: **2019**; pp 37-119.

19. Gahleitner, M.; Paulik, C., Polypropylene and other polyolefins. In *Brydson's Plastic Materials*, Eighth Edition ed.; Gilbert, M., Ed. Elsevier: **2017**; pp 279-309.

20. Pantani, R.; Santis, F. D.; Speranza, V., Morphology development and control. In *Polypropylene Handbook: Morphology, Blends and Composites*, Karger-Kocsis, J.; Bárány, T., Eds. Springer: **2019**; pp 243-294.

21. Peacock, A. J., *Handbook of Polyethylene: Structure, Properties and Applications*. New York, **2000**.

22. Ronca, S., Polyethylene. In *Brydson's Plastic Materials*, Eighth edition ed.; Gilbert, M., Ed. Elsevier: **2017**; pp 247-278.

23. Fay, J. J.; King, R. E., Additives for polyethylene: degradation and stabilization of polyethylene. In *Handbook of Industrial Polyetylene and Technology. Definitive guide to manufacturing, properties, processing, applications and markets.*, Spalding, M. A.; Chatterjee, A. M., Eds. Scrivener Publishing, LLC: BASF Corporation, Tarrytown, New York, USA, **2018**; Vol. Part 3, pp 753-770.

24. Silvestre, C.; Cimmino, S.; Di Pace, E., Morphology of polyolefins. In *Handbook of Polyolefins*, Second edition, revised and expanded ed.; Vasile, C., Ed. Marcel Dekker, Inc.: **2000**; pp 175-205.

25. Gedde, U. W.; Mattzzi, A., Polyethylene morphology. *Advanced Polymer Science* **2004**, *169*, 29-73.

26. Seven, K. M.; Cogen, J. M.; Person, T.; Reffner, J. R.; Gilchrist, J. F., The effect of inorganic and organic nucleating agents on the electrical breakdown strength of polyethylene. *Journal of Applied Polymer Science* **2018**.

27. Paul, D. R.; Robeson, L. M., Polymer nanotechnology: Nanocomposites. *Polymer* **2008**, *49*, 3187-3204.

28. Utracki, L. A.; Wilkie, C. A., *Polymer Blends Handbook*. Kluwer Academic Publisher: **2002**.

29. Sadiku, E. R.; Ogunniran, E. S., Compatibilization as a tool for nanostructure formation. In *Nanostructured Polymer Blends*, Thomas, S.; Shanks, R.; Chandrasekharakurup, S., Eds. William Andrew Publishing: Oxford, **2014**; pp 101-131.

30. Koning, C.; Van Duin, M.; Pagnoulle, C.; Jerome, R., Strategies for compatibilization of polymer blends. *Progress in Polymer Science* **1998**, *23*, 707-757.

31. Chow, W. S., Polypropylene blends: properties control by design. In *Polypropylene Handbook: Morphology, Blends and Composites*, Karger-Kocsis, J.; Bárány, T., Eds. Springer: **2019**; pp 418-480.

32. Sarath, C. C.; Shanks, R. A.; Thomas, S., Polymer Blends. In *Nanostructured Polymer Blends*, Thomas, S.; Shanks, R.; Chandrasekharakurup, S., Eds. William Andrew Publishing: Oxford, **2014**; pp 1-14.

33. McCrum, N. G.; Buckley, C. P.; Bucknall, C., *Principles of Polymer Engineering*. Oxford University Press: New York, **1996**.

34. Taguet, A.; Cassagnau, P.; Lopez-Cuesta, J. M., Structuration, selective dispersion and compatibilizing effect of (nano)fillers in polymer blends. *Progress in Polymer Science* **2014**, *39*, 1526-1563.

35. Khonakdar, H. A.; Jafari, S. H.; Mirzadeh, S.; Kalaee, M. R.; Zare, D.; Saeb, M. R., Rheology-morphology correlation in PET/PP blends: influence of type of compatibilizer. *Journal of Vinyl and Additive Technology* **2013**, 25-30.

36. Boutevin, B.; Lusinchi, J. M.; Pietrasanta, Y.; Robin, J. J., Improving poly(ethylene terephthalate)/high density polyethylene blends by using graft copolymers. *Polymer Engireering and Science* **1996**, *36*, 879-884.

37. Li; W.; Karger-Kocsis, J.; Schlarb, A. K., Dispersion of TiO_2 particles in PET/PP/TiO_2 and PET/PP/PP-g-MA/TiO_2 composites prepared with different blending procedures. *Macromolecular Materials and Engineering* **2009**, *294*, 582-589.

38. Nuzzo, A.; Bilotti, E.; Peijs, T.; Acierno, D.; Filoppone, G., Nanoparticle-induced co-continuity in immiscible polymer blends - A comparative study on bio-based PLA-PA11 blends filled with organoclay, sepiolite, and carbon nanotubes. *Polymer* **2014**, *55*, 4908-4919.

39. Filippone, G.; Causa, A.; Luna, M. S.; Sanguigno, L.; Acierno, D., Assembly of plate-lie nanoparticles in immiscible polymer blends - effect of the presence of a preferred liquid-liquid interface. *Soft Matter* **2014**, *10*, 3183-3191.

40. Sinha Ray, S.; Bousmina, M., Effect of organic modification on the compatibilization efficiency of clay in an immiscible polymer blend. *Macromolecular Rapid Communications* **2005**, *26*, 1639-1646.

41. Sinha Ray, S.; Pouliot, S.; Bousmina, M.; Utracki, L. A., Role of organically modified layered silicate as an active interfacial modifier in immiscible polystyrene/polypropylene blends. *Polymer* **2004**, *45*, 8403-8413.

42. Chen, B.; Evans, J. R. G., Mechanical properties of polymer-blend nanocomposites with organoclays: Polystyrene/ABS and high impact polystyrene/ABS. *Journal of Polymer Science Part B: Polymer Physics* **2011**, *49*, 443-454.

43. Entezam, M.; Khonakdar, H. A.; Yousefi, A. A.; Jafari, S. H.; Wagenknecht, U.; Heinrich, G., On nanoclay localization in polypropylene/poly(ethylene terephthalate) blends: Correlation with thermal and mechanical properties. *Materials and Design* **2013**, *45*, 110-117.

44. Jafari, S. H.; Kalati-vahid, A.; Khonakdar, H. A.; Asadinezhad, A.; Wagenknecht, U., Crystallization and melting behavior of nanoclay-containing polypropylene/poly(trimethylene terephthalate) blends. *Polymer Letters* **2012**, *6* (2), 148-158.

45. Ville, J.; Médéric, P.; Huitric, J.; Aubry, T., Structural and rheological investigation of interphase in polyethylene/polyamide/nanoclay ternary blends. *Polymer* **2012**, *53*, 1733-1740.

46. Labaume, I.; Médéric, P.; Huitric, J.; Aubry, T., Comparative study of interphase viscoelastic properties in polyethylene/polyamide blends compatibilized with clay nanoparticles or with a graft copolymer. *Journal of Rheology* **2013**, *57*, 377-392.

47. Monfared, A.; Jalali-Arani, A., Morphology and rheology of (styrene-butadiene rubber/acrylonitrile-butadiene rubber) blends filled with organoclay: the effect of nanoparticle localization. *Applied Clay Science* **2015**, *108*, 1-11.

48. Genoyer, J.; Yee, M.; Soulestin, J.; Demarquette, N., Compatibilization mechanism induced by organoclay in PMMA/PS blends. *Journal of Rheology* **2017**, *61*, 613-626.

49. Ock, H. G.; Kim, D. H.; Ahn, K. H.; Lee, S. J.; Maia, J. M., Effect of organoclay as a compatibilizer in poly(lactic acid) and natural rubber blends. *European Polymer Journal* **2016**, *76*, 216-227.

50. Hong, J. S.; Namkung, H.; Ahn, K. H.; Lee, S. J.; Kim, C., The role of organically modified layered silicate in the breakup and coalescence of droplets in PBT/PE blends. *Polymer* **2006**, *47*, 3967-3975.

51. Laoutid, F.; Estrada, E.; Michell, R. M.; Bonnaud, L.; Müller, A. J., The influence of nanosilica on the nucleation, crystallization and tensile properties of PP-PC and PP-PA blends. *Polymer* 2013, *54*, 3982-3993.

52. Laoutid, F.; Francois, D.; Paint, Y.; Bonnaud, L.; Dubois, P., Using nanosilica to fine-tune morphology and properties of polyamide 6/poly(propylene) blends. *Macromolecular Materials and Engineering* **2013**, *298*, 328-338.

53. Laoutid, F.; Francois, D.; Paint, Y.; Bonnaud, L.; Dubois, P., Morphology and properties of polyamide 6/poly(propylene) blends fine-tuned with nanosilica. *Macromolecular Symposia* **2012**, *321-322*, 90-94.

54. Elias, L.; Fenouillot, F.; Majeste, J. C.; Martin, G.; Cassagnau, P., Migration of silica nanoparticles in polymer blends. *Polmyer Science, Part B: Polymer Physics* **2008**, *46*, 1976-1983.

55. Elias, L.; Fenouillot, F.; Majesté, J. C.; Alcouffe, P.; Cassagnau, P., Immiscible polymer blends stabilized by nano-silica particles: rheology and effective interfacial tension. *Polymer* **2008**, *49*, 4379-4385.

56. Elias, L.; Fenouillot, F.; Majeste, J. C.; Cassagnau, P., Morphology and rheology of immiscible polymer blends filled with silica nanoparticles. *Polymer* **2007**, *48*, 6029.

57. Vermant, J.; Cioccolo, G.; Golapan Nair, K.; Moldenaers, P., Coalescence suppression in model immiscible polymer blends by nano-sized colloidal particles. *Rheological Acta* **2004**, *43*, 529-538.

58. Sangroniz, L.; Palacios, J. P.; Fernández, M.; Eguiazabal, J. I.; Santamaría, A.; Müller, A. J., Linear and non-linear rheological behaviour of polypropylene/polyamide blends modified with a compatibilizer agent and nanosilica and its relationship with the morphology. *European Polymer Journal* **2016**, *83*, 10-21.

59. Sangroniz, L.; Moncerrate, M. A.; De Amicis, V. A.; Palacios, J. P.; Fernández, M.; Santamaría, A.; Sánchez, J. J.; Laoutid, F.; Dubois, P.; Müller, A. J., The

outstanding ability of nanosilica to stabilize dispersions of nylon 6 droplets in a polypropylene matrix. *Polymer Physics* **2015**, *53*, 1567-1579.

60. Li, W.; Spoelstra, A. B.; Goossens, J. G. P., Morphology and rheological properties of silica-filled poly(carbonate)/poly(methyl methacrylate) blends. *Polymer Engineering and Science* **2015**, *55*, 1951-1959.

61. Salehiyan, R.; Ray, S. S.; Bandyopadhyay, J.; Ojijo, V., The distribution of nanoclay particles at the interface and their influence on the microstructure development and rheological properties of reactively processed biodegradable polylactide/poly(butylene succinate) blend nanocomposites. *Polymers* **2017**, *9*, 350.

62. Yu, F.; Huang, H. X., Simultaneously toughening and reinforcing poly(lactic acid)/thermoplastic polyurethane blend via enhancing interfacial adhesion by hydrophobic silica nanoparticles. *Polymer Testing* **2015**, *45*, 107-113.

63. You, W.; Yu, W., Onset reduction and stabilization of cocontinuous morphology in immiscible polymer blends by snowmanlike janus nanoparticles. *Langmuir* **2018**, *34*, 11092-11100.

64. Yan, X.; Cayla, A.; Devaux, E.; Salaün, F., Microstructure evolution of immiscible PP-PVA blends tunned by polymer ratio and silica nanoparticles. *Polymers* **2018**, *10*, 1031.

65. Palacios, J. K.; Sangroniz, A.; Eguiazabal, J. I.; Etxeberria, A.; Müller, A. J., Tailoring the properties of PP/PA6 nanostructured blends by the addition of nanosilica and compatibilizer agents *European Polymer Journal* **2016**, *85*, 532-552.

66. Baudouin, A. C.; Auhl, D.; Tao, F.; Devaux, J.; Bailly, C., Polymer blend emulsion stabilization using carbon nanotubes interfacial confinement. *Polymer* **2011**, *52*, 149-156.

67. Baudouin, A. C.; Bailly, C.; Devaux, J., Interface localization of carbon nanotubes in blends of two copolymers. *Polymer Degradation and Stability* **2010**, *95*, 389-398.

68. Koysuren, O.; Yesil, S.; Bayram, G., Effect of solid state grinding on properties of PP/PET blends and their composites with carbon nanotubes. *Journal of Applied Polymer Science* **2010**, *118*, 3041-3048.

69. Mishra, R. K.; Mishra, P.; Verma, K.; Joseph, K., Manipulation of thermo-mechanical, morphological and electrical properties of PP/PET polymer blend using MWCNT as nano compatibilizer: a comprehensive study of hybrid nanocomposites. *Vacuum* **2018**, *157*, 433-441.

70. Cardinaud, R.; McNally, T., Localization of MWCNTs in PET/LDPE blends. *European Polymer Journal* **2013**, *49*, 1287-1297.

71. Wu, M.; Shaw, L., Electrical and mechanical behaviors of carbon nanotube-filled polymer blends. *Journal of Applied Polymer Science* **2006**, *99*, 477-488.

72. Heeley, E. L.; Hughes, D. J.; Crabb, E. M.; Bowen, J.; Bikondoa, O.; Mayoral, B.; Laung, S.; McNally, T., The formation of a nanohybrid shish-kebab (NHSK) structure in melt-processed composites of poly(ethylene terephthalate) (PET) and multi-walled carbon nanotubes (MWCNTs). *Polymer* **2017**, *117*, 208-219.

73. Roman, C.; García-Morales, M.; Gupta, J.; McNally, T., On the phase affinity of multi-walled carbon nanotubes in PMMA: LDPE immiscible polymer blends. *Polymer* **2017**, *118*, 1-11.

74. Gumede, T. P.; Luyt, A. S.; Pérez-Camargo, R. A.; Tercjak, A.; Müller, A. J., Morphology, nucleation, and isothermal crystallization kinetics of poly(butylene succinate) mixed with a polycarbonate/MWCNT masterbatch *Polymers* **2018**, *10*, 424.

75. Gubbels, F.; Jerome, R.; Vanlathem, E.; Deltour, R.; Blacher, S.; Brouers, F., Kinetic and thermodynamic control of the selective localization of carbon black at the interface of immiscible polymer blends. **1998**, *10*, 1227-1235.

76. Wu, D.; Zhang, Y.; Zhang, M.; Yu, W., Selective localization of multiwalled carbon nanotubes in poly(ε-caprolactone)/polylactide blend. *Biomacromolecules* **2009**, *10*, 417-424.

77. Ko, S. W.; Hong, M. K.; Park, B. J.; Gupta, R. K.; Choi, H. J.; Bhattacharya, S. N., Morphological and rheological characterization of multi-walled carbon-nanotube/PLA/PBAT blend nanocomposites. *Polymer Bulletin* **2009**, *63*, 125-134.

78. Urquijo, J.; Aranburu, N.; Dagréou, S.; Guerrica-Echevarría, G.; Eguiazábal, J. I., CNT-induced morphology and its effect on properties in PLA/PBAT-based nanocomposites. *European Polymer Journal* **2017**, *93*, 545-555.

79. Gumede, T. P.; Luyt, A. S.; Pérez-Camargo, R. A.; Tercjak, A.; Müller, A. J., Morphology, nucleation, and isothermal crystallization kinetics of poly(butylene succinate) mixed with a polycarbonate/MWCNT masterbatch. *Polymers* **2018**, *10*, 424.

80. Gumede, T. P.; Luyt, A. S.; Müller, A. J., Review on PCL, PBS and PCL/PBS blends containing carbon nanotubes. *Express Polymer Letters* **2018**, *12*, 505-529.

81. Bai, L.; He, S.; Fruehwirth, W. J.; Stein, A.; Macosko, C. W.; Cheng, X., Localizing graphene at the interface of cocontinuous polymer blends: morphology, rheology, and conductivity of cocontinuous conductive polymer composites. *Journal of Rheology* **2017**, *61*, 575-587.

82. Liebscher, M.; Blais, M. O.; Pötschke, P.; Heinrich, G., A morphological study on the dispersion and selective localization behavior of graphene nanoplatelets in immiscible polymer blends of PC and SAN. *Polymer* **2013**, *54*, 5875-5882.

83. Mao, C.; Zhu, Y.; Jiang, W., Design of electrical conductive composites: Tuning the morphology to improve the electrical properties of graphene filled immiscible polymer blends. *ACS Applied Materials and Interfaces* **2012**, *4*, 5281-5286.

84. Li, W.; Karger-Kocsis, J.; Thomann, R., Compatibilization effect of TiO_2 nanoparticles on the phase structure of PET/PP/TiO_2 nanocomposites. *Journal of Polymer Science* **2009**, *47*, 1616.

85. Mofokeng, J. P.; Luyt, A. S., Morphology and thermal degradation studies of melt-mixed poly(hydroxybutyrate-*co*-valerate) (PHBV)/poly(ε-caprolactone)(PCL) biodegradable polymer blend nanocomposites with TiO_2 as filler. *Polymer Testing* **2015**, *45*, 93-100.

86. Mofokeng, J. P.; Luyt, A. S., Dynamic mechanical properties of PLA/PHBV, PLA/PCL, PHBV/PCL blends and their nanocomposites with TiO_2 as nanofiller. *Thermochimica Acta* **2015**, *613*, 41-53.

87. Li, W.; Schlarb, A. K.; Evstatiev, M., Study of PET/PP/TiO_2 microfibrillar-structured composites, Part 1: Preparation, morphology, and dynamic mechanical analysis of fibrillized blends. *Journal of Applied Polymer Science* **2009**, *113*, 1471-1479.

88. Li, W.; Schlarb, A. K.; Evstatiev, M., Study of PET/PP/TiO_2 microfibrillar-structured composites, Part 2: Morphology and mechanical properties. *Journal of Applied Polymer Science* **2008**, *113*, 3300-3306.

89. Xiu, H.; ai, H. W.; Huang, C. M.; Xu, C. L.; Li, X. Y.; Fu, Q., Selective localization of titanium dioxide nanoparticles at the interface and its effect on the impact toughness of poly(L-lactide)/poly(ether)urethane blends. *Polymer Letters* **2013**, *7*, 261-271.

90. Melle, S.; Lask, M.; Fuller, G. G., Pickering emulsions with controllable stability. *Langmuir* **2005**, *21*, 2158-2162.

91. Chevalier, Y.; Bolzinger, M. A., Emulsions stabilized with solid nanoparticles: Pickering emulsions. *Colloids and Surfaces A: Physicochemical and Engineering Aspects* **2013**, *439*, 23-34.

92. Scaffaro, R.; Botta, L., Nanofilled Thermoplastic-Thermoplastic Polymer Blends. *Elsevier* **2014**, 133.

93. Salzano de Luna, M.; Filippone, G., Effects of nanoparticles on the morphology of immiscible polymer blends-Challenges and opportunities. *European Polymer Journal* **2016**, *83*, 10-21.

94. Sangroniz, L.; Santamaría, A.; Müller, A. J., Rheology of polymer blend nanocomposite. In *Rheology of Polymer Blends and Nanocomposites*, Thomas, S.; Chandrasekharakurup, S.; Chandran, N., Eds. Elsevier: **2019**.

95. Canto, L. B., Aspects regarding the efficiency of nanosilica as an interfacial compatibilizer of a polypropylene/ethylene vinyl-acetate immiscible blend. *Polymer Testing* **2019**, *73*, 135-142.

96. Fenouillot, F.; Cassagnau, P.; Majesté, J. C., Uneven distribution of nanoparticles in immiscible fluids: Morphology development in polymer blends. *Polymer* **2009**, *50*, 1333-1350.

97. Huitric, J.; Ville, J.; Mederic, P.; Aubry, T., Solid-state morphology, structure, and tensile properties of polyethylene/polyamide/nanoclay blends: Effect of clay fraction. *Polymer Testing* **2017**, *58*, 96-103.

98. Ageyeva, T.; Bárány, T.; Karger-Kocsis, J., Composites. In *Polypropylene handbook: Morphology, Blends and Composites*, Karger-Kocsis, J.; Bárány, T., Eds. Springer: **2019**; pp 481-578.

99. Tang, Y.; Hu, Y.; Zhang, R.; Gui, Z.; Wang, Z.; Chen, Z.; Fan, W., Investigation on polypropylene and polyamide-6 alloys/montmorillonite nanocomposites. *Polymer* **2004**, *45*, 5317-5326.

100. Yang, H.; Zhang, X.; Qu, C.; Li, B.; Zhang, L.; Zhang, Q.; Fu, Q., Largely improved toughness of PP/EPDM blends by adding nano-SiO_2 particles. *Polymer* **2007**, *48*, 860-869.

101. Chen, J.; Shi, Y.; Yang, J.; Zhang, N.; Huang, T.; Chen, C.; Wang, Y.; Zhou, Z., A simple strategy to achieve very low percolation threshold via the selective distribution of carbon nanotubes at the interface of polymer blends. *Journal of Materials Chemistry* **2012**, *22*, 22398-22404.

102. Scaffaro, R.; Mistretta, M. C.; La Mantia, F. P., Compatibilized polyamide 6/polyethylene blend-clay nanocomposites: effect of the degradation and stabilization of the clay modifier. *Polymer Degradation and Stability* **2008**, *93*, 1267-1274.

103. Groeninckx, G.; Harrats, C.; Vanneste, M.; Everaert, V., Crystallization, micro- and nano-structure, and melting behavior of polymer blends. In *Polymer blends handbook*, Second Edition ed.; Utracki, L. A., Ed. Springer Netherlands: Dordrecht, **2014**; pp 291-446.

104. Agwuncha, S. C.; Owonubi, S. J.; Sadiku, E. R.; Varaprasad, K.; Ray, S. S.; Selvam, S. P.; Shittu, T. A.; Shanavas, A.; Mukwevho, E., Crystallization and morphological changes in nanostructured polymer blends. In *Design and applications of nanostructured polymer blends and nanocomposite systems*, Shanks, R.; Chandrasekharakrup, S., Eds. Wiliam Andrew Publishing: Boston, **2016**; pp 287-312.

105. Ajji, A., Interphase and compatibilization by addition of a compatibilizer. In *Polymer Blends Handbook*, Second Edition ed.; Utracki, L. A.; Wilkie, C. A., Eds. Springer: Dordrecht, **2014**; pp 447-516.

106. Arnal, M. L.; Matos, M. E.; Morales, R. A.; Santana, O. O.; Müller, A. J., Evaluation of the fractionated crystallization of dispersed polyolefins in a polystyrene matrix. *Macromolecular Chemistry and Physics* **1998**, *199*, 2275-2298.

107. Müller, A. J.; Arnal, M. L.; Lorenzo, A. T., Crystallization in nano-confined polymeric systems. In *Handbook of Polymer Crystallization*, Piorkowska, E.; Rutledge, G. C., Eds. John Wiley and Sons: Hoboken, New Jersey (USA), **2013**; pp 347-372.

108. Macosko, C. W., Morphology development and control in inmiscible polymer blends. *Macromolecular Symposia* **2000**, (149), 171-184.

109. Li, W.; Schlarb, A.; Evstatiev, M., Study of PET/PP/TiO_2 microfibrillar-structured composites, Part 1: preparation, morphology and dynamic mechanical analysis. *Journal of Applied Polymer Science* **2009**, *113*, 1471.

110. Qu, C.; Yang, H.; Liang, D.; Cao, W.; Fu, Q., Morphology and properties of PET/PA-6/Si-O_2 ternary composites. *Journal of Applied Polymer Science* **2007**, *104*, 2288.

111. Hong, J. S.; Kim, Y. K.; Ahn, K. H.; Lee, S., Shear-induced migration of nanoclay during morphology evolution of PBT/PS blend. *Journal of Applied Polymer Science* **2008**, *108*, 565.

112. Wu, G. Z.; Asai, S.; Sumita, M., Entropy penalty-induced self-assembly in carbon black or carbon fiber filled polymer blends. *Macromolecules* **2002**, *35*, 945-951.

113. Lee, M. W.; Hu, X.; Li, L.; Yue, C. Y.; Tam, K. C., Effect of fillers on the structure and mechanical properties of LCP/PP/SiO_2 in-situ hybrid nanocomposites. *Composite Science and Technology* **2003**, *63*, 339-346.

114. Zhang, Q.; Yang, H.; Fu, Q., Kinetics-controlled compatibilization of immiscible polypropylene/polystyrene blends using nano-SiO_2 particles. *Polymer* **2004**, *45*, 1913-1922.

115. Selvin, T. P.; Kuruvilla, J.; Sabu, T., Mechanical properties of titanium dioxide-filled polystyrene microcomposites *Materials Letters* **2004**, *58*, 281-289.

116. Aubry, T., An overview on clay-mediated compatibilization of polyethylene/polyamide blends with droplet morphology. *Applied Clay Science* **2019**, *175*, 184-189.

117. Pazokifard, S.; Farrokhpay, S.; Mirabedini, M.; Esfandeh, M., Surface treatment of TiO_2 nanoparticles via sol-gel method: Effect of silane type on hydrophobicity of the nanoparticles. *Progress in Organic Coatings* **2015**, *87*, 36-44.

118. Lorenzo, A. T.; Arnal, M. L.; Albuerne, J.; Müller, A. J., DSC isothermal polymer crystallization kinetics measurements and the use of the Avrami equation to fit the data: Guidelines to avoid common problems. *Polymer Testing* **2007**, *26*, 222-231.

119. Asthana, H.; Jayaraman, K., Rheology of reactively compatibilized polymer blends with varying extent of interfacial reaction. *Macromolecules* **1999**, *32*, 3412-3219.

120. Shi, D.; Ke, Z.; Yang, J.; Gao, Y.; Wu, J.; Yin, J., Rheology and morphology of reactively compatibilized PP/PA6 blends. *Macromolecules* **2002**, *35*, 8005-8012.

121. Yousfi, M.; Soulestin, J.; Vergnes, B.; Lacrampe, M. F.; Krawczak, P., Morphology and mechanical properties of PET/PE blends compatibilized by nanoclays: effect of thermal stability of nanofiller organic modifier. *Journal of Applied Polymer Science* **2013**, 2766-2778.

122. Zhang, Y.; Zhang, S.; Wu, S., Room-temperature fabrication of TiO_2-PHEA nanocomposite coating with high transmittance and durable superhydrophilicity. *Chemical Engineering Journal* **2019**, *371*, 609-617.

123. Hebbar, R. S.; Isloor, A. M.; Ismail, A. F., Contact angle measurements. In *Membrane Characterization*, Elsevier: **2017**; pp 219-255.

124. Zucchi, F.; Grassi, V.; Frignani, A.; Trabanelli, G.; Monticelli, G., Octadecyl-trimethoxy-silane film formed on copper in different conditions. *Materials Chemistry and Physics* **2007**, *103*, 340-344.

125. Pérez, R. A.; López, J. V.; Hoskins, J. N.; Zhang, B.; Grayson, S. M.; Casa, M. T.; Puiggalí, J.; Müller, A. J., Nucleation and antinucleation effects of functionalized carbon nanotubes on cyclic and linear poly(ε-caprolactones). *Macromolecules* **2014**, *47*, 3553-3566.

126. Norton, D. R.; Keller, A., The spherulitic and lamellar morphology of melt-crystallized isotactic polypropylene. *Polymer* **1985**, *26*, 704-716.

127. Antoniadis, G.; Paraskevopoulos, K. M.; Vassiliou, A. A.; Papageorgiou, G. Z.; Bikiaris, D.; Chrissafis, K., Nonisothermal melt-crystallization kinetics for in situ prepared poly(ethyleneterephthalate/montmorillonite (PET/OMMT). *Thermochimica Acta* **2011**, *521*, 161-169.

128. Lorenzo, A. T.; Müller, A. J., Estimation of the nucleation and crystal growth contributions to the overall crystallization energy barrier. *Polymer Science, Part B: Polymer Physics* **2008**, *46*, 1478-1487.

129. Avrami, M., Granulation, Phase change and microstructure. *Journal of Chemical Physics* **1941**, *9*, 177-184.

Chapter 5

Multicrystalline Block Polymers: Tricrystalline Triblock Terpolymers containing PE, PEO, PCL and PLLA Blocks

5.1. Introduction

Crystallization in block copolymers is a subject widely studied in the last few decades[1-11]. It is vital to understand the final morphology upon crystallization since it is directly related to the final properties. Many different applications can take advantage of these materials due to the different chemical nature of the segments that form a block copolymer [9, 12-14]. In addition, other factors such as block composition, molecular weight, crystallization conditions, or segregation strength and block miscibility affect the crystallization behavior. As different morphologies can be developed, the final performance of the materials can be tuned by varying these factors[2, 4, 7, 9, 11, 15-18], and many publications and have been published due to the high interest of these materials in polymer physics[2, 6, 7, 15, 19-21].

Particularly, biodegradable and biocompatible polymers, such as poly (ethylene oxide) (PEO), poly (ε-caprolactone) (PCL), and poly (L-lactide) (PLLA) have attracted attention due to their potential application in the biomedical field.

a) Poly (ethylene oxide) (PEO)

It is a thermoplastic synthesized by the heterogeneous polymerization of ethylene oxide[22]. The living anionic ring-opening polymerizations leads to a PEO with controlled chain length and narrow dispersity, with a repetitive unit of two methylene units and an ether group[13, 23].

It is a highly crystalline polymer, and molecular weights up to 7 x 10^6 g/mol can be obtained. It shows a glass transition temperature between -80 and -20 ºC, and a melting temperature of around 60 ºC, depending on the molecular weight. Mechanical properties are good, with high elongation at break and tensile resistance (PEO films have ~ 550 % of elongation, 16 MPa of tensile strength and 80 kN/m of impact resistance). It shows good solubility in water and in common organic solvents at room temperature[13].

Extrusion, injection molding or extrusion blow molding are the most employed industrial techniques for processing. It is widely employed in

pharmaceutical and biomedical industries, for example, as adhesives, in wound dressing o drug release systems[22]. In addition, there is high interest in the functionalization of the PEO, in its blending and in the creation of block copolymers due to its advantageous properties[13].

b) Poly (ε-caprolactone) (PCL)

This polyester is synthesized by ring-opening polymerization of the monomer ε-caprolactone using anionic, cationic or co-ordination catalysts[24]. The repeating unit of PCL consists of five methylene groups and a single ester group[25].

PCL has high crystallinity, up to 70 % depending on the molecular weight. The glass transition temperature is around -60 ºC, and the melting temperature varies from 59 to 64 ºC[24, 26, 27]. Due to its low glass transition temperature, PCL is very flexible and elastic, with high elongation at break (> 700 %) although its tensile strength is low (approximately 23 MPa)[26]. It shows good solubility in many organic solvents[27].

PCL can be easily processed by the usual processing techniques, and many biomedical applications can take advantage of its biocompatible nature. It is used in drug delivery, medical devices such as sutures or in wound dressing, and tissue engineering (scaffolds for bone or skin, nerve and cartilage engineering. In addition, PCL functionalization has been performed to improve its hydrophylicity and biocompatibility. Blending of PCL with other polymers improves mechanical properties such as stress crack resistance[24].

c) Poly (lactide) (PLA)

It is a linear aliphatic polyester synthesized by the ring-opening polymerization of lactide, or by the polymerization of the lactid acid. However, as the lactide monomer exists in two optically active forms (L-lactide and D-lactide), its properties are influenced by this stereochemistry

(74): it can be semicrystalline (L-lactide content higher than 93 %) or amorphous[28].

The crystalinity of PLA is usually around 35 % and depends on molecular weight and the processing conditions. The glass transition temperature of PLLA is around 60 ºC and the melting temperature is approximately 175 ºC[26]. Nevertheless, at low molecular weight and high D-lactide content, the melting temperature decreases, and the glass transition and cold crystallization temperatures are affected[29]. Semicrystalline PLA has good thermal and barrier properties, high modulus (around 4.8 GPa) and good tensile strength[26]. However, the understanding of its crystalline behavior is essential since mechanical performance, degradation behaviour and barrier and optical properties will be affected. PLA can show different crystalline structures depending on the crystallization conditions: the α-form is the most common crystal, although the α'-form, β-form and γ-form can sometimes be identified[29].

PLLA can be processed by extrusion, injection molding, thermoforming, blow molding, film blowing and melt spinning. Its relatively low price, commercial availability and good processability makes PLA a very good material for applications in the agricultural or biomedical fields, in tissue engineering, film packaging, or in the fabrication of fibers, bottles, and other disposable food-contact materials[28].

In the last years, the interest in PLLA has increased due to its biodegradability and good properties[30]. However, it is brittle at room temperature, has low elongation at break and it can suffer hydrolysis and pyrolysis at high processing temperatures. It is a rigid material with low impact resistance, and that is why copolymerization and blending with other biodegradable polymers is done[28].

Many works have been published about AB-type diblock copolymers with one or two crystallizable blocks, especially with the PEO block, the PCL block and the PLLA block. However, other studies using the apolar PE block as one of the potentially crystallizable blocks have also been reported.

Among medium or strongly segregated systems, the diblock copolymer PE-*b*-PLLA[18, 31-36] is a well-known system. Müller et al.[31-33] reported large segregation strength and thus heterogeneous lamellar morphology. Although they did not see any spherulitic-type morphology with the PLLA or the PE block crystallized, some authors[37] employed diblock copolymers with higher PLLA amounts (89-96 %), and they observed PLLA spherulites by PLOM. Furthermore, the overall crystallization rate of both the PLLA block and the PE block in the diblock copolymer was slower than that of the analogous PLLA and PE homopolymer. In addition, coincident crystallization occurs since the crystallization transitions of the PE block and the PLLA block overlap employing cooling rates higher than 2 ºC/min. Slower cooling rates or self-nucleation experiments have to be done in order to separate the crystallization exotherms of both blocks.

PE-*b*-PEO diblock copolymers have also been a matter of subject[7, 38-44]. Generally, these types of diblock copolymers show well-defined and separated thermal transitions of their crystallizable blocks. Studies employing high molecular and low molecular PEO blocks have already been published. Particularly, Castillo et al.[42] analyzed block copolymers with high molecular PEO. In all the copolymers they studied, fractionated crystallization was found (the crystallization phenomena takes place in two steps), showing well-separated crystallization peaks corresponding to each of the blocks in the DSC cooling scan. In addition, SAXS and TEM results showed percolated, and isolated PEO spheres through the PE matrix. Regarding low molecular PEO block copolymers, Weiyu et al.[43] analyzed phase transitions of those block copolymers with PEO 500 and 1100 g/mol. They found an alternating crystalline lamellae structure of PEO and PE at low temperatures, which developed into different morphologies as temperature increases.

Other well-studied systems are the PE-*b*-PCL diblock copolymers[45-49]. Nojima et al. reported many studies that analyzed the morphology and crystallization of these copolymers by DSC, SAXS, WAXS and TEM[45-48]. SAXS experiments allow determining the evolution of the microdomain structures with crystallization temperature. With low PE block content (≤ 58 %) and at temperatures in which only the PE block could crystallize, the melt microdomain structure transformed into PE lamellar morphology, whereas with higher PE block content (≥ 73 %) the melt microdomain structure remained unchanged.

The dependence of segregation strength with block compositions was also demonstrated by Nojima et al.[46]. Regarding the crystallization of the PCL block, at low crystallization temperatures, the previously formed PE lamellar morphology remains unchanged, but at high crystallization temperatures, the initial PE lamellar structure is destroyed while the crystallization of the PCL block occurs. In addition, the crystallization behaviour of the PCL block is affected by the PE block composition.

In addition, Nojima et al.[50] also studied the crystallization behavior of the PCL block in low molecular weight PCL-*b*-PE diblock copolymers employing different crystallization temperatures (T_c). The PCL block started to crystallize from a solid lamellar morphology formed in advance by the crystallization of the PE blocks. At high T_c values, the crystallization of the PCL blocks destroyed the PE lamellar morphology. At low T_c values, no macroscopic changes were observed in morphology during the crystallization of the PCL blocks.

Other block copolymers show miscible or weakly segregated behaviors, and several works have been published about the crystallization process of these systems[7, 51-58], although the most relevant ones turned out to be the following: PEO-*b*-PCL[7, 59-76], PEO-*b*-PLLA[77-90], and PCL-*b*-PLA[54, 55, 57, 91-99], due to their possible applications in the biomedical field because of the biodegradable and biocompatible nature of the blocks[14, 100-103]. Nevertheless, other systems have also been studied[104-107].

Generally, the PEO-*b*-PCL diblock copolymers show melt miscibility[65, 74-76], and the crystallization and melting temperature of the blocks are lower compared to the corresponding homopolymers. In addition, the smaller the content of the block under consideration, the higher the reduction in the crystallization temperature[73, 75, 102, 108-110], due to confined crystallization, the first crystalline block causes the crystallization of the second block. Consequently, the morphology is defined by the block that crystallizes first, since the second block crystallizes into the previously formed lamellar structure[75], which will form spherulitic-type superstructures[63, 73, 74, 76, 111, 112]. However, depending on factors such as block composition, block molecular weight or molecular architecture, the PEO block or the PCL block can be the first one to crystallize, although crystallization occurs in the same temperature range. In general, if the PCL content is higher than the PEO content, the PCL block crystallizes first, followed by the PEO block[73, 76]. In addition, several studies reported crystallization of both blocks in a wide composition range[75, 76, 102].

In the case of PEO-*b*-PLLA diblock copolymers[77-90], the crystallization of the PLLA block occurs at higher temperatures than the crystallization of the PEO block. Although both signals are recorded independently, the PEO block crystallization is influenced by the crystallization conditions of the PLLA block, and confined crystallization of the PEO blocks happens into the previously formed PLLA crystals[7, 13, 80, 83-85, 87, 88]. Furthermore, isothermal crystallization of both blocks in PEO-*b*-PLLA diblock copolymers was studied by Xue et al.[84] by SAXS/WAXS measurements. They reported that the PEO block crystallizes in the rigid environment of PLLA, after PLLA has crystallized until saturation, forming a lamellar phase with alternating layers of the blocks.

The effect of block composition and self-nucleation experiments were also studied by Arnal et al.[77]. When the content of the PLLA block is high (≥ 80%), fractionated crystallization of the PEO block occurs, a phenomenon previously observed in block copolymers with two crystallizable blocks[3, 42, 75, 113]. When the PLLA content is between 50 % and 71 %, however, the PEO crystallization is

nucleated by the previously formed PLLA crystals[77]. The morphology in these diblock copolymers is determined by the crystallization of the PLLA block and the subsequent crystallization of the PEO block, noticeable by a significant change in birefringence, which do not alter the previously formed structure and occurs inside the PLLA crystals. Superstructures such as axialites, dendrites, and spherulites are observed by PLOM and AFM experiments[114].

Other well-studied systems are PCL-*b*-PLA diblock copolymers[54, 55, 57, 91-99], in which no phase segregation in the melt is reported in general[7, 54, 56, 57, 94-96, 99, 115]. Morphology is determined by the firstly crystallized PLLA block upon cooling from the melt, forming a lamellar structure in which the PCL block crystallizes at second place. Peponi et al.[94] investigated the effect of molecular weight and block length in PCL-*b*-PLLA diblock copolymers. The minimum molecular weight for the PLLA block to crystallize was reported to be 964 g/mol. The crystallinity of the PLLA block increases by increasing its molecular weight independently of the block composition, and this hinders in some way the crystallization of the PCL block. Cold crystallization of the PLLA block was also reported in some works[55].

The isothermal crystallization behavior of PCL-*b*-PLA diblock copolymers has also been a matter of study during the last decades[54, 57, 91, 94, 95, 97, 99]. Morphology and crystallization kinetics employing different block compositions were studied by Müller et al. The PLLA block suffers a reduction in crystallization rate due to the diluent effect of the PCL block. They also reported a decrease in the PLLA crystallization rate comparing with the PLLA homopolymer. Although PLLA contents lower than 10 % are needed to see changes with block composition, the crystallization rate of the PCL block was greatly affected. Regarding morphology, as the PLLA is the first block crystallizing upon cooling from the melt, the PLLA block is the one to template the final morphology, as the PCL block crystallizes inside the interlamellar regions of the PLLA crystals, as demonstrated by Castillo et al.[55] employing block copolymers with different PLLA contents.

Additionally, some ABA-type systems have also been analyzed, such as PBT-*b*-PEO-*b*-PBT[116], PEO-*b*-PEB-*b*-PEO[117], or PLLA-*b*-PVDF-*b*-PLLA[118], for instance. The addition of a potential third crystallizable block into diblock copolymers makes the analysis of the crystalline behavior more complex. Few works have been published about tricrystalline triblock terpolymers, such as ABC-type triblock terpolymers and ABCBA pentablock terpolymers, including the apolar PE block, and the polar PEO, PCL and PLLA blocks[17, 36, 62, 67, 113, 119-133].

For instance, Sun et al.[125] prepared PLLA-*b*-PCL-*b*-PEO-*b*-PCL-*b*-PLLA pentablock terpolymers. They demonstrated the coexistence of the three crystalline structures by DSC and WAXS experiments, although the crystallization of the central PCL block was hindered by the crystallization of the other PEO and PLLA blocks. On the other hand, Tamboli et al.[126] only demonstrated crystallization of the PCL and PLLA blocks by WAXS in a PLLA-*b*-PCL-*b*-PEO-*b*-PCL-*b*-PLLA pentablock terpolymer.

Recent advances in the synthesis of ABC linear triblock terpolymers have made available these types of well-defined materials[12]. The novelty of these ABC-type triblocks consists of new morphologies that can be obtained compared to AB diblock copolymers, such as tricontinuous gyroids, core-shell cylinders, and spheres, or cylinders-in-lamellae, opening a window to new materials design[134, 135]. To our knowledge, few reports have been published for ABC type triblock terpolymers with three crystallizable blocks[122, 128-132].

Palacios et al. investigated the morphology and crystallization of ABC triblock terpolymers with three crystallizable blocks: PEO, PCL and PLLA[128-132]. In addition, Chiang et al.[122] also investigated these PEO-*b*-PCL-*b*-PLLA terpolymers, and they reported the melt miscibility and triple crystalline behavior of the materials.

Palacios et al.[132] investigated PEO-*b*-PCL-*b*-PLLA triblock terpolymers, and after studying the different competitive effects such as nucleation,

plasticization, antiplasticization, and confinement that took place within the blocks, they were able to show the triple crystalline nature of the samples by DSC and SAXS/WAXS experiments. The sequential crystallization of the blocks from the melt (first the PLLA, then the PCL, and finally the PEO block) was determined by DSC and WAXS measurements, while SAXS results evidenced melt miscibility on the melt. They demonstrated that the PCL and PEO blocks caused a plasticizing effect over PLLA crystallization and that the crystallization of the PEO block suffers confinement if the other two blocks are previously crystallized. Furthermore, triple crystalline spherulites were detected by PLOM, first PLLA spherulitic templates were formed, and further cooling allowed the PCL and PEO blocks to crystallize within the interlamellar regions of the previously formed PLLA templates, forming unique tricrystalline spherulites with PLLA, PCL and PEO lamella. There are many examples of confined crystallization of one block within the lamellae of another block previously crystallized[1, 7, 20, 136].

Furthermore, by SAXS and AFM experiments, Palacios et al.[130] were able to identify a trilamellar self-assembly with lamellae of the three blocks at room temperature. After their observations, they proposed an alternation of single lamellae of PEO or PCL in between two PLLA lamellae. However, they could not clearly determine such arrangement of the lamellae, but they employed in situ hot-stage AFM measurements to identify the nanoscale lamellar morphology[17]. Very few reports have been published about crystal observations in AB diblock copolymers and ABC triblock terpolymers from the melt by this technique, and only two blocks crystallize in the studied samples[137, 138]. Other studies were carried out with samples crystallized from solution[139, 140].

Moreover, Palacios et al.[17] analyzed the evolution of this tri-lamellar morphology on the subsequent melting of the PEO-*b*-PCL-*b*-PLLA triblock terpolymer by in situ hot-stage AFM. They were successful since cross-sectional height measurements detected three different lamellar populations at different temperatures, and the melting of each of the populations gives information about the corresponding block: the thinnest lamellae correspond to the PEO block (the

first block to melt at 45 ºC), the medium size lamellae to the PCL block (melted at 60 ºC), and the thickest PLLA lamellae melt at the highest temperature. A clear lamellar self-assembly was identified, and mechanical properties of the three lamellae populations as a function of temperature were determined.

Nevertheless, few works have been published using the apolar PE block as one of the crystallizable blocks in triblock terpolymers. Vivas et al.[62] synthesized an ABC type triblock terpolymer incorporating polyethylene (hydrogenated polybutadiene) as one of the potentially crystallisable blocks: polyethylene-*b*-poly (ethylene oxide)-*b*-poly (ε-caprolactone). They reported the crystallization of the PE and PCL blocks by DSC and WAXS, but the PEO block was not able to crystallize due to topological restrictions caused by the previous crystallization of the end blocks.

In this section, two novel triple-crystalline triblock terpolymers, $PE_{21}^{2.6}$-*b*-$PEO_{32}^{4.0}$-*b*-$PLLA_{47}^{5.9}$ and $PE_{21}^{7.1}$-*b*-$PCL_{12}^{4.2}$-*b*-$PLLA_{67}^{23.0}$ (subscripts indicate composition in wt% and superscripts indicate the number-average molecular weight (M_n) values in g mol^{-1}) are studied, as well as their precursor copolymers and homopolymers. In these triblock terpolymers, it must be emphasized that the PE blocks are nearly perfectly linear polyethylene (PE) (with only 1 % methyl side group along the chains), as opposed to previous literature on semi-crystalline block copolymers where the PE blocks were obtained from the hydrogenation of poly(butadiene) with 90% 1,4-units and 10% 1,2-units, generating at least 10% of ethyl branches along the chains)[62]. The interest of incorporating the apolar PE block to a terpolymer that contains two polar blocks (PLLA and PEO or PCL) resides in the fact that the melting of each of the blocks occurs in a well-differentiated temperature range and thus the melting of each of the blocks can be independently determined. In addition, the use of the apolar PE block in conjunction with two other polar blocks, will generate higher phase segregation even if break out occurs when one of the blocks crystallizes. We study for the first time the sequential crystallization and the effect of the cooling rate on the morphology and crystallization of novel $PE_{21}^{2.6}$-*b*-$PEO_{32}^{4.0}$-*b*-$PLLA_{47}^{5.9}$ and

$PE_{21}^{7.1}$-*b*-$PCL_{12}^{4.2}$-*b*-$PLLA_{67}^{23.0}$ tricrystalline triblock terpolymers by *in situ* Small Angle and Wide Angle X-ray scattering (SAXS and WAXS), Differential Scanning Calorimetry (DSC) and Polarized Light Optical Microscopy (PLOM). Investigating the complex structure and crystallization behavior of these tricrystalline triblock terpolymers is essential to understand their properties and potential applications.

5.2. Melt-segregation by Small-Angle X-ray Scattering

Phase segregation in diblock copolymers can be predicted by calculating the segregation strength, which is the product of χN. χ is the Flory-Huggins interaction parameter, and N is the polymerization degree. The Flory-Huggins interaction parameter (χ) can be calculated for a diblock copolymer using the approximation given by Equation 5.1[141]:

$$\chi_{12} = 0.34 + \frac{V_1}{RT}(\delta_1 - \delta_2)^2 \qquad \text{Eq. 5.1}$$

where V_1 is the molar volume of component 1, T (K) is a temperature where both polymers are in the molten state (453 K or 180 °C), R is 1.987 cal/K mol and δ_1, and δ_2 are the solubility parameters of each block in $(cal/cm^3)^{1/2}$.

For the calculation of the interaction parameter (χ) of the samples, a reference molar volume of 100 cm^3/mol was employed, and solubility parameters for each pair of the blocks taken from the literature (δ_{PE}=7.9, δ_{PEO}=9.9, δ_{PCL}=9.39, δ_{PLLA}=9.79 $(cal/cm^3)^{1/2}$)[85, 141] are used. Then, the segregation strength (χN) was calculated. Results of the calculations made for equivalent diblock copolymers that are components within the triblock terpolymers are shown in Table 5.1.

According to this theory, if χN is ≤ 10 the diblock copolymers are miscible in the melt, if χN is between 10-30, they are weakly segregated, if χN is between 30 and 50, the segregation is intermediate, and if $\chi N > 50$, the system is strongly segregated. The estimation of the miscibility of ABC-type triblock terpolymers by

this rough approximation cannot be made, as three components are involved. However, these results may give an idea about the segregation behavior of our pair of blocks in the triblock terpolymers.

Table 5.1. Values of χ and χN calculated for the di(tri)block co(ter)polymers at 180 °C

	$PE_{39}^{2.6}$-*b*-$PEO_{61}^{4.0}$		$PE_{63}^{7.1}$-*b*-$PCL_{37}^{4.2}$		$PE_{21}^{2.6}$-*b*-$PEO_{32}^{4.0}$-*b*-$PLLA_{47}^{5.9}$		$PE_{21}^{7.1}$-*b*-$PCL_{12}^{4.2}$-*b*-$PLLA_{67}^{23.0}$	
	χ	χN	χ	χN	χ	χN	χ	χN
PE-*b*-PEO	0.78	38			0.78	37		
PE-*b*-PCL			0.59	25			0.59	25
PE-*b*-PLLA					0.74	36	0.74	141
PEO-*b*-PLLA					0.34	15		
PCL-*b*-PLLA							0.36	38

According to Table 5.1 the diblock copolymers with compositions and molecular weights equivalent to those incorporated in the triblock terpolymers are in the weak or intermediate phase segregation in the melt, as most of the χN values are between 10 and 50. The copolymerization of the apolar PE block with any polyester block generally increases segregation strength as expected. The values reported in Table 5.1 do not represent the segregation strength in the triblock terpolymers as a whole, but they give an idea of the range of values to be expected.

SAXS experiments of diblock copolymers and triblock terpolymers were performed in order to analyze this phase segregation in the melt. Figure 5.1 shows the plot of intensity as a function of the scattering vector (q) of the samples in the melt, in which the presence of the diffraction peaks at low q values indicate that all

samples are phase segregated in the melt. These results agree well with the segregation strength calculations reported in Table 5.1, which indicate that phase segregation in the melt exists, but it is not very strong as crystallization overcomes phase segregation during cooling from the melt.

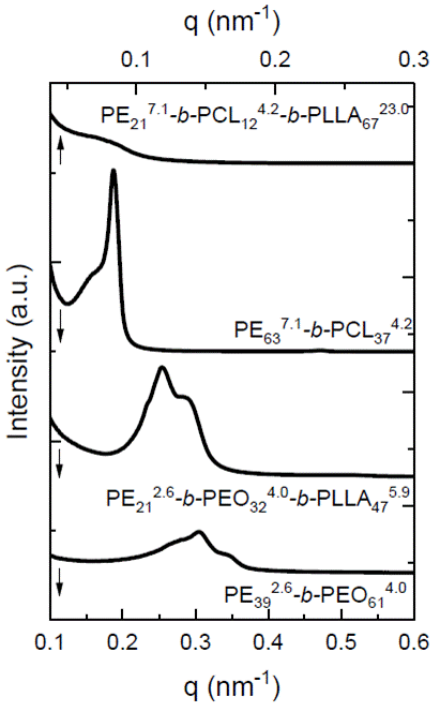

Figure 5.1. SAXS patterns of $PE_{39}^{2.6}$-*b*-$PEO_{61}^{4.0}$ and $PE_{63}^{7.1}$-*b*-$PCL_{37}^{4.2}$ diblock copolymers at 160 °C; and $PE_{21}^{2.6}$-*b*-$PEO_{32}^{4.0}$-*b*-$PLLA_{47}^{5.9}$ and $PE_{21}^{7.1}$-*b*-$PCL_{12}^{4.2}$-*b*-$PLLA_{67}^{23.0}$ triblock terpolymers at 170 °C

Figure 5.2a and 5.2b show SAXS patterns taken during cooling from the melt for the $PE_{39}^{2.6}$-*b*-$PEO_{61}^{4.0}$ diblock copolymer and the $PE_{21}^{2.6}$-*b*-$PEO_{32}^{4.0}$-*b*-$PLLA_{47}^{5.9}$ triblock terpolymer, respectively. Both materials show phase segregation in the melt, as indicated by the presence of discrete scattering peaks in the molten state. In both samples, a similar change occurs during cooling from the melt. At temperatures of 100 °C and lower, a dramatic change in the intensity and the *q* values of the main SAXS peaks occurs. This coincides with the crystallization of the PE block (as confirmed by WAXS measurements to be

presented below) within both the diblock copolymer (Figure 5.2a) and triblock terpolymer (Figure 5.2b). The crystallization "break-out" destroys the phase structure generated by the phase segregation in the melt in such a way that the resulting morphology is that of spherulites or axialites (shown and discussed below). The SAXS curves at 100 °C and lower tend to show broad maxima that are caused by the long period of the crystalline lamellar stacks within the formed superstructures (i.e., spherulites or axialites).

The different blocks of a diblock copolymer or a triblock terpolymer crystallize when cooling from the melt, forming superstructures such as axialites or spherulites (depending on composition) only if the material crystallizes from a one-phase melt or from a weakly segregated melt. If the segregation in the melt is very strong (χN values larger than 150), the crystallizable blocks would be forced to crystallize within the microdomains formed in the melt (e.g., lamellae, cylinders, spheres, etc., depending on copolymer composition) and there will be no formation of any superstructures like spherulites or axialites. In our samples, as are discussed below, PLLA spherulites (the first block crystallizing using 1 °C/min as the cooling rate) can be observed when break out occurs, confirming the weakly segregated behavior of the samples indicated by SAXS in Figures 5.2a and 5.2b.

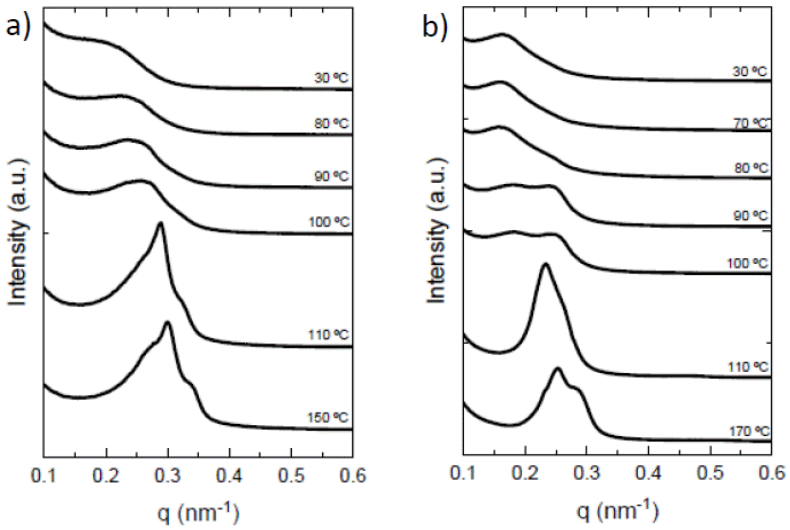

Figure 5.2. SAXS patterns taken during cooling (20 °C/min) from the melt at different temperatures for a) $PE_{39}^{2.6}$-*b*-$PEO_{61}^{4.0}$, b) $PE_{21}^{2.6}$-*b*-$PEO_{32}^{4.0}$-*b*-$PLLA_{47}^{5.9}$

In the case of the $PE_{63}^{7.1}$-*b*-$PCL_{37}^{4.2}$ diblock copolymer and the $PE_{21}^{7.1}$-*b*-$PCL_{12}^{4.2}$-*b*-$PLLA_{67}^{23.0}$ triblock terpolymer, they both show phase segregation in the melt, and "break out" occurs when the first block, PE, starts crystallizing (see Figures 5.3a and 5.3b).

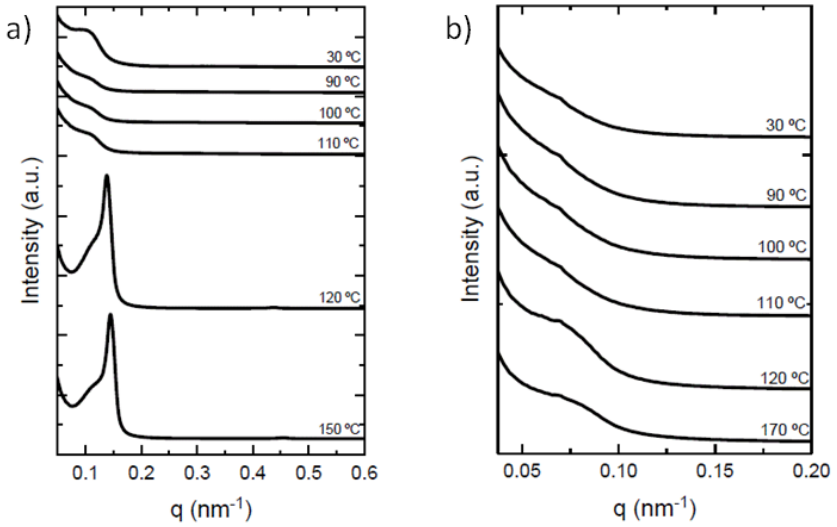

Figure 5.3. SAXS patterns taken during cooling from the melt at 20 °C/min at different temperatures for a) the $PE_{63}^{7.1}$-*b*-$PCL_{37}^{4.2}$ diblock copolymer and b) $PE_{21}^{7.1}$-*b*-$PCL_{12}^{4.2}$-*b*-$PLLA_{67}^{23.0}$ triblock terpolymer

5.3. Triblock Terpolymer $PE_{21}^{2.6}$-*b*-$PEO_{32}^{4.0}$-*b*-$PLLA_{47}^{5.9}$

5.3.1. Non-isothermal Crystallization via DSC

Non-isothermal DSC experiments were performed in order to analyze the crystallization of each block in the diblock copolymers and triblock terpolymers. DSC scans demonstrate that each of the blocks is able to crystallize separately. Figure 5.4 shows the cooling scans of the $PE^{2.6}$ homopolymer, $PE_{39}^{2.6}$-*b*-$PEO_{61}^{4.0}$ diblock copolymer, and $PE_{21}^{2.6}$-*b*-$PEO_{32}^{4.0}$-*b*-$PLLA_{47}^{5.9}$ triblock terpolymer at 20 °C/min. The exothermic crystallization peaks of each of the blocks (T_c) have been assigned employing the WAXS data obtained under identical cooling conditions at the synchrotron (shown and described below). A color code has been used throughout this work to indicate the crystallization and melting of the different

blocks by using colored arrows: green for PLLA, red for PEO, and violet for PE. The sharp exotherm (Figure 5.4a) and subsequent endotherm (Figure 5.4b) of the neat $PE^{2.6}$ precursor is a consequence of its highly linear character, as it is synthesized by polyhomologation.

In the $PE_{39}^{2.6}$-*b*-$PEO_{61}^{4.0}$ diblock copolymer, the first block crystallizing upon cooling from the melt is PE (violet arrow), followed by the crystallization of the PEO block (red arrow). There is a fractionated crystallization of the PE block, which means crystallization does not occur in a single step, as there are two exothermic crystallization peaks for PE (at 105 °C and 80 °C). In the $PE_{21}^{2.6}$-*b*-$PEO_{32}^{4.0}$-*b*-$PLLA_{47}^{5.9}$ triblock terpolymer, the crystallization sequence upon cooling at 20 °C/min from the melt turned out to be unexpected. The sequence of blocks crystallization is: PE (violet), PLLA (green), and PEO (red). It may seem that the crystallization temperature of PLLA is too low, but many experiments were performed to establish the correct sequence, and WAXS measurements that are discussed below (Figure 5.8) confirm this crystallization sequence by determining the crystallization ranges of PLLA and PE employing the intensity vs. temperature plots of the characteristic signals of each component.

Figure 5.4b shows the subsequent heating scans with clear endothermic melting peaks (T_m). The melting peak at the lowest temperature corresponds to the melting of the PEO block crystals (red), the next one to the PE block crystals (violet), and finally, the melting peak at the highest temperature corresponds to the PLLA block crystals (green).

Nevertheless, an interesting fact here is the absence of the typical cold crystallization peak of the PLLA block, which has been reported for several block copolymers that contain PLLA blocks or even for PLLA homopolymers at similar scanning rates. The additional crystallization in the heating scan does not occur because the PLLA block is able to crystallize until saturation in the previous cooling scan. All data obtained from the DSC cooling and heating scans are collected in Tables A.5.1 – A.5.3 in the Appendix.

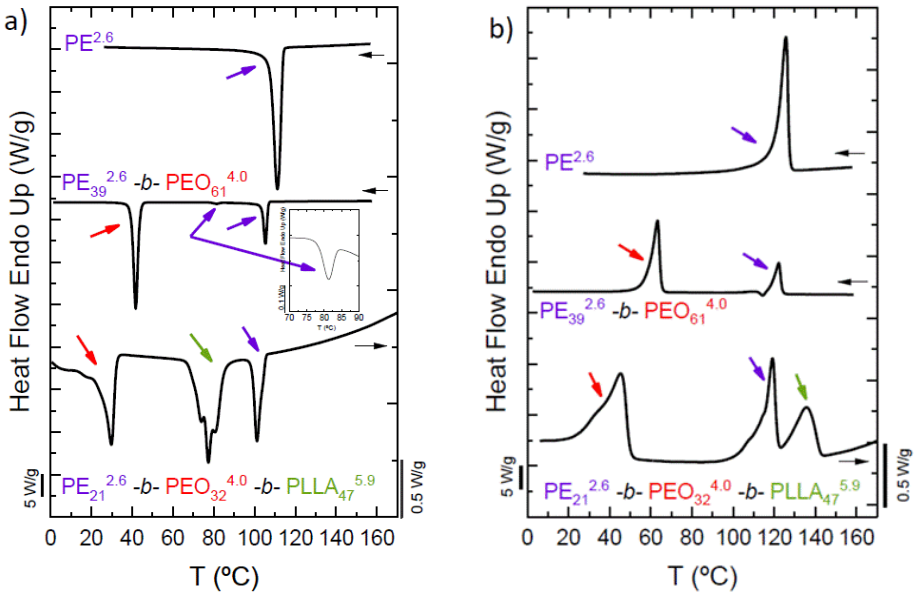

Figure 5.4. DSC scans at 20 °C/min for $PE^{2.6}$, $PE_{39}{}^{2.6}$-*b*-$PEO_{61}{}^{4.0}$ and $PE_{21}{}^{2.6}$-*b*-$PEO_{32}{}^{4.0}$-*b*-$PLLA_{47}{}^{5.9}$ with arrows indicating transitions for each block (violet for PE, green for PLLA and red for PEO) of a) cooling from the melt and b) subsequent heating

Figure 5.5 represents the cooling and subsequent heating scans at 1 °C/min. The crystallization sequence of each of the blocks is the same as when the sample is cooled at 20 °C/min. The first block to crystallize from the melt is PE (violet arrow), followed by the PLLA block (green arrow), and finally, the PEO block (red arrow).

The melting peaks of the blocks are assigned in the same way as in Figure 5.4. The difference between employing 20 ºC/min or 1 ºC/min is the amount that the PE block can crystallize before the crystallization of the PLLA block starts (compare Figure 5.4a and Figure 5.5). All thermal properties of the scans performed at 1 ºC/min are reported in Table A.5.4.

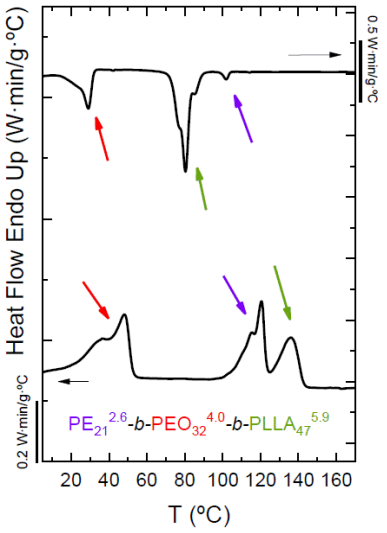

Figure 5.5. Cooling and subsequent heating scans at 1 °C/min for $PE_{21}^{2.6}$-*b*-$PEO_{32}^{4.0}$-*b*-$PLLA_{47}^{5.9}$ with arrows indicating transitions for each block (violet for PE, green for PLLA and red for PEO)

5.3.2. Wide-Angle X-Ray Scattering (WAXS)

With *in situ* WAXS experiments performed at the synchrotron, the data is obtained in real-time as samples are cooled and heated using different rates. This is very advantageous since we can directly compare the WAXS results with those obtained by DSC (obtained at identical cooling and heating rates) to better understand the crystallization sequence in these complex triblock terpolymers.

The obtained WAXS patterns confirm the triple-crystalline nature of the ABC-type triblock terpolymers employed in this work. The presence of crystalline scattering peaks pointed out in colors (violet for PE, green for PLLA, red for PEO, and blue for PCL) confirms that each block is able to crystallize separately. According to literature, PLLA, PCL and PE crystallize in orthorhombic unit cells[62, 63, 89], and PEO does it in a monoclinic one[63]. The crystal unit cell dimensions are the following: a=10.56 Å, b=6.05 Å and c=28.90 Å for PLLA[89]; a=7.48 Å, b=4.98 Å and c=17.26 Å for PCL[142]; a=7.96 Å, b=13.11 Å, c=19.39 Å (chain direction) and β=124º48' for PEO[143]; and a=7.40 Å, b=4.96 Å, and c=2.53 Å for PE[144]. All reflections observed in our samples correspond only to the α-form

of PLLA; no signals were detected for the α'-form[128]. Table 5.2 reports the indexation that agrees well with assignments widely published in the literature for PE, PEO, PCL and PLLA crystals[54, 57, 63, 85, 89, 91, 115, 128, 145]

Table 5.2. WAXS indexation for all the blocks studied in the samples

Blocks	(hkl) planes	q values (nm^{-1})
PLLA	(010)	10.3
PLLA	(110)/(200)	12.0
PLLA	(113)/(203)	13.5
PEO	(120)	13.8
PE	(110)	15.4
PCL	(110)	15.5
PLLA	(210)	15.7
PEO	(032)/(112)/(132)/(212)	16.4
PCL	(200)	16.7
PE	(200)	16.9

WAXS patterns of the $PE^{2.6}$ homopolymer in Figure 5.6a show the characteristic PE scattering peaks (violet) at 15.4 and 16.9 nm^{-1} corresponding to the (110) and (200) crystallographic planes, which first appear, upon cooling from the melt, when PE starts crystallizing at 112 °C. To better visualize the detection of the PE block crystallization, the intensity of the PE_{110} (15.4 nm^{-1}) reflection was measured, normalized (by dividing the intensity by the maximum value achieved at the minimum temperature employed, so that the normalized intensity varies between 0 and 1) and plotted as a function of temperature along with a DSC cooling scan also obtained at 20 °C/min. Figure 5.6b clearly shows the PE block crystallization as a sharp change in the (100) intensity starting at 112 °C (we have employed filled symbols to denote crystal scattering was present and recorded). Figure 5.6b also shows the good match with the DSC cooling scan, where the crystallization peak (T_c) in the DSC scan approximately corresponds with the maximum rate of slope change in the WAXS data.

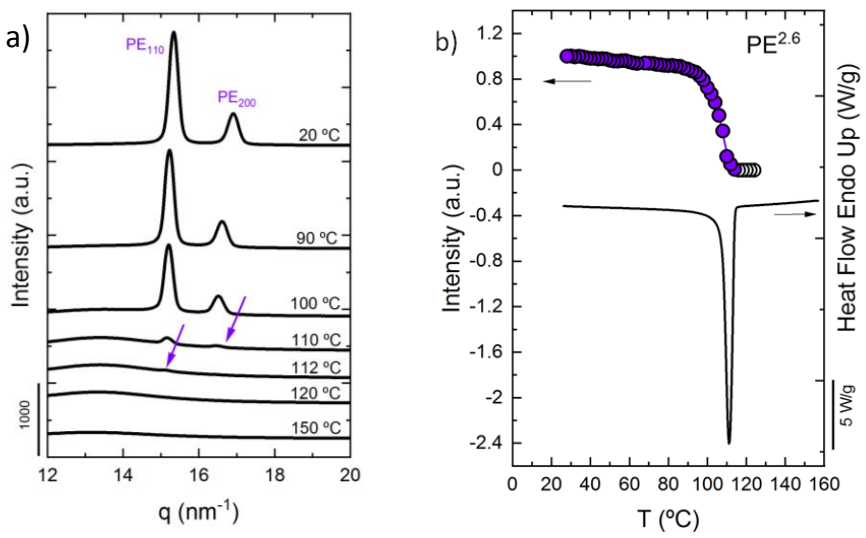

Figure 5.6. a) WAXS patterns taken during cooling from the melt at 20 °C/min for $PE^{2.6}$ at different temperatures with violet arrows indicating the crystallization of the PE block and the corresponding (hkl) planes, and b) Normalized WAXS intensity of the PE_{110} (15.4 nm^{-1}) reflection as a function of temperature from WAXS data represented in a, along with the DSC cooling scan also performed at 20 °C/min

Figure 5.7 corresponds to the $PE_{39}^{2.6}$-*b*-$PEO_{61}^{4.0}$ diblock copolymer. As can be seen in Figure 5.7a, the first block that crystallizes upon cooling from the melt is the PE (violet) at 108 °C, with its scattering peaks at 15.4 and 16.9 nm^{-1} (reflections (110) and (200)). At much lower temperatures, i.e., 36 °C, the PEO block (red) starts to crystallize with its (120) and (032)/(112)/(132)/(212) reflections at 13.8 and 16.4 nm^{-1}, respectively. In this case, Figure 5.4a clearly shows the sequential crystallization of the PE and PEO blocks by their corresponding crystallization exotherms. Nevertheless, we wanted to check if a similar assignment can be made by measuring the intensity of the WAXS main reflections. As the reflection of $PEO_{032/112/132/212}$ (16.4 nm^{-1}) coincides with that of PE_{200} (16.9 nm^{-1}), the normalized intensity of the joint reflection peak was measured to clarify the crystallization range of each block.

Figure 5.7b shows a slight but clear increase in intensity at 108 °C due to the scattering from the (200) planes of PE (16.9 nm^{-1}). The sharp increase at 36 °C corresponds to the $PEO_{032/112/132/212}$ (16.4 nm^{-1}) planes. The normalized intensity of the PE_{110} (15.3 nm^{-1}) reflection has also been calculated and plotted in Figure 5.7b. A sharp increase due to the crystallization of the PE block can be observed at 108 °C, as expected. The WAXS intensity trend corresponding to the PE reflections in Figure 5.7b (filled violet color points) as cooling from the melt proceeds indicates a bimodal crystallization with two sharp increases at approximately 108 °C and 80 °C. The DSC cooling scan from the melt also shows two exotherms upon cooling from the melt, the most intense with a peak at 108 °C and a second much smaller peak at 80 °C. This fractionated crystallization of the PE block within $PE_{39}^{2.6}$-*b*-$PEO_{61}^{4.0}$ diblock copolymer may be due to a complex morphology formed during the break out from the phase-separated melt microdomains of this minority component[18, 146, 147].

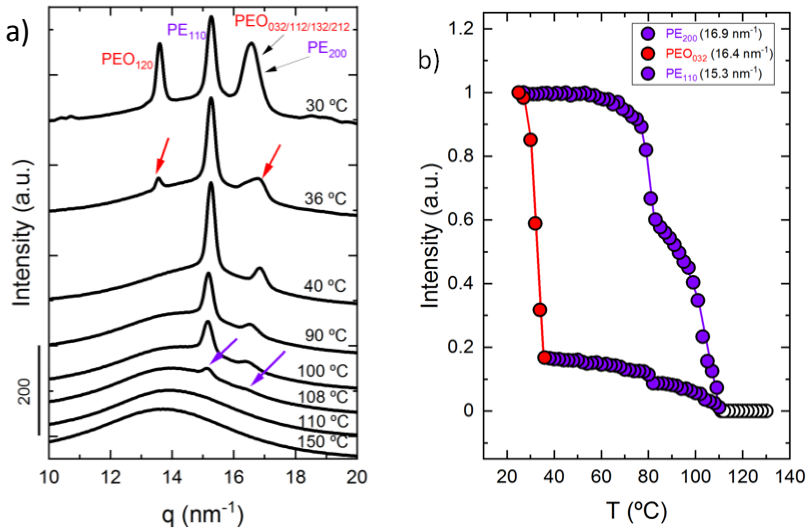

Figure 5.7. a) WAXS patterns taken during cooling from the melt at 20 °C/min for $PE_{39}^{2.6}$-*b*-$PEO_{61}^{4.0}$ at different temperatures with arrows indicating crystallization of the PE block (violet), the PEO block (red) with their corresponding (hkl) planes, and b) Normalized WAXS intensity of PE_{200} (16.9 nm^{-1}) and $PEO_{032/112/132/212}$ (16.4 nm^{-1}) with square symbols and PE_{110} (15.3 nm^{-1}) with triangle symbols as a function of temperature taken from WAXS data represented in a

The correspondence between DSC and WAXS, once again, is very good. However, both the homopolymer and the diblock copolymer cases are easy examples where the crystallization signals can be clearly identified both in DSC and WAXS. For the triblock terpolymers, the assignment is not as easy.

Figure 5.8 shows the WAXS patterns for the $PE_{21}^{2.6}$-*b*-$PEO_{32}^{4.0}$-*b*-$PLLA_{47}^{5.9}$ triblock terpolymer. In this case, the PE block (violet) is the first one crystallizing upon cooling from the melt at 20 °C/min, as revealed by the appearance of the PE_{110} reflection at 106 °C and the PE_{200} reflection at 100 °C. The intensity of the PE_{110} reflection at 15.4 nm^{-1} is analyzed to check the crystallization range of PE. Figure 5.8a shows how the PE block starts crystallizing at 108 °C with a sharp increase in relative intensity (between 108 and 90 °C approximately) that corresponds to the first sharp crystallization exotherm registered upon cooling from the melt by DSC in Figure 5.4a. A second and more gradual increase in relative intensity occurs between 90 and 50 °C, which corresponds to some residual PE block crystallization that cannot be easily seen in the DSC trace, as it is masked by the PLLA block crystallization and the baseline curvature. It must be remembered that this triblock contains only 21 wt% PE. From this 21 % PE only about 23% crystallizes (see Table A.5.3).

The next block crystallizing upon cooling at 20 °C/min is the PLLA block (green), as indicated by the appearance of the following crystalline reflections: $PLLA_{110/200}$ at 96 °C, $PLLA_{113/203}$ at 90 °C, and $PLLA_{210}$ at 80 °C in Figure 5.8a. We have followed the relative intensity of the $PLLA_{110/200}$ reflection, as it is due exclusively to PLLA crystals diffraction (with no overlap of reflections from PE crystals). According to Figure 5.8c, the PLLA block starts crystallizing at approximately 98 °C, i.e., at a temperature that is 10 degrees lower than the temperature at which the PE block starts crystallizing. The relative intensity of the $PLLA_{110/200}$ reflection sharply increases in the range 98 to 60 °C approximately, in close agreement with the second crystallization exotherm seen in Figure 5.4a by DSC, which peaks at temperatures close to 80 °C. Even though PLLA is the major component in this triblock (47 wt %), it can only crystallize up to 25% according

to Table A.5.3. This relatively low degree of crystallization is associated with the typically low crystallization rate of PLLA when cooled from the melt at 20 °C/min.

The last block to crystallize upon further cooling at 20 °C/min is the PEO block (red) at 34 °C, according to Figure 5.8a. As there is not any single WAXS scattering peak that corresponds only to PEO crystalline reflection, the $PLLA_{113/203}$ signal (13.5 nm^{-1}) that overlaps with the PEO_{120} (13.8 nm^{-1}) was taken to plot the relative intensity vs. temperature to determine the exact temperature at which PEO starts crystallizing. Figure 5.8d shows that the PEO block starts crystallizing at 35 °C. The PEO block amounts to 32 wt% of the triblock terpolymer under consideration, and even though it is the last block to crystallize, it can still achieve a crystallinity degree of 40% (see Table A.5.3). In addition, Figure 5.8d corroborates the PLLA block crystallization range, which closely matches that shown in Figure 5.8c.

The results shown above have demonstrated the peculiar crystallization behaviour of the $PE_{21}^{2.6}$-*b*-$PEO_{32}^{4.0}$-*b*-$PLLA_{47}^{5.9}$ tricrystalline triblock terpolymer. Even though PLLA is the most abundant block, its non-isothermal crystallization kinetics is slower than that of the PE block.

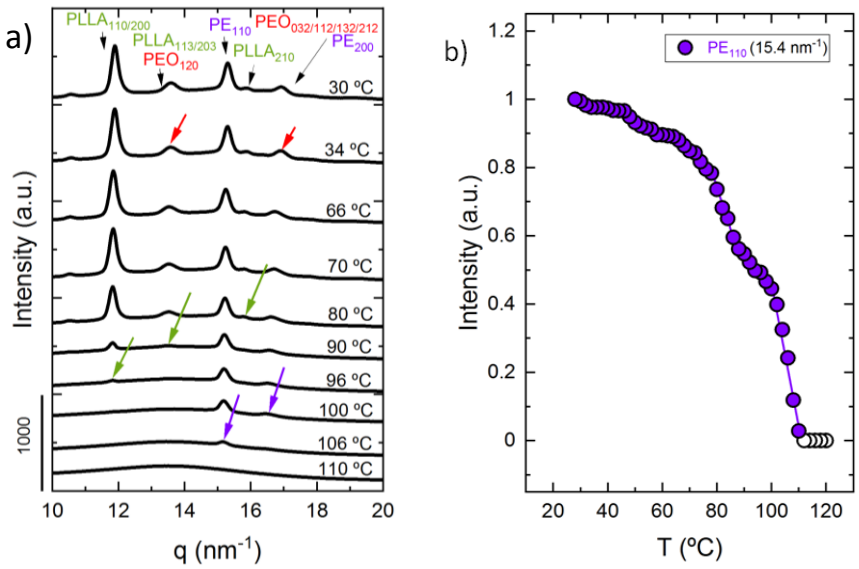

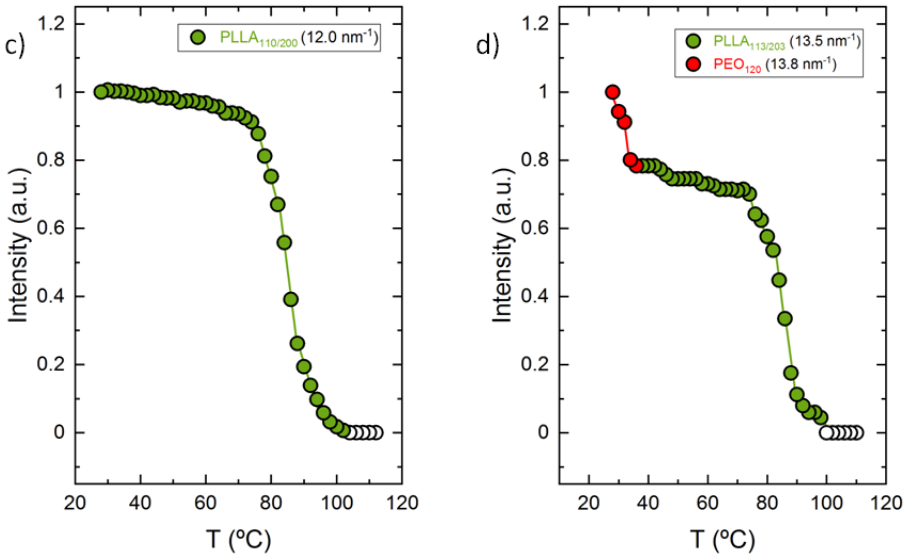

Figure 5.8. a) WAXS patterns taken during cooling from the melt at 20 °C/min for $PE_{21}^{2.6}$-*b*-$PEO_{32}^{4.0}$-*b*-$PLLA_{47}^{5.9}$ at different temperatures with arrows indicating crystallizations of the PE block (violet), the PLLA block (green) and the PEO block (red) with their corresponding (hkl) planes and, b) Normalized WAXS intensity of PE_{110} (15.4 nm^{-1}), c) Normalized WAXS intensity of $PLLA_{110/200}$ (12.0 nm^{-1}) and, d) Normalized WAXS intensity of PEO_{120} (13.8 nm^{-1}) and $PLLA_{113/203}$ (13.5 nm^{-1})

As a result, the PE block can crystallize first upon cooling from the melt at 20 °C/min, followed by the PLLA block and lastly by the PEO block. On the contrary, as PLLA crystals melt at a higher temperature, the order of the sequential tricrystalline melting structure is: PEO block crystals first, PE block crystals then and finally PLLA block crystals. This melting sequence was clearly observed by DSC, as the three components have well-spaced distinct melting temperatures. In addition, *in situ* WAXS experiments during heating also corroborated the melting sequence observed by DSC (WAXS heating scans and normalized intensity measurements are shown in Figures A.5.1-A.5.3 in the Appendix). The crystallization sequence is remarkably different from the melting sequence of the three types of crystals in the sample. As shown in the next section, a change in the chemical structure and composition of the terpolymer can make a difference in this special crystallization behaviour from the melt.

5.4. Triblock Terpolymer $PE_{21}^{7.1}$-*b*-$PCL_{12}^{4.2}$-*b*-$PLLA_{67}^{23.0}$

5.4.1. Non-isothermal Crystallization via DSC

The non-isothermal crystallization behavior of the $PE^{7.1}$ homopolymer, $PE_{63}^{7.1}$-*b*-$PCL_{37}^{4.2}$ diblock copolymer, and $PE_{21}^{7.1}$-*b*-$PCL_{12}^{4.2}$-*b*-$PLLA_{67}^{23.0}$ triblock terpolymer was also studied. These DSC scans demonstrate that each of the blocks is able to crystallize separately. Figure 5.9a shows the cooling scans for these samples at 20 °C/min, whereas Figure 5.9b shows the subsequent heating scans performed at the same rate. Crystallization (T_c) and melting peaks (T_m) of each of the blocks have been assigned employing WAXS data obtained under identical cooling and heating conditions (shown and described below). The same color code previously used is applied to indicate transitions of the different blocks (green for PLLA, blue for PCL, and violet for PE).

Figure 5.9a shows that in the case of the $PE_{63}^{7.1}$-*b*-$PCL_{37}^{4.2}$ diblock copolymer, the first block crystallizing upon cooling from the melt is PE (violet arrow) followed by the crystallization of the PCL block (blue arrow) at the lowest temperature. In the $PE_{21}^{7.1}$-*b*-$PCL_{12}^{4.2}$-*b*-$PLLA_{67}^{23.0}$ triblock terpolymer, the sequence of block crystallization is: PE (violet), PLLA (green) and PCL (blue). This crystallization sequence upon cooling from the melt at 20 °C/min is not the expected one, as we may consider PLLA's crystallization to be too low. However, WAXS measurements discussed below (Figure 5.13) confirm this crystallization sequence seen by DSC.

In the subsequent heating scans shown in Figure 5.9b, the endothermic melting peaks (T_m) of the blocks are assigned to each of the blocks. For the $PE_{63}^{7.1}$-*b*-$PCL_{37}^{4.2}$ diblock copolymer, the PCL block (blue) crystals melt firstly at the lowest temperature, followed by the melting of the PE block (violet) crystals at higher temperatures. In the $PE_{21}^{7.1}$-*b*-$PCL_{12}^{4.2}$-*b*-$PLLA_{67}^{23.0}$ triblock terpolymer, it can be observed the typical cold crystallization exothermic peak (T_{cc}) of the PLLA block at 77 °C along with its melting peak at 154 °C. The presence of the cold

crystallization peak in the heating scan means that the PLLA block does not crystallize until saturation in the previous cooling scan shown in Figure 5.9a.

The presence of this cold crystallization peak (T_{cc}) depends on the length of the PLLA block, copolymer composition, and cooling conditions. Comparing this heating scan of $PE_{21}^{7.1}$-*b*-$PCL_{12}^{4.2}$-*b*-$PLLA_{67}^{23.0}$ in Figure 5.9b with the one for $PE_{21}^{2.6}$-*b*-$PEO_{32}^{4.0}$-*b*-$PLLA_{47}^{5.9}$ in Figure 5.4b, the most significant change is the presence of the cold crystallization peak of the PLLA block. As the cooling rate employed in both systems is 20 °C/min, the difference is due to copolymer composition and the length of the PLLA block. In the $PE_{21}^{7.1}$-*b*-$PCL_{12}^{4.2}$-*b*-$PLLA_{67}^{23.0}$ triblock terpolymer, the PLLA content is higher, and longer PLLA polymer chains (with slower crystallization) are present. That is why all the PLLA is not able to crystallize until saturation in the cooling scan, and it does so in the subsequent heating scan showing this cold crystallization peak in Figure 5.9b.

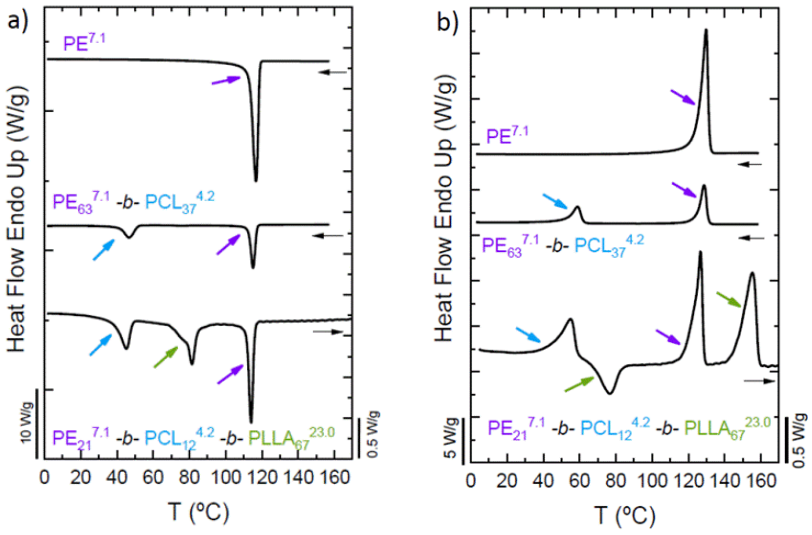

Figure 5.9. DSC scans at 20 °C/min for $PE^{7.1}$, $PE_{63}^{7.1}$-*b*-$PCL_{37}^{4.2}$ and $PE_{21}^{7.1}$-*b*-$PCL_{12}^{4.2}$-*b*-$PLLA_{67}^{23.0}$ with arrows indicating transitions for each block (violet for PE, green for PLLA and blue for PCL) of a) cooling from the melt and b) subsequent heating

However, significant changes can be observed in the crystallization of $PE_{21}^{7.1}$-*b*-$PCL_{12}^{4.2}$-*b*-$PLLA_{67}^{23.0}$ if the cooling rate is decreased from 20 °C/min to 1 °C/min (see Figure 5.10). Regarding the cooling scan in the upper side of Figure 5.10, the very broad crystallization peak at 145 °C corresponds to the PLLA block crystallization (green arrow). The PLLA block continues crystallizing as temperature decreases until 60 °C, as WAXS measurements discussed below demonstrate that the crystallization of the PLLA block occurs between temperatures ranging from 145 °C to 60 °C (Figure 5.14b). The next block crystallizing upon cooling from the melt is the PE block (violet arrow). Its crystallization is overlapped in part of the temperature range where the PLLA block crystallizes. WAXS measurements allowed the determination of the exact crystallization range of the PE block, which goes from 118 °C to 78 °C (Figure 5.14c-d). Finally, the crystallization of the PCL block (blue) starts at 55 °C, as can be seen in the DSC cooling scan. In summary, at 1 °C/min the cooling rate is slow enough to allow the PLLA block to start crystallizing from the melt at higher temperatures than the PE block (just the reverse of what occurs at 20 °C/min, at which the PE block starts crystallizing first or at higher temperatures than the PLLA block).

In the subsequent heating scan of the $PE_{21}^{7.1}$-*b*-$PCL_{12}^{4.2}$-*b*-$PLLA_{67}^{23.0}$ sample, the PCL block (blue) is the first block whose crystals melt, followed by the PE block (violet) crystals and finally the PLLA block (green) crystals. In this case, there is no cold crystallization peak of the PLLA block, since using 1 °C/min as heating rate, the PLLA block had enough time during the cooling scan to crystallize until saturation. All data obtained from DSC cooling and heating scans at 20 and 1 °C/min are collected in Tables A.5.1 – A.5.4the Appendix.

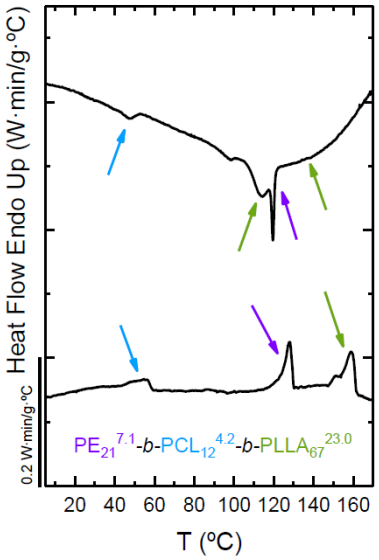

Figure 5.10. DSC cooling and subsequent heating scans at 1 °C/min for $PE_{21}^{7.1}$-*b*-$PCL_{12}^{4.2}$-*b*-$PLLA_{67}^{23.0}$ with arrows indicating transitions for each block (violet for PE, green for PLLA and blue for PCL)

5.4.2. Wide Angle X-Ray Scattering (WAXS)

All WAXS patterns shown below were taken during cooling from the melt at 20 °C/min. All *q* values with their crystallographic planes of the different blocks are listed in Table 5.2. Figure 5.11a shows the characteristic scattering peaks of the PE precursor (violet), PE_{110} at 15.4 $nm^{-1,}$ and PE_{200} at 16.9 nm^{-1}, which first appear upon cooling from the melt at 118 °C, when this PE precursor starts crystallizing. In order to determine the crystallization range of this PE, the intensity of the PE_{110} (15.4 nm^{-1}) reflection was measured (normalized) and plotted as a function of temperature along with a DSC cooling scan employing the same cooling rate, 20 °C/min. The sharp change starting at 118 °C in the (110) intensity in Figure 5.11b confirms the crystallization of the PE block, as well as the good match with the DSC cooling scan as the crystallization peak (T_c) of the scan corresponds with the maximum rate of slope change in the WAXS data.

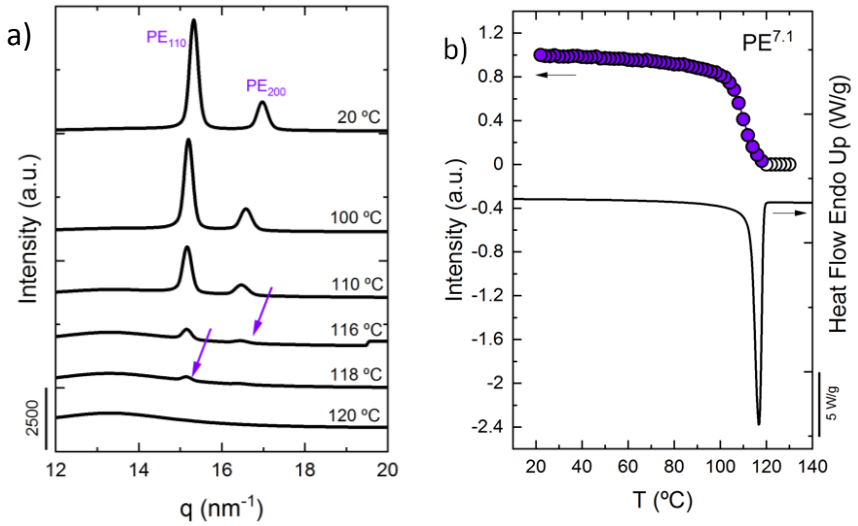

Figure 5.11. a) WAXS patterns taken during cooling from the melt at 20 °C/min for $PE^{7.1}$ at different temperatures with violet arrows indicating crystallization of the PE block and the corresponding (hkl) planes, and b) Normalized WAXS intensity of the PE_{110} (15.4 nm^{-1}) reflection as a function of temperature from WAXS data represented in a, with the DSC cooling scan performed at 20 °C/min

Figure 5.12 corresponds to the $PE_{63}^{7.1}$-*b*-$PCL_{37}^{4.2}$ diblock copolymer. As shown in Figure 5.12a, the crystallization of the PE block (violet) starts at 114 °C, showing the characteristic (110) and (200) crystallographic planes at 15.4 nm^{-1} and 16.9 nm^{-1} in the WAXS diffractogram. The PCL block (blue) is the second block crystallizing, as confirmed by the DSC scan in Figure 5.9a, but it is difficult to determine the exact temperature at which it starts crystallizing using data represented in Figure 5.12a. As the PE_{110} and PCL_{110} reflections overlap in WAXS measurements, this joint reflection is used to measure the change in intensity that will determine at what temperature the PCL block starts to crystallize. Figure 5.12b shows the normalized intensity of this joint reflection as a function of temperature in order to determine the crystallization range of each of the blocks. The first sharp increase at 114 °C corresponds to the crystallization of the PE block (violet), whereas the second lighter increase at 44 °C is due to the

crystallization of the PCL block (blue). The match between DSC and WAXS data is again excellent for this diblock copolymer.

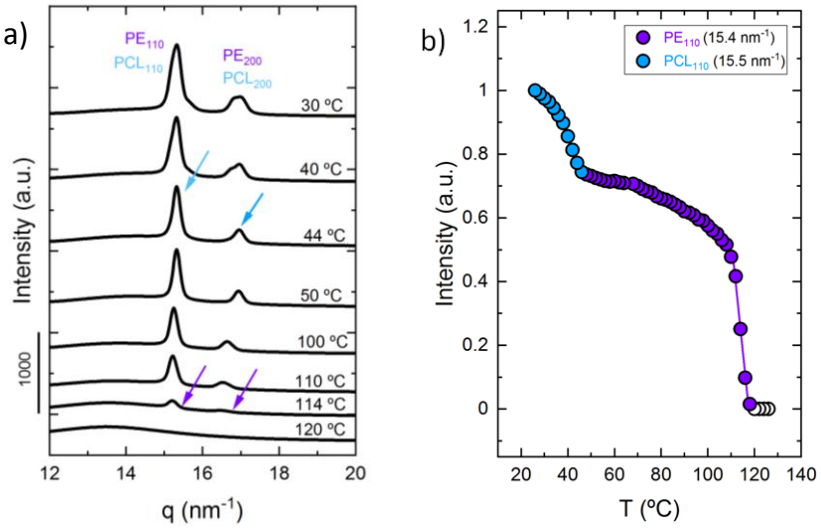

Figure 5.12. a) WAXS patterns taken during cooling from the melt at 20 °C/min for $PE_{63}^{7.1}$-*b*-$PCL_{37}^{4.2}$ at different temperatures with arrows indicating crystallization of the PE block (violet) and the PCL block (blue) with their corresponding (hkl) planes, and b) Normalized WAXS intensity of the PE_{110} (15.4 nm^{-1}) and PCL_{110} (15.5 nm^{-1}) reflections as a function of temperature from WAXS data represented in a

Figure 5.13a presents WAXS patterns for the $PE_{21}^{7.1}$-*b*-$PCL_{12}^{4.2}$-*b*-$PLLA_{67}^{23.0}$ triblock terpolymer taken as the sample was cooled from the melt. The first block crystallizing upon cooling from the melt at 20 °C/min is the PE block (violet), as determined by the appearance of the PE_{110} and PE_{200} reflections at 116 °C and at 110 °C, respectively. In this case, there are no signals that correspond to just the PE block, so the joint reflection of the PE_{110} (15.4 nm^{-1}) and the PCL_{110} (15.5nm^{-1}) is employed to determine the temperature range at which the PE block crystallizes. Figure 5.13c shows the normalized intensity as a function of temperature, in which the first sharp increase corresponds to the PE block (violet) crystallization starting at 116 °C. This result agrees well with the sharp crystallization exotherm registered by DSC in Figure 5.9a. Note that this triblock

contains only 21 wt% PE, and from this 21% PE only about 34% crystallizes (see Table A.5.3). The crystallization range of the PE is wide (see Figure 5.11b), covering a range from 116 °C down to approximately 40 °C.

In Figure 5.13a it is determined that the next block crystallizing upon cooling the $PE_{21}^{7.1}$-*b*-$PCL_{12}^{4.2}$-*b*-$PLLA_{67}^{23.0}$ sample from the melt is the PLLA block (green), as the $PLLA_{110/200}$ reflection appears at 100 °C followed by the $PLLA_{113/203}$ reflection at 90 °C. In order to check the very first crystallization temperature of the PLLA block, we used the results of Figure 5.13b shows the normalized intensity of the $PLLA_{110/200}$ (12.0 nm^{-1}) reflection which corresponds exclusively to PLLA crystal. The PLLA block starts to crystallize approximately at 100°C, according to Figure 5.13b. Note that the PLLA block crystallization occurs at 16 °C lower than the temperature at which the PE block starts crystallizing, which agrees well with the DSC data obtained in Figure 5.9a, in which the second exothermic peak was assigned to the PLLA block crystallization. Even if PLLA is the major component of this triblock terpolymer (67 wt%), it can only achieve a crystallinity degree of 22% (see Table A.5.3).

The last block to crystallize in the $PE_{21}^{7.1}$-*b*-$PCL_{12}^{4.2}$-*b*-$PLLA_{67}^{23.0}$ triblock terpolymer upon cooling from the melt at 20 °C/min is the PCL block (blue). Figure 5.13c shows the normalized intensity of the PCL_{110} (15.5 nm^{-1}) and PE_{110} (15.4 nm^{-1}) overlapped reflections as a function of temperature. As previously mentioned, the first sharp increase corresponds to the beginning of the PE block (violet) crystallization at 116 °C. The second change in intensity that starts at 42 °C corresponds to the crystallization of the PCL block (blue). Although this triblock terpolymer only contains 12 wt% PCL and it is the last block to crystallize, it is able to crystallize up to 74% (see Table A.5.3).

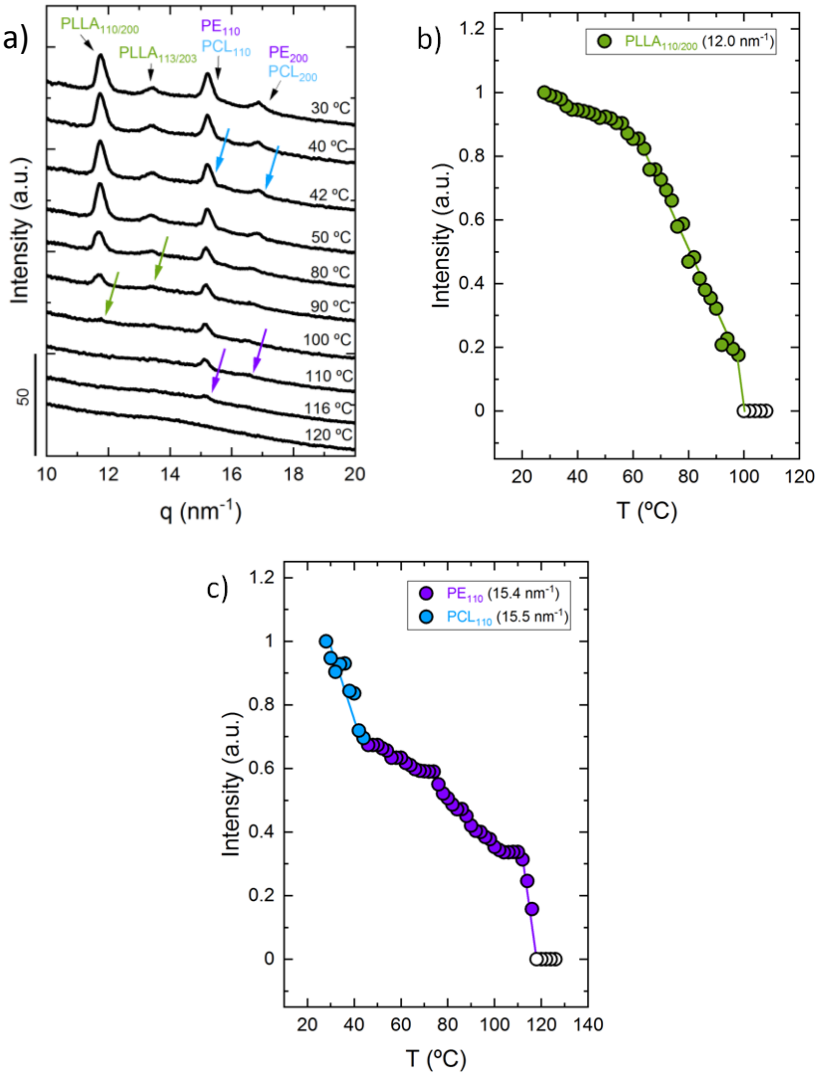

Figure 5.13. a) WAXS patterns taken during cooling from the melt at 20 °C/min for $PE_{21}^{7.1}$-*b*-$PCL_{12}^{4.2}$-*b*-$PLLA_{67}^{23.0}$ at different temperatures with arrows indicating crystallization of the PE block (violet), the PLLA block (green) and the PCL block (blue), with their (hkl) planes; b) Normalized WAXS intensity of $PLLA_{110/200}$ (12.0 nm^{-1}); c) Normalized WAXS intensity of PE_{110} (15.4 nm^{-1}) and PCL_{110} (15.5nm^{-1})

An additional measurement was performed on the $PE_{21}^{7.1}$-*b*-$PCL_{12}^{4.2}$-*b*-$PLLA_{67}^{23.0}$ triblock terpolymer but employing 1 °C/min in order to study the effect of the cooling rate in the crystallization behavior of the blocks (equivalent to DSC cooling scans of Figure 5.10). In this case, the results were not performed at the synchrotron but in a laboratory apparatus with fast measurement capabilities, as described in the experimental part. The results are shown in Figure 5.14a.

In this case, the order of the crystallization of the blocks changes in comparison to a faster cooling rate, such as that applied in Figure 5.13a. The first block to crystallize upon cooling from the melt at 1 °C/min at 145 °C is the PLLA block (green): the $PLLA_{110/200}$ (12.0 nm^{-1}), $PLLA_{113/203}$ (13.5 nm^{-1}) and $PLLA_{210}$ (15.7 nm^{-1}) reflections appear at 145 °C, 135 °C, and 115 °C, respectively. Figure 5.14b shows the normalized intensity as a function of the temperature of the $PLLA_{110/200}$ (12.0 nm^{-1}) reflection (which does not overlap with reflections from PE or PCL crystal planes). The crystallization of the PLLA block is indeed very broad, it starts at 145 °C and ends at approximately 66 °C. Figure 5.14b indicates that the maximum non-isothermal crystallization rate for the PLLA block is around 120 °C. At this temperature, the corresponding DSC cooling scan shows a relatively sharp exotherm that is followed by another broader one at lower temperatures. It was essential to check the crystallization range of the PLLA block by the analysis of the normalized intensity in Figure 5.14b, as the DSC cooling scan performed at 1 °C/min in Figure 5.10 does not show clearly the crystallization onset of the PLLA. On the other hand, both PLLA and PE blocks crystallize with overlapping exotherms at temperatures between 125 and 100 °C (see Figures 5.14c and 5.14d). The major component in this triblock terpolymer is the PLLA block with 67 wt%, and it achieves a crystallinity value of 41% (see Table A.5.4).

Then, the next block to crystallize when the temperature is further decreased (Figure 5.14a) within the $PE_{21}^{7.1}$-*b*-$PCL_{12}^{4.2}$-*b*-$PLLA_{67}^{23.0}$ triblock terpolymer is the PE block (violet) starting at 115 °C, as indicated by the appearance of the PE_{110} (15.4 nm^{-1}) reflection. As in this case, there is not any signal that corresponds only to the PE block, the signals of PE_{110} (15.4 nm^{-1}) and PCL_{110} (15.5 nm^{-1}), and PE_{200} (16.9 nm^{-1}) and PCL_{200} (16.7 nm^{-1}) where the crystallization of both PE and PCL blocks overlap have been used. The first sharp increase in the normalized intensities as a function of temperature in Figures 5.14c and 5.14d corresponds to the crystallization of the PE block, which occurs approximately between 115 °C and 75 °C. The comparison of Figure 5.14b with Figure 5.14c and 5.14d shows that even though the PLLA block starts

crystallization at a much higher temperature (145 °C), both PE block and the PLLA block crystallize coincidentally from 115 °C down to 75 °C, as the PLLA block continues crystallizing when the PE block starts to crystallize. Both crystallizations are overlapped, and that is why the crystallization of the PLLA and PE blocks cannot be distinguished clearly in the DSC cooling scan shown in Figure 5.10. The percentage of PE in this triblock terpolymer is 21 wt%, and it only crystallizes up to 34% (see Table A.5.4).

The last block to crystallize is the very short PCL block (blue), showing its 110 (15.1 nm^{-1}) and 200 (16.7 nm^{-1}) reflections. Again, in this case, we need to take the overlapped PE_{110} (15.4 nm^{-1}) and PCL_{110} (15.5 nm^{-1}) (Figure 5.14c), or PE_{200} (16.9 nm^{-1}) and PCL_{200} (16.7 nm^{-1}) (Figure 5.14d) reflections to check the intensity change that occurs when the PCL block starts crystallizing. Analyzing both Figures, it is clear that the second increase in intensity corresponds to the PCL block (blue), which starts approximately at 55 °C. This is in close agreement with the results obtained by DSC in Figure 5.10, in which the exothermic peak at the lowest temperature corresponds to the crystallization of the PCL block (blue). Although the PCL block is the last one crystallizing and it is in a percentage of 12 wt%, it can crystallize up to 58% (see Table A.5.4).

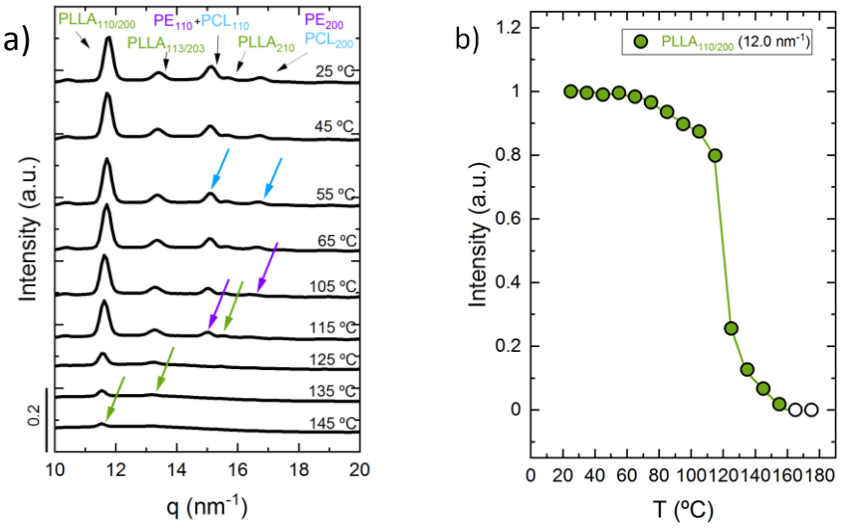

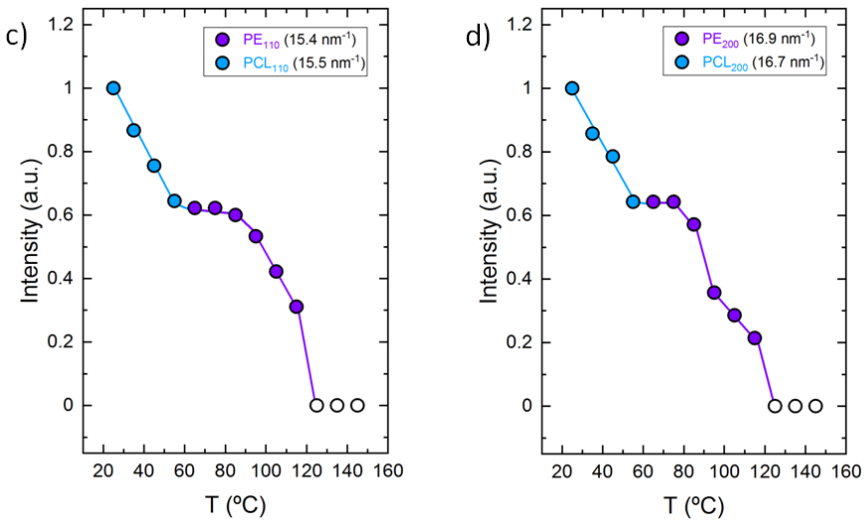

Figure 5.14. a) WAXS patterns taken during cooling from the melt at 1 °C/min for $PE_{21}^{7.1}$-*b*-$PCL_{12}^{4.2}$-*b*-$PLLA_{67}^{23.0}$ at different temperatures with arrows indicating crystallization of the PLLA block (green), the PE block (violet) and the PCL block (blue), with their (hkl) planes; Normalized WAXS intensities of b) $PLLA_{110/200}$ (12.0 nm^{-1}), c) PE_{110} (15.4 nm^{-1}) and PCL_{110} (15.5 nm^{-1}); d) PE_{200} (16.9 nm^{-1}) and PCL_{200} (16.7 nm^{-1})

WAXS measurements performed to the $PE_{21}^{7.1}$-*b*-$PCL_{12}^{4.2}$-*b*-$PLLA_{67}^{23.0}$ sample (Figure 5.14) demonstrate that the crystallization sequence depends on the cooling rate employed for this sample. The PE block is the first block to crystallize when a cooling rate of 20 °C/min is employed, whereas changing it to 1 °C/min the first crystallizing block is the PLLA. This change in the crystallization sequence is demonstrated by DSC and WAXS, as we were able to perform both experiments with identical cooling and heating rates and thus compare the results obtained by both techniques to understand the crystallization sequence.

The melt sequence remains unchanged, as it depends on the large differences in melting points of the three different blocks, unlike the crystallization sequence that depends on the relative non-isothermal crystallization rate of the different crystallisable blocks and PLLA in particular. The subsequent WAXS heating results are presented in Figures A.5.4 – A.5.7 in the Appendix.

5.4.3. Polarized Light Optical Microscopy (PLOM)

Polarized Light Optical Microscopy (PLOM) experiments have been performed in order to study the sequential crystallization and superstructural organization of the materials. One of the advantages of using PLOM is that we can perform experiments with the same thermal protocols already employed in the DSC and the *in situ* real-time SAXS/WAXS experiments. In this way, a complete study of the non-isothermal crystallization and morphology of the samples can be carried out using three different techniques, as we are able to directly compare the results obtained. This study was only possible in the $PE_{21}^{7.1}$-*b*-$PCL_{12}^{4.2}$-*b*-$PLLA_{67}^{23.0}$ triblock terpolymer case, as its morphology was easy to observe by PLOM due to the sizes of the superstructures formed. In the case of the other terpolymer sample ($PE_{21}^{2.6}$-*b*-$PEO_{32}^{4.0}$-*b*-$PLLA_{47}^{5.9}$) the nucleation density was too high and the birefringent structures impinged when their sizes were very small to detect their evolution with PLOM.

Figure 5.15 shows the cooling from the melt at 20 °C/min of the $PE_{21}^{7.1}$-*b*-$PCL_{12}^{4.2}$-*b*-$PLLA_{67}^{23.0}$ triblock terpolymer. When the material is in the melt, at 120 °C, at the scale of the micrographs there are no observable features. If the sample displays weak phase segregation in the melt (as indicated by SAXS in Figure 5.1), it contains microdomains smaller than 0.4 μm that cannot be observed by PLOM). A schematic temperature *versus* time plot in Figure 5.15 indicates the phases that crystallize upon cooling from the melt based on the information provided by DSC/WAXS. Also, we have indicated with a legend on top of each micrograph the crystalline phases that should be present according to the previous DSC/WAXS evidence.

The micrograph taken at 110 °C (a temperature at which only PE crystals should be present according to WAXS and DSC evidence) is the first one obtained during cooling where small birefringent spots are observed in the $PE_{21}^{7.1}$-*b*-$PCL_{12}^{4.2}$-*b*-$PLLA_{67}^{23.0}$ triblock terpolymer. In some cases, they are microscopic spherulites with Maltese cross patterns and retardation colors that identify them as

negative spherulites. These crystalline superstructures indicate that a "break-out" must have occurred, as the PE block content in this triblock terpolymer is only 21%. A larger number of spherulites appear at 100 °C, a temperature at which both PE and PLLA blocks can crystallize. Although the crystallinity value of PE is higher than that for PLLA (34 % vs. 22 %, see Table A.5.3), note that the percentage of the PLLA block in the triblock terpolymer is much higher than that of PE block (67 wt% vs. 21 wt%). Both PLLA and PE blocks continue crystallizing until approximately 40 °C, according to WAXS. The micrograph taken at 50 °C shows a large number of small double crystalline spherulites (with a wide size range) that cover the entire microscope view field. Note that as the blocks are covalently bonded together, at 50 °C, the double crystalline spherulites must contain PLLA and PE crystalline lamellae and interlamellar regions composed of amorphous PCL blocks plus the non-crystallized PLLA and PE chains.

Finally, the last block crystallizing is the PCL block, according to DSC/WAXS results shown in Figures 5.9 and 5.13 at approximately 42 °C. There is not a significant change from 50 °C to 30 °C since the percentage of the PCL block in the sample is only 12 wt%, although its crystallinity is 74% (see Table A.5.3). The PLOM image at 30 °C in Figure 5.15 shows the morphology of the triblock terpolymer with all its blocks crystallized. This represents tricrystalline spherulites, where the three types of lamellar crystals co-exist.

Figure 5.16 shows the subsequent heating of the sample after the quenching performed in Figure 5.15. At 30 °C the three blocks are crystallized, PE, PLLA and PCL. Heating up the sample to 60 °C, the PCL block remains in the molten state, but there is not a significant change, as previously said, because of its low percentage in the sample. At 100 °C still, the PE and PLLA blocks are crystallized, but heating the sample to 130 °C, the only block that remains crystallized is the PLLA block. At this temperature, the PE block has melted, and there is not a big change in morphology since the percentage of PE (21 wt %), and its crystallinity value (34%, Table A.5.3) is low to notice significant changes in the previously

formed PLLA spherulitic templates. Finally, at 170 °C all blocks of the sample remain in the molten state.

So, the low percentages of the PE and PCL blocks make it difficult to see morphological changes in the quenching and heating of the samples at 20 °C/min. In addition, both PE and PLLA blocks crystallize with some overlap in their temperature ranges (at least within 115 and 66 °C), it is hard to notice the crystallization of each block separately.

Figure 5.17 shows a series of PLOM micrographs obtained by slow cooling the sample from the melt at 1 °C/min (in correspondence with DSC, Figure 5.10, and WAXS results, Figure 5.14). As the schematic representation of temperature versus time shows, in this case, the sequence of crystallizing blocks is PLLA (at 145 °C), then PE (at 115 °C), and finally PCL (at 55 °C). Both PLLA and PE overlap their respective crystallization in the range 115 °C to 66 °C.

Cooling at a slower rate has the advantage for PLOM that the nucleation density is much smaller, hence larger spherulites are generated. The first nascent PLLA spherulite (or spherulitic template, as it consists of radially grown PLLA lamellae with interlamellar regions of amorphous PLLA, PE, and PCL chains within the $PE_{21}^{7.1}$-*b*-$PCL_{12}^{4.2}$-*b*-$PLLA_{67}^{23.0}$ triblock terpolymer) image was recorded at 128 °C, as shown in Figure 5.17. It grew radially into a fully developed negative spherulite that can be observed at 125 °C and 120 °C. The negative sign was determined by the retardation colors observed thanks to the insertion of a red tint plate at 45 °C in between the crossed polarizers. The first and third quadrant in the spherulite shows a yellow color, while the second and fourth quadrants exhibit a blue color. This indicates that even in this complex triblock terpolymer the PLLA block (67% by weight of the sample) can form spherulites that have radially growing lamellae with their chain axis tangential to the spherulite, thus determining the negative sign of the birefringence[148]. The spherulite formation fixes the morphological template inside which the other two covalently bonded

blocks will be forced to crystallize (within the interlamellar and interfibrillar regions of the spherulite).

Figure 5.14 demonstrated that the PE block crystallizes in an approximate temperature range of 115 °C-75°C. The PLOM micrograph at 110 °C in Figure 5.17 shows the morphological texture of the double crystallized material. The original PLLA spherulite appears to have stopped growing with identical texture when the PE block started to crystallize. Nevertheless, radial birefringent spikes can still be observed as a kind of extension of the original spherulite, which is probably nucleating the further radial growth of both PLLA and PE lamellae at temperatures between 115 and 110 °C. The retardation colors, although not as clear as in the large bright spherulite, are also extended and are mostly yellow along the lines extending away from the first quadrant and mostly blue along those extending away from the fourth quadrant. The morphology seems completely fixed once both PLLA and PE blocks have crystallized to a large extent at 110 °C and are kept almost invariant at 100 °C and 70 °C. As the field of the micrograph was slightly changed at 70 °C, the diffuse extension of the Maltese cross to the outer regions of the main central spherulite can be clearly appreciated.

At 70 °C, both the PLLA and PE blocks have finished crystallizing. Further cooling of the sample to room temperature causes the crystallization of the PCL block. The change in birefringence is very slight (but can be noticed upon close inspection of the micrograph taken at 30 °C and comparing it with that at 70 °C) due to the low percentage of PCL in the sample (12 wt %). The PCL intraspherulitic crystallization occurs within the interlamellar regions. At 30 °C the material has a tricrystalline spherulitic superstructure, which has been evidenced by DSC and WAXS in this work (see Figures 5.10 and 5.14).

Figure 5.18 shows the subsequent heating of the $PE_{21}^{7.1}$-*b*-$PCL_{12}^{4.2}$-*b*-$PLLA_{67}^{23.0}$ tricrystalline triblock terpolymer sample after the cooling shown in Figure 5.17. At 30 °C all components are crystallized. Heating the sample up to 70 °C melts the PCL block crystals with slight concomitant changes in birefringence.

Increasing the temperature to 140 °C causes the melting of the PE block crystals. It should be noted that qualitatively the morphology remains the same before and after the melting of the PE block crystals. The PLLA texture left at 140 °C constitutes the template inside which the other two blocks crystallized during the slow cooling applied. It is necessary to further increase the temperature to 170 °C to also melt the PLLA crystals.

Figures 5.15 and 5.17 illustrate how the morphology of this complex $PE_{21}^{7.1}$-*b*-$PCL_{12}^{4.2}$-*b*-$PLLA_{67}^{23.0}$ tricrystalline triblock terpolymer strongly depends on cooling rate. The order of the sequential crystallization of the blocks changes when the cooling rate is slowed down, and the final morphology of the tricrystalline superstructural texture radically differs from one another. Such larger differences in morphology could impact the mechanical properties of the materials, an aspect that needs further investigation. Therefore, the properties of these complex triblock copolymers can be tuned by controlling the cooling rate and composition.

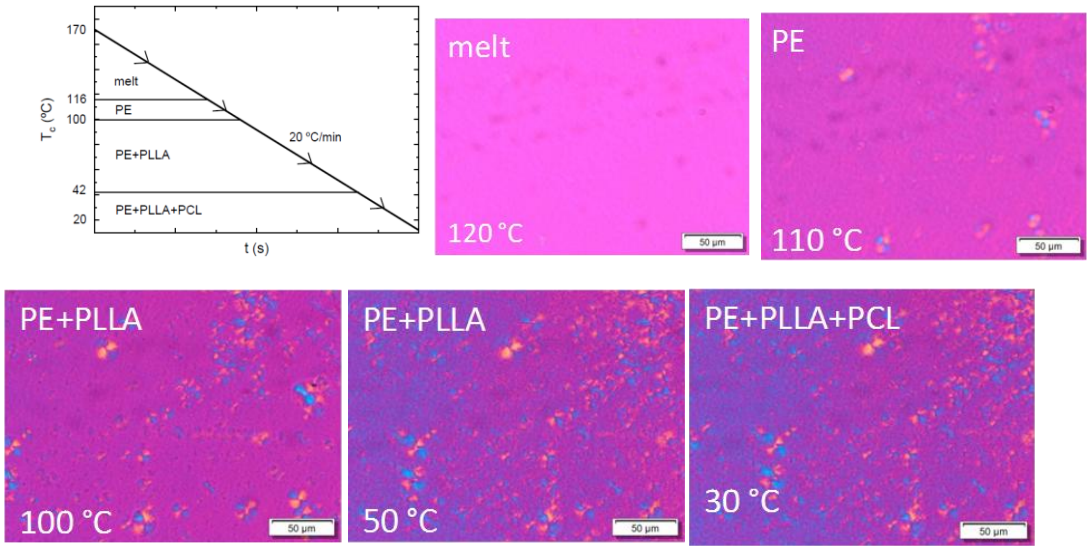

Figure 5.15. PLOM scheme and micrographs taken at 50 µm of cooling from the melt at 20 °C/min for $PE_{21}^{7.1}$-*b*-$PCL_{12}^{4.2}$-*b*-$PLLA_{67}^{23.0}$

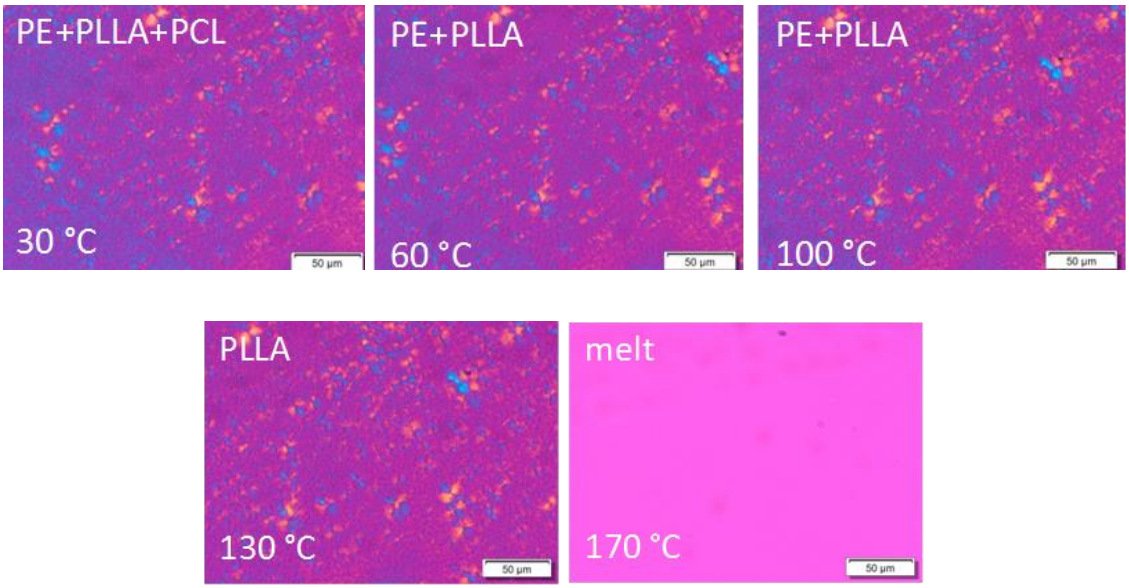

Figure 5.16. PLOM micrographs taken at 50 µm of the subsequent heating of Figure 5.15 at 20 °C/min for $PE_{21}^{7.1}$-*b*-$PCL_{12}^{4.2}$-*b*-$PLLA_{67}^{23.0}$

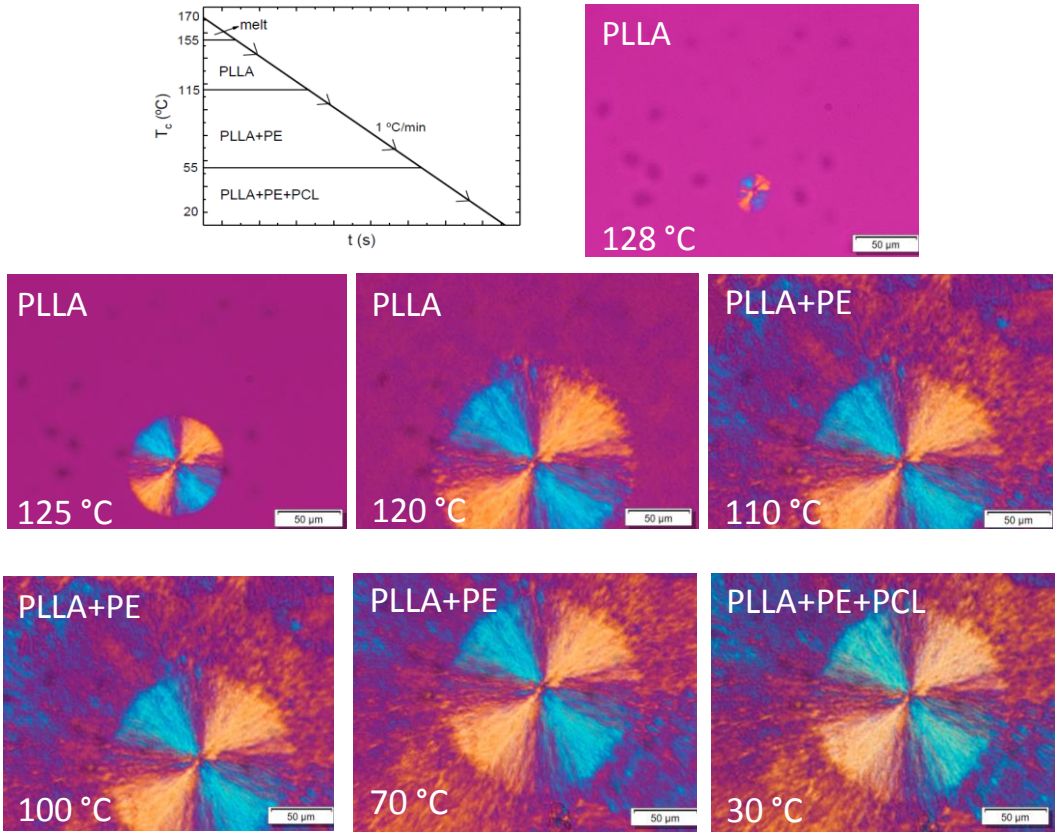

Figure 5.17. PLOM micrographs taken at 50 µm of cooling from the melt at 1 °C/min for $PE_{21}^{7.1}$-*b*-$PCL_{12}^{4.2}$-*b*-$PLLA_{67}^{23.0}$

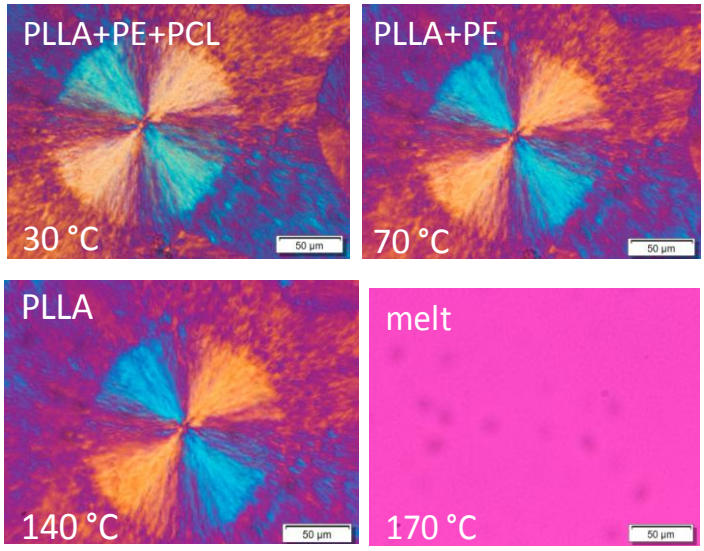

Figure 5.18. PLOM micrographs taken at 50 µm of the subsequent heating of Figure 5.17 at 1 °C/min for $PE_{21}^{7.1}$-*b*-$PCL_{12}^{4.2}$-*b*-$PLLA_{67}^{23.0}$

5.5. Conclusions

The complex crystallization behavior of the materials employed here is due to the ability of each of the blocks of the diblock and triblock co(ter)polymers to crystallize. The analysis of the crystallization is more challenging as the number of potentially crystallizable blocks increases, especially if there are temperature ranges where the crystallization of more than one block occurs spontaneously. All copolymer precursors and triblock terpolymers studied here are weakly segregated, as "break out" takes place when the crystallization of the first block occurs upon cooling from the melt.

The crystallization sequence of the materials depends on the cooling rate and triblock terpolymer composition. In the case of the $PE_{21}^{2.6}$-*b*-$PEO_{32}^{4.0}$-*b*-$PLLA_{47}^{5.9}$ triblock terpolymer, the practically perfect linear PE block can always start the crystallization process upon cooling from the melt (in the range of 20-1 ºC/min) closely followed by the PLLA block and finally by the PEO block. On the other hand, the melting sequence is that expected based on the melting points of the three blocks dictated by their chemical structure (and lamellar thicknesses): PEO first, PE second, and PLLA third.

In the case of the $PE_{21}^{7.1}$-*b*-$PCL_{12}^{4.2}$-*b*-$PLLA_{67}^{23.0}$ triblock terpolymer, the crystallization order can be tuned by cooling rate. Hence, at 20 ºC/min the crystallization starts with the PE block, but at 1 ºC/min, the PLLA block is the first to crystallize. This also has a tremendous impact on the triple crystalline superstructures generated in the material. PLOM demonstrated the sequential crystallization and melting of this triblock and the remarkable changes that the cooling rate has on its morphology. Therefore, the crystallization sequence could play a key role in the possible applications of these fascinating materials.

5.6. References

1. Hamley, I., *Crystallization in Block Copolymers*. Advances in Polymer Science: **1999**; Vol. 148.

2. Abetz, V.; Simon, P. F. W., Phase behaviour and morphologies of block copolymers. *Advances in Polymer Science* **2005,** *189*, 125-212.

3. Müller, A. J.; Balsamo, V.; Arnal, M. L., Nucleation and crystallization in diblock and triblock copolymers. In *Block Copolymers II*, Abetz, V., Ed. Springer, Berlin, Heidelberg: Advances in Polymer Science, **2005**; Vol. 190, pp 1-63.

4. Müller, A. J.; Arnal, M. L.; Balsamo, V., Crystallization in block copolymers with more than one crystallizable block. In *Progress in Understanding of Polymer Crystallization*, Reiter, G.; Strobl, G. R., Eds. Lecture Notes in Physics: Springer, Berlin, Heidelberg, **2007**; Vol. 714, pp 229-259.

5. Michell, R. M.; Müller, A. J., Confined crystallization of polymeric materials. *Progress in Polymer Science* **2016,** *54-55*, 183-216.

6. Nakagawa, S.; Marubayashi, H.; Nojima, S., Crystallization of polymer chains confined in nanodomains. *European Polymer Journal* **2015,** *70*, 262-275.

7. Castillo, R. V.; Müller, A. J., Crystallization and morphology of biodegradable or biostable single and double crystalline block copolymers. *Progress in Polymer Science* **2009,** *34*, 516-560.

8. Li, S.; Register, A., Crystallization in Copolymers. In *Handbook of Polymer Crystallization*, Piorkowska, E.; Rutledge, G. C., Eds. John Wiley and Sons: Hoboken, NJ, **2013**; p 327.

9. Huang, S.; Jiang, S., Structures and morphologies of biocompatible and biodegradable block copolymers. *RSC Advances* **2014,** *4*, 24566-24583.

10. Hamley, I. W., *The Physics of Block Copolymers*. Oxford Universit Press: Oxford, **1998**.

11. Arif P., M.; Kalarikkal, N.; Thomas, S., Introduction on crystallization in multiphase polymer systems. In *Crystallization in Multiphase Polymer Systems*, Thomas, S.; Arif P., M.; Gowd, E. B.; K., K., Eds. Elsevier: **2018**; pp 1-13.

12. Hadjichristidis, N.; Pitsikalis, M.; Iatrou, H., Synthesis of block copolymers. *Advances in Polymer Science* **2005,** *189*, 1-124.

13. Barthel, M. J.; Schacher, F. H.; Schubert, U. S., Poly(ethylene oxide)(PEO)-based ABC triblock terpolymers - synthetic complexity vs. application benefits. *Polymer Chemistry* **2014,** *5*, 2647.

14. Guo, X.; Wang, L.; Wei, X.; Zhou, S., Polymer-based drug delivery systems for cancer treatment. *Journal of Polymer Science, Part A: Polymer Chemistry* **2016,** *54*, 3525-3530.

15. Van Horn, R. M.; Steffen, M. R.; O'connor, D., Recent progress in block copolymer crystallization. *Polymer Crystallization* **2018,** *1*, e10039.

16. Palacios, J. P.; Mugica, A.; Zubitur, M.; Müller, A. J., Crystallization and morphology of block copolymers and terpolymers with more than one crystallizable block. In *Crystallization in Multiphase Polymer Systems*, Thomas, S.; Arif P., M.; Gowd, E. B.; Kalarikkal, N., Eds. Elsevier: **2018**; pp 123-171.

17. Palacios, J. K.; Zhang, H.; Zhang, B.; Hadjichristidis, N.; Müller, A. J., Direct identification of three crystalline phases in PEO-*b*-PCL-*b*-PLLA tribock terpolymer by in situ hot-stage atomic force microscopy. *Polymer* **2020,** *205*, 122863.

18. Müller, A. J.; Arnal, M. L.; Lorenzo, A. T., Crystallization in nano-confined polymeric systems. In *Handbook of Polymer Crystallization*, Piorkowska, E.; Rutledge, G. C., Eds. John Wiley and Sons: Hoboken, New Jersey (USA), **2013**; pp 347-372.

19. Yu, C.; Xie, Q.; Bao, Y.; Shan, G.; Pan, P., Crystalline and spherulitic morphology of polymers crystallized in confined systems. *Crystals* **2017,** *7* (147), 1-20.

20. He, W. N.; Xu, J. T., Crystallization assisted self-assembly of semicrystalline block copolymers. *Progress in Polymer Science* **2012,** *37*, 1350-1400.

21. Takeshita, H.; Shiomi, T.; Takenaka, K.; Arai, F., Crystallization and higher-order structure of multicomponent polymeric systems. *Polymer* **2013,** *54*, 4776-4789.

22. Back, D. M.; Schmitt, R. L., Ethylene Oxide Polymers. In *Encyclopedia of Polymer Science and Technology*, John Wiley & Sons, Inc.: **2002**.

23. Richards, D. H.; Szwarc, M., Block polymers of ethylene oxide and its analogues with styrene. *Transactions of the Faraday Society* **1959,** *55*, 1644-1650.

24. Woodruff, M. A.; Hutmacher, D. W., The return of a forgotten polymer - Polycaprolactone in the 21st century. *Progress in Polymer Science* **2010,** *35*, 1217-1256.

25. Perrin, D. E.; English, J. P., Polycaprolactone. In *Handbook of Biodegradable Polymers*, Domb, A. J.; Kost, J.; Wiseman, D. M., Eds. CRC Press: USA, **1997**.

26. Nair, L. S.; Laurencin, C. T., Biodegradable polymers as biomaterials. *Progress in Polymer Science* **2007,** *32*, 762-798.

27. Sisson, A. L.; Ekinci, D.; Lendlein, A., The contemporary role of ε-caprolactone chemistry to create advanced polymer architetures. *Polymer* **2013,** *54*, 4333-4350.

28. Fiori, S., Industrial uses of PLA. In *Poly(lactid acid) Science and Technology: Processing, Properties, Additives and Applications*, Jimenez, A.; Peltzer, M.; Ruseckaite, R., Eds. Cambridge: The Royal Society of Chemistry, **2015**; Vol. 12, pp 317-333.

29. Müller, A. J.; Avila, M.; Saenz, G.; Salazar, J., Crystallization of PLA-based materials. In *Poly(lactid acid) Science and Technology: Processing, Properties, Additives and Applications*, Jimenez, A.; Peltzer, M.; Ruseckaite, R., Eds. Cambridge: The Royal Society Chemistry, **2015**; Vol. 12, pp 66-98.

30. Auras, R.; Lim, L. T.; Selke, S. E. M.; Tsuji, H., *Poly(lactid acid). Synthesis, Structures, Properties, Processing, and Applications*. John Wiley & Sons: Hoboken, NJ, USA, **2010**.

31. Castillo, R. V.; Müller, A. J.; Lin, M. C.; Chen, H. L.; Jeng, U. S.; Hillmyer, M. A., Confined crystallization and morphology of melt segregated PLLA-*b*-PE and PLDA-*b*-PE diblock copolymers. *Macromolecules* **2012,** *45*, 4254-4261.

32. Müller, A. J.; Castillo, R. V.; Hillmyer, M., Nucleation and crystallization of PLDA-*b*-PE and PLLA-*b*-PE diblock copolymers. *Macromolecular Symposia* **2006,** *242*, 174-181.

33. Müller, A. J.; Lorenzo, A. T.; Castillo, R. V.; Arnal, M. L.; Boschetti-de-Fierro, A.; Abetz, V., Crystallization kinetics of homogeneous and melt segregated PE containing diblock copolymers. *Macromolecular Symposia* **2006,** *245-246*, 154-160.

34. Lin, M. C.; Wang, Y. C.; Chen, J. H.; Chen, H. L.; Müller, A. J.; Su, C. J.; Jeng, U. S., Orthogonal crystal orientation in double-crystalline block copolymer. *Macromolecules* **2011,** *44*, 6875-6884.

35. Bao, J.; Dong, X.; Chen, S.; Lu, W.; Zhang, X.; Chen, W., Confined crystallization, melting behavior and morphology in PEG-*b*-PLA diblock copolymers: amorphous versus crystalline PLA. *Journal of Polymer Science* **2020**, 1-11.

36. Bao, J.; Dong, X.; Chen, S.; Lu, W.; Zhang, X.; Chen, W., Fractionated crystallization and fractionated melting behaviors of poly(ethylene glycol) induced by poly(lactide) stereocomplex in their block copolymers and blends. *Polymer* **2020,** *190*, 122189.

37. Ring, J. O.; Thomann, R.; Mülhaupt, R.; Raquez, J.-M.; Degée, P.; Dubois, P., Controled synthesis and characterization of Poly[ethylene-*block*-(L,L-lactide)]s by combining catalytic ethylene oligomerization with "Coordination-insertion" ring-opening polymerization. *Macromolecular Chemistry and Physics* **2007,** *208*, 896-902.

38. Sun, L.; Liu, Y.; Zhu, L.; Hsiao, B. S.; Avila-Orta, C. A., Pathway-dependent melting in a low-molecular weight polyethylene-*block*-poly(ethylene oxide) diblock copolymer. *Macromolecular Rapid Communications* **2004,** *25*, 853-857.

39. Boschetti-de-Fierro, A.; Müller, A. J.; Abetz, V., Synthesis and characterization of novel linear PB-*b*-PS-*b*-PEO and PE-*b*-PS-*b*-PEO triblock terpolymers. *Macromolecules* **2007,** *40*, 1290-1298.

40. Boschetti-De-Fierro, A.; Fierro, D.; Albuerne, J.; Funari, S. S.; Abetz, V., Thermal monitoring of morphology in triblock terpolymers with crystallizable blocks. *Journal of Polymer Science B: Polymer Physics* **2007,** *45*, 3197-3206.

41. Boschetti-de-Fierro, A.; Lorenzo, A. T.; Müller, A. J.; Schmalz, H.; Abetz, V., Crystallization kinetics of PEO and PE in different terpolymers: effect of microdomain geometry and confinement. *Macromolecular Chemistry and Physics* **2008,** *209*, 476-487.

42. Castillo, R. V.; Arnal, M. L.; Müller, A. J.; Hamley, I. W.; Castelleto, V.; Schmalz, H.; Abetz, V., Fractionated crystallization and fractionated melting of confined PEO microdomains in PB-*b*-PEO and PE-*b*-PEO diblock copolymers. *Macromolecules* **2008,** *41*, 879-889.

43. Weiyu, C.; Tashiro, K.; Hanesaka, M.; Takeda, S.; Masunaga, H.; Sasaki, S.; Takata, M., Relationship between morphological change and crystalline phase transitions of polyethylene-poly(ethylene oxide) diblock copolymers, revealed by the temperature-dependent synchrotron WAXD/SAXS and infrared/Raman spectral measurements. *Journal of Physical Chemistry B* **2009,** *113*, 2338-2346.

44. Sun, L.; Liu, Y.; Zhu, L.; Hsiao, B. S.; Avila-Orta, C. A., Self-assembly and crystallization behavior of a double-crystalline polyethylene-*block*-poly(ethylene oxide) diblock copolymer. *Polymer* **2004,** *45*, 8181-8193.

45. Nojima, S.; Akutsu, Y.; Washino, A.; Tanimoto, S., Morphology of melt-quenched poly (ε-caprolactone)-*block*-polyethylene copolymers. *Polymer* **2004,** *45*, 7317-7324.

46. Nojima, S.; Ito, K.; Ikeda, H., Composition dependence of crystallized lamellar morphology formed in crystalline-crystalline diblock copolymers. *Polymer* **2007,** *48*, 3607-3611.

47. Sakurai, T.; Ohguma, Y.; Nojima, S., Morphological evolution during isothermal crystallization observed in a crystalline-crystalline diblock copolymer. *Polymer Journal* **2008,** *40*, 971-978.

48. Sakurai, T.; Nagakura, H.; Gondo, S.; Nojima, S., Crystallization of poly(ε-caprolactone) blocks confined in crystallized lamellar morphology of poly(ε-caprolactone)-*block*-polyethylene copolymers:effects of polyethylene crystallinity and confinement size. *Polymer Journal* **2013,** *45*, 436-443.

49. Sakurai, T.; Nojima, S., Significant increase in melting temperature of poly(ε-caprolactone) blocks confined in crystallized lamellar morphology of poly(ε-caprolactone)-*block*-polyethylene copolymers. *Polymer Journal* **2011,** *43*, 370-377.

50. Nojima, S.; Akutsu, Y.; Akaba, M.; Tanimoto, S., Crystallization behavior of poly(ε-caprolactone) blocks starting from polyethylene lamellar morphology in poly (ε-caprolactone)-*block*-poly (ethylene) copolymers. *Polymer* **2005,** *46*, 4060-4067.

51. Müller, A. J.; Albuerne, J.; Marquez, L.; Raquez, J. M.; Degée, P.; Dubois, P.; Hobbs, J.; Hamley, I. W., Self-nucleation and crystallization kinetics of double crystalline poly(p-dioxanone)-*b*-poly(ε-caprolactone) diblock copolymers. *Faraday Discuss* **2005,** *128*, 231-252.

52. Müller, A. J.; Albuerne, J.; Esteves, L. M.; Marquez, L.; Raquez, J.-M.; Degée, P.; Dubois, P.; Collins, S.; Hamley, I. W., Confinement effects on the crystallization

kinetics and self-nucleation of double crystalline poly(p-dioxanone)-*b*-poly(ε-caprolactone) diblock copolymers. *Macromolecular Symposia* **2004,** *215*, 369-382.

53. Albuerne, J.; Máquez, L.; Müller, A. J.; Raquez, J. M.; Degée, P.; Dubois, P.; Castelleto, V.; Hamley, I. W., Nucleation and crystallization in double crystalline poly(p-dioxanone)-*b*-poly(ε-caprolactone) diblock copolymers. *Macromolecules* **2003,** *36*, 1633-1644.

54. Hamley, I. W.; Parras, P.; Castelletto, V.; Castillo, R. V.; Müller, A. J.; Pollet, E.; Dubois, P.; Martin, C. M., Melt structure and its transformation by sequential crystallization of the two blocks within poly(L-lactide)-*block*- poly(ε-caprolactone) double crystalline diblock copolymers. *Macromolecular Chemistry and Physics* **2006,** *207*, 941-953.

55. Castillo, R. V.; Müller, A. J.; Raquez, J. M.; Dubois, P., Crystallization kinetics and morphology of biodegradable double crystalline PLLA-*b*-PCL diblock copolymers. *Macromolecules* **2010,** *43*, 4149-4160.

56. Laredo, E.; Prutsky, N.; Bello, A.; Grimau, M.; Castillo, R. V.; Müller, A. J.; Dubois, P., Miscibility in poly(L-lactide)-*b*-poly(ε-caprolactone) double crystalline diblock copolymers. *European Physical Journal E* **2007,** *23*, 295-303.

57. Hamley, I. W.; Castelletto, V.; Castillo, R. W.; Müller, A. J.; Martin, C. M.; Pollet, E.; Dubois, P., Crystallization in poly(L-lactide)-*b*-poly(ε-caprolactone) double crystalline diblock copolymers: a study using X-ray scattering, differential scanning calorimetry and polarized optical microscopy. *Macromolecules* **2005,** *38*, 463-472.

58. Myers, S. B.; Register, R. A., Crystalline-crystalline diblock copolymers of linear polyethylene and hydrogenated polynorbornene. *Macromolecules* **2008,** *41*, 6773-6779.

59. Ponjavic, M.; Nikolic, M. S.; Jevtic, S.; Roga, J.; Stevanovic, S.; Djonlagic, J., Influence of a low content of PEO segment on the thermal, surface and morphological properties of triblock and diblock PCL copolymers. *Macromolecular Research* **2016,** *24*, 323-335.

60. Li, L.; Meng, F.; Zhong, Z.; Byelov, D.; De Jeu, W. H.; Feijen, J., Morphology of a highly asymmetric double crystallizable poly(ε-caprolactone-*b*-ethylene oxide) block copolymer. *The Journal of Chemical Physics* **2007,** *126*, 024904.

61. Van Horn, R. M.; Zheng, J. X.; Sun, H. J.; Hsiao, M. S.; Zhang, W. B.; Dong, X. H.; Xu, J.; Thomas, E. L.; Lotz, B.; Chen, S. Z. D., Solution crystallization behavior of crystalline-crystalline diblock copolymers of poly(ethylene oxide)-*block*-poly(ε-caprolactone). *Maromolecules* **2010,** *43*, 6113-6119.

62. Vivas, M.; Contreras, J.; López-Carrasquero, F.; Lorenzo, A. T.; Arnal, M. L.; Balsamo, V.; Müller, A. J.; Laredo, E.; Schmalz, H.; Abetz, V., Synthesis and characterization of triblock terpolymers with three potentially crystallisable blocks: polyethylene-*b*-poly(ethylene oxide)-*b*-poly(ε-caprolactone). *Macrolecular Symposia* **2006,** *239*, 58-67.

63. Jiang, S.; He, C.; An, L.; Chen, X.; Jiang, B., Crystallization and ring-banded spherulite morphology of poly(ethylene oxide)-*block*-poly(ε-caprolactone) diblock copolymer. *Macromolecular Chemistry and Physics* **2004,** *205*, 2229-2234.

64. Arnal, M. L.; López-Carrasquero, F.; Laredo, E.; Müller, A. J., Coincident or sequential crystallization of PCL and PEO blocks within polystyrene-*b*-poly(ethylene oxide)-*b*-poly(ε-caprolactone) linear triblock copolymers. *European Polymer Journal* **2004,** *40*, 1461-1476.

65. Nojima, S.; Ono, M.; Ashida, T., Crystallization of block copolymers II. Morphological study of poly (ethylene glycol)-poly (ε-caprolactone) block copolymers. *Polymer Journal* **1992,** *24*, 1271-1280.

66. Wei, Z.; Liu, L.; Yu, F.; Wang, P.; Qi, M., Synthesis and characterization of poly(ε-caprolactone)-*b*-poly(ethylene glycol)-*b*-poly(ε-caprolactone) triblock copolymers with dibutylmagnesium as catalyst. *Journal of applied polymer science* **2009,** *111*, 429-436.

67. Arnal, M. L.; Balsamo, V.; López-Carrasquero, F.; Contreras, J.; Carrillo, M.; Schmalz, H.; Abetz, V.; Laredo, E.; Müller, A. J., Synthesis and characterization of polystyrene-*b*-poly(ethylene oxide)-*b*-poly(ε-caprolactone) block copolymers. *Macromolecules* **2001,** *34*, 7973-7982.

68. Li, Y.; Zhou, J.; Zhang, J.; Gou, Q.; Gu, Q.; Wang, Z., Morphology of poly(ethylene oxide)-*b*-poly(ε-caprolactone) spherulites formed under compressed CO_2. *Journal of Macromolecular Science, Part B: Physics* **2014,** *53* (6), 1137-1144.

69. Li, Y.; Huang, H.; Wang, Z.; He, T., Tuning radial lamellar packing and orientation into diverse ring-banded spherulites: effects of structural feature and crystallization condition. *Macromolecules* **2014,** *47*, 1783-1792.

70. Xue, F.-F.; Chen, X.-S.; An, L.-J.; Funari, S. S.; Jiang, S.-C., Confined lamella formation in crystalline-crystalline poly(ethylene-oxide)-*b*-poly(ε-caprolactone) diblock copolymers. *Chinese Journal of Polymer Science* **2013,** *31* (9), 1260-1270.

71. Xue, F.; Chen, X.; An, L.; Funari, S. S.; Jiang, S., Soft nanoconfinement effects on the crystallization behaviour of asymmetric poly(thylene oxide)-*block*-poly(ε-caprolactone) diblock copolymers. *Polymer International* **2012,** *61*, 909-917.

72. Sun, J.; He, C.; Zhuang, X.; Jing, X.; Chen, X., The crystallization behavior of poly(ethylene glycol)-poly(ε-caprolactone) diblock copolymers with asymmetric block compositions. *Journal of Polymer Research* **2011,** *18*, 2161-2168.

73. Hua, C.; Dong, C.-M., Synthesis, characterization, effect of architecture on crystallization of biodegradable poly(ε-caprolactone)-*b*-poly(ethylen oxide) copolymers with different arms and nanoparticles thereof. *Journal of Biomedical Materials Research, Part A* **2007,** *82*, 689-700.

74. He, C.; Sun, J.; Zhao, T.; Hong, Z.; Zhuang, X.; Chen, X.; Jin, X., Formation of a unique crystal morphology for the poly(ethylene glycol)-poly(ε-caprolactone) diblock copolymer. *Biomacromolecules* **2006,** *7*, 252-258.

75. Piao, L.; Dai, Z.; Deng, M.; Chen, X.; Jing, X., Synthesis and characterization of PCL/PEG/PCL triblock copolymers by using calcium catalyst. *Polymer* **2003,** *44*, 2025-2031.

76. He, C.; Sun, J.; Deng, C.; Zhao, T.; Deng, M.; Chen, X.; Jing, X., Study of the synthesis, crystallization, and morphology of poly(ethylene glycol)-poly(ε-caprolactone) diblock copolymers. *Biomacromolecules* **2004,** *5*, 2040-2047.

77. Arnal, M. L.; Boissé, S.; Müller, A. J.; Meyer, F.; Raquez, J. M.; Dubois, P.; Prud`homme, R. E., Interplay between poly(ethylene oxide) and poly(L-lactide) blocks during diblock copolymer crystallization. *CrystEngComm* **2016,** *18*, 3635-3649.

78. Zhou, D.; Sun, J.; Shao, J.; Bian, X.; Huang, S.; Li, G.; Chen, X., Unusual crystallization and melting behaviour induced by microphase separation in MPEG-*b*-PLLA diblock copolymer. *Polymer* **2015,** *80*, 123-129.

79. Yang, J.; Liang, Y.; Han, C. C., Effect of crystallization temperature on the interactive crystallization behavior of poly(L-lactide)-*block*-poly (ethylene glycol) copolymer. *Polymer* **2015,** *79*, 56-64.

80. Huang, S.; Li, H.; Jiang, S.; Chen, X.; An, L., Morphologies and structures in poly(L-lactide-*b*-ethylene oxide) copolymers determined by crystallization, microphase separation and vitrification. *Polymer Bulletin* **2011,** *67*, 885-902.

81. Huang, L.; Kiyofuji, G.; Matsumoto, J.; Fukagawa, Y.; Gong, C.; Nojima, S., Isothermal crystallization of poly (b-propiolactone) blocks starting from lamellar microdomain structures of double crystalline poly (b-propiolactone)-*block*-polyethylene copolymers. *Polymer* **2012,** *53*, 5856-5863.

82. Sun, J.; Hong, Z.; Yang, L.; Tang, Z.; Chen, X.; Jing, X., Study on crystalline morphology of poly(L-lactide)-poly(ethylene glycol) diblock copolymer. *Polymer* **2004,** *45*, 5969-5977.

83. Shin, D.; Shin, K.; Aamer, K. A.; Tew, G. N.; Russell, T. P.; Lee, J. H.; Jho, J. Y., A morphological study of a semicrystalline poly(L-lactic acid-*b*-ethylene oxide-*b*-L-lactic acid) triblock copolymer. *Macromolecules 38*, 104-109.

84. Xue, F.; Chen, X.; An, L.; Funari, S. S.; Jiang, S., Crystallization induced layer-to-layer transitions in symmetric PEO-*b*-PLLA block copolymer with synchrotron simultaneous SAXS/WAXS investigations. *RSC Advances* **2014,** *4*, 56346-56354.

85. Huang, S.; Jiang, S.; An, L.; Chen, X., Crystallization and morphology of poly(ethylene oxide-*b*-lactide) crystalline-crystalline diblock copolymers. *Journal of Polymer Science, Part B: Polymer Physics* **2008,** *46*, 1400-1411.

86. Yang, J.; Zhao, T.; Zhou, Y.; Liu, L.; Li, G.; Zhou, E.; Chen, X., Single crystals of the poly(L-lactide) block and the poly(ethylene glycol) block in poly(L-lactide)-poly(ethylene glycol) diblock copolymer. *Macromolecules* **2007,** *40*, 2791-2797.

87. Cai, C.; Wang, L. U.; Donc, C. M., Synthesis, characterization, effect of architecture on crystallization, and spherulitic growth ofpoly(L-lactide)-*b*-poly(ethylene

oxide) copolymers with different branch arms. *Journal of Polymer Science, Part A: Polymer Chemistry* **2006,** *44*, 2034-2044.

88. Yang, J.; Zhao, T.; Cui, J.; Liu, L.; Zhou, Y.; Li, G.; Zhou, E.; Chen, X., Nonisothermal crystallization behavior of the poly(ethylene glycol) block in poly(L-lactide)-poly(ethylene glycol) diblock copolymers: effect of the poly(L-lactide) block length. *Journal of Polymer Science, Part B: Polymer Physics* **2006,** *44*.

89. Huang, C. I.; Tsai, S. H.; Chen, C. M., Isothermal crystallization behaviour of poly(L-lactide) in poly(L-lactide)-*block*-poly(ethylene glycol) diblock copolymers. *Journal of Polymer Science: Part B: Polymer Physics* **2006,** *44*, 2438-2448.

90. Kim, K. S.; Chung, S.; Chin, I. J.; Kim, M. N.; Yoon, J. S., Crystallization behavior of biodegradable amphiphilic poly(ethylene glycol)-poly(L-lactide) block copolymers. *Journal of Applied Polymer Science* **1999,** *72*, 341-348.

91. Wang, J. L.; Dong, C. M., Synthesis, sequential crystallization and morphological evolution of well-defined star-shaped poly(ε-caprolactone)-*b*-poly(L-lactide) block copolymer. *Macromolecular Chemistry and Physics* **2006,** *207*, 554-562.

92. Liénard, R.; Zaldua, N.; Josse, T.; Winter, J. D.; Zubitur, M.; Mugica, A.; Iturrospe, A.; Arbe, A.; Coulembier, O.; Müller, A. J., Synthesis and characterization of double crystalline cyclic diblock copolymers of poly(ε-caprolactone) and poly(L(D)-lactide) (c(PCL-*b*-PL(D)LA)). *Macromolecular Rapid Communications* **2016,** *37*, 1676-1681.

93. Navarro-Baena, I.; Marcos-Fernández, A.; Fernández-Torres, A.; Kenny, J. M.; Peponi, L., Synthesis of PLLA-*b*-PCL-*b*-PLLA linear tri-block copolymers and their corresponding poly(ester-urethane)s: Effect of the molecular weight on their crystallization and mechanical properties. *RSC Advances* **2014,** *4*, 8510-8524.

94. Peponi, L.; Navarro-Baena, I.; Báez, J. E.; Kenny, J. M.; Marcos-Fernández, A., Effect of the molecular weight on the crystallinity of PCL-*b*-PLLA di-block copolymers. *Polymer* **2012,** *53*, 4561-4568.

95. Ho, R.-M.; Hsieh, P.-Y.; Tseng, W.-H.; Lin, C.-C.; Huang, B.-H.; Lotz, B., Crystallization-induced orientation for microstructures of Poly(L-lactide)-*b*-poly(ε-caprolactone) diblock copolymers. *Macromolecules* **2003,** *36*, 9085-9092.

96. Kim, J. K.; Park, D.-J.; Lee, M.-S.; Ihn, K. J., Synthesis and crystallization behavior of poly(L-lactide)-*block*-poly(ε-caprolactone) copolymer. *Polymer* **2001,** *42*, 7429-7441.

97. Yan, D.; Huang, H.; He, T.; Zhang, F., Coupling of microphase separation and dewetting in weakly segregated di-block copolymer ultrathin films. *Langmuir* **2011,** *27*, 11973-11980.

98. Casas, M. T.; Puiggalí, J.; Raquez, J. M.; Dubois, P.; Córdova, M. E.; Müller, A. J., Single crystals morphology of biodegradable double crystalline PLLA-*b*-PCL diblock copolymers. *Polymer* **2011,** *52*, 5166-5177.

99. Jeon, O.; Lee, S. H.; Kim, S. H.; Lee, Y. M.; Kim, Y. H., Synthesis and characterization of poly(L-lactide)-poly(ε-caprolactone) multiblock copolymers. *Macromolecules* **2003,** *36*, 5585-5592.

100. Danafar, H., Applications of copolymeric nanoparticles in drug delivery systems. *Drug Research* **2016,** *66* (10), 506-519.

101. Ostacolo, L.; Marra, M.; Ungaro, F.; Zappavigna, S.; Maglio, G.; Quaglia, F.; Abbruzzese, A.; Caraglia, M., *In vitro* anticancer activity of docetaxel-loaded micelles based on poly(ethylene oxide)-poly(ε-caprolacone) block copolymers: Do nanocarrier properties have a role? *Journal of Controlled Release* **2010,** *148*, 255-263.

102. Zhou, S.; Deng, X.; Yang, H., Biodegradable poly(ε-caprolactone)-poly(ethylene glycol) block copolymers: characterization and their use as drug carriers for a controlled delivery system. *Biomaterials* **2003,** *24*, 3563-3570.

103. Lim, D. W.; Park, T. G., Stereocomplex formation between enantiomeric PLA-PEG-PLA triblock copolymers: characterization and use as protein delivery microparticulate carriers. *Journal of Applied Polymer Science* **2000,** *75*, 1615-1623.

104. Michell, R. M.; Müller, A. J.; Castelleto, V.; Hamley, I.; Deshayes, G.; Dubois, P., Effect of sequence distribution on the morphology, crystallization, melting, and biodegradation of poly(ε-caprolactone-*co*-ε-caprolactam) copolymers. *Macromolecules* **2009,** *42*, 6671-6681.

105. Chromcova, D.; Baslerova, L.; Roda, J.; Brozek, J., Polymerization of lactams: 99 preparation of polyesteramides by the anionic copolymerization of ε-caprolactam and ε-caprolactone. *European Polymer Journal* **2008,** *44*, 1733-1742.

106. Ge, J.; He, M.; Xie, N.; Yang, X.; Ye, Z.; Qiu, F., Microphase separation and crystallization in all-conjugated poly(3-alkylthiophene) diblock copolymers. *Macromolecules* **2015,** *48*, 279-286.

107. Prosa, T. J.; Bauer, B. J.; Amis, E. J.; Tomalia, D. A.; Scherrenberg, M., A SAXS study of the internal structure of dendritic polymer systems. *Journal of Polymer Science, Part B: Polymer Physics* **1997,** *35*, 2913-2924.

108. Choi, Y. K.; Bae, Y. H.; Kim, S. W., Star-shaped poly(ether-ester) block copolymers: synthesis, characterization, and their physical properties. *Macromolecules* **1998,** *31*, 8766-8774.

109. Lu, C.; Guo, S. R.; Zhang, Y.; Yin, M., Synthesis and aggregation behavior of four types of different shaped PCL-PEG block copolymers. *Polymer International* **2006,** *55*, 694-700.

110. Du, Z. X.; Xu, J. T.; Yang, Y.; Fan, Z. Q., Synthesis and characterization of poly(ε-caprolactone)-*b*-poly(ethylene-glycol) block copolymers prepared by salicylaldimine-aluminium complex. *Journal of Applied Polymer Science* **2007,** *105*, 771-776.

111. Zhu, W.; Xie, W.; Tong, X.; Shen, Z., Amphiphilic biodegradable poly(CL-*b*-PEG-*b*-CL) triblock copolymers prepared by novel rare earth complex: synthesis and crystallization properties. *European Polymer Journal* **2007,** *43*, 3522-3530.

112. Du, Z. X.; Yang, Y.; Xu, J. T.; Fan, Z. Q., Effect of molecular weight on spherulitic growth rate of poly(ε-caprolactone) and poly(ε-caprolactone)-*b*-poly(ethylene glycol). *Journal of Applied Polymer Science* **2007,** *104*, 2986-2991.

113. Müller, A. J.; Balsamo, V.; Arnal, M. L.; Jakob, T.; Schmalz, H.; Abetz, V., Homogeneous nucleation and fractionated crystallization in block copolymers. *Macromolecules* **2002,** *35*, 3048-3058.

114. Yang, J.; Liang, Y.; Luo, J.; Zhao, C.; Han, C., Multilength scale studies of the confined crystallization in poly(L-lactide)-*block*-poly(ethylene glycol) copolymer. *Macromolecules* **2012,** *45*, 4254-4261.

115. Maglio, G.; Migliozzi, A.; Palumbo, R., Thermal properties of di- and triblock copolymers of poly (L-lactide) with poly(oxyethylene) or poly (ε-caprolactone). *Polymer* **2003,** *44*, 369-375.

116. Chen, J.; Huang, W.; Xu, Q.; Tu, Y.; Zhu, X.; Chen, E., PBT-*b*-PEO-*b*-PBT triblock copolymers: synthesis, characterization and double crystalline properties. *Polymer* **2013,** *54*, 6725-6731.

117. Schmalz, H.; Van Guldener, M.; Gabriëlse, W.; Lange, R.; Abetz, V., Morphology, surface structure, and elastic properties of PBT-based copolyesters with PEO-*b*-PEB-*b*-PEO triblock copolymer soft segments. *Macromolecules* **2002,** *35*, 5491-5499.

118. Voet, V. S. D.; Alberda van Ekenstein, G. O. R.; Meereboer, N. L.; Hoffman, A. H.; Ten Brinke, G.; Loos, K., Double crystalline PLLA-*b*-PVDF-*b*-PLLA triblock copolymers: preparation and crystallization. *Polymer Chemistry* **2014,** *5*, 2219-2230.

119. Balsamo, V.; Müller, A. J.; Von Gyldenfeldt, F.; Stadler, R., Ternary ABC block copolymers based on one glassy and two crystallizable blocks: polystyrene-*block*-polyethylene-*block*-poly(ε-caprolactone). *Macromolecular Chemistry and Physics* **1998,** *199*, 1063-1070.

120. Balsamo, V.; Paolini, Y.; Ronca, G.; Müller, A. J., Crystallization of the polyethylene block in polystyrene-*b*-polyethylene-*b*-polycaprolactone triblock copolymers, 1: self-nucleation behaviour. *Macromolecular Chemistry and Physics* **2000,** *201*, 2711-2720.

121. Balsamo, V.; Müller, A. J.; Stadler, R., Antinucleation effect of the polyethylene block on the polycaprolactone block in ABC triblock copolymers. *Macromolecules* **1998,** *31*, 7756-7763.

122. Chiang, Y. W.; Hu, Y. Y.; Li, J. N.; Huang, S. H.; Kuo, S. W., Trilayered single crystals with epitaxial growth in poly(ethylene oxide)-*block*-poly(ε-caprolactone)-*block*-poly(L-lactide)thin films. *Macromolecules* **2015,** *48*, 8526-8533.

123. Zhao, J.; Pahovnik, D.; Gnanou, Y.; Hadjichristidis, N., Sequential polymerization of ethylene oxide, ε-caprolactone and ʟ-lactide: a one-pot metal-free route to tri- and pentablock terpolymers. *Polymer Chemistry* **2014,** *5*, 3750-3753.

124. Guillerm, B.; Lemaur, V.; Ernould, B.; Cornil, J.; Lazzaroni, R.; Gohy, J. F.; Dubois, P.; Coulembier, O., A one-pot two-step efficent metal-free process for the generation of PEO-PCL-PLA amphiphilic triblock copolymers. *RSC Advances* **2014,** *4*, 10028-10038.

125. Sun, L.; Shen, L. J.; Zhu, M. Q.; Dong, C. M.; Wei, Y., Synthesis, self-assembly, drug-release behavior, and cytotoxicity of triblock and pentablock copolymers composed of poly(ε-caprolactone), poly(ʟ-lactide), and poly(ethylene glycol). *Journal of Polymer Science Part A: Polymer Chemistry* **2010,** *48*, 4583-4593.

126. Tamboli, V.; Mishra, G. P.; Mitra, A. K., Novel pentablock copolymer (PLA-PCL-PEG-PCL-PLA)-based nanoparticles for controlled drug delivery: effect of copolymer composition on the crystallinity of copolymers and in vitro drug release profile from nanoparticles. *Colloid and Polymer Science* **2013,** *291*, 1235-1245.

127. Hadjichristidis, N.; Iatrou, H.; Pitsikalis, M.; Pispas, S.; Avgeropoulos, A., Linear and non-linear triblock terpolymers. Synthesis, self-assembly in selective solvents and in bulk. *Progress in Polymer Science* **2005,** *30*, 725-782.

128. Palacios, J. K.; Mugica, A.; Zubitur, M.; Iturrospe, A.; Arbe, A.; Liu, G.; Wang, D.; Zhao, J.; Hadjichristidis, N.; Müller, A. J., Sequential crystallization and morphology of triple crystalline biodegradable PEO-*b*-PCL-*b*-PLLA triblock terpolymers. *Royal Society of Chemistry Adv.* **2016,** *6*, 4739.

129. Palacios, J. K.; Zhao, J.; Hadjicrhistidis, N.; Müller, A. J., How the complex interplay between different blocks determines the isothermal crystallization kinetics of triple-crystalline PEO-*b*-PCL-*b*-PLLA triblock terpolymers. *Macromolecules* **2017,** *50*, 9683-9695.

130. Palacios, J. K.; Tercjak, A.; Liu, G.; Wang, D.; Zhao, J.; Hadjicrhistidis, N.; Müller, A. J., Trilayered morphology of an ABC triple crystalline triblock terpolymer. *Macromolecules* **2017,** *50*, 7261-7281.

131. Palacios, J. K.; Mugica, A.; Zubitur, M.; Müller, A. J., Crystallization and morphology of block copolymers and terpolymers with more than one crystallizable block. In *Crystallization in Multiphase Polymer Systems*, Inc., E., Ed. **2018**; pp 123-180.

132. Palacios, J. K.; Liu, G.; Wang, D.; Hadjichristidis, N.; Müller, A. J., Generating triple crystalline superstructures in melt-miscible PEO-*b*-PCL-*b*-PLLA triblock terpolymers by controlling thermal history and sequential crystallization. *Macromolecular Chemistry and Physics* **2019,** *220*, 1900292.

133. Matxinandiarena, E.; Múgica, A.; Zubitur, M.; Zhang, B.; Ladelta, V.; Zapsas, G.; Hadjichristidis, N.; Müller, A. j., The effect of the cooling rate on the morphology and crystallization of triple crystalline PE-*b*-PEO-*b*-PLLA and PE-*b*-PCL-*b*-PLLA triblock terpolymers. *ACS Applied Polymer Materials* **2020,** *2*, 4952-4963.

134. The ABCs of block polymers. *Macromolecules* **2020,** *53*, 2765-2768.

135. Xu, Y.; Hu, W., Formation of multicontinuous 3D network nanostructures with increased complexity in ABC-type block copolymers. *Langmuir* **2020,** *36*, 11324-11331.

136. Loo, Y. L.; Register, R. A.; Ryan, A. J., Modes of crystallization in block copolymer microdomains: breakout, templated and confined. *Macromolecules* **2002,** *35*, 2365-2374.

137. Schmalz, H.; Knoll, A.; Müller, A. J.; Abetz, V., Synthesis and characterization of ABC triblock copolymers with two different crystalline end blocks: influence of confinement on crystallization behavior and morphology. *Macromolecules* **2002,** *35*, 10004-10013.

138. Cui, D.; Tang, T.; Bi, W.; Cheng, J.; Chen, W.; Huang, B., Ring-opening polymerization and block copolymerization of L-lactide with divalent samarocene complex. *Journal of Polymer Science, Part A: Polymer Chemistry* **2003,** *41* (17), 2667-2675.

139. Huang, Y.; Liu, X. B.; Zhang, H. L.; Zhu, D. S.; Sun, Y. J.; Yan, S. K.; Wang, J.; Chen, X. F.; Wan, X. H.; Chen, E. Q.; Zhou, Q. F., AFM study of crystallization and melting of a poly(ethylene oxide) diblock copolymer containing a tablet-like block of poly[2,5-bis[(4-methoxyphenyl) oxycarbonyl]styrene] in ultrathin films. *Polymer* **2006,** *47* (4), 1217-1225.

140. Zhang, P.; Wang, Z.; Huang, H.; He, T., Direct observation of the relief structure formation in the nearly symmetric poly(styrene-*block*-poly(ε-caprolactone) diblock copolymer thin film. *Macromolecules* **2012,** *45* (22), 9139-9146.

141. Hiemenz, P. C.; Lodge, T. P., *Polymer Chemistry*. CRC Press: **2007**.

142. Hu, H.; Dorset, D. L., Crystal structure of poly (ε-caprolactone). *Macromolecules* **1990,** *23*, 4604-4607.

143. Lin, H.; Wagner, E. V.; Swinnea, J. S.; Freeman, B. D.; Pas, S. J.; Hill, A. J.; Kalakkunnath, S.; Kalika, D. S., Transport and structural characteristics of crosslinked poly (ethylene oxide) rubbers. *Journal of Membrane Science* **2006,** *276*, 145-161.

144. Shen, M.; Hansen, W. N.; Romo, P. C., Thermal expansion of the polyethylene unit cell. *The journal of Chemical Physics* **1969,** *51*, 425-430.

145. Zhang, J.; Tashiro, K.; Tsuji, H.; Domb, J., Disorder-to-order phase transition and multiple melting behavior of poly(L-lactide) investigated by simultaneous measurements of WAXD and DSC. *Macromolecules* **2008,** *41*, 1352-1357.

146. Lorenzo, A. T.; Arnal, M. L.; Müller, A. J.; Boschetti de Fierro, A.; Abetz, V., Confinement effects on the crystallization and SSA thermal fractionation of the PE block within PE-*b*-PS diblock copolymers. *European Polymer Journal* **2006,** *42*, 516-533.

147. Müller, A. J.; Michell, R. M., Differential scanning calorimetry of polymers. In *Polymer Morphology: Principles, Characterization and Processing*, Guo, Q., Ed. John Wiley and Sons: Hoboken, New Jersey (USA), **2016**; pp 72-99.

148. Crist, B.; Schultz, J. M., Polymer spherulites: a critical review. *Progress in Polymer Science* **2016,** *56*, 1-63.

Chapter 6

Multicrystalline Block Polymers: Tetracrystalline Tetrablock Quarterpolymers and their Precursors containing PE, PEO, PCL and PLLA Blocks

6.1 Introduction

As mentioned in the introduction of Chapter 5, the crystallization of multiphasic block copolymers is a complex process that depends on several variables, and several reviews and publications have been published due to their versatility and possible applications in several areas. We have already mentioned the background of AB-type diblock copolymers and ABC-type triblock terpolymers with two and three crystallizable blocks, respectively.

However, the synthesis of well-defined tetracrystalline tetrablock quarterpolymers is a challenge, and to the best of our knowledge, there is only one report about this ABCD type material. Hadjichristidis et al.[1] reported a one-pot synthesis of tetracrystalline tetrablock quarterpolymers poly (ethylene)-*b*-poly (ethylene oxide)-*b*-poly (*ε*-caprolactone)-*b*-poly (*L*-Lactide) (PE-*b*-PEO-*b*-PCL-*b*-PLLA) from PE-OH macroinitiator by an organic/organic or organic/metal "catalyst switch" strategy. The formation of a tetrablock quarterpolymer was confirmed by ^{1}H NMR spectroscopy (in liquid and solid-state) and gel-permeation chromatography.

In this section, the crystallization behavior of novel tetracrystalline tetrablock quarterpolymers PE-*b*-PEO-*b*-PCL-*b*-PLLA is studied. Two different block compositions are considered, varying block content and the molecular weight of each of the blocks (quarterpolymer Q1 and Q2). Their precursors are also studied for comparison purposes: triblock terpolymers $PE_{22}^{7.1}$-*b*-$PEO_{46}^{15.1}$-*b*-$PCL_{32}^{10.4}$ (T1) and $PE_{37}^{9.5}$-*b*-$PEO_{34}^{8.8}$-*b*-$PCL_{29}^{7.6}$ (T2); diblock copolymers $PE_{32}^{7.1}$-*b*-$PEO_{68}^{15.1}$ and $PE_{52}^{9.5}$-*b*-$PEO_{48}^{8.8}$; and homopolymers $PE^{7.1}$ and $PE^{9.5}$.

We study for the first time the ability of all the blocks to crystallize in these tetrablock complex materials. The influence of the restrictions imposed during the crystallization on the morphology and the final lamellar structure will be explored and correlated with the mechanical properties measured by nanoindentation. This study is carried out employing Differential Scanning Calorimetry (DSC), *in situ* Small-Angle and Wide-Angle X-ray scattering (SAXS/WAXS) measurements,

Polarized Light Optical Microscopy (PLOM), Atomic Force Microscopy (AFM), and nanoindentation. These characterization techniques allow performing a comprehensive investigation of the crystalline behavior of these novel materials and the impact on relevant properties such as mechanical ones. The understanding of the complex crystalline nature is vital in order to tune properties and design new interesting materials for potential applications.

In this Chapter, we will first analyze and compare the precursor PE homopolymers, PE-*b*-PEO diblock copolymers, and PE-*b*-PEO-*b*-PCL triblock terpolymers (T1 and T2) of the tetrablock quarterpolymers $PE_{18}^{7.1}$ -*b* -$PEO_{37}^{15.1}$ -*b*- $PCL_{26}^{10.4}$ -*b*- $PLLA_{19}^{7.6}$ (Q1) and $PE_{29}^{9.5}$ -*b*- $PEO_{26}^{8.8}$ -*b*- $PCL_{23}^{7.6}$ -*b*- $PLLA_{22}^{7.3}$ (Q2), which are listed in Table 3.3 of the Experimental Part.

6.2 PE Homopolymers, PE-*b*-PEO Diblock Copolymers and PE-*b*-PEO-*b*-PCL Triblock Terpolymers (T1 and T2)

6.2.1 Small-angle X-Ray Scattering (SAXS)

SAXS measurements are useful to study not only the phase segregation in the melt but also if the phase segregation is kept when the block components crystallize or if crystallization destroys it by breaking out the phase structure of the melt. Figures 6.1 show the SAXS patterns of the homopolymer $PE^{7.1}$, the diblock copolymer $PE_{32}^{7.1}$-*b*-$PEO_{68}^{15.1}$, and the triblock terpolymer $PE_{22}^{7.1}$-*b*-$PEO_{46}^{15.1}$-*b*-$PCL_{32}^{10.4}$ (T1) upon cooling from the melt.

There is no phase segregation in the melt for the homopolymer $PE^{7.1}$ and the diblock copolymer $PE_{32}^{7.1}$-b-$PEO_{68}^{15.1}$ (Figure 6.1a and 6.1b), as evidenced by the lack of scattering peaks in the molten state. The broad peak that appears at lower temperatures corresponds to the diffraction from crystalline lamellar stacks in the formed superstructures (i.e., spherulites or axialites).

However, there is weak phase segregation for the $PE_{22}^{7.1}$-*b*-$PEO_{46}^{15.1}$-*b*-$PCL_{32}^{10.4}$ (T1) triblock terpolymer (Figure 6.1c) since there is a broad scattering peak in the melt which disappears as crystallization breaks out when the first block upon cooling the melt starts to crystallize (the PE block). This behavior is evidenced by the shift in *q* values between the reflection in the melt and the weaker reflection at room temperature, which appears at lower *q* values. The broad peak at room temperature corresponds to the average long period of the lamellae formed during the crystallization process because the phase structure formed by phase segregation in the melt is destroyed.

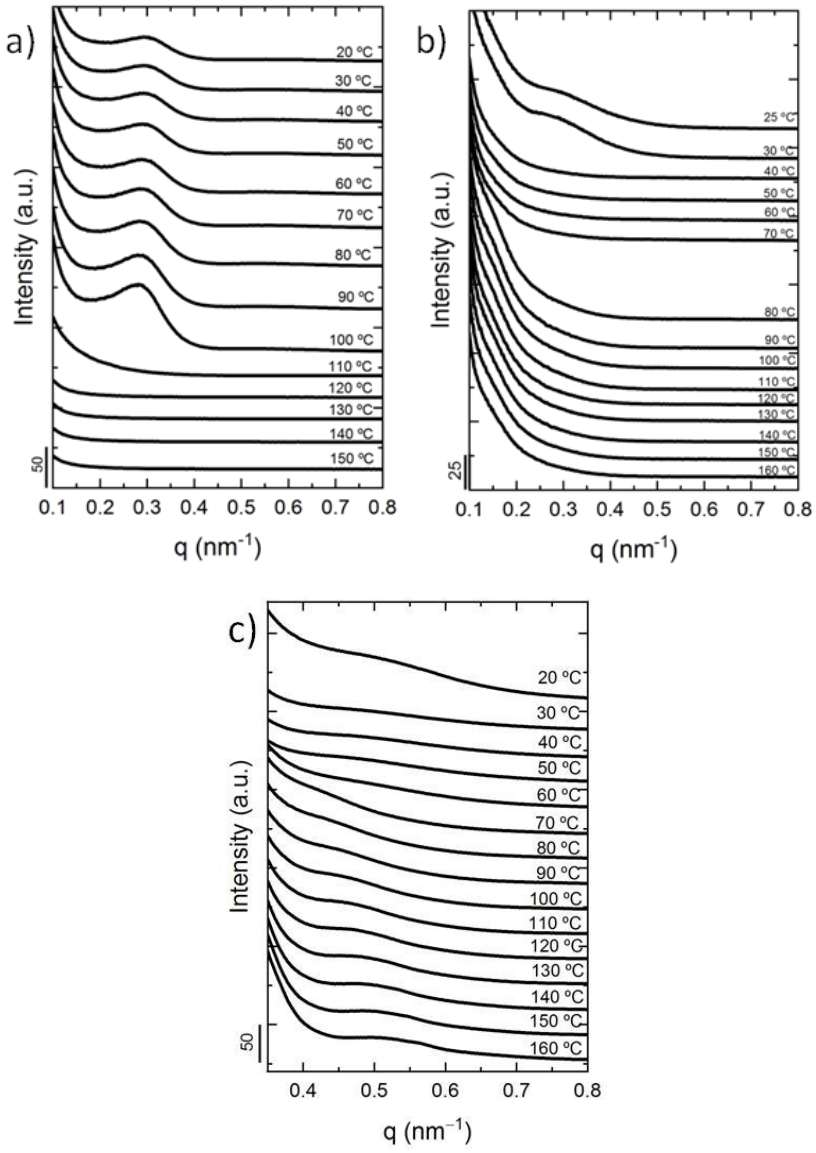

Figure 6.1. SAXS ramp down patterns at 20 ºC/min for a) $PE^{7.1}$, b) $PE_{32}^{7.1}$-*b*-$PEO_{68}^{15.1}$ and c) $PE_{22}^{7.1}$-*b*-$PEO_{46}^{15.1}$-*b*-$PCL_{32}^{10.4}$ (T1) at the indicated temperatures

Figure 6.2 shows SAXS patterns of the homopolymer $PE^{9.5}$, the diblock copolymer $PE_{52}{}^{9.5}$-*b*-$PEO_{48}{}^{8.81}$, and the triblock terpolymer $PE_{37}{}^{9.5}$-*b*-$PEO_{34}{}^{8.8}$-*b*-$PCL_{29}{}^{7.6}$ (T2) at the indicated temperatures reached upon cooling. In this case, the behavior of the homopolymer $PE^{9.5}$ (Figure 6.2a) is the same as for the homopolymer $PE^{7.1}$ (Figure 6.1a) explained above, not showing any phase segregation in the melt, as expected for the homopolymer.

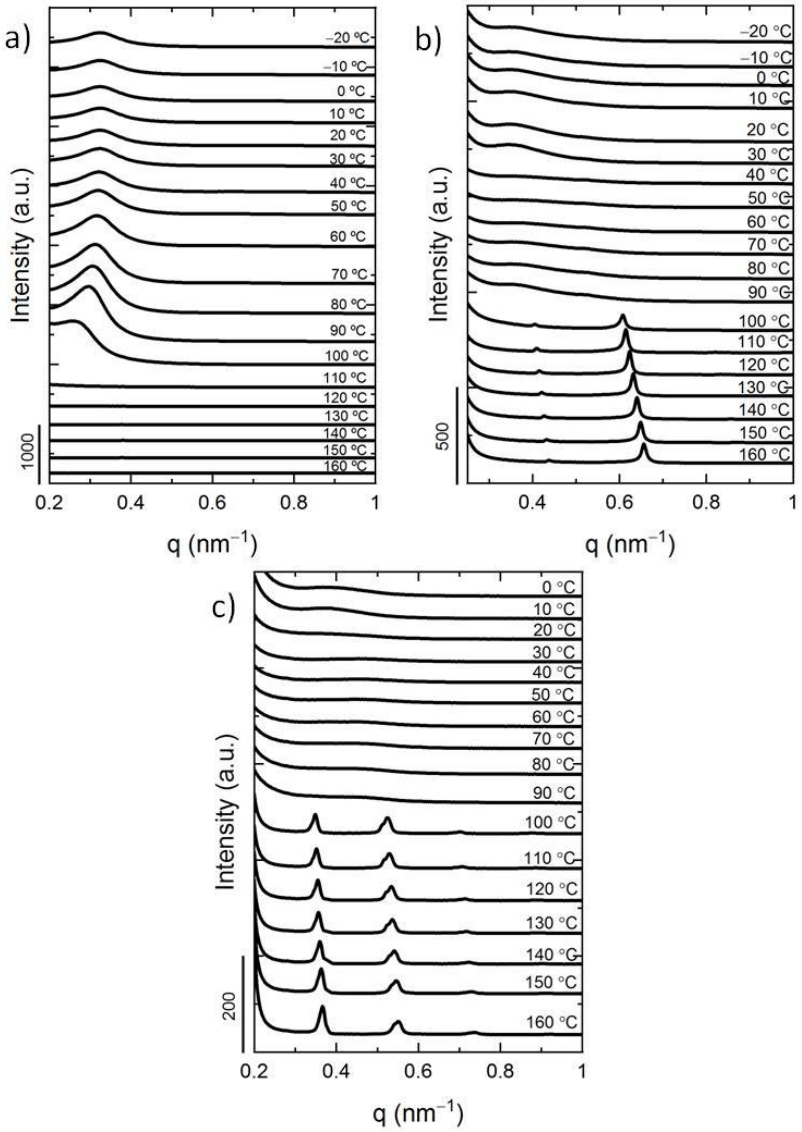

Figure 6.2. SAXS ramp down patterns at 20 ºC/min for a) $PE^{9.5}$, b) $PE_{52}{}^{9.5}$-*b*-$PEO_{48}{}^{8.81}$ and c) $PE_{37}{}^{9.5}$-*b*-$PEO_{34}{}^{8.8}$-*b*-$PCL_{29}{}^{7.6}$ (T2) at the indicated temperatures

The diblock copolymer $PE_{52}^{9.5}$-*b*-$PEO_{48}^{8.81}$ (Figure 6.2b) and the triblock terpolymer $PE_{37}^{9.5}$-*b*-$PEO_{34}^{8.8}$-*b*-$PCL_{29}^{7.6}$ (T2) (Figure 6.2c) are phase segregated in the melt, with possible lamellar and interpenetrated morphologies, respectively, although more detailed analysis of the scattering curves would be needed to ascertain the exact melt morphology. The clear scattering peaks in the molten state in these two materials corroborate the phase segregation behavior; however, their phase segregation is weak, since when the first block crystallizes upon cooling, i.e., the PE block at 100 ºC, the phase structure generated by phase segregation in the melt is destroyed, as deduced by the change in q values and intensities of the scattering peaks.

One way to predict the segregation strength in linear diblock copolymers is by multiplying the Flory-Huggins interaction parameter (χ) (evaluated in the melt) by N (total degree of polymerization). The estimation becomes more difficult in the case of triblock terpolymers. Different behaviors can be predicted depending on the segregation strength values. Values equal or lower to 10 indicates miscibility in the melt, between 10-30 weak phase segregation, between 30-50 intermediate segregation, and if values are higher than 50, the systems are strongly segregated. A rough approximation for each pair of blocks is reported in Table A.6.1 of the Appendix, using solubility parameters of PE, PEO, and PCL from the literature[2, 3]. In this case, the predicted values suggest that at least the diblock copolymers should be strongly segregated, but the experimental SAXS findings indicate miscibility for $PE_{32}^{7.1}$-*b*-$PEO_{68}^{15.1}$ and weak segregation for the $PE_{52}^{9.5}$-*b*-$PEO_{48}^{8.8}$.

As the dominant behavior during crystallization is that of break out, the final morphology is that of crystalline lamellae arranged in superstructures like axialites or spherulites. Therefore, we will not explore in detail the morphology of the materials in the melt, as it is destroyed upon crystallization.

6.2.2 Non-isothermal Crystallization by DSC

DSC cooling and heating scans of the homopolymers, diblock copolymers, and triblock terpolymers of the two systems (Table 3.3 in the Experimental Chapter) are discussed in this section. In addition, all data obtained are collected in Tables A.6.2-A.6.4 of the Appendix.

Figure 6.3 shows the cooling (A) and heating (B) scans for the $PE^{7.1}$ homopolymer, the $PE_{32}^{7.1}$-*b*-$PEO_{68}^{15.1}$ diblock copolymer, and the $PE_{22}^{7.1}$-*b*-$PEO_{46}^{15.1}$-*b*-$PCL_{32}^{10.4}$ (T1) triblock terpolymer recorded at 20 °C/min. The crystallization peaks of the blocks (T_c) have been assigned using WAXS data collected under identical conditions at the synchrotron (shown and described below, Figure 6.5). The same color code is used throughout the whole work to highlight the crystallization and melting of the different blocks (blue for PCL, red for PEO, and violet for PE). The sharp exotherm (Figure 6.3Aa) and subsequent endotherm (Figure 6.3Ba) of the neat $PE^{7.1}$ precursor is a consequence of its linear character (synthesized by polyhomologation).

In the $PE_{32}^{7.1}$-*b*-$PEO_{68}^{15.1}$ diblock copolymer, PE (violet arrow) is the first block crystallizing upon cooling from the melt, followed by the crystallization of the PEO block (red arrow) (Figure 6.3Ab). The crystallization of the PE block does not occur in a unique step since three exothermic crystallization peaks appear for the PE block crystallization: at 118 °C, 82 °C and 79 °C. This indicates that the PE block crystallizes in a fractioned way, which means that a series of crystallization exotherms appear at lower temperature instead of a single crystallization exotherm that corresponds to the bulk crystallization temperature of the PE block. Note that as shown in Figure 6.1b, this diblock copolymer shows miscibility in the melt, and as crystallization occurs from a homogeneous melt, as well as only having 32 wt % of PE block content and a relatively low molecular weight, the crystallization of the PE block is somehow hindered, as evidenced by its crystallization enthalpy value of 22 J/g (Table A.6.2). On the contrary, the sharp crystallization exotherm of the PEO block along with the high block content (68

wt %) suggests its high crystallization ability, as the enthalpy for the PEO is 177 J/g (Table A.6.2).

The crystallization in the $PE_{22}^{7.1}$-*b*-$PEO_{46}^{15.1}$-*b*-$PCL_{32}^{10.4}$ (T1) triblock terpolymer (Figure 6.3Ac) starts with the PE block (violet arrow). In this case, the PE block content is low (22 wt %), and a very small crystallization exotherm is observed in the cooling scan (14 J/g) (Table A.6.2). Crystallization continues with the PCL block (blue arrow) and the PEO block (red arrow). Although the crystallization peaks of the PEO and the PCL blocks are overlapped, WAXS results below demonstrate that the PCL block crystallizes some degrees above the PEO block (Figure 6.5c). As we are not able to distinguish between both transitions, an estimation of the crystallization enthalpies is reported in Table A.6.2 by employing block content for the calculations.

Figure 6.3B shows the subsequent heating scans with the endothermic melting peaks (T_m) for each sample; data are collected in Table A.6.3. The homopolymer $PE^{7.1}$ (Figure 6.3Ba) shows a crystallinity value of 75 % (Table A.6.4), as expected, observing the sharp melting transition. For the diblock copolymer (Figure 6.3Bb), melting starts with the PEO block (red) with a crystallinity value of 85 %; and it continues with the PE block melting (violet), with a crystallinity value of only 7 % (Table A.6.4), because as previously mentioned, small block content and cooling from a homogenous melt is not the best scenario to enhance crystallization. The overlapped melting peak at the lowest temperature for the triblock terpolymer (Figure 6.3Bc) corresponds to the PEO (red) and the PCL (blue) blocks (an estimation of the crystallinity values is provided in Table A.6.4), whereas the melting at the highest temperatures occurs for the PE block crystals, although its crystallinity degree is only 5 % (Table A.6.4) of its 32 wt % block content in the terpolymer. WAXS melting transitions and normalized intensity measurements recorded in Figures A.6.1-A.6.2 in the Appendix corroborate these DSC results.

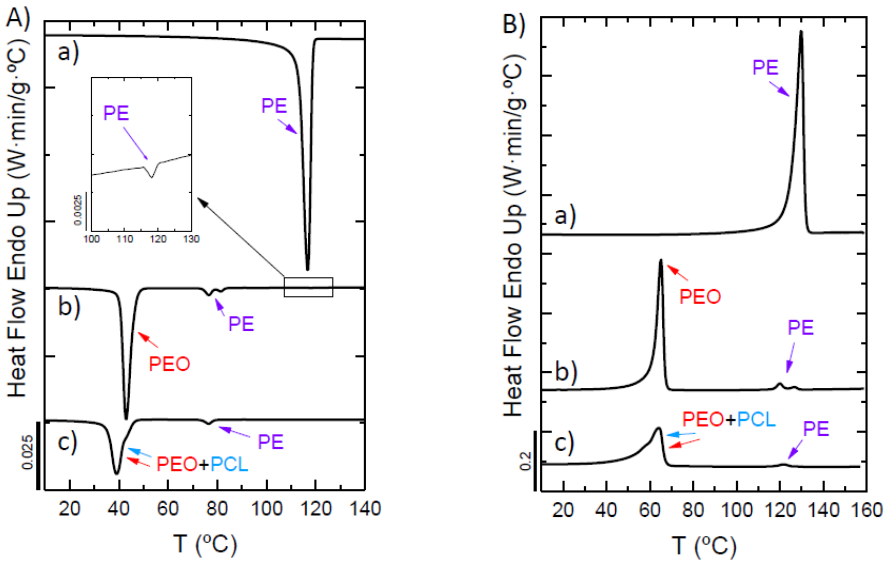

Figure 6.3. DSC scans at 20 ºC/min for a) $PE^{7.1}$, b) $PE_{32}{}^{7.1}$ -*b*- $PEO_{68}{}^{15.1}$ and c) $PE_{22}{}^{7.1}$ -*b*- $PEO_{46}{}^{15.1}$ -*b*- $PCL_{32}{}^{10.4}$ (T1) of A) cooling from the melt, with a close-up to notice the very first crystallization exotherm of the PE block and B) subsequent heating with arrows indicating transitions for each block

Figure 6.4 shows cooling and heating scans of the $PE^{9.5}$ homopolymer, the $PE_{52}{}^{9.5}$ -*b*- $PEO_{48}{}^{8.8}$ diblock copolymer, and the $PE_{37}{}^{9.5}$ -*b*- $PEO_{34}{}^{8.8}$ -*b*- $PCL_{29}{}^{7.6}$ (T2) triblock terpolymer. The crystallization and melting transitions of the blocks in these samples (Figure 6.4Ac-6.4Bc) follow the same trend described before in Figure, but with some differences due to the phase behaviour of the materials.

The crystallization of $PE^{9.5}$ homopolymer (Figure 6.4Aa) occurs in a single and sharp transition. In the case of the $PE_{52}{}^{9.5}$ -*b*- $PEO_{48}{}^{8.8}$ diblock copolymer (Figure 6.4Ab), the crystallization of the PE block (violet) occurs at high temperatures, followed by the crystallization of the PEO block (red) at lower temperatures. Note that the PE block crystallizes in a unique crystallization step in this diblock copolymer, not in a fractionated way as in the previous diblock copolymer discussed before (Figure 6.3Ab). The difference remains in the phase behavior in the melt, on the one hand, since this diblock copolymer shows weak phase segregation (as evidenced by SAXS experiments shown in Figure 6.2b), and

the fact of being segregated in the melt enhances the crystallization of the PE block. On the other hand, the PE block content is higher in this copolymer (52 wt %) with a higher molecular weight (9500 vs. 7100 g/mol). So, higher PE content and cooling from a segregated melt, do not largely hinder its crystallization, showing a crystallization enthalpy of 81 J/g (Table A.6.2).

The crystallization sequence in the $PE_{37}^{9.5}$ -*b*- $PEO_{34}^{8.8}$ -*b*- $PCL_{29}^{7.6}$ (T2) triblock terpolymer is the same as the one explained in the previous triblock terpolymer (T1) (Figure 6.3Ac): first the PE block (violet), and then the PCL (blue) and PEO (red) blocks. Although also, in this case, the crystallization of the PCL and PEO blocks are overlapped, WAXS measurements below demonstrate (Figures 6.7c and 6.8c) that the PCL block crystallizes a few degrees higher than the PEO block; and estimations of the enthalpies are provided in Table A.6.2.

The subsequent heating scans are reported in Figure 6.4B. The homopolymer $PE^{9.5}$ in Figure 6.4Ba shows a clear melting transition and a crystallinity value of 55 % (Table A.6.4). In the case of the $PE_{52}^{9.5}$ -*b*- $PEO_{48}^{8.8}$ diblock copolymer (Figure 6.4Bb), the melting starts with the PEO block (red) and ends with the PE block (violet). As previously mentioned, segregation in the melt and higher PE content enhances its crystallization, and thus, a clear and sharp melting transition with a crystallinity value of 27 % is obtained (Table A.6.4). Finally, the $PE_{37}^{9.5}$ -*b*- $PEO_{34}^{8.8}$ -*b*- $PCL_{29}^{7.6}$ (T2) triblock terpolymer follows the same trend as in the triblock terpolymer T1 (Figure 6.3Bc): melting of the PEO (red) and PCL (blue) blocks occur with a difference of some degrees, although not enough to distinguish between both DSC melting transitions (demonstrated by WAXS experiments in Figures A.6.3c-A.6.4c); and melting of the PE block showing a higher crystallinity degree (44 %) (Table A.6.4).

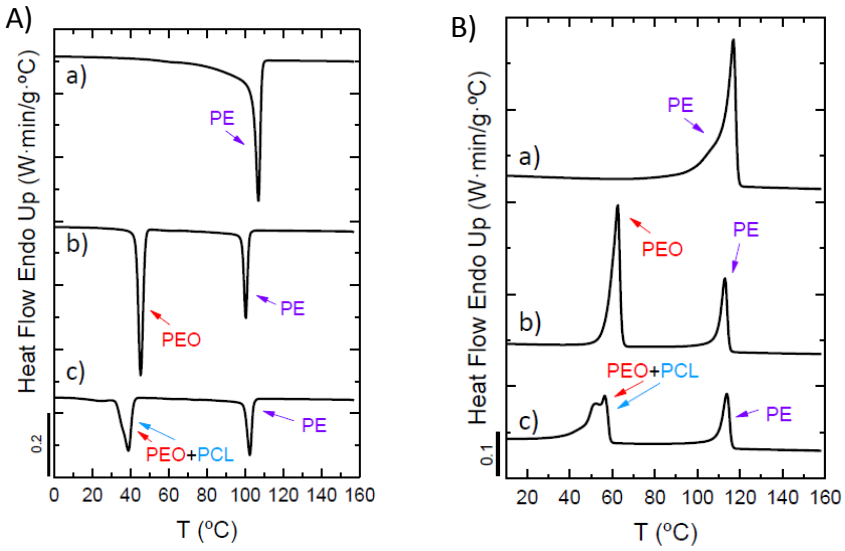

Figure 6.4. DSC scans at 20 ºC/min for a) $PE^{9.5}$, b) $PE_{52}{}^{9.5}$ -*b*- $PEO_{48}{}^{8.8}$ and c) $PE_{37}{}^{9.5}$ -*b*- $PEO_{34}{}^{8.8}$ -*b*- $PCL_{29}{}^{7.6}$ (T2) of A) cooling from the melt and B) subsequent heating with arrows indicating transitions for each block

6.2.3 *In situ* Wide Angle X-Ray Scattering (WAXS)

To identify the crystallization of each block in WAXS patterns, the crystal planes indexing for the PE, PCL and PEO blocks is reported in Table A.6.5[3-11]. In addition, normalized intensity measurements as a function of temperature upon cooling from the melt at 20 ºC/min are provided, confirming the double and triple crystalline nature of the samples.

As shown in Figure 6.5, all blocks are able to crystallize, as demonstrated by the presence of their characteristic scattering peaks at certain *q* values, pointed out with the colors we are employing throughout the whole work.

The $PE^{7.1}$ homopolymer crystallization starts at 118 ºC (Figure 6.5a), as its characteristic scattering peak at 15.4 nm^{-1} (violet arrow) corresponding to the (110) crystallographic plane appears at this temperature. Cooling down the sample, at 16.9 nm^{-1}, the other scattering peak of the (200) plane confirms PE crystallization. In addition, the normalized WAXS intensity calculation as a function of

temperature for the PE_{110} (15.4 nm^{-1}) reflection in Figure 6.6a confirms PE crystallization of the PE block by the sharp increase in the intensity.

Figure 6.5b shows that the first block to crystallize, during cooling from the melt, in the $PE_{32}^{7.1}$ -*b*- $PEO_{68}^{15.1}$ diblock copolymer is PE at 118 ºC (violet arrows) with its scattering peaks at 15.4 and 16.9 nm^{-1} (reflections (110) and (200), respectively). At lower temperatures, 34 ºC, the PEO block (red arrows) starts to crystallize with its (120) and (032)/(112)/(132)/(212) reflections at 13.8 and 16.4 nm^{-1}, respectively. Although the crystallization of these two blocks is clear, the normalized WAXS intensities calculated in Figure 6.6b, show this sequential crystallization by analyzing separately the unique scattering peaks of the PEO_{120} (13.8 nm^{-1}) and the PE_{110} (15.4 nm^{-1}). At high temperatures, the intensity starts to increase at 118 ºC due to PE crystallization, and the second increase at 82 ºC also corresponds to PE, because as reported in Figure 6.3Ab, PE crystallizes in two steps.

Figure 6.5c corresponds to the $PE_{22}^{7.1}$ -*b*- $PEO_{46}^{15.1}$ -*b*- $PCL_{32}^{10.4}$ (T1) triblock terpolymer. In this case, the crystallization sequence starts with the PE crystallization (violet arrows), as evidenced by the PE_{110} reflection at 82 ºC and the PE_{200} reflection at 70 °C. One may find this crystallization temperature low for the PE block, but as discussed previously in Figure 6.3Ac, the PE content is low (22 wt %) and the crystallization enthalpy (14 J/g). The next block to crystallize is the PCL block (blue arrows). At 42 ºC, the PCL_{110} (15.5 nm^{-1}), PCL_{111} (15.6 nm^{-1}) and PCL_{200} (16.7 nm^{-1}) reflections indicate the presence of PCL block crystals. The last block crystallizing upon cooling from the melt is the PEO block (red arrows). The presence of its scattering peak at 13.8 nm^{-1} correspondings to the (120) crystallographic plane at 32 ºC confirms the crystallization. At lower temperatures, the other characteristic peak of PEO (16.4 nm^{-1}) appears at 30 ºC corresponding to the (032/112/132/212) plane (Figure 6.5c).

The normalized intensities are analyzed to detect the exact temperature at which each of the blocks crystallizes (Figure 6.6c). The joint reflections of PE_{110} (15.4 nm^{-1}) and PCL_{110} (15.5 nm^{-1}) are used to determine their crystallization temperature ranges. The first slight change in intensity at 82 ºC confirms PE crystallization (violet), barely noticeable due to the low content of the PE block in the terpolymer (22 wt %). Then, the sharp increase at 42 ºC indicates the crystallization of the PCL block (blue). The single PEO_{120} (13.8 nm^{-1}) reflection (along with the other PE and PCL reflections) confirms its crystallization by a sharp increase in intensity.

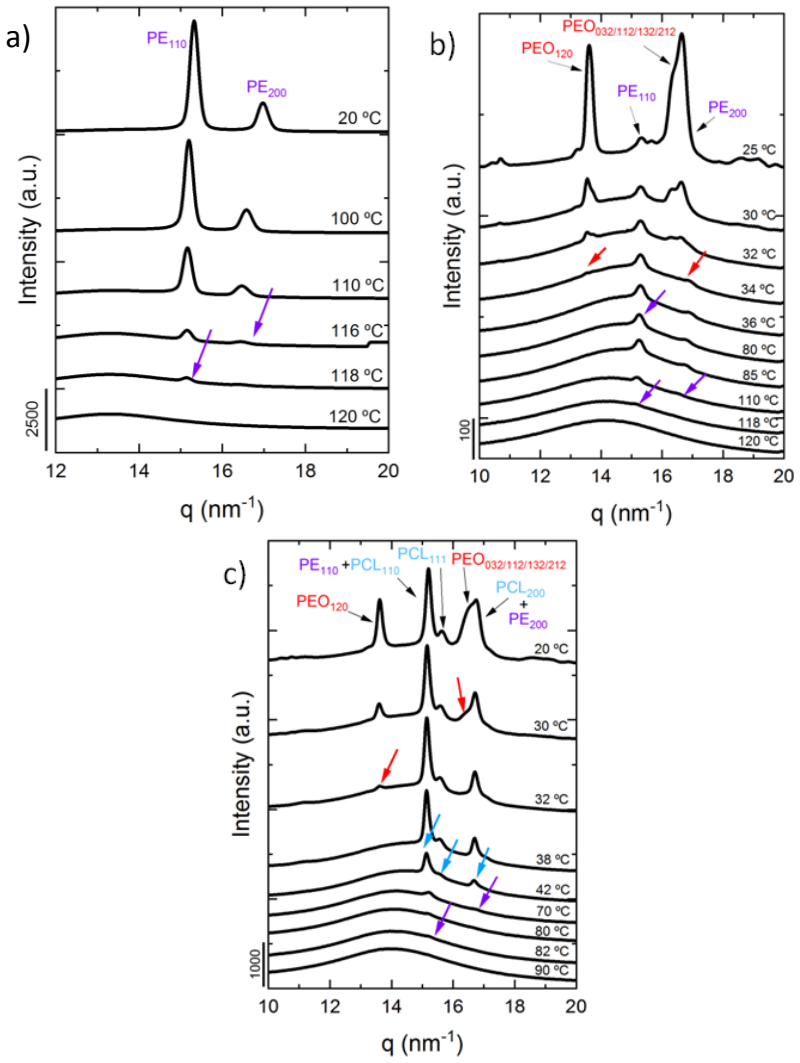

Figure 6.5. WAXS patterns upon cooling from the melt at 20 ºC/min for a) $PE^{7.1}$, b) $PE_{32}{}^{7.1}$ -*b*- $PEO_{68}{}^{15.1}$ and c) $PE_{22}{}^{7.1}$ -*b*- $PEO_{46}{}^{15.1}$ -*b*- $PCL_{32}{}^{10.4}$ (T1) at different temperatures with coloured arrows indicating crystallization of each block and with the corresponding (hkl) planes of the blocks

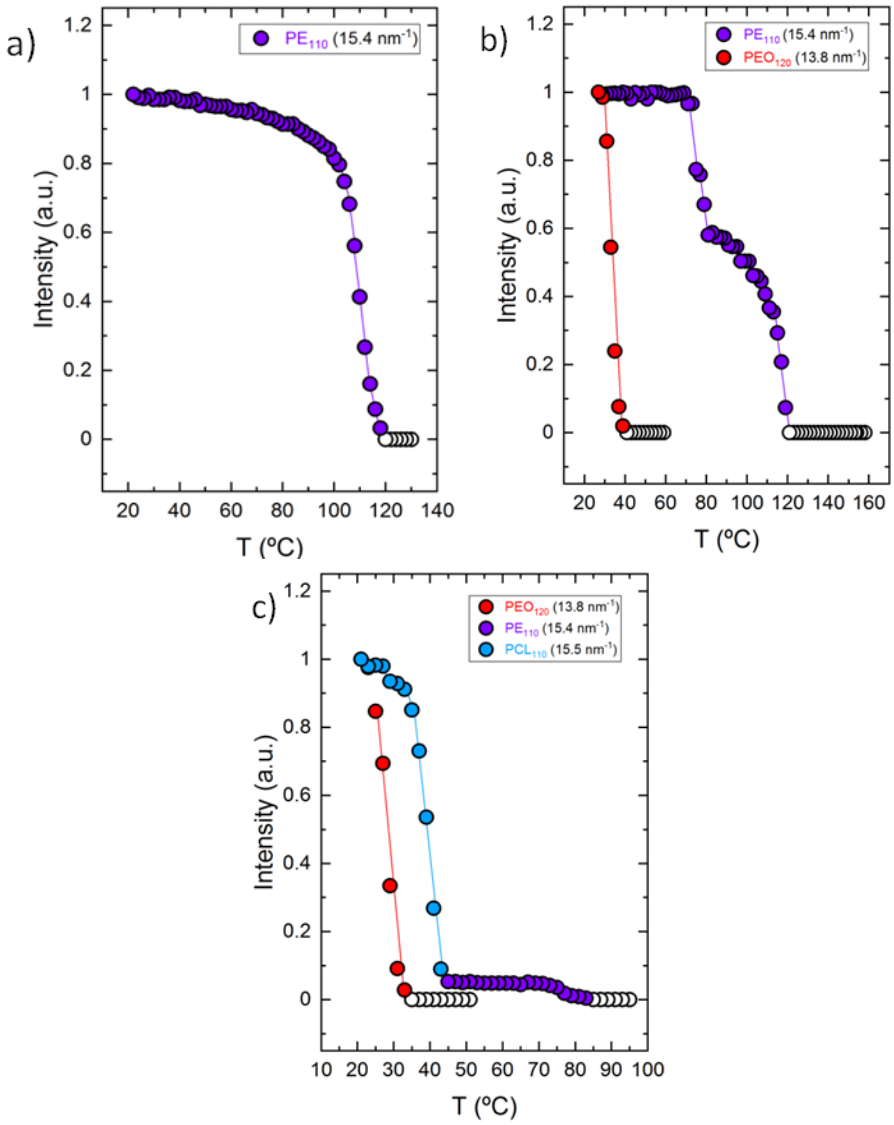

Figure 6.6. Normalized WAXS intensities as a function of temperature calculated from WAXS data represented in Figure 6.5 for a) $PE^{7.1}$ (PE_{110} (15.4 nm^{-1})), b) $PE_{32}{}^{7.1}$ -*b*- $PEO_{68}{}^{15.1}$ (PE_{110} (15.4 nm^{-1}) and PEO_{120} (13.8 nm^{-1})) and c) $PE_{22}{}^{7.1}$ -*b*- $PEO_{46}{}^{15.1}$ -*b*- $PCL_{32}{}^{10.4}$ (PEO_{120} (13.8 nm^{-1}), PE_{110} (15.4 nm^{-1}) and PCL_{110} (15.5 nm^{-1})) with colored data points and lines indicating crystallization of the corresponding blocks. Empty data points represent the molten state

In the same way, in Figures 6.7 and 6.8, WAXS patterns upon cooling the melt at 20 ºC/min as well as the normalized intensity measurements confirm crystallization of all blocks in the other set of samples listed in Table 3.3 in the

Experimental Chapter: the homopolymer $PE^{9.5}$, the diblock copolymer $PE_{52}^{9.5}$ -*b*- $PEO_{48}^{8.8}$ and the triblock terpolymer $PE_{37}^{9.5}$ -*b*- $PEO_{34}^{8.8}$ -*b*- $PCL_{29}^{7.6}$ (T2).

In this case, Figure 6.7a shows that the crystallization of the homopolymer $PE^{9.5}$ starts at 112 ºC (PE_{110} at 15.4 nm^{-1}), and the second scattering peak appears at 100 ºC, PE_{200} (16.9 nm^{-1}) (see violet arrows). Figure 6.8a shows the broad temperature range at which PE crystallizes since a plateau is not reached until approximately 60 ºC, determining this way that PE crystallizes in between 112-60 ºC.

Continuing with Figure 6.7b, the first reflection at 103 ºC ((110) reflection at 15.4 nm^{-1}) corresponds to the PE block, along with the (200) reflection (16.9 nm^{-1}) at 100 ºC (see violet arrows). The second block to crystallize in this diblock copolymer at 39 ºC is the PEO block (red arrows), identified due to the presence of the (120) reflection at 13.8 nm^{-1} and ((032)/(112)/(132)/(212) reflections at 16.4 nm^{-1}. Once again, normalized intensities in Figure 6.8b confirm the temperature ranges at which both the PE and the PEO blocks start to crystallize due to the sharp increase in the intensity of the corresponding peaks.

To conclude, Figure 6.7c shows the WAXS patterns for the $PE_{37}^{9.5}$ -*b*- $PEO_{34}^{8.8}$ -*b*- $PCL_{29}^{7.6}$ (T2) triblock terpolymer. The crystallization sequence remains the same as in the previous triblock terpolymer discussed above (Figure 6.5c): the PE block first (violet arrows) at 110 ºC ((110) and (200) reflections at 15.4 and 16.9 nm^{-1}); then the PCL block (blue arrows) at 46 ºC ((110) and (200) reflections at 15.5 and 16.7 nm^{-1}); and finally the PEO block (red arrows) at 34 ºC ((120) and (032)/(112)/(132)/(212) reflections at 13.8 and 16.4 nm^{-1}). In addition, the normalized intensities shown in Figure 6.8c demonstrate the crystallization of the three blocks by analyzing the joint reflection that the three blocks show at *q* values between 16.4-16.9 nm^{-1}. Note that as the PE content is higher in this triblock terpolymer (T2) (37 wt % vs. 22 wt %), the increase in intensity is clearer than in the previous triblock terpolymer (T1), in which it was very low (Figure 6.6c.

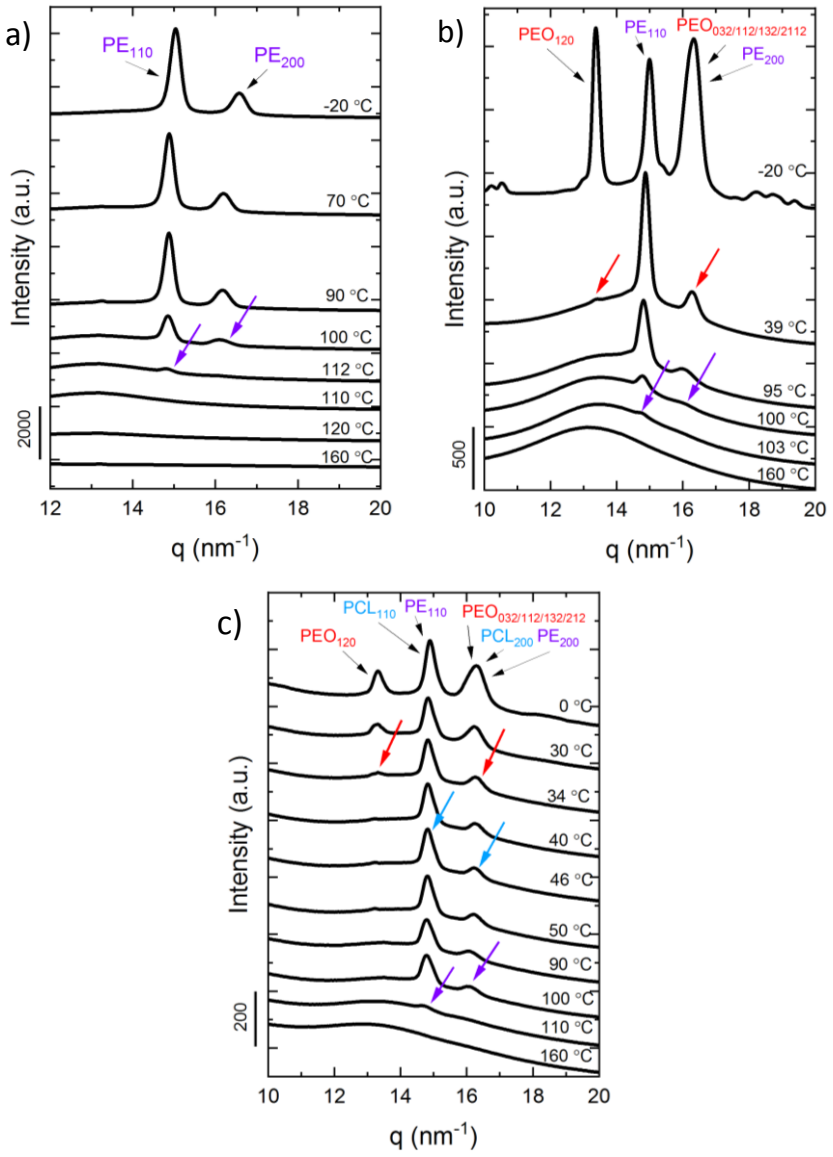

Figure 6.7. WAXS patterns upon cooling from the melt at 20 ºC/min for a) $PE^{9.5}$, b) $PE_{52}^{9.5}$ -*b*- $PEO_{48}^{8.8}$ and c) $PE_{37}^{9.5}$ -*b*- $PEO_{34}^{8.8}$ -*b*- $PCL_{29}^{7.6}$ (T2) at different temperatures with coloured arrows indicating crystallization of each block and with the corresponding (hkl) planes of the blocks

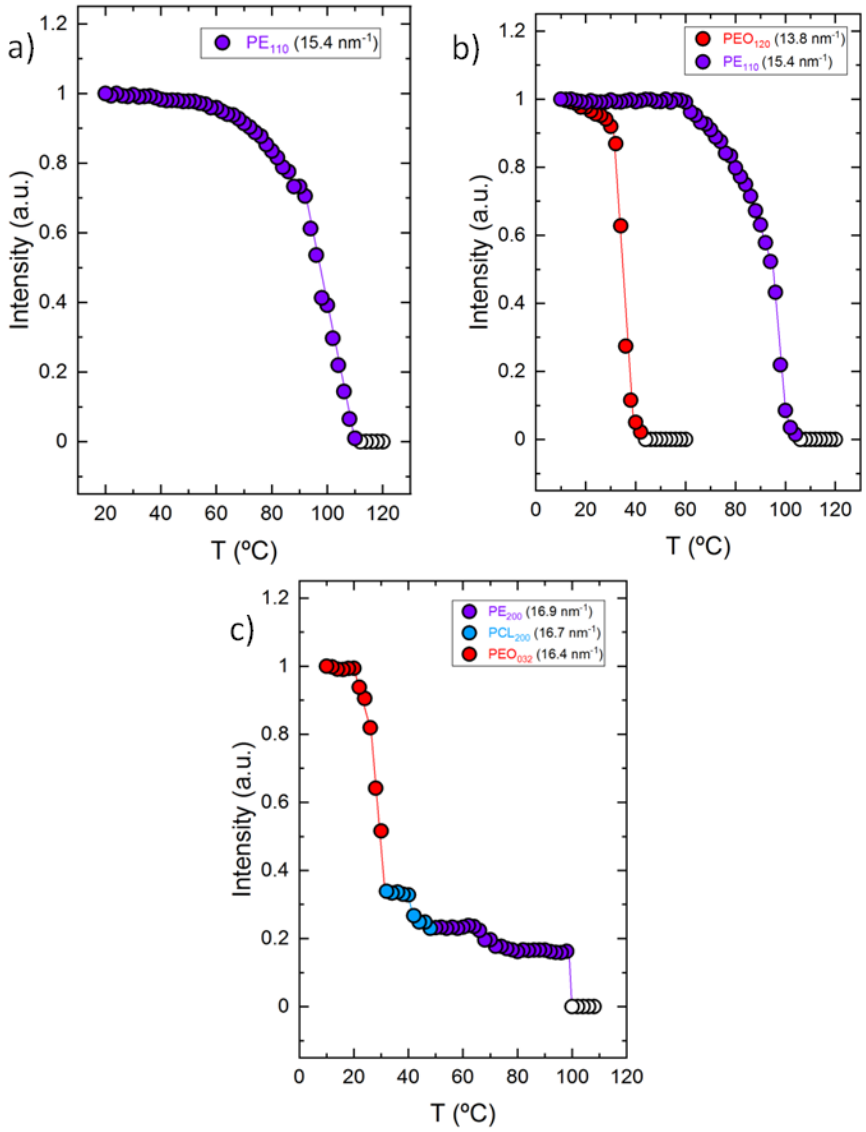

Figure 6.8. Normalized WAXS intensities as a function of temperature from WAXS data represented in Figure 6.7 for a) $PE^{9.5}$ (PE_{110} (15.4 nm^{-1})), b) $PE_{52}{}^{9.5}$ -*b*- $PEO_{48}{}^{8.8}$ (PE_{110} (15.4 nm^{-1}) and PEO_{120} (13.8 nm^{-1})) and c) $PE_{37}{}^{9.5}$ -*b*- $PEO_{34}{}^{8.8}$ -*b*- $PCL_{29}{}^{7.6}$ (PE_{200} (16.9 nm^{-1}), (PCL_{1200} (16.7nm^{-1}) and (PEO_{032} (16.4 nm^{-1})) with colored data points and lines indicating crystallization of the corresponding blocks. Empty data points represent the molten state

In addition, to confirm the crystallization of each of the blocks in the cooling scans, results for the subsequent heating scans are provided in the Appendix. Figures A.6.1-A.6.4 report WAXS diffraction patterns and normalized intensity measurements of both triblock terpolymers here analyzed (T1 and T2).

6.2.4 Polarized Light Optical Microscopy (PLOM)

PLOM was employed to follow the crystallization of the blocks and give evidence of the final morphology. Micrographs taken at room temperature after cooling the samples at 20 ºC/min are shown in Figures 6.9 and 6.12.

Figure 6.9a corresponds to the homopolymer $PE^{7.1}$, showing very small spherulites. In Figure 6.9b, the $PE_{32}^{7.1}$ -*b*- $PEO_{68}^{15.1}$ diblock copolymer shows large spherulites characteristic of PEO. According to the evidence gathered in the previous sections, the PE block crystallizes first, probably forming microspherulites that are later engulfed by the much larger PEO block spherulites.

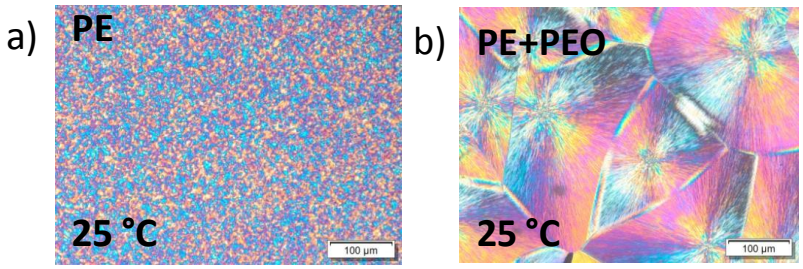

Figure 6.9. PLOM micrographs taken at room temperature after cooling from the melt at 20 ºC/min for a) $PE^{7.1}$ and b) $PE_{32}^{7.1}$ -*b*- $PEO_{68}^{15.1}$, indicating the crystalline phases at 25 ºC.

The triple crystalline morphology of the $PE_{22}^{7.1}$ -*b*- $PEO_{46}^{15.1}$ -*b*- $PCL_{32}^{10.4}$ (T1) triblock terpolymer is shown in Figure 6.10, in which the whole cooling process at 20 ºC/min was followed. Figure 6.10a indicates that the sample at 120 ºC is in the molten state. Cooling the sample to 80 ºC (Figure 6.10b), the first block to crystallize is the PE block, forming very small and barely observable microspherulites. Due to this difficulty, light intensity measurements as a function of temperature were calculated since slight changes in the PLOM micrographs can be better detected.

Figure 6.11 shows all intensity changes that occur during the cooling scan of this sample. As shown in Figure 6.11a, the increase in intensity refers to the crystallization of the PE block, which crystallizes until saturation at 80 ºC. Going back to Figure 6.10c, the second block to crystallize is the PCL block at 40 ºC. A slight change is appreciable in this micrograph, but the difference in intensity in Figure 6.11b confirms the crystallization of the PCL block. Finally, Figure 6.10d-e shows the crystallization of the PEO block, which corresponds to the sharp increase in intensity in Figure 6.11c. Due to the crystallization of the three blocks, a triple crystalline block copolymer is obtained. .

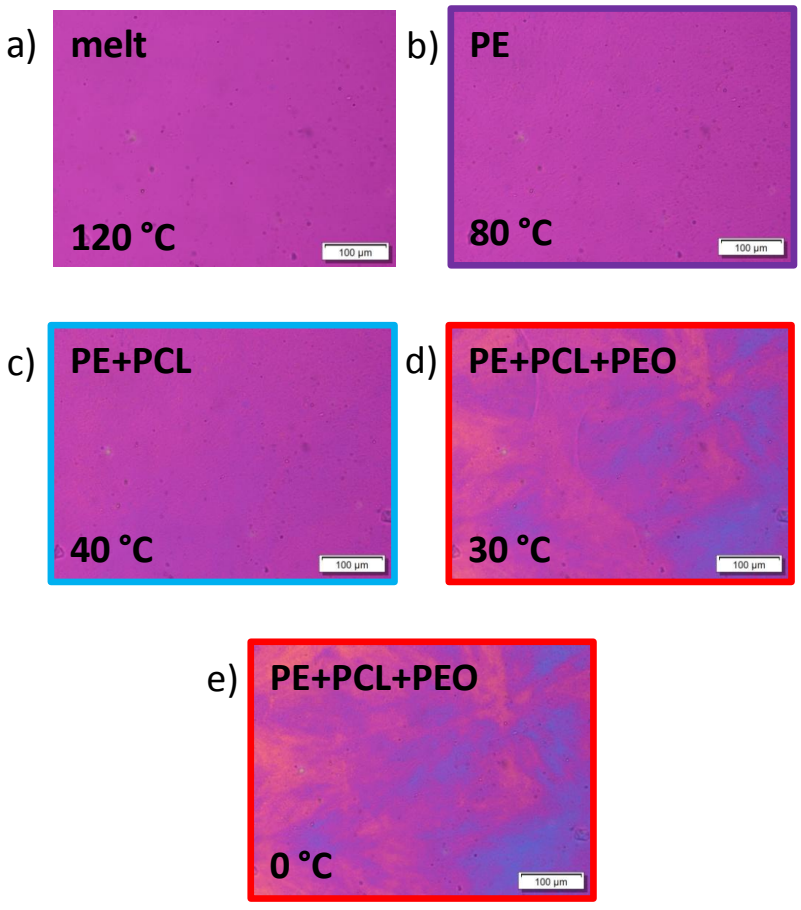

Figure 6.10. PLOM micrographs of the triblock terpolymer $PE_{22}^{7.1}$-*b*-$PEO_{46}^{15.1}$-*b*-$PCL_{32}^{10.4}$ (T1) cooling the sample from the melt at 20 ºC/min. Colored squares (violet for PE, blue for PCL, and red for PEO) refer to the crystallized block at their corresponding temperature, indicated at the top of the micrographs for a) molten state at 120 ºC, b) PE at 80 ºC, c) PE and PCL at 40 ºC, d) PE, PCL and PEO at 30 ºC, and e) PE, PCL, and PEO at 0 ºC

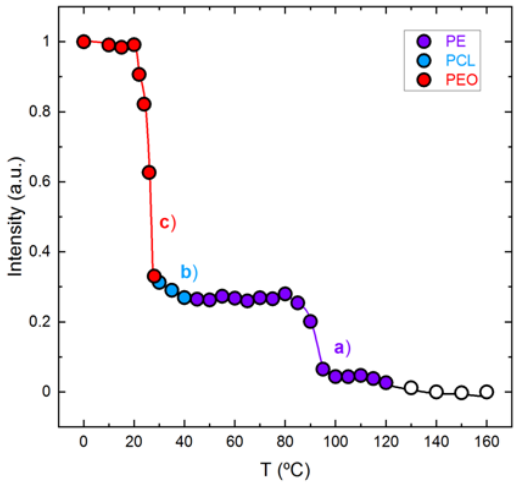

Figure 6.11. PLOM intensity measurement calculation from data in Figure 6.10 as a function of temperature during cooling from the melt at 20 ºC/min, indicating crystallization of: a) the PE block, b) the PCL block, and c) the PEO block for the triblock terpolymer $PE_{22}^{7.1}$ -*b*- $PEO_{46}^{15.1}$ -*b*- $PCL_{32}^{10.4}$ (T1). Ccolored data points and lines (violet for PE, blue for PCL and red for PEO) are employed in order to follow the crystallization of the blocks. Empty data points represent the molten state of the sample

The micrographs taken during the subsequent heating of this $PE_{22}^{7.1}$ -*b*- $PEO_{46}^{15.1}$ -*b*- $PCL_{32}^{10.4}$ (T1) triblock terpolymer are provided in Figure A.6.5 in the Appendix, along with the normalized intensity calculations as a function of temperature also in the Appendix (Figure A.6.6). These graphs show the melting of all blocks, demonstrating the triple crystalline behavior of the sample. In addition, all PLOM observations match very well with DSC (Figure 6.3) and WAXS (Figures 6.5 and 6.6) results previously discussed.

Regarding the second system listed in Table 3.3 in the Experimental Chapter, the same PLOM observations were performed in order to compare the crystalline behavior of both series of samples. Figure 6.12 shows the PLOM micrographs at 25 ºC of the precursors of the $PE_{37}^{9.5}$ -*b*- $PEO_{34}^{8.8}$ -*b*- $PCL_{29}^{7.6}$ (T2) triblock terpolymer after cooling the samples at a constant rate of 20 ºC/min.

Figure 6.12a corresponds to the $PE^{9.5}$ homopolymer, in which very small PE spherulites can be observed. The micrograph in Figure 6.12b, on the contrary, refers to the $PE_{52}^{9.5}$ -*b*- $PEO_{48}^{8.8}$ diblock copolymer. Although there are no clear PEO spherulites, it shows a double crystalline morphology at room temperature.

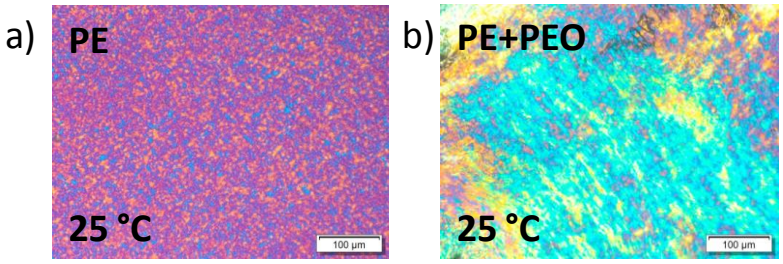

Figure 6.12. PLOM micrographs taken at room temperature after cooling the samples from the melt at 20 ºC/min for a) $PE^{9.5}$ and b) $PE_{52}^{9.5}$ -*b*- $PEO_{48}^{8.8}$, indicating the crystallized blocks at room temperature

Figure 6.13 shows the cooling process using 20 ºC/min as cooling rate for the triblock terpolymer $PE_{37}^{9.5}$ -*b*- $PEO_{34}^{8.8}$ -*b*- $PCL_{29}^{7.6}$ (T2). As indicated in Figure 6.13a, at 118 ºC, the sample is melted. Decreasing temperature to 110 ºC (Figure 6.13b), a slight change in the micrograph indicates that the crystallization of the PE block occurred. In addition, Figure 6.13c shows that all PE has crystallized until saturation at 50 ºC. Once again, it is challenging to notice meaningful changes in the micrographs, so the normalized intensity calculations as a function of temperature are provided in Figure 6.14. The first increase in intensity corresponds to the crystallization of the PE block (Figure 6.14a). The following slight increase in intensity corresponds to the crystallization of the PCL block (Figure 6.14b), also shown in Figure 6.13d at 40 ºC. Cooling down the sample, the last block to crystallize is the PEO block (Figure 6.13e-f), and its crystallization continues until saturation is obtained at approximately 0 ºC (Figure 6.13g). Figure 6.14c indicates that the crystallization of the PEO block starts at around 28 ºC and continues with further decreases in temperature.

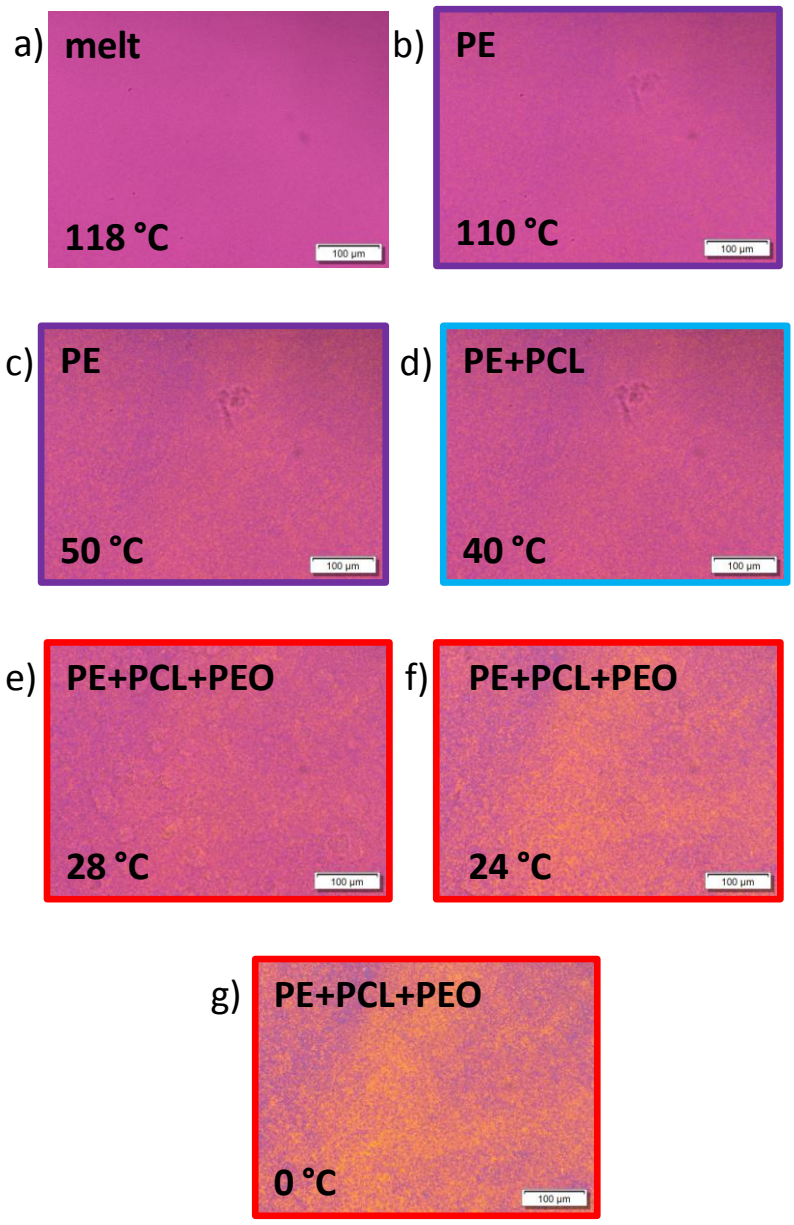

Figure 6.13. PLOM micrographs of the triblock terpolymer $PE_{37}^{9.5}$ -*b*- $PEO_{34}^{8.8}$ -*b*- $PCL_{29}^{7.6}$ (T2) cooling the sample from the melt at a constant rate of 20 ºC/min. Coloured squares (violet for PE, blue for PCL, and red for PEO) refer to the crystallized block at the corresponding temperature indicated on the top of the micrographs for a) molten state at 118 ºC, b) PE at 110 ºC, c) PE at 50 ºC, d) PE and PCL at 40 ºC, e) PE, PCL and PEO at 28 ºC, f) PE, PCL, and PEO at 24 ºC, and g) PE, PCL, and PEO at 0 ºC

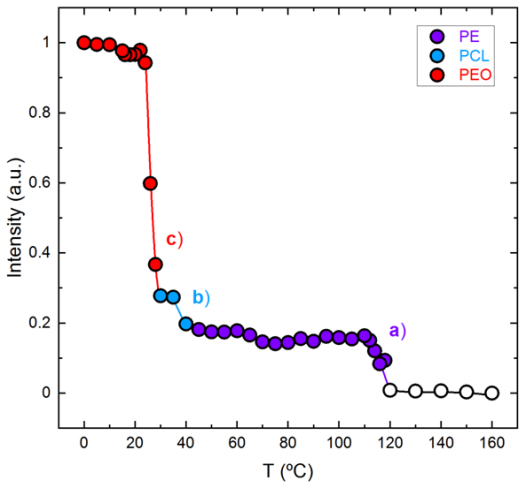

Figure 6.14. PLOM intensity measurement calculations from data in Figure 6.13 as a function of temperature during cooling from the melt at 20 ºC/min, indicating crystallization of: a) the PE block, b) the PCL block, and c) the PEO block for the triblock terpolymer $PE_{37}^{9.5}$ -*b*- $PEO_{34}^{8.8}$ -*b*- $PCL_{29}^{7.6}$ (T2). Colored data points and lines (violet for PE, blue for PCL and red for PEO) are employed in order to follow the crystallization of the blocks. Empty data points represent the molten state of the sample

Figure A.6.7 and A.6.8 in the Appendix provide the subsequent heating scan and the normalized intensity measurements of the $PE_{37}^{9.5}$ -*b*- $PEO_{34}^{8.8}$ -*b*- $PCL_{29}^{7.6}$ (T2) triblock terpolymer, respectively. The discussed results agree well with DSC (Figure 6.4) and WAXS (Figures 6.7 and 6.8), as shown previously.

6.3 PE-*b*-PEO-*b*-PCL-*b*-PLLA Tetrablock Quarterpolymers (Q1 and Q2)

6.3.1 Small-angle X-Ray Scattering (SAXS)

SAXS measurements of all materials were employed to asess the possible phase segregation in the melt. Figure 6.15 shows the SAXS patterns, in which the intensity is plotted as a function of the scattering vector (*q*), of the tetrablock quarterpolymers in the molten state (Figure 6.15a) and at room temperature (Figure 6.15b). Since in the tetrablock $PE_{18}^{7.1}$ -*b* -$PEO_{37}^{15.1}$ -*b*- $PCL_{26}^{10.4}$ -*b*- $PLLA_{19}^{7.6}$ (Q1) there are no diffraction peaks in the melt (Figure 6.15aQ1), the only sample which is probably phase segregated in the melt is the tetrablock quarterpolymer $PE_{29}^{9.5}$ -*b*- $PEO_{26}^{8.8}$ -*b*- $PCL_{23}^{7.6}$ -*b*- $PLLA_{22}^{7.3}$ (Q2) (Figure 6.15aQ2), because of the presence of a sharp diffraction peak at low *q* values and a very weak second order reflection located at 2*q* with respect to the first. Therefore, lamellar phase segregation is most probably present in the Q2 melt.

However, when the sample is cooled down, a crystallization break out occurs (see the shift in q values between the sharp reflection in the melt and the weaker reflection at room temperature that appears at lower q values). The phase structure formed by phase segregation in the melt was probably destroyed and replaced by crystalline lamellae that scattered X-rays at lower *q* values. Break-out usually occurs when the phase segregation between block components is weak (Figure 6.15bQ2). This weak phase segregation behavior was corroborated by the presence of small PE spherulites observed by PLOM in the Q2 quarterpolymer, even when the PE content in the material is only 29%, as it will be discussed below.

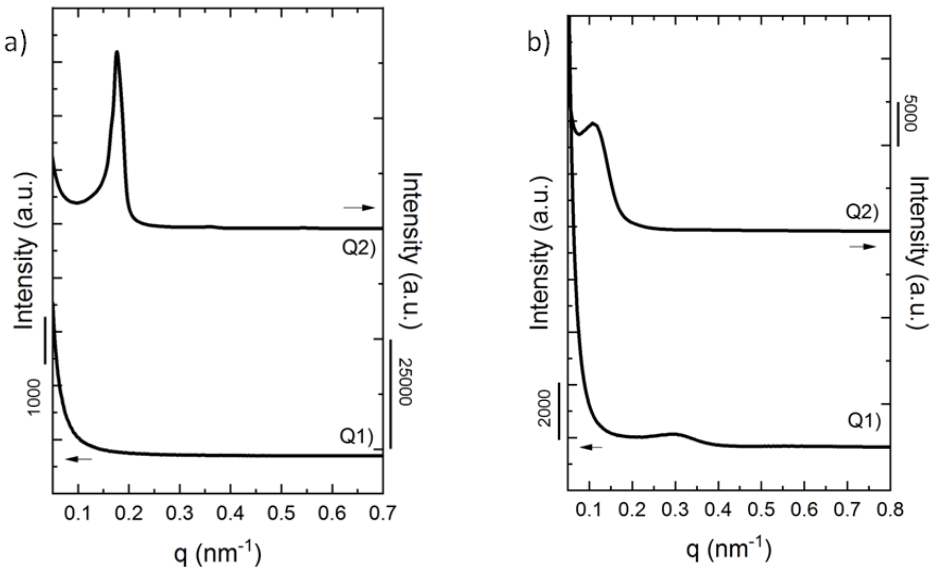

Figure 6.15. SAXS patterns of Q1) $PE_{18}^{7.1}$ -*b* -$PEO_{37}^{15.1}$ -*b*- $PCL_{26}^{10.4}$ -*b*- $PLLA_{19}^{7.6}$, and Q2) $PE_{29}^{9.5}$ -*b*- $PEO_{26}^{8.8}$ -*b*- $PCL_{23}^{7.6}$ -*b*- $PLLA_{22}^{7.3}$at a) molten state at 180 °C indicating a lamellar structure in the melt by 1:2 *q* position of the scattering peaks, and b) room temperature 25 °C

The segregation strength in diblock copolymers can be predicted by calculating the Flory-Huggins interaction parameter (χ) and multiplying it by *N*, the polymerization degree. However, the mean-field segregation theory was derived for diblock copolymers, and when analyzing triblock or tetrablock copolymers the theoretical estimation of the segregation strength becomes more complicated. To our knowledge, the experimental determination of χ values for terpolymers or quarterpolymers has not been reported yet. Nevertheless, an approximate estimation for each pair of blocks has been calculated by using the solubility parameters of PE, PEO, PCL, and PLLA reported in literature[2, 3].

If the segregation strength χN is lower or equal to 10 the diblock copolymers are miscible in the melt, if χN is between 10-30 they are weakly segregated, if χN is between 30-50 the segregation is intermediate, and if $\chi N > 50$ the system is strongly segregated. The values do not fully represent the whole interactions in our samples, and as data in Table A.6.1 in the Appendix shows,

there is a wide range in the obtained values. As previously mentioned, only one tetrablock studied here is phase segregated in the melt (Figure 6.15aQ2), which suggests that the molecular weight of the blocks and composition affects phase behaviour due to the contribution of each pair of blocks to the segregation strength.

6.3.2 Non-isothermal Crystallization by DSC

Non-isothermal DSC scans show that each block is able to crystallize, although some crystallization transitions overlap. DSC experiments upon cooling from the melt at 20 °C/min in Figure 6.16 show the exothermic crystallization peaks of the blocks of the corresponding tetrablock quarterpolymers: Figure 6.16a corresponds to $PE_{18}^{7.1}$ -*b* -$PEO_{37}^{15.1}$ -*b*- $PCL_{26}^{10.4}$ -*b*- $PLLA_{19}^{7.6}$ (Q1), and Figure 6.16b to $PE_{29}^{9.5}$ -*b*- $PEO_{26}^{8.8}$ -*b*- $PCL_{23}^{7.6}$ -*b*- $PLLA_{22}^{7.3}$ (Q2). Block content and molecular weight of each of the blocks (subscripts indicate composition in wt% and superscripts indicate the number-average molecular weight (M_n) values in kg/mol) is different in both tetrablock quarterpolymers (Q1 vs. Q2). Crystallization (T_c) of each of the blocks has been assigned by analysing the WAXS data measured under identical cooling conditions (shown and described below).

Figure 6.16a shows the crystallization of all blocks, and the sequence is as follows: PLLA block, PE block, PCL block, and PEO block (colored arrows indicate crystallization peaks of each block, green for PLLA block, violet for PE block, blue for PCL block and red for PEO block). Note that a close-up is inserted in Figure 6.16a to properly identify the crystallization exotherms of the PLLA and the PE blocks since both crystallizations are almost overlapped. However, this close-up clarifies that the PLLA block is the first block to crystallize at 84 °C followed by the PE block at 82 °C. This temperature value for the crystallization temperature of the PLLA block may seem to be too low, but WAXS measurements presented below confirm this crystallization sequence (Figure 6.18a and Figure 6.19a). The crystallization of the PCL and PEO blocks occurs in the same

temperature range; however, in this case, the very first peak at 42 °C corresponds to the PCL block, followed by the crystallization of the PEO block at the lowest temperature, also confirmed by WAXS results in Figure 6.18a and Figure 6.19a.

Figure 6.16b corresponds to the $PE_{29}^{9.5}$ -*b*- $PEO_{26}^{8.8}$ -*b*- $PCL_{23}^{7.6}$ -*b*- $PLLA_{22}^{7.3}$ tetrablock quarterpolymer (Q2). In this case, the crystallization of the PLLA block does not occur, as the first block to crystallize is the PE block (violet arrow). In addition, a close-up shows the presence of another crystallization peak between 60-75 °C, which also corresponds to the crystallization of the PE block (also demonstrated by WAXS measurements in Figure 6.18b and Figure 6.19b). This behavior is called fractionated crystallization, in which different crystallization events are observed for one component, the PE block in this case[12]. Then, at lower temperatures, overlapped crystallizations of the PCL and the PEO block occurs. We are not able to identify each of the crystallizations by DSC, but WAXS measurements below (Figure 6.18b and Figure 6.19b) determine that the PCL block crystallizes a few degrees higher than the PEO block.

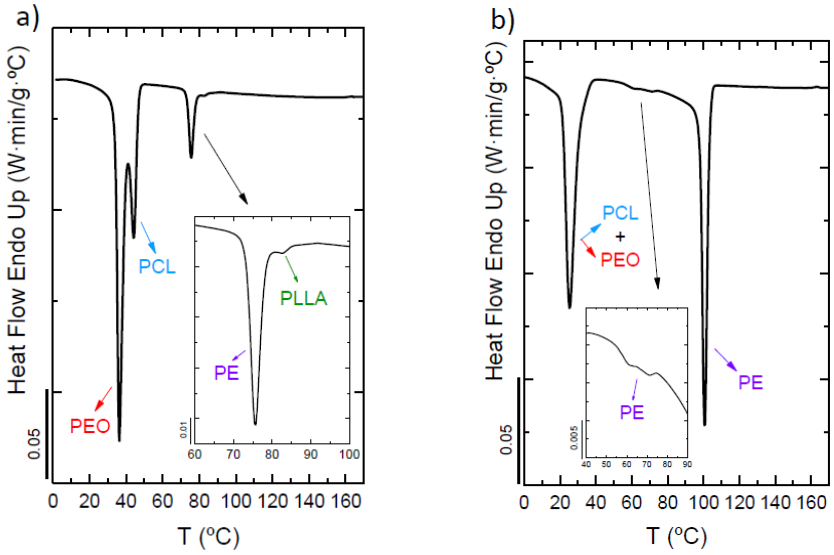

Figure 6.16. DSC cooling scans at 20 °C/min for tetrablock quarterpolymers a) $PE_{18}^{7.1}$ -*b* -$PEO_{37}^{15.1}$ -*b*- $PCL_{26}^{10.4}$ -*b*- $PLLA_{19}^{7.6}$ (Q1) and b) $PE_{29}^{9.5}$ -*b*- $PEO_{26}^{8.8}$ -*b*- $PCL_{23}^{7.6}$ -*b*- $PLLA_{22}^{7.3}$ (Q2) with arrows indicating transitions for each block (violet for PE, green for PLLA, blue for PCL and red for PEO) and close-ups to better identify crystallization peaks

Figures 6.16a and 6.16b show the effect of block content and molecular weight in the crystallization behavior, since the same blocks constitute these two tetrablock quarterpolymers. Table 6.1 summarizes the crystallization ability of the blocks in these materials. In the first quarterpolymer (Q1), all blocks are able to crystallize. In the second quarterpolymer (Q2), the PLLA block does not crystallize due to its low isotacticity (see experimental part). Both the PLLA content (19 ~ 22) and the molecular weight are almost the same (7.3 ~ 7.6 kg/mol). So the main difference in both quarterpolymers is the low isotacticity of the PLLA block within quarterpolymer Q2. In addition, the PE content in this Q2 quarterpolymer is higher than in the other quarterpolymer Q1 (29 > 18), with almost the same molecular weight (9.5 > 7.1). The content of the other two blocks constituting the quarterpolymer do not vary significantly. So, these results show that mostly the block nature plays a key role in the crystallization behavior of complex quarterpolymers with four potentially crystallizable blocks, although block content may also affect the crystallization behavior.

Table 6.1. Tetrablock quarterpolymers Q1 and Q2. The mark indicates the crystallization ability of each of the blocks. Subscripts indicate composition in wt%, and superscripts represent M_n values of each block in kg/mol.

	PLLA	**PE**	**PCL**	**PEO**
Q1. $PE_{18}^{7.1}$–*b*–$PEO_{37}^{15.1}$–*b*-$PCL_{26}^{10.4}$–*b*-$PLLA_{19}^{7.6}$	✓	✓	✓	✓
Q2. $PE_{29}^{9.5}$–*b*-$PEO_{26}^{8.8}$–*b*-$PCL_{23}^{7.6}$–*b*-$PLLA_{22}^{7.3}$	-	✓	✓	✓

Figure 6.17 shows the subsequent DSC heating scans of the tetrablock quarterpolymers at 20 °C/min with the corresponding melting peaks (T_m) of the blocks. Although in both cases, the melting of the PEO and PCL blocks occurs in the same temperature range, the first block to melt is the PEO block followed by the PCL block, according to WAXS studies. Then, the melting of the PE block occurs, and finally, the PLLA block is the last one to melt for Q1 (Figure 6.17

curve a) in which the PLLA and the PE block crystallize. A close-up in the range of 100-160 ºC is inserted in the Figure so that the melting transitions of both the PE block and the PLLA block can be clearly appreciated. In the other case, for the quarterpolymer Q2 (Figure 6.17 curve b), the PLLA block does not melt as it cannot crystallize. All these transitions and the melting sequences are confirmed by WAXS measurements (Figure A.6.9 in the Appendix).

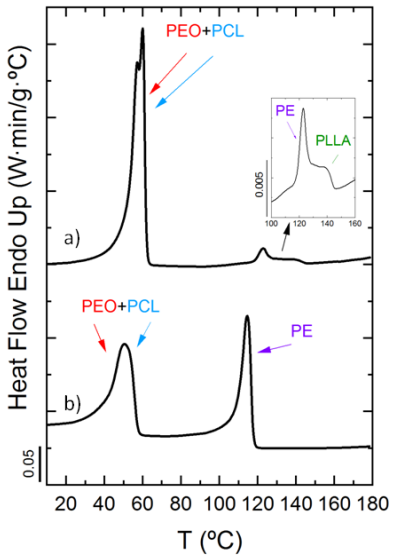

Figure 6.17. DSC heating scans at 20 °C/min for a) $PE_{18}^{7.1}$ –*b*– $PEO_{37}^{15.1}$ –*b*- $PCL_{26}^{10.4}$ –*b*- $PLLA_{19}^{7.6}$ (Q1) and b) $PE_{29}^{9.5}$ –*b*- $PEO_{26}^{8.8}$ –*b*- $PCL_{23}^{7.6}$ –*b*- $PLLA_{22}^{7.3}$ (Q2), with arrows indicating transitions for each block (violet for PE, green for PLLA, blue for PCL and red for PEO) and a close-up to better identify melting peaks

In addition, all DSC data regarding the two quarterpolymers is collected in Tables A.6.6 – A.6.8 in the Appendix, since crystallization peak temperatures (T_c) and enthalpies (ΔH_c), melting peak temperatures (T_m) and enthalpies (ΔH_m), and crystallinity degrees of each of the blocks (X_c) calculated from cooling and heating scans are provided. Note that as cooling and heating transitions of the PE and PLLA blocks, and PEO and PCL blocks overlap and estimation of the crystallinity values according to block content is provided.

6.3.3 *In situ* Wide Angle X-Ray Scattering (WAXS)

WAXS data was compared to DSC results; both sets of experiments were performed employing the same cooling/heating rates. This is very advantageous since direct comparison of DSC and WAXS results allows a better understanding of the crystallization sequence in these complex and novel tetrablock quarterpolymers.

According to literature, PLLA, PCL, and PE crystallize in orthorhombic unit[4, 5, 13] cells and PEO in a monoclinic[5] one. The crystal unit cell dimensions are the following: a=10.56 Å, b=6.05 Å and c=28.90 Å for PLLA[4]; a=7.48 Å, b=4.98 Å and c=17.26 Å for PCL[14]; a=7.96 Å, b=13.11 Å, c=19.39 Å (chain direction) and β=124º48' for PEO[15]; and a=7.40 Å, b=4.96 Å, and c=2.53 Å for PE[16]. All reflections observed in our samples correspond only to the α-form of PLLA; no signals were detected for the α'-form[6]. Table A.6.5 in the Appendix reports the indexing that agrees well with assignments widely published in the literature for PE, PEO, PCL, and PLLA crystals[3-11].

Figure 6.18 presents WAXS patterns upon cooling from the melt at 20 °C/min for the two tetrablock quarterpolymers. In the tetrablock quarterpolymer represented in Figure 6.18a (Q1) all blocks are able to crystallize, and the crystallization sequence is the following: the PLLA block at 84 °C (green), the PE block at 82 °C (violet), the PCL block at 42 °C (blue) and finally the PEO block at 24 °C (red). We are able to determine this crystallization sequence due to the characteristic reflection peaks of each of the components: $PLLA_{110/200}$ (q=12.0 nm^{-1}), $PLLA_{113/203}$ (q=13.5 nm^{-1}), PEO_{120} (q=13.8 nm^{-1}), PE_{110} (q=15.4 nm^{-1}), PCL_{110} (q=15.0 nm^{-1}), PCL_{111} (q=15.6 nm^{-1}), $PLLA_{210}$ (q=15.7 nm^{-1}), $PEO_{032/112/132/212}$ (q=16.4 nm^{-1}), PCL_{200} (q=16.7 nm^{-1}) and PE_{200} (q=16.9 nm^{-1}). The presence of these scattering peaks at their corresponding q values corroborates the crystallization of each of the blocks.

In the same way, in Figure 6.18b, the scattering peaks of the corresponding blocks of the tetrablock quarterpolymer (Q2) are assigned with colored arrows. The first block to crystallize is the PE block at 104 °C (violet), followed by the PCL block (blue) at 32 °C, and finally by the PEO block (red) at 20 °C. These results confirm that the crystallization of the PLLA block in this sample does not occur, as its characteristic scattering peaks are not present in the WAXS patterns. These results confirm what was previously shown in the DSC scans in Figure 6.16b.

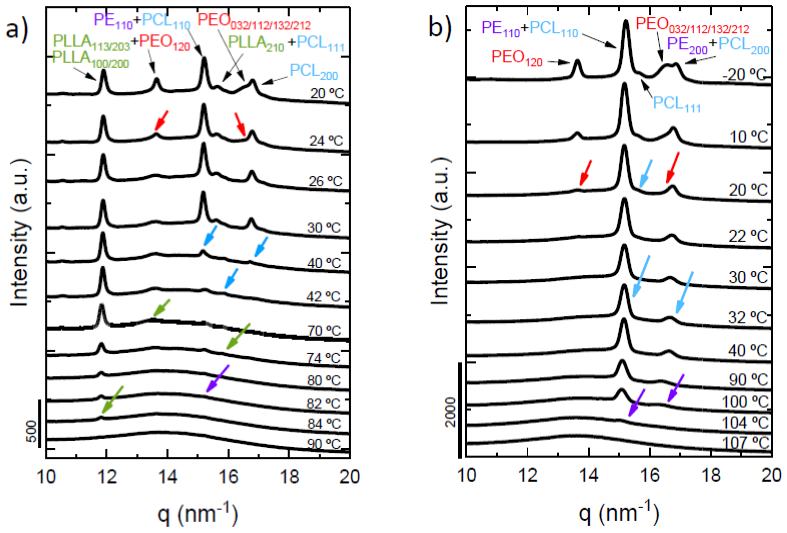

Figure 6.18. WAXS patterns taken during cooling from the melt at 20 °C/min for a) $PE_{18}^{7.1}$ -*b*- $PEO_{37}^{15.1}$ -*b*- $PCL_{26}^{10.4}$ -*b*- $PLLA_{19}^{7.6}$ (Q1) and b) $PE_{29}^{9.5}$ -*b*- $PEO_{26}^{8.8}$ -*b*- $PCL_{23}^{7.6}$ -*b*- $PLLA_{22}^{7.3}$ (Q2) at different temperatures with arrows indicating transitions for each block (violet for PE, green for PLLA, blue for PCL and red for PEO) and the corresponding (hkl) planes of the blocks

In order to determine the exact temperatures at which crystallization of each of the blocks starts and the whole temperature range in which they crystallize, the normalized intensities of the scattering peaks as a function of temperature are plotted in Figure 6.19. The same color code employed previously is used to facilitate comprehension of the plots. Figure 6.19a shows the results for the $PE_{18}^{7.1}$ -*b*- $PEO_{37}^{15.1}$ -*b*- $PCL_{26}^{10.4}$ -*b*- $PLLA_{19}^{7.6}$ tetrablock quarterpolymer (Q1), in which all four blocks are able to crystallize. The exclusive $PLLA_{100/200}$ (green) and

PEO_{032} (red) signals are employed to determine their crystallization ranges because these signals correspond only to PLLA or PEO crystals. The first sharp increase in the $PLLA_{100/200}$ (green) signal corresponds to the PLLA block crystallization starting at 90 °C, whereas the increase starting at 24 °C in the PEO_{032} (red) confirms its crystallization. However, for the PE and PCL blocks, the joint reflection of PE_{110} (violet) and PCL_{110} (blue) is used, as there are no signals that correspond only to the PE or the PCL block. The first increase corresponds to the PE block crystallization starting at 82 °C, and the second sharp increase to the PCL block crystallization at 42 °C. The same methodology is employed for the $PE_{29}^{9.5}$ -*b*- $PEO_{26}^{8.8}$ -*b*- $PCL_{23}^{7.6}$ -*b*- $PLLA_{22}^{7.3}$ (Figure 6.19b) tetrablock quarterpolymer (Q2) in order to determine the crystallization ranges of the blocks.

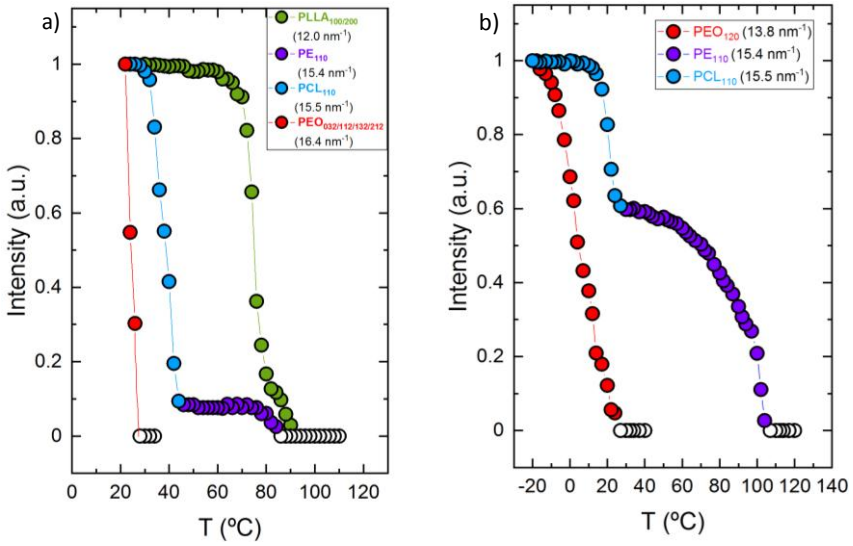

Figure 6.19. Normalized WAXS intensities as a function of temperature of the indicated block reflections for a) $PE_{18}^{7.1}$ -*b*- $PEO_{37}^{15.1}$ -*b*- $PCL_{26}^{10.4}$ -*b*- $PLLA_{19}^{7.6}$ (Q1) and b) $PE_{29}^{9.5}$ -*b*- $PEO_{26}^{8.8}$ -*b*- $PCL_{23}^{7.6}$ -*b*- $PLLA_{22}^{7.3}$ (Q2) with colored data points and lines (violet for PE, green for PLLA, blue for PCL and red for PEO) to follow the crystallization of each block. Empty data points represent the molten state of the corresponding block in the samples.

The WAXS subsequent heating transitions are reported in Figure A.6.9 in the Appendix, which also confirm the presence of the crystalline blocks identified during cooling from the melt by WAXS (Figure 6.18).

6.3.4 Polarized Light Optical Microscopy (PLOM)

Polarized light optical microscopy (PLOM) experiments allow studying the sequential crystallization of the blocks of the tetrablock quarterpolymers, as well as their superstructural organization. PLOM experiments have been performed using the same cooling and heating conditions employed in DSC and *in situ* WAXS experiments, thus results are directly comparable, and the crystalline behaviour and morphology of the materials can be determined.

Figure 6.20 shows PLOM micrographs upon cooling from the melt at 20 °C/min for the $PE_{18}^{7.1}$ -*b*- $PEO_{37}^{15.1}$ -*b*- $PCL_{26}^{10.4}$ -*b*- $PLLA_{19}^{7.6}$ tetrablock quarterpolymer (Q1). When the sample is in the molten state, at 95 °C (see micrograph a), there are no observable features. A legend on the top of the micrographs indicates the crystalline phases that should be present at the indicated temperatures according to previously mentioned DSC and WAXS evidence. In addition, the same color code is employed to follow the crystallization of the different blocks.

Micrograph b (Figure 6.20) shows the first PLLA block spherulites at 88 °C; the small birefringent spots indicate crystallization of PLLA block crystals has started. Cooling down the sample to 80 °C in micrograph c (Figure 6.20), both PLLA block spherulites (which can already contain some PE lamellae within them) and smaller PE block spherulites grow simultaneously, as the crystallization of the PLLA block and the PE block is overlapped in a temperature range of approximately 70-90 °C (Figure 6.18a). We have a collection of PLLA block nucleated spherulites and PE block nucleated spherulites, which may start simultaneously but eventually contain both PLLA and PE crystalline lamellae within them; hence they are double crystalline spherulites.

Cooling down the sample to 45 °C, the number of PLLA and PE nuclei has increased, as shown in micrograph d (Figure 6.20), PLLA nucleated spherulites and PE nucleated spherulites have grown at the same temperature range. Then, as

crystallization of the PCL starts at 42 °C according to WAXS measurements (Figure 6.18a), a triple crystalline material is presented at 40 °C in micrograph e (Figure 6.20), with wide size range of triple crystalline spherulites covering the entire microscope view field. PCL lamellae nucleate inside the PLLA and PE-based spherulites.

At 34 °C the crystallization of the PEO blocks starts, and it is evident since there is a clear change in the birefringence as shown in the left side of micrograph f (Figure 6.20), in addition to the WAXS results reported in Figure 6.18a. Micrograph g (Figure 6.20) shows that almost all the PEO block has already crystallized at 30 °C, as there are no more observable differences in birefringence upon cooling the sample to 0 °C in micrograph h (Figure 6.20). So, these PLOM micrographs show that the crystallization of all blocks has occurred, finally obtaining tetracrystalline spherulites. As far as we are aware, this is the first time that a polymeric sample with tetracrystalline spherulites has been reported.

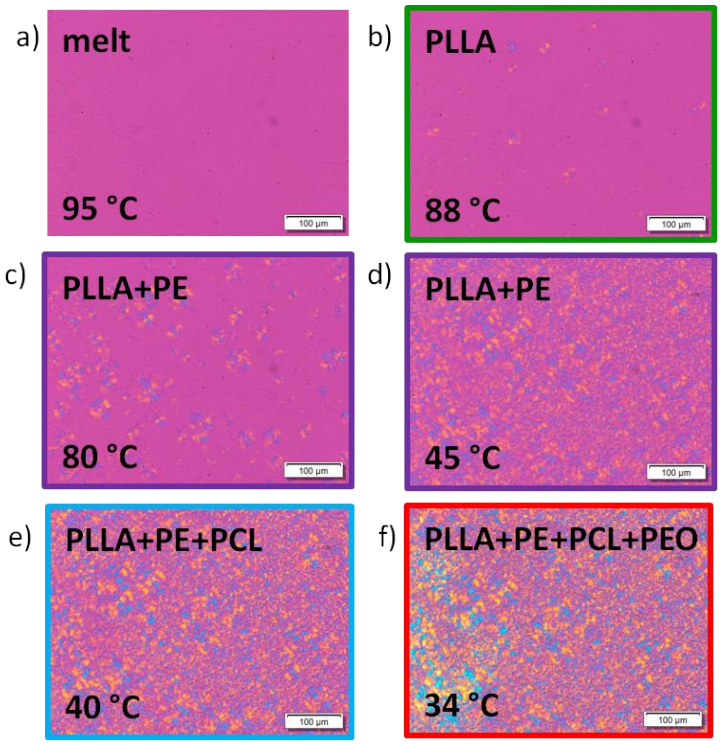

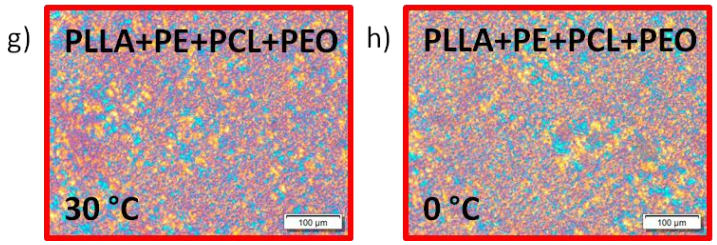

Figure 6.20. PLOM micrographs taken upon cooling from the melt at 20 °C/min with colored boxes indicating the crystallization of each of the blocks (violet for PE, green for PLLA, blue for PCL and red for PEO) for the tetrablock quarterpolymer $PE_{18}^{7.1}$ -*b* -$PEO_{37}^{15.1}$ -*b*- $PCL_{26}^{10.4}$ -*b*- $PLLA_{19}^{7.6}$ (Q1): a) molten state at 95 ºC, b) PLLA at 88 ºC, c) PLLA and PE at 80 ºC, d) PLLA and PE at 45 ºC, e) PLLA, PE and PCL at 40 ºC, f) PLLA, PE, PCL and PEO at 34 ºC, g) PLLA, PE, PCL and PEO at 30 ºC, and h) PLLA, PE, PCL and PEO at 0 ºC.

In addition, in order to properly analyze the crystallization of each of the blocks in the PLOM micrographs, light intensity measurements[17] were performed. Figure 6.21 shows the recorded change in intensity as a function of temperature, with a-e colored letters of the micrographs in Figure 6.20 in order to see the corresponding morphology at those temperatures. Starting from the molten state (a), the first slight intensity increase corresponds to the crystallization of the PLLA block (b), followed by a sharper increase due to the PE block crystallization (c). Then, the crystallization of the PCL block increases the intensity value (d), and finally, the sharpest increase in intensity is due to the crystallization of the PEO block (e). This complements the micrographs shown in Figure 6.20, since it is hard to notice slight changes in intensity by human eyes, although the change caused by the crystallization of the PEO block is well noticeable in micrograph e in Figure 6.20.

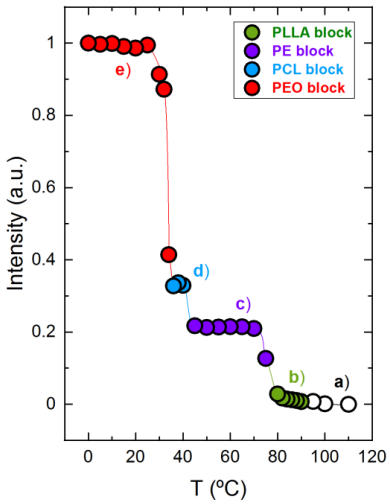

Figure 6.21. PLOM intensity measurements corresponding to the micrographs of Figure 6.20 as a function of temperature indicating: a) melt and the progressive crystallization upon cooling of: b) PLLA block, c) PE block, d) PCL block, and e) PEO block for the tetrablock quarterpolymer $PE_{18}^{7.1}$ –*b*– $PEO_{37}^{15.1}$ –*b*- $PCL_{26}^{10.4}$ –*b*- $PLLA_{19}^{7.6}$ (Q1), with colored data points and lines (green for PLLA, violet for PE, blue for PCL and red for PEO) to follow the crystallization of each block. Empty data points represent the molten state of the sample

In addition, subsequent heating after quenching the quarterpolymer Q1 was performed in order to corroborate these results, and analogous observations were recorded. For more details, additional results are shown in Figures A.6.10 and A.6.11 in the Appendix.

Furthermore, an additional measurement was performed with PLOM in order to see the morphology within larger spherulites than those obtained in Figure 6.20h. After melting the $PE_{18}^{7.1}$ –*b* –$PEO_{37}^{15.1}$ –*b*- $PCL_{26}^{10.4}$ –*b*- $PLLA_{19}^{7.6}$ (Q1) quarterpolymer, an isothermal step at 88 ºC was performed for 40 minutes to let the PLLA block crystallize until saturation forming large spherulites (Figure 6.22a). The whole microscope field was filled with PLLA spherulites that are much larger than those obtained during the non-isothermal experiment discussed above (Figure 6.20h). These PLLA block spherulites can be considered a template partially filled with PLLA block crystalline lamellae (notice that the PLLA content

is only 19% and not all of this material can crystallize) and the rest is composed by amorphous chains of all the tetrablock constituents (i.e., PLLA, PE, PCL and PEO). It is remarkable that these spherulitic templates can display Maltese Crosses and a negative sign, indicating that the PLLA chains are tangential to the spherulitic radius and also a banding extinction pattern.

Once complete crystallization of the PLLA block occurred at 88 ºC, the sample was cooled down at 20 ºC/min to room temperature, allowing the rest of the blocks of the quarterpolymer (the PE block, the PCL block and the PEO block) to crystallize at their corresponding crystallization temperatures obtaining finally the morphology shown in Figure 6.22b. The clear change in birefringence corroborates the crystallization of the last block (the PEO block, as discussed above in Figure 6.20), but since the PE block and the PCL block also crystallize during cooling, the final morphology corresponds to tetracrystalline spherulites that also display Maltese crosses, negative signs and banding patterns. Such typical spherulitic characteristics probably indicate that the spherulite is composed of four types of lamellar crystals that grow radially within the PLLA template skeleton. The inner lamellar morphology of the spherulites was visualized by AFM (see below).

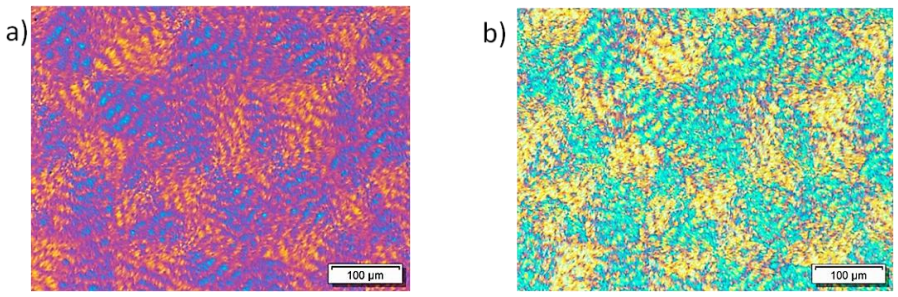

Figure 6.22. PLOM micrograph of the tetrablock quarterpolymer $PE_{18}^{7.1}$ –*b*– $PEO_{37}^{15.1}$ –*b*- $PCL_{26}^{10.4}$ –*b*- $PLLA_{19}^{7.6}$ (Q1) of a) after isothermally crystallizing the sample at 88 ºC during 40 minutes (a temperature at which only the PLLA block can crystallize), and b) at room temperature after cooling the sample at 20 ºC/min allowing the crystallization of the other three blocks within the PLLA spherulites, so that tetracrystalline spherulites are formed

In Figure 6.23, light intensity measurements and PLOM micrographs of the tetrablock quarterpolymer $PE_{29}^{9.5}$ -*b*- $PEO_{26}^{8.8}$ -*b*- $PCL_{23}^{7.6}$ -*b*- $PLLA_{22}^{7.3}$ (Q2) are presented. Note that the PLLA block does not crystallize according to DSC/WAXS results (Figure 6.16b and Figure 6.18b). The light intensity analysis corroborates that crystallization of the PLLA does not occur (Figure 6.23). The first sharp increase at approximately 100 °C corresponds to the crystallization of the PE block, and the pattern that shows the PLOM micrographs at 100 °C confirms so, as the PE block precursor has also been measured and found to have a very high nucleating density that leads to a microspherulitic morphology (not shown). Cooling down the sample crystallization of the PCL block happens at 32 °C, and the change in birefringence is evident in the micrograph shown at 28 °C. Then, crystallization of the PEO block that starts at 20 °C is recorded by the increase in intensity as well as in the brightness of the micrograph at 10 °C (Figure 6.23).

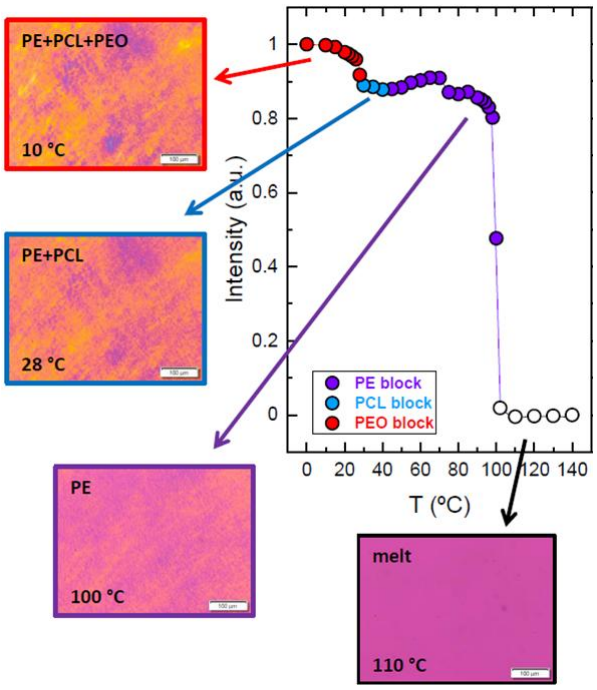

Figure 6.23. PLOM intensity measurements as a function of temperature with micrographs of cooling from the melt at 20 °C/min at the indicated temperatures with coloured arrows and data points indicating crystallization of each block for the tetrablock quarterpolymer $PE_{29}^{9.5}$ -*b*- $PEO_{26}^{8.8}$ -*b*- $PCL_{23}^{7.6}$ -*b*- $PLLA_{22}^{7.3}$ (Q2) (violet for PE, blue for PCL and red for PEO)

6.3.5 Atomic Force Microscopy (AFM)

The lamellar structure of the samples was analyzed by AFM employing two different thermal protocols to crystallize the blocks within the samples. The AFM phase micrographs correspond to the tetrablock quarterpolymer $PE_{18}^{7.1}$ -*b*- $PEO_{37}^{15.1}$ -*b*- $PCL_{26}^{10.4}$ -*b*- $PLLA_{19}^{7.6}$ (Q1). The cooling rates employed in the preparation of the samples before obtaining these AFM micrographs at room temperature are the following: 50 ºC/min for Figure 6.24a and 20 ºC/min for Figure 6.24b.

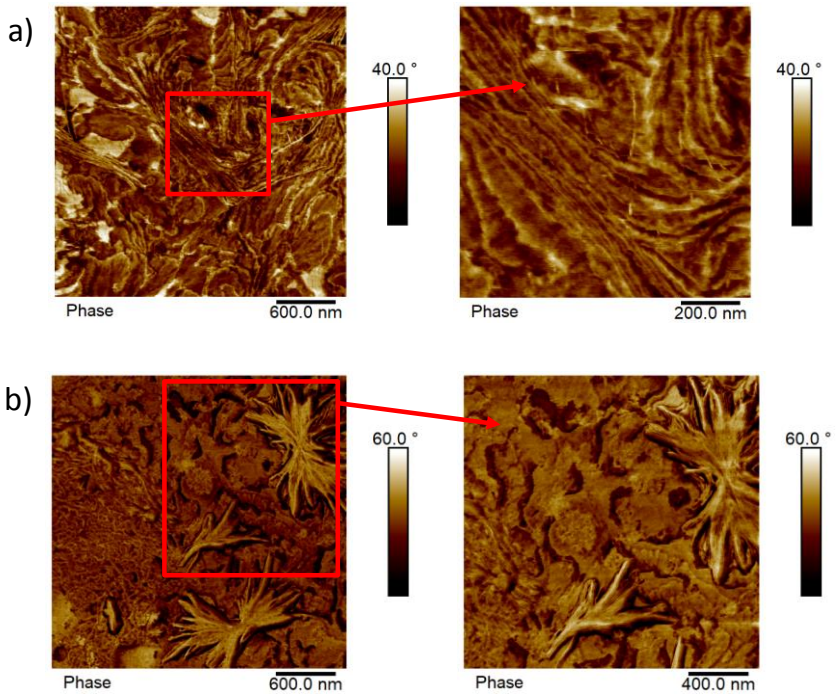

Figure 6.24. AFM micrographs of the tetrablock quarterpolymer $PE_{18}^{7.1}$ -*b*- $PEO_{37}^{15.1}$ -*b*- $PCL_{26}^{10.4}$ -*b*- $PLLA_{19}^{7.6}$ (Q1) observed at 25 ºC with close-ups of the indicated regions enclosed by a red box, applying two different thermal protocols: a) Cooling from the melt at 50 ºC/min, and b) Cooling from the melt at 20 ºC/min

A close observation of the microstructure in these AFM micrographs makes it difficult to distinguish among the four crystalline blocks of the sample. It is very difficult to identify lamellae of different average thicknesses that correspond to

each of the blocks. In addition, as some of the lamellae are edge-on, the calculation of an approximate value of average lamellar thickness is difficult. In the sample that was cooled at 20 ºC/min, Figure 6.24b shows nascent spherulites with sizes below 1 micron, composed of abundant radial lamellae that must correspond to lamellae of the four different crystalline components.

Figure 6.25 shows AFM micrographs for the $PE_{29}^{9.5}$ -*b*- $PEO_{26}^{8.8}$ -*b*- $PCL_{23}^{7.6}$ -*b*- $PLLA_{22}^{7.3}$ tetrablock quarterpolymer (Q2). The sample was prepared by using 20 ºC/min as cooling rate; no other rates were employed since no significant changes were obtained. The micrographs show the lamellar microstructure of the sample. The PLLA block in this tetrapolymer does not crystallize (Figures 6.16b and Figure 6.18b). Nevertheless, even having one crystalline block less than in the previous case (Figure 6.24), the distinction of the PE, PCL, and PEO crystalline lamellae remains complicated. An attempt to identify the three blocks was made by calculating the size of the lamellae detected in the micrographs, but as shown in Figure 6.26, a broad monomodal-like lamellar size distribution is obtained, making the differentiation of the 3 lamellar types impossible.

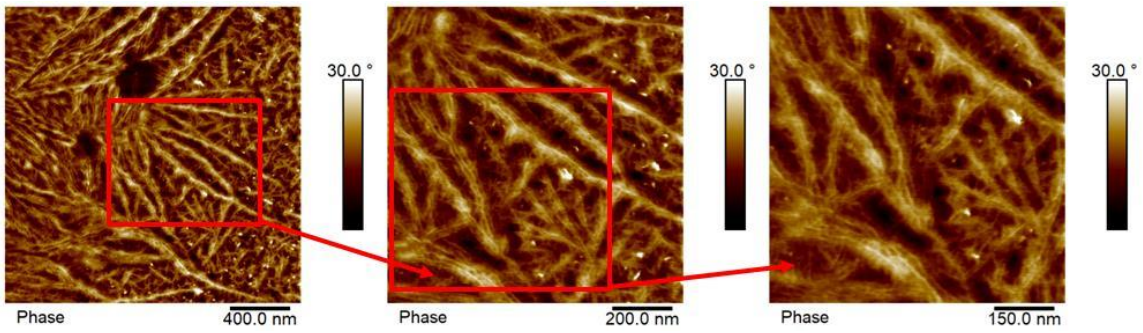

Figure 6.25. AFM micrographs of the tetrablock quarterpolymer $PE_{29}^{9.5}$ -*b*- $PEO_{26}^{8.8}$ -*b*- $PCL_{23}^{7.6}$ -*b*- $PLLA_{22}^{7.3}$ (Q2) observed at 25 ºC with close-ups of the indicated regions enclosed by a red box, using 20 ºC/min as cooling rate in the preparation of the sample

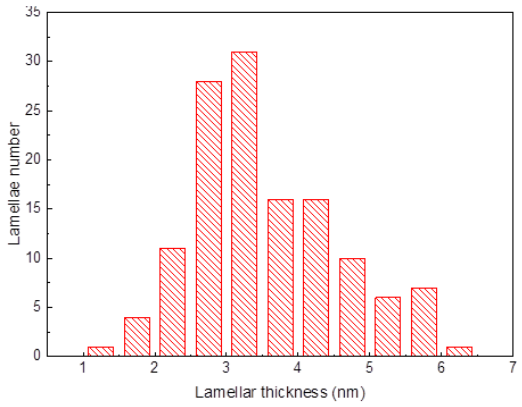

Figure 6.26. Lamellar thickness histogram obtained from the analysis of AFM micrographs shown in Figure 6.25.

6.3.6 Mechanical Properties by Nanoindentation

The above results show that the composition and molecular weight of the four blocks in the quarterpolymers strongly influence the course of lamellar development and the final lamellar nanostructure. In turn, such nanostructural differences are expected to influence the final properties of the material and, in particular, the mechanical properties. Storage modulus and hardness of the two tetrablock quarterpolymers were assessed by indentation, and results are collected in Table 6.2 (at an arbitrary indentation depth of 400 nm). Values of the ratio between the loss modulus and the storage modulus are also included. For the sake of comparison, Table 6.2 also includes data for the homopolymers, the precursors, and one triblock copolymer with high PLLA content.

Table 6.2. Indentation storage modulus and hardness and the ratio between loss and storage modulus for the two tetrablock quarterpolymers and their precursors. Values for one triblock terpolymer, including a PLLA block, are also reported for the sake of comparison. For PEO, the size of the indentations was significantly smaller than the spherulites radius; hence, *E´* and *H* data do not represent the mean values but just the range of experimental mechanical properties determined at different locations. Melting points and crystallinity values are calculated from DSC heating scans.

Sample	*E´* (GPa)	*H* (MPa)	*E´´/E´*	X_c (%)	T_m (ºC)
$PE^{7.1}$	3 ± 1	123± 56	0.10	78	124^{PE}
$PE_{32}^{7.1}$-*b*-$PEO_{68}^{15.1}$	0.86 ± 0.09	32 ± 5	0.18	8^{PE} 85^{PEO}	$112,120^{PE}$ 49^{PEO}
$PE_{22}^{7.1}$-*b*-$PEO_{46}^{15.1}$-*b*-$PCL_{32}^{10.4}$	0.8 ± 0.2	49 ± 8	0.17	4^{PE} 49^{PEO} 76^{PCL}	$114,120^{PE}$ $46^{PEO+PCL}$
$PE_{21}^{7.1}$-*b*-$PCL_{12}^{4.2}$-*b*-$PLLA_{67}^{23}$	2.0 ± 0.3	87 ± 20	0.12	31^{PE} 67^{PCL} 36^{PLLA}	119^{PE} 40^{PCL} 158^{PLLA}
$PE_{18}^{7.1}$-*b*-$PEO_{37}^{15.1}$-*b*-$PCL_{26}^{10.4}$-*b*-$PLLA_{19}^{7.6}$ (Q1)	1.1 ± 0.1	50 ± 9	0.14	7^{PE} 44^{PEO} 69^{PCL} 4^{PLLA}	117^{PE} 136^{PLLA} $44^{PEO+PCL}$
$PE^{9.5}$	1.8 ± 0.2	58 ±7	0.12	62	108^{PE}
$PE_{52}^{9.5}$-*b*-$PEO_{48}^{8.8}$	0.96 ± 0.07	57± 6	0.13	35^{PE} 82^{PEO}	106^{PE} 48^{PEO}
$PE_{37}^{9.5}$-*b*-$PEO_{34}^{8.8}$-*b*-$PCL_{29}^{7.6}$	0.64 ± 0.05	28 ± 4	0.16	46^{PE} 48^{PEO} 74^{PCL}	107^{PE} $40^{PEO+PCL}$
$PE_{29}^{9.5}$-*b*-$PEO_{26}^{8.8}$-*b*-$PCL_{23}^{7.6}$-*b*-$PLLA_{22}^{7.3}$ (Q2)	0.56 ± 0.07	27 ± 4	0.17	51^{PE} 57^{PEO} 88^{PCL} 0^{PLLA}	109^{PE} $39^{PEO+PCL}$
PEO^{20}	0.25 – 1.5	46 – 80		79	55^{PEO}
$PCL^{8.4}$	1.2 ± 0.2	91 ± 11	0.09	55	44^{PCL}
$PLLA^{5.0}$	5.1 ± 0.7	341 ± 20	0.067	71	157^{PLLA}

Crystallinity values of all blocks were calculated from the DSC heating scans of samples prepared following the procedure described in the experimental section, and results are reported in Table 6.2. Note that as the crystallization and melting transitions of the PE and the PLLA blocks on the one hand, and the PEO and the PCL blocks on the other hand overlap, an estimation of the individual crystallinities is quite a difficult task. For the PE and PLLA blocks, the crystallization and melting signals are bimodal, and we adopted an approximate determination of crystallinity by separating the enthalpy values of each block. In the case of PEO and PCL, an estimation of the crystallinity values is given by assuming an enthalpic contribution proportional to the content of each of block.

Figure 6.27 illustrates *E´* and *H* data that serve as representative examples of the influence of composition and molecular weight on the mechanical behaviour of the copolymers. The bars on the left- and the right-hand side of Figure 6.27 correspond to the $PE^{7.1}$ and the $PLLA^{5.0}$ homopolymers, respectively, and those in-between relate to the copolymers. $PE^{7.1}$ and $PLLA^{5.0}$ display the highest *E´* and *H* values of the four homopolymers (Table 6.2) and represent the "hard" blocks in the copolymers.

Table 6.2 shows that the higher molecular weight $PE^{9.5}$ displays lower mechanical properties than $PE^{7.1}$, and this can be attributed to the presence of thinner lamellar crystals, as suggested by the lower melting point of the 9500 g/mol material (i.e., melting point values of 124 ºC and 108 ºC for $PE^{7.1}$ and $PE^{9.5}$ blocks respectively, Table 6.2). This can be attributed to the different molecular architecture of $PE^{7.1}$ and $PE^{9.5}$, as revealed by NMR and explained in the experimental part. In Q1, $PE^{7.1}$ contains 0.32% propyl side groups and 3% methyl groups while $PE^{9.5}$ of Q2 has 0.45% propyl side groups and 2% methyl groups.

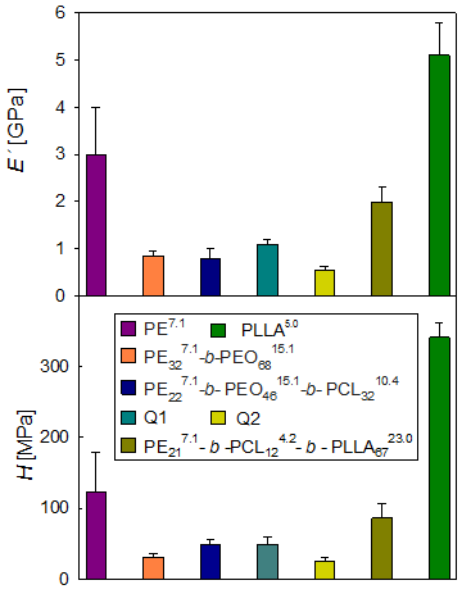

Figure 6.27. Storage modulus and hardness values (penetration depth = 400 nm), for the homopolymers, the two tetrablock quarterpolymers, the precursors including $PE^{7.1}$ and one triblock copolymer with high PLLA content

Figure 6.27 reveals that the incorporation of PEO blocks to $PE^{7.1}$ produces a remarkable decrease of modulus and hardness values. This can be partially attributed to the lower mechanical properties of PEO, representing 68% of the molar fraction in the copolymer. However, in addition, PE crystallization is substantially hindered, and the low levels of crystallinity (8%) and the lamellar characteristics (T_m decreases by 12 ºC with respect to the homopolymer) are also important factors that are expected to contribute to the *E´* and *H* drop. Concurrent to this drop is the relevant change of *E´´/E´* ratio (Table 6.2) that raises from 0.1 for $PE^{7.1}$ to 0.18 for the diblock copolymer. This result suggests enhanced viscous behavior and can be related to the significant increase of amorphous PE material.

The incorporation of PCL as a third block ($PE_{22}{}^{7.1}$-*b*-$PEO_{46}{}^{15.1}$-*b*-$PCL_{32}{}^{10.4}$) does not produce a substantial change of storage or loss modulus with respect to the diblock (Figure 6.27) because both PCL and PEO represent the compliant blocks in the terpolymer and in addition, crystallinity levels of PE remain quite

low (Table 6.2). However, a small *H* – increase is observed with the incorporation of the PCL block, and this could be related to the higher *H* values of PCL with respect to PEO.

Finally, Figure 6.27 shows that the addition of the fourth block to the terpolymer (Q1) does not produce a significant mechanical enhancement despite PLLA holding the highest *E´* and *H* values of all blocks. This can be attributed to the low degree of crystallinity developed by PLLA (4%) while that of PE remains limited (7%, see Table S9). In contrast, the *E´´/E´* ratio significantly decreases (Table 6.2) and this seems to be attributed to the contribution of the PLLA block that exhibits restricted viscous response. Concerning the Q2 copolymer, lower *E´* and *H* values are found with respect to Q1 (Figure 6.27). This could be explained due to the inferior mechanical properties of the $PE^{9.5}$ block in Q2 with respect to the $PE^{7.1}$ one in Q1 (Table 6.2).

As a final point, the role of crystalline PLLA and PE can be clearly discerned with the triblock terpolymer $PE_{21}{}^{7.1}$-*b*-$PCL_{12}{}^{4.2}$-*b*-$PLLA_{67}{}^{23}$. In this case, both PE and PLLA exhibit significant crystallinity levels around 30 – 35%, which seem low compared to typical values for the homopolymers (Table 6.2), but appear to be enough to produce a clear *E´* and *H* improvement (and a *E´´/E´* decrease, Table 6.2) with respect to the terpolymer $PE_{22}{}^{7.1}$-*b*-$PEO_{46}{}^{15.1}$-*b*-$PCL_{32}{}^{10.4}$.

In summary, the mechanical properties of the tetrablock quarterpolymers and their precursors can be explained on the basis of the mechanical properties of the individual blocks, the block molar ratio, and the nanostructural characteristics arising after the crystallization process, such as the degree of crystallinity and the crystal lamellar thickness.

6.4 Conclusions

The analysis of the crystallization behavior in multiple block polymers becomes more complex as the number of potentially crystallizable blocks is increased and even more challenging if the temperature ranges at which crystallization of more than one block occurs. The main objective of this study is the analysis of the crystallization behavior and morphology of triblock terpolymers with three potentially crystallizable blocks (the apolar PE, and the polar PEO and PCL blocks), on one hand; and tetracrystalline tetrablock quarterpolymers with four potentially crystallizable blocks (the apolar PE, and the polar PEO, PCL and PLLA blocks), on the other hand. The analysis of the corresponding precursor is also performed. Although adding a third and fourth block makes the study more challenging, it was possible to determine the crystallization sequence of each of the blocks following the crystallization process by three complementary techniques: DSC, WAXS, and PLOM.

The first part of this Chapter corresponds to triblock terpolymers and their precursors. The aim of comparing two of them, $PE_{22}^{7.1}$ -*b*- $PEO_{46}^{15.1}$ -*b*- $PCL_{32}^{10.4}$ (T1) and $PE_{37}^{9.5}$ -*b*- $PEO_{34}^{8.8}$ -*b*- $PCL_{29}^{7.6}$ (T2), was to determine the effect of composition and molecular weight on the properties. Regarding melt miscibility, both triblock terpolymers (T1 and T2) show weak phase segregation, and the microstructure present in the melt is destroyed when crystallization of the first block starts (PE crystallization). Furthermore, the crystallization of the three blocks upon cooling from the melt at 20 ºC/min in both triblock terpolymers is identified. The crystallization sequence is described as follows: the PE block crystallizes first, followed by the PCL block, and finally by the PEO block, as evidenced by DSC, *in situ* WAXS experiments, and PLOM observations with light intensity calculations as a function of temperature.

The crystalline behavior of both triblock terpolymers (T1 and T2) is very similar regardless of molecular weight and composition. However, in the case of their corresponding diblock copolymer precursors, the effect of the PE block

content and the molecular weight is significant. The $PE_{32}^{7.1}$ -*b*- $PEO_{68}^{15.1}$ diblock copolymer is melt miscible, and the crystallization of the PE block is hindered due to this and to its low content (32 wt %). Nevertheless, in the $PE_{52}^{9.5}$ -*b*- $PEO_{48}^{8.8}$ diblock copolymer, the crystallization of the PE block is enhanced due to its higher content (52 wt %), and phase segregated nature in the melt.

The fact that three different blocks can crystallize in a triblock terpolymer forming a triple crystalline material opens a window for new applications, such as drug delivery devices. In this respect, a comprehensive understanding of these materials could be beneficial to tune their crystallizability and obtain new materials with enhanced properties.

The second part of the Chapter focuses on the analysis of tetrablock quarterpolymers and their precursor materials. Both tetrablock quarterpolymers present small differences in composition and molecular weight of the blocks, as well as in the isotacticity percentage of PLLA. These differences are nevertheless significant, as the behavior of the two quarterpolymers examined is very different from one another. The $PE_{18}^{7.1}$ -*b* -$PEO_{37}^{15.1}$ -*b*- $PCL_{26}^{10.4}$ -*b*- $PLLA_{19}^{7.6}$ (Q1) tetrablock quarterpolymer did not exhibit any phase segregation in the melt and was able to develop novel tetracrystalline spherulites upon cooling from the melt as all of its four blocks were able to crystallize. On the other hand, the $PE_{29}^{9.5}$ -*b*- $PEO_{26}^{8.8}$ -*b*- $PCL_{23}^{7.6}$ -*b*- $PLLA_{22}^{7.3}$ (Q2) tetrablock quarterpolymer is characterized by presenting a weak lamellar phase segregation in the melt (as indicated by SAXS) and a break out crystallization where the PLLA block cannot crystallize (low isotacticity). Therefore, for this material the morphology consisted of tricrystalline microspherulites.

The use of synchrotron *in situ* WAXS, DSC and PLOM (both observations and light intensity measurements) techniques were found to be essential to separate the overlapping crystallization processes of both PE/PLLA and PEO/PCL blocks and thus the sequence of crystallization of each of the four blocks within the quarter polymers.

The specific nanostructural features appearing as a result of the sequential crystallization of the blocks in the quarterpolymers are found to have a consequent impact on the mechanical properties. Storage modulus and hardness were assessed by nanoindentation, and it was found that both Q1 and Q2 exhibit relatively low E' and H values ($E' \leq 1$ GPa; $H \leq 50$ MPa) attributed to the small fraction of PE and PLLA crystals. Moreover, Q2 exhibits inferior mechanical properties than Q1, and this could be associated with the occurrence of thin PE crystal lamellae.

These complex tetrablock quarterpolymers containing apolar and biocompatible PE blocks and polar and biodegradable PEO, PCL, and PLLA blocks could find applications where their amphiphilic character could be useful, i.e., encapsulation, drug delivery, among others. From the academic point of view, it is remarkable that four different blocks can crystallize and self-assemble into highly ordered tetracrystalline negative spherulites that exhibit Maltese crosses and banding extinction patterns, even though they are formed by at least four different lamellar types (e.g., in the case of Q1).

6.5 References

1. Ladelta, V.; Zapsas, G.; Abou-Hamad, E.; Gnanou, Y.; Hadjichristidis, N., Tetracrystalline tetrablock quarterpolymers: Four different crystallites under the same roof. *Angewandte Chemie International Edition* **2019,** *58*, 16267-16274.

2. Hiemenz, P. C.; Lodge, T. P., *Polymer Chemistry*. CRC Press: **2007**.

3. Huang, S.; Jiang, S.; An, L.; Chen, X., Crystallization and morphology of poly(ethylene oxide-*b*-lactide) crystalline-crystalline diblock copolymers. *Journal of Polymer Science, Part B: Polymer Physics* **2008,** *46*, 1400-1411.

4. Huang, C. I.; Tsai, S. H.; Chen, C. M., Isothermal crystallization behaviour of poly(L-lactide) in poly(L-lactide)-*block*-poly(ethylene glycol) diblock copolymers. *Journal of Polymer Science: Part B: Polymer Physics* **2006,** *44*, 2438-2448.

5. Jiang, S.; He, C.; An, L.; Chen, X.; Jiang, B., Crystallization and ring-banded spherulite morphology of poly(ethylene oxide)-*block*-poly(ε-caprolactone) diblock copolymer. *Macromolecular Chemistry and Physics* **2004,** *205*, 2229-2234.

6. Palacios, J. K.; Mugica, A.; Zubitur, M.; Iturrospe, A.; Arbe, A.; Liu, G.; Wang, D.; Zhao, J.; Hadjichristidis, N.; Müller, A. J., Sequential crystallization and morphology of triple crystalline biodegradable PEO-*b*-PCL-*b*-PLLA triblock terpolymers. *Royal Society of Chemistry Adv.* **2016,** *6*, 4739.

7. Maglio, G.; Migliozzi, A.; Palumbo, R., Thermal properties of di- and triblock copolymers of poly (L-lactide) with poly(oxyethylene) or poly (ε-caprolactone). *Polymer* **2003,** *44*, 369-375.

8. Hamley, I. W.; Castelletto, V.; Castillo, R. W.; Müller, A. J.; Martin, C. M.; Pollet, E.; Dubois, P., Crystallization in poly(L-lactide)-*b*-poly(ε-caprolactone) double crystalline diblock copolymers: a study using X-ray scattering, differential scanning calorimetry and polarized optical microscopy. *Macromolecules* **2005,** *38*, 463-472.

9. Hamley, I. W.; Parras, P.; Castelletto, V.; Castillo, R. V.; Müller, A. J.; Pollet, E.; Dubois, P.; Martin, C. M., Melt structure and its transformation by sequential crystallization of the two blocks within poly(L-lactide)-*block*- poly(ε-caprolactone) double crystalline diblock copolymers. *Macromolecular Chemistry and Physics* **2006,** *207*, 941-953.

10. Wang, J. L.; Dong, C. M., Synthesis, sequential crystallization and morphological evolution of well-defined star-shaped poly(ε-caprolactone)-*b*-poly(L-lactide) block copolymer. *Macromolecular Chemistry and Physics* **2006,** *207*, 554-562.

11. Zhang, J.; Tashiro, K.; Tsuji, H.; Domb, J., Disorder-to-order phase transition and multiple melting behavior of poly(L-lactide) investigated by simultaneous measurements of WAXD and DSC. *Macromolecules* **2008,** *41*, 1352-1357.

12. Sangroniz, L.; Wang, B.; Su, Y.; Liu, G.; Cavallo, D.; Wang, D.; Müller, A. J., Fractionated crystallization in semicrystalline polymers. *Progress in Polymer Science* **2021,** *115*, 101376.

13. Vivas, M.; Contreras, J.; López-Carrasquero, F.; Lorenzo, A. T.; Arnal, M. L.; Balsamo, V.; Müller, A. J.; Laredo, E.; Schmalz, H.; Abetz, V., Synthesis and characterization of triblock terpolymers with three potentially crystallizable blocks: polyethylene-*b*-poly(ethylene oxide)-*b*-poly(ε-caprolactone). *Macrolecular Symposia* **2006,** *239*, 58-67.

14. Hu, H.; Dorset, D. L., Crystal structure of poly (ε-caprolactone). *Macromolecules* **1990,** *23*, 4604-4607.

15. Lin, H.; Wagner, E. V.; Swinnea, J. S.; Freeman, B. D.; Pas, S. J.; Hill, A. J.; Kalakkunnath, S.; Kalika, D. S., Transport and structural characteristics of crosslinked poly (ethylene oxide) rubbers. *Journal of Membrane Science* **2006,** *276*, 145-161.

16. Shen, M.; Hansen, W. N.; Romo, P. C., Thermal expansion of the polyethylene unit cell. *The journal of Chemical Physics* **1969,** *51*, 425-430.

17. Carmeli, E.; Wang, B.; Moretti, P.; Tranchida, D.; Cavallo, D., Estimating the nucleation ability of various surfaces towards isotactic polypropylene via light intensity induction time measurements. *Entropy* **2019,** *21*, 1068.

Chapter 7

Final Remarks, Appendix and Publications

7.1 Final Remarks

Multiphasic polymer systems have been widely investigated during the past decades, but new technological requirements demand new materials with specific properties. Understanding the structure and properties is vital to design materials with enhanced properties, in order to develop top-notch applications in the near future.

Regarding polymer blends, their production will continue as plastic materials are produced worldwide. Many different applications such as packaging, sports equipment, automotive or medical devices, for instance, take advantage of their versatility. Particularly, large quantities of plastic materials are produced every day to satisfy the demand in the packaging field, although recycling techniques should also be developed to deal with plastic waste. Due to the high demand of these materials, the study of polymer blends becomes important to tune the production processes and obtain high-performance materials. The most relevant strategies to develop polymer blends with enhanced properties is the addition of nanofillers and compatibilizing agents.

Recently, titanium dioxide nanoparticles are used in plastic milk bottles. Extensive research has been performed regarding the dispersion and migration of nanofillers, because depending on their final location, mechanical properties can be affected. Therefore, controlling the morphology becomes important, and optimization of polymer blends will continue by changing many parameters that affect the final performance, for instance, the type and composition of the fillers or mixing conditions. In addition, as the relatively new presence of titanium dioxide nanoparticles in plastic bottles, recycling processes should also be optimized in order to save energy, as well as promoting sustainability.

Block copolymers are very interesting multiphasic polymer systems. They have been in the focus of polymer researchers due to their properties. Many applications take advantage of these materials, such as lithography or medical devices. The next step consists of the study of multicrystalline materials with

potentially three and four crystalline phases. However, the synthesis of these materials is complex, although some new synthetic routes are now being developed. Therefore, the recent availability of triple crystalline terpolymers and tetracrystalline quarterpolymers allows the study of their complex crystallization behavior. Therefore, a deep comprehension of such materials will lead to the possibility of designing new interesting materials.

Particularly, the PE-*b*-PEO-*b*-PCL triblock terpolymers and PE-*b*-PEO-*b*-PCL-*b*-PLLA tetrablock quarterpolymers are potential materials for many applications, due to their biodegradable nature. The crystallization of the blocks depends on the composition and molecular weight of each of the blocks, the crystallization conditions, and many other parameters. That is why a deep analysis becomes important, as this knowledge will allow designing new materials with specific properties to satisfy the technological demands of the future.

7.2 Appendix

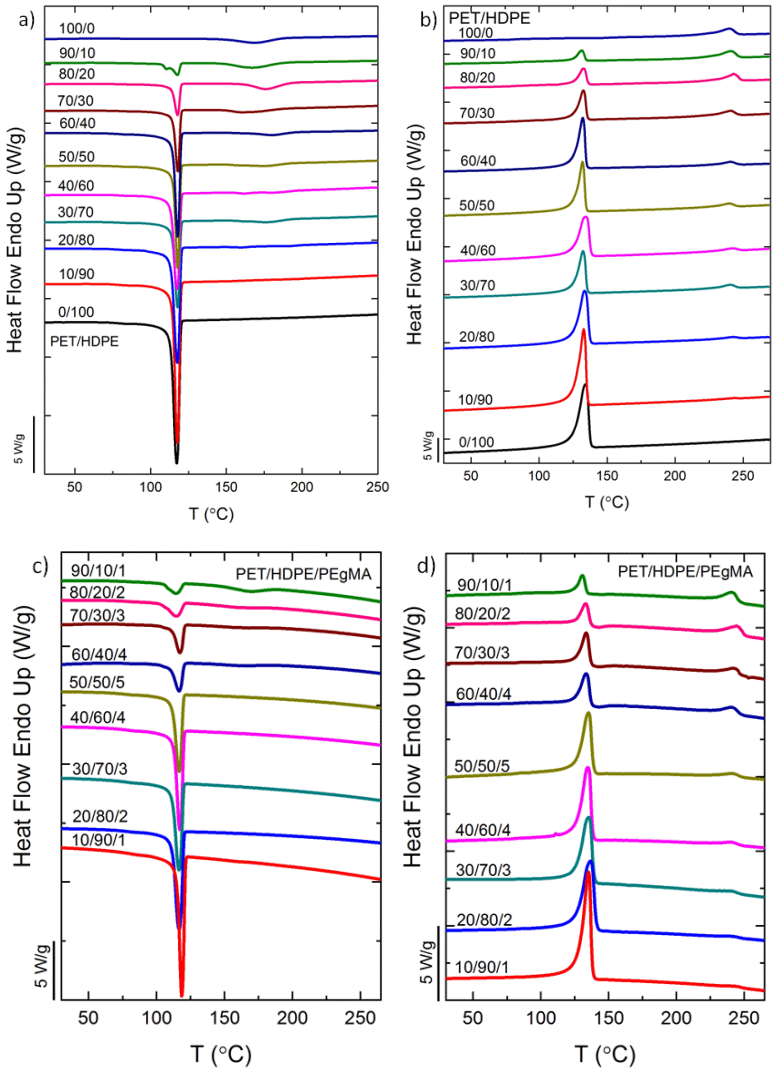

Figure A.4.1. DSC scans at 20 °C/min of the indicated blend compositions, a) cooling and b) heating for PET/HDPE blends; c) cooling and d) heating for PET/HDPE/PEgMA blends

Table A.4.1. Thermal properties of PET and HDPE in PET/HDPE blends during cooling from the melt at 20 °C/min. Enthalpies are normalized

PET/HDPE	$T_{c,onset,\ PET}$ (°C)	$\Delta H_{c,\ PET}$ (J/g)	$T_{c,onset,\ HDPE}$ (°C)	$\Delta H_{c,\ HDPE}$ (J/g)
100/0	188	31.5	-	-
90/10	187	33.4	120	256.2
80/20	188	36.0	120	214.9
70/30	188	26.4	120	230.6
60/40	195	15.8	120	283.0
50/50	191	20.0	120	226.6
40/60	174	27.9	120	228.3
30/70	193	39.1	120	160.3
20/80	169	6.2	120	202.7
10/90	165	4.4	120	209.6
0/100	-	-	119	198.7

Table A.4.2. Thermal properties of PET and HDPE in PET/HDPE blends during heating at 20 °C/min, enthalpies are normalized

PET/HDPE	$T_{m,peak,\ PET}$ (°C)	$\Delta H_{m,\ PET}$ (J/g)	$X_{c,\ PET}$ (%)	$T_{c,peak,\ HDPE}$ (°C)	$\Delta H_{m,\ HDPE}$ (J/g)	$X_{c,\ HDPE}$ (%)
100/0[1]	240	30.0	21	-	-	-
90/10	241	35.6	25	131	231.9	79
80/20	243	31.9	23	132	201.6	69
70/30	241	21.8	16	132	216.5	74
60/40	240	14.0	10	132	258.0	88
50/50	240	18.2	13	132	210.5	72
40/60	242	20.6	15	134	208.9	71
30/70	241	34.1	24	132	140.9	48
20/80	242	19.8	14	133	192.8	66
10/90	243	16.4	12	133	201.1	69
0/100	-	-	-	134	189.6	65

[1] $T_{cc,PET}$ = 146 °C and $\Delta H_{cc,\ PET}$ = 1.0 J/g

Table A.4.3. Thermal properties of PET and HDPE in PET/HDPE/PEgMA blends during cooling from the melt at 20 °C/min, enthalpies are normalized

PET/HDPE/ PEgMA	$T_{c,onset,\ PET}$ (°C)	$\Delta H_{c,\ PET}$ (J/g)	$T_{c,onset,\ HDPE}$ (°C)	$\Delta H_{c,\ HDPE}$ (J/g)
100/0/0	188	31.5	-	-
90/10/1	184	33.4	120	248.4
80/20/2	183	36.0	121	192.2
70/30/3	179	26.4	121	180.5
60/40/4	181	15.8	120	145.2
50/50/5	-	-	120	243.5
40/60/4	-	-	120	248.0
30/70/3	-	-	120	210.5
20/80/2	-	-	120	198.7
10/90/1	-	-	121	193.7
0/100/0	-	-	119	198.7

Table A.4.4. Thermal properties of PET and HDPE in PET/HDPE/PEgMA blends during heating at 20 °C/min. Enthalpies are normalized

PET/HDPE/ PEgMA	$T_{m,peak,\ PET}$ (°C)	$\Delta H_{m,\ PET}$ (J/g)	$X_{c,\ PET}$ (%)	$T_{c,peak,\ HDPE}$ (°C)	$\Delta H_{m,\ HDPE}$ (J/g)	$X_{c,\ HDPE}$ (%)
100/0/0	240	30.0	21	-	-	-
90/10/1	241	30.5	22	131	243.2	83
80/20/2[1]	244	31.3	20	132	131.8	45
70/30/3[2]	242	28.3	17	132	137.2	47
60/40/4[3]	241	27.0	17	132	117.3	40
50/50/5	242	16.4	12	132	228.3	78
40/60/4	241	17.8	13	134	236.0	81
30/70/3	240	14.6	10	132	191.2	65
20/80/2	241	10.8	8	133	195.1	67
10/90/1	244	22.1	16	133	199.1	68
0/100/0	-	-	-	134	189.6	65

[1] $T_{cc,PET}$ = 142 °C and $\Delta H_{cc,\ PET}$ = 3.8 J/g
[2] $T_{cc,PET}$ = 142 °C and $\Delta H_{cc,\ PET}$ = 4.5 J/g
[3] $T_{cc,PET}$ = 142 °C and $\Delta H_{cc,\ PET}$ = 3.1 J/g

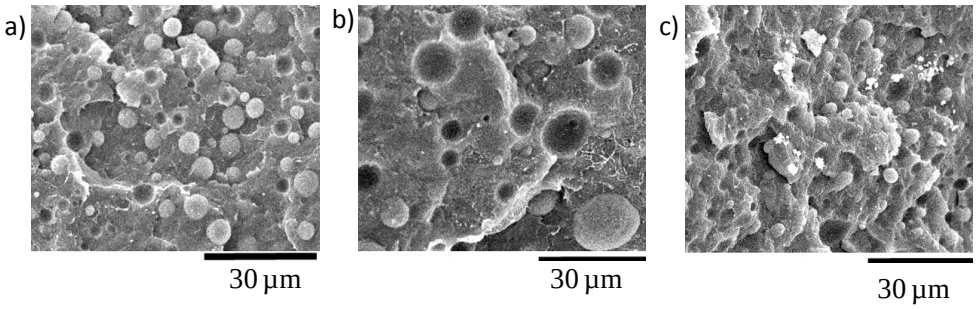

Figure A.4.2. SEM image of PBNANO-hphi with a) 3%, b) 7% and c) 12%

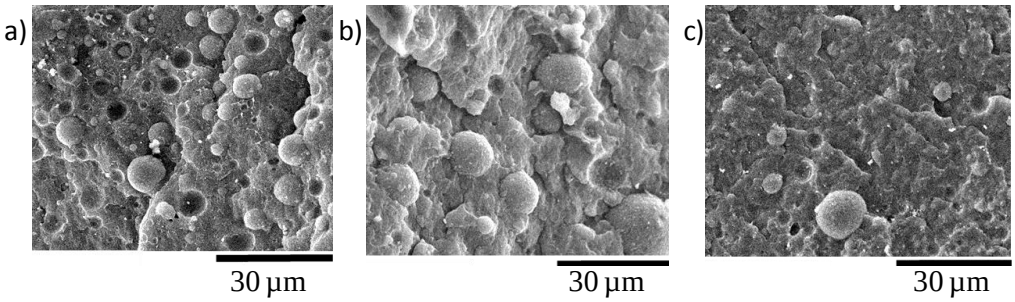

Figure A.4.3. SEM image of PBNANO-hpho with a) 3%, b) 7% and c) 12%

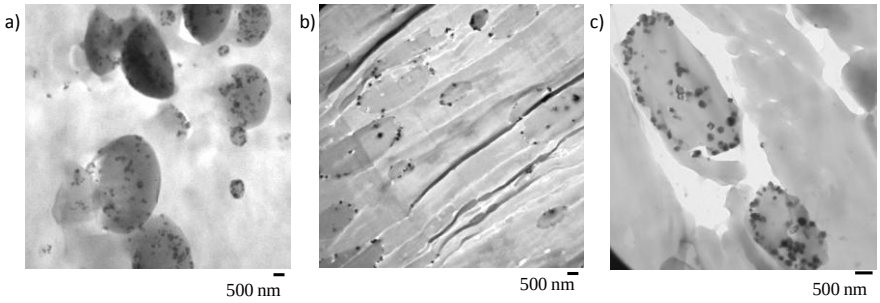

Figure A.4.4. TEM image of PBNANO-hphi with a) 3%, b) 7% and c) 12%

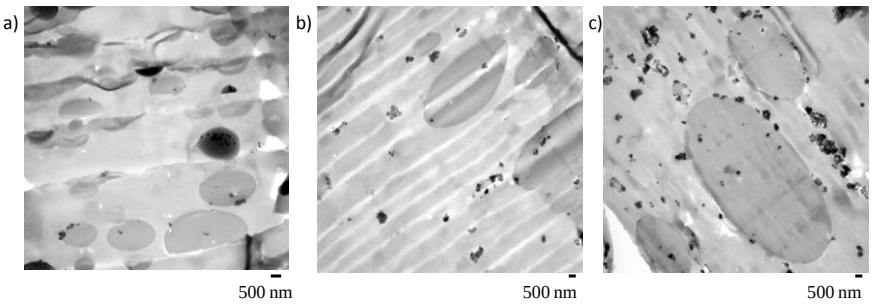

Figure A.4.5. TEM image of PBNANO-hpho with a) 3%, b) 7% and c) 12%

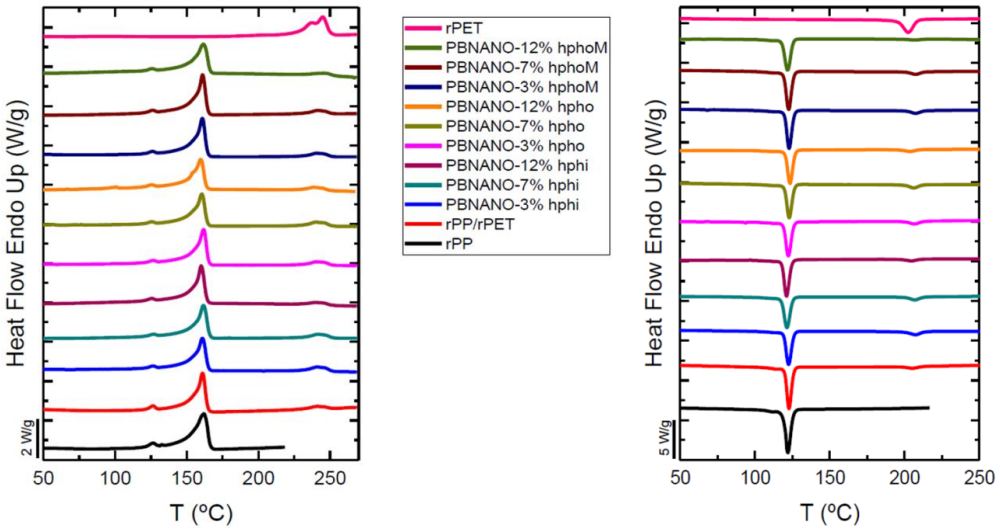

Figure A.4.6. Non-isothermal DSC cooling scan down (left) and the subsequent heating (right)

Table A.4.5. Calorimetric properties obtained from non-isothermal cooling DSC experiments

			$T_{c,PP}$ (°C)	$\Delta H_{c,PP}$ (J/g)	$T_{c,PET}$ (°C)	$\Delta H_{c,PET}$ (J/g)	$X_{c,PP}$ (°C)	$X_{c,PET}$ (°C)
rPP			125.5	93	-	-	45	-
80rPP/20rPET	**Total % hydrophilic TiO_2 (hphi)**	2	126.5	89	212.7	31	43	22
		3	126.3	80	213.2	56	39	40
		5	125.9	82	214.4	53	40	38
		7	125.3	81	212.9	49	39	35
		9.5	125.6	88	212.2	39	43	28
		12	124.6	94	210.8	33	45	24
	Total % hydrophobic TiO_2 (hpho)	3	125.7	81	212.3	44	39	31
		5	126.4	95	212.1	36	46	26
		7	126.2	80	212.7	53	38	38
		9.5	126.3	89	210.6	36	43	25
		12	126.8	85	210.1	38	41	27
	Total % hydrophobically modified TiO_2 (hphoM)	3	125.6	86	212.9	43	42	30
		5	125.5	89	213.5	44	43	33
		7	126.4	90	213.3	41	43	31
		9.5	122.5	94	200.9	24	46	17
		12	121.8	89	206.5	17	43	12
rPET			-	-	203.4	41	-	29

Table A.4.6. Calorimetric properties obtained from non-isothermal heating DSC experiments

			$T_{m,PP}$ (°C)	$\Delta H_{m,PP}$ (J/g)	$T_{m,PET}$ (°C)	$\Delta H_{m,PET}$ (J/g)
rPP			162.0	78	-	-
80rPP/20rPET	**Total % hydrophilic TiO_2 (hphi)**	2	161.3	65	241.1	25
		3	161.1	73	241.5	49
		5	161.4	78	241.8	45
		7	161.7	76	241.3	41
		9.5	162.9	88	244.7	37
		12	160.0	96	240.4	26
	Total % hydrophobic TiO_2 (hpho)	3	162.1	80	241.6	36
		5	161.5	88	240.8	27
		7	161.3	75	240.9	46
		9.5	160.6	94	240.0	27
		12	160.4	90	240.1	34
	Total % hydrophobically modified TiO_2 (hphoM)	3	161.8	82	241.3	34
		5	161.2	83	241.4	35
		7	161.4	86	241.1	35
		9.5	160.3	92	243.7	23
		12	161.6	94	246.4	32
rPET			-	-	243.6	34

Table A.4.7. Tensile mechanical parameters of the materials studied

Sample	**Elastic Modulus (GPa)**	**Yielding strength (Mpa)**	**Yielding strain (%)**	**Strain at break (%)**
rPET-O	2.20 ± 0.03	57.3 ± 0.5	3.1 ± 0.1	268 ± 13
rPP	1.07 ± 0.03	21.8 ± 0.2	4.9 ± 0.2	19 ± 4
PBNANO-0	1.26 ± 0.01	19.8 ± 0.5	4.2 ± 0.2	29 ± 2
PBNANO-hpho	1.42 ± 0.03	21.5 ± 0.5	3.2 ± 0.1	11 ±4
PBNANO-hphoM	1.33 ± 0.02	20.7 ± 0.3	2.5 ± 0.3	5.7 ± 0.3
PBNANO-hphi	1.34 ± 0.04	20.1 ± 0.3	4.2 ± 0.2	29 ± 5

Table A.5.1. Thermal properties obtained from DSC cooling scans at 20 °C/min

Samples	$T_{c,PE}$ (°C)	$\Delta H_{c,PE}$ (J/g)	$T_{c,PEO/PCL}$ (°C)	$\Delta H_{c,PEO/PCL}$ (J /g)	$T_{c,PLLA}$ (°C)	$\Delta H_{c,PLLA}$ (J/g)
$PE^{2.6}$	116.6	229	-	-	-	-
$PE_{39}{}^{2.6}$-*b*-$PEO_{61}{}^{4.0}$	105.5	110	41.7	174	-	-
$PE_{21}{}^{2.6}$-*b*-$PEO_{32}{}^{4.0}$-*b*-$PLLA_{47}{}^{5.9}$	101.2	41	29.8	56	77.4	50
$PE^{7.1}$	116.6	219	-	-	-	-
$PE_{63}{}^{7.1}$-*b*-$PCL_{37}{}^{4.2}$	115.1	108	46.7	106	-	-
$PE_{21}{}^{7.1}$-*b*-$PCL_{12}{}^{4.2}$-*b*-$PLLA_{67}{}^{23.0}$	114.0	54	45.0	61	81.4	15

Table A.5.2. Thermal properties obtained from DSC heating scans at 20 °C/min

Samples	$T_{m,PE}$ (°C)	$\Delta H_{m,PE}$ (J/g)	$T_{m,PEO/PCL}$ (°C)	$\Delta H_{m,PEO/PCL}$ (J/g)	$T_{m,PLLA}$ (°C)	$\Delta H_{m,PLLA}$ (J/g)
$PE^{2.6}$	129.7	228	-	-	-	-
$PE_{39}{}^{2.6}$-*b*-$PEO_{61}{}^{4.0}$	122.3	94	63.4	176	-	-
$PE_{21}{}^{2.6}$-*b*-$PEO_{32}{}^{4.0}$-*b*-$PLLA_{47}{}^{5.9}$	119.2	68	45.4	84	135.9	23
$PE^{7.1}$	129.7	245	-	-	-	-
$PE_{63}{}^{7.1}$-*b*-$PCL_{37}{}^{4.2}$	128.6	104	59.05	113	-	-
$PE_{21}{}^{7.1}$-*b*-$PCL_{12}{}^{4.2}$-*b*-$PLLA_{67}{}^{23.0}$	126.6	101	55.04	103	155.3	37

*PLLA shows cold crystallization at the heating run, T_{cc}=76.5 °C and ΔH_{cc}=17 J/g

Table A.5.3. Crystallinity values (%)calculated from DSC data in Table A.5.2 taking into account the mass fractions and using $X_c=(\Delta H_m/\ \Delta H_{m,100\%})\cdot 100$ and enthalpy of fusion of 100% crystalline polymers ($\Delta H_{m,100\%}$) is taken from literature: 293 J/g for PE[1], 139 J/g for PCL[2], 214 J/g for PEO[3] and 93 J/g for PLLA[4]

Samples	***X_c PE*** **(%)**	***X_c PEO*** **(%)**	***X_c PCL*** **(%)**	***X_c PLLA*** **(%)**
$PE^{2.6}$	78	-	-	-
$PE_{39}{}^{2.6}$-*b*-$PEO_{61}{}^{4.0}$	32	82	-	-
$PE_{21}{}^{2.6}$-*b*-$PEO_{32}{}^{4.0}$-*b*-$PLLA_{47}{}^{5.9}$	23	40	-	25
$PE^{7.1}$	83	-	-	-
$PE_{63}{}^{7.1}$-*b*-$PCL_{37}{}^{4.2}$	35	-	82	-
$PE_{21}{}^{7.1}$-*b*-$PCL_{12}{}^{4.2}$-*b*-$PLLA_{67}{}^{23.0}$	34	-	74	22

Table A.5.4. Thermal properties of $PE_{21}{}^{7.1}$-*b*-$PCL_{12}{}^{4.2}$-*b*-$PLLA_{67}{}^{23.0}$ obtained from DSC heating scans at 1 °C/min. Crystallinity values of the blocks are calculated using $X_c=(\Delta H_m/\Delta H_{m,100\%})\cdot 100$ and enthalpy of fusion of 100% crystalline polymers ($\Delta H_{m,100\%}$) is taken from literature: 293 J/g for PE[1], 139 J/g for PCL[2], 214 J/g for PEO[3] and 93 J/g for PLLA[4]

Sample	**$PE_{21}{}^{7.1}$-*b*-$PCL_{12}{}^{4.2}$-*b*-$PLLA_{67}{}^{23.0}$**
T_m *PE* (°C)	129.2
ΔH_m *PE* (J/g)	99
X_c *PE* (%)	34
T_m *PCL* (°C)	57.6
ΔH_m *PCL* (J/g)	80
X_c *PCL* (%)	58
T_m *PLLA* (°C)	159.9
ΔH_m *PLLA* (J/g)	38
X_c *PLLA* (%)	41

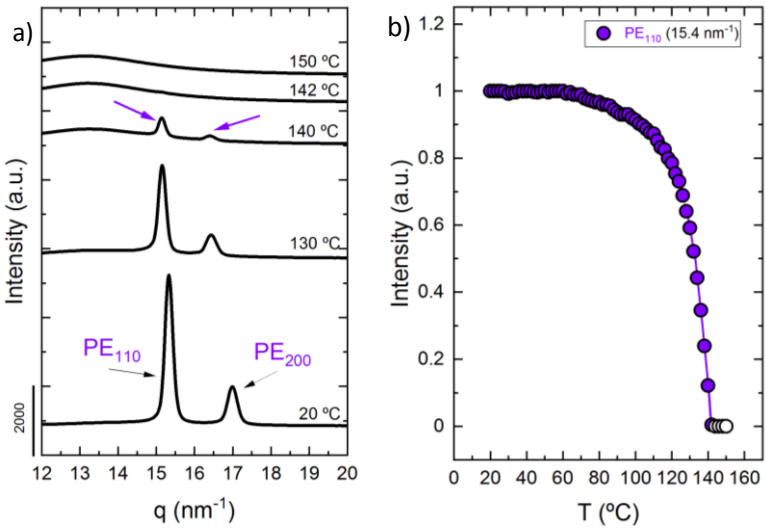

Figure A.5.1. a) WAXS patterns taken during subsequent heating at 20 ºC/min for $PE^{2.6}$ at different temperatures with arrows indicating melting of the PE block (violet), b) Normalized WAXS intensity of PE_{110} (15.4 nm^{-1})

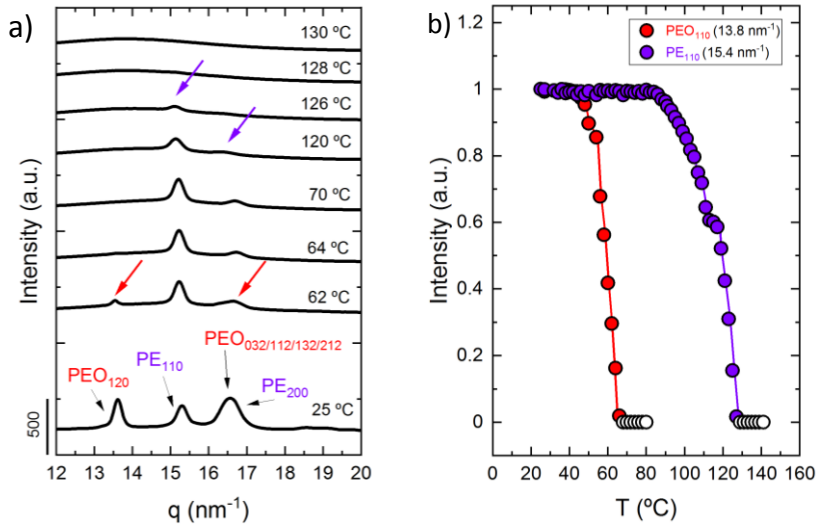

Figure A.5.2. a) WAXS patterns taken during subsequent heating at 20 ºC/min for $PE_{39}^{2.6}$-*b*-$PEO_{61}^{4.0}$ at different temperatures with arrows indicating melting of the PEO block (red) and the PE block (violet), with their corresponding (hkl) planes, and b) Normalized WAXS intensity of PE_{110} (15.4 nm^{-1}) and PEO_{110} (13.8 nm^{-1})

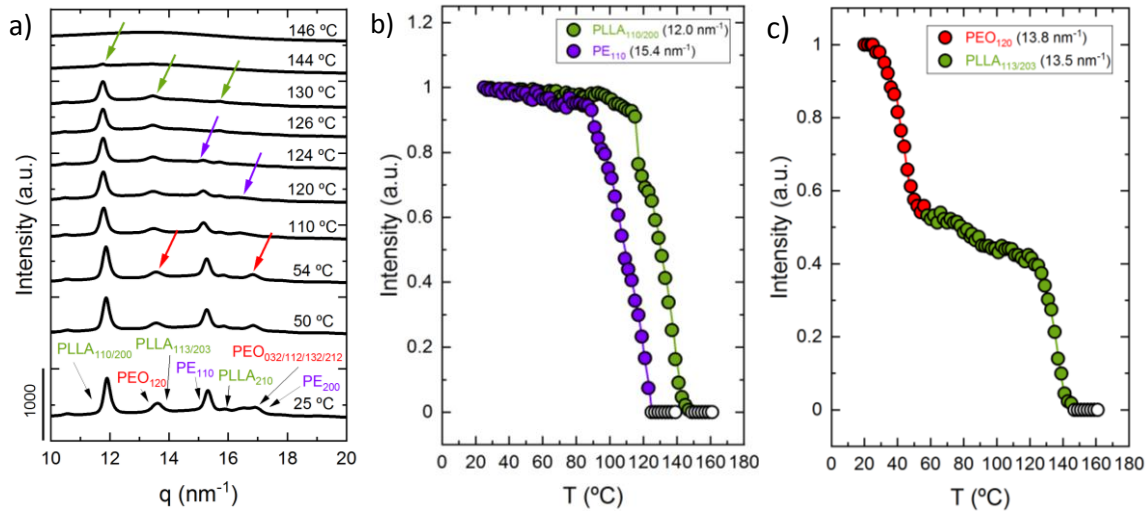

Figure A.5.3. a) WAXS patterns taken during subsequent heating at 20 ºC/min for $PE_{21}^{2.6}$-*b*-$PEO_{32}^{4.0}$-*b*-$PLLA_{47}^{5.9}$ at different temperatures with arrows indicating melting of the PEO block (red), PE block (violet) and the PLLA block (green), with their corresponding (hkl) planes, b) Normalized WAXS intensity of PE_{110} (15.4 nm^{-1}) and $PLLA_{110/200}$ (12.0 nm^{-1}) and, c) Normalized WAXS intensity of PEO_{120} (13.8 nm^{-1}) and $PLLA_{113/203}$ (13.5 nm^{-1})

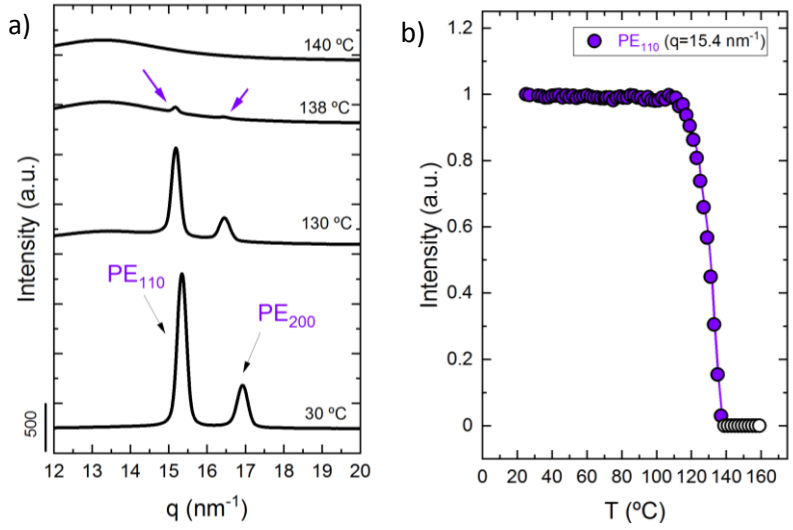

Figure A.5.4. a) WAXS patterns taken during subsequent heating at 20 ºC/min for $PE^{7.1}$ at different temperatures with arrows indicating melting of the PE block (violet), b) Normalized WAXS intensity of PE_{110} (15.4 nm^{-1})

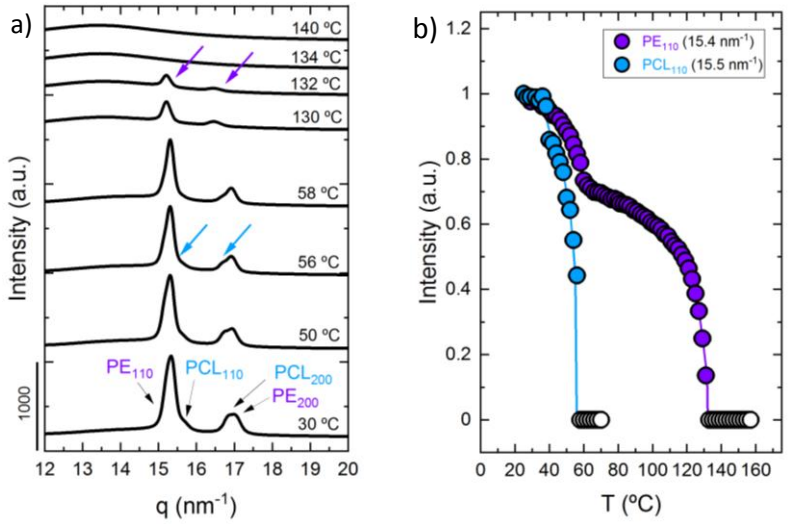

Figure A.5.5. a) WAXS patterns taken during subsequent heating at 20 ºC/min for $PE_{39}^{2.6}$-*b*-$PEO_{61}^{4.0}$ at different temperatures with arrows indicating melting of the PCL block (blue) and the PE block (violet), with their corresponding (hkl) planes, and b) Normalized WAXS intensity of PE_{110} (15.4 nm^{-1}) and PCL_{110} (15.5nm^{-1})

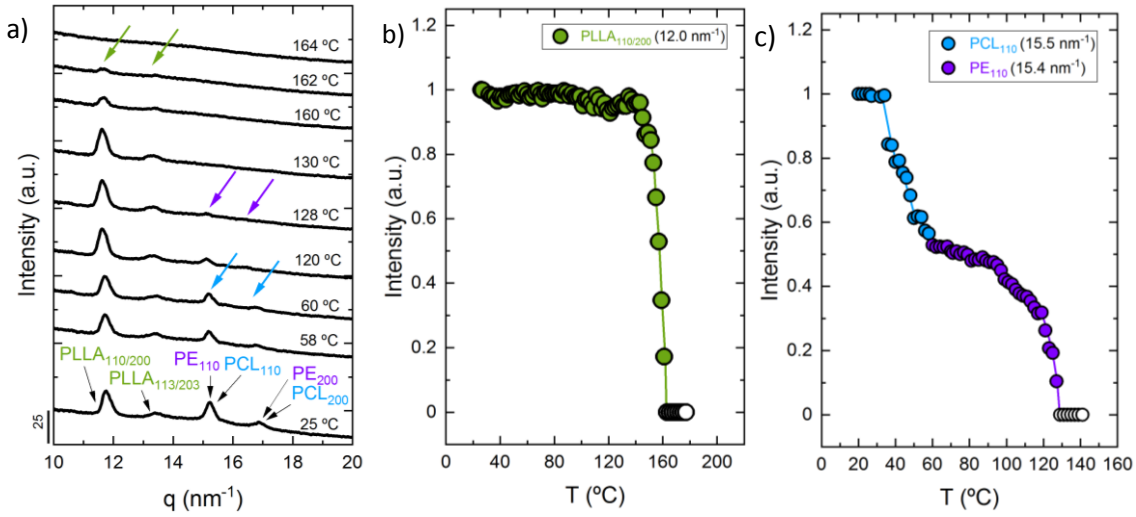

Figure A.5.6. a) WAXS patterns taken during subsequent heating at 20 ºC/min for $PE_{21}^{2.6}$-*b*-$PEO_{32}^{4.0}$-*b*-$PLLA_{47}^{5.9}$ at different temperatures with arrows indicating melting of the PCL block (blue), PE block (violet) and the PLLA block (green), with their corresponding (hkl) planes, b) Normalized WAXS intensity of $PLLA_{110/200}$ (12.0 nm^{-1}) and, c) Normalized WAXS intensity of PCL_{110} (15.5 nm^{-1}) and PE_{110} (15.4 nm^{-1})

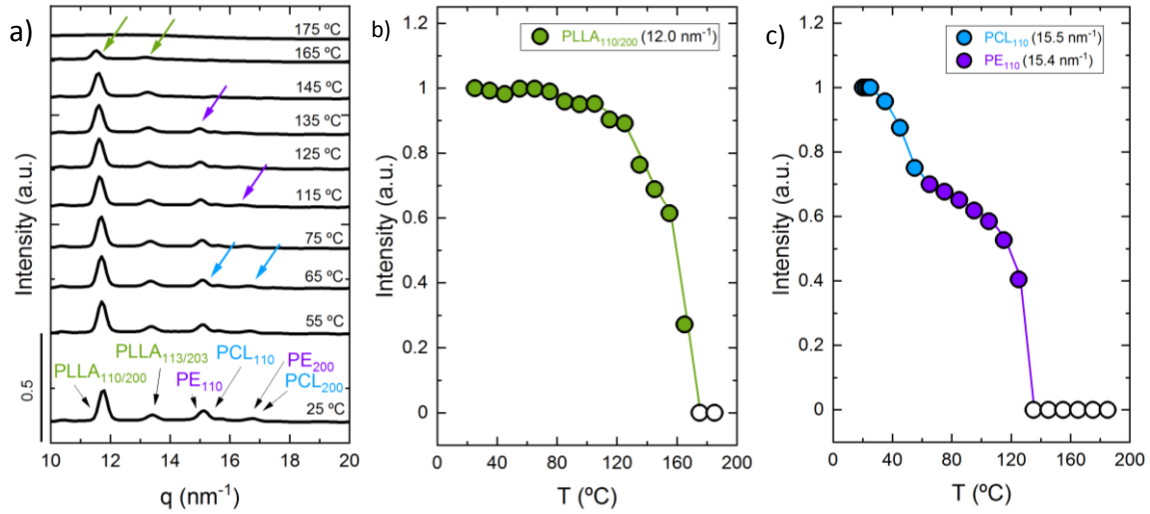

Figure A.5.7. a) WAXS patterns taken during subsequent heating at 1 ºC/min for $PE_{21}^{2.6}$-*b*-$PEO_{32}^{4.0}$-*b*-$PLLA_{47}^{5.9}$ at different temperatures with arrows indicating melting of the PCL block (blue), PE block (violet) and the PLLA block (green), with their corresponding (hkl) planes, b) Normalized WAXS intensity of $PLLA_{110/200}$ (12.0 nm^{-1}) and, c) Normalized WAXS intensity of PCL_{110} (15.5 nm^{-1}) and PE_{110} (15.4 nm^{-1})

Table A.6.1. Values of χ and χN calculated for the tetrablock quarterpolymers at 180 °C

		$PE_{18}^{7.1}$-*b*-$PEO_{37}^{15.1}$-*b*-$PCL_{26}^{10.4}$-*b*-$PLLA_{19}^{7.6}$	$PE_{29}^{9.5}$-*b*-$PEO_{26}^{8.8}$-*b*-$PCL_{23}^{7.6}$-*b*-$PLLA_{22}^{7.3}$
	χ	χN	χN
PE-*b*-PEO	0.78	135	99
PE-*b*-PCL	0.59	37	36
PE-*b*-PLLA	0.74	54	63
PEO-*b*-PCL	0.37	31	19
PEO-*b*-PLLA	0.34	37	24
PCL-*b*-PLLA	0.36	18	14

Table A.6.2. Thermal DSC cooling properties of the homopolymers PE, diblock copolymers PE-*b*-PEO, and triblock terpolymers PE-*b*-PEO-*b*-PCL (T1 and T2). Crystallization enthalpies are normalized according to block content

	$T_{c,\,PEO}$ (ºC)	$T_{c,\,PCL}$ (ºC)	$T_{c,\,PE}$ (ºC)	$\Delta H_{c,\,PEO}$ (J/g)	$\Delta H_{c,\,PCL}$ (J/g)	$\Delta H_{c,\,PE}$ (J/g)
$PE^{7.1}$	-	-	116.6	-	-	229.0
$PE_{32}{}^{7.1}$-*b*-$PEO_{68}{}^{15.1}$	43.1	-	76.4 81.4 118.4	177.05	-	21.5
$PE_{22}{}^{7.1}$-*b*-$PEO_{46}{}^{15.1}$-*b*-$PCL_{32}{}^{10.4}$ (T1)	39.1*		76.5	35.4	24.6	13.5
$PE^{9.5}$	-	-	107.2	-	-	156.2
$PE_{52}{}^{9.5}$-*b*-$PEO_{48}{}^{8.8}$	45.2	-	100.5	177.0	-	80.9
$PE_{37}{}^{9.5}$-*b*-$PEO_{34}{}^{8.8}$-*b*-$PCL_{29}{}^{7.6}$ (T2)	38.8*		102.5	21.0	17.9	113.4

*As crystallization temperatures of the PEO/PCL blocks are overlapped, a single T_c value is provided, and enthalpies are an estimation calculated according to block content

Table A.6.3. Thermal DSC heating properties of the homopolymers PE, diblock copolymers PE-*b*-PEO, and triblock terpolymers PE-*b*-PEO-*b*-PCL (T1 and T2). Melting enthalpies are normalized according to block content

	$T_{m,\,PEO}$ (ºC)	$T_{m,\,PCL}$ (ºC)	$T_{m,\,PE}$ (ºC)	$\Delta H_{m,\,PEO}$ (J/g)	$\Delta H_{m,\,PCL}$ (J/g)	$\Delta H_{m,\,PE}$ (J/g)
$PE^{7.1}$	-	-	129.7	-	-	224.8
$PE_{32}{}^{7.1}$-*b*-$PEO_{68}{}^{15.1}$	65.1	-	120.0 126.7	181.5	-	20.8
$PE_{22}{}^{7.1}$-*b*-$PEO_{46}{}^{15.1}$-*b*-$PCL_{32}{}^{10.4}$ (T1)	64.2*		122.0	38.7	26.9	13.1
$PE^{9.5}$	-	-	117.0	-	-	160.2
$PE_{52}{}^{9.5}$-*b*-$PEO_{48}{}^{8.8}$	62.6	-	113.0	184.6	-	78.8
$PE_{37}{}^{9.5}$-*b*-$PEO_{34}{}^{8.8}$-*b*-$PCL_{29}{}^{7.6}$ (T2)	51.4	56.3	113.7	22.8	19.4	127.6

*As crystallization temperatures of the PEO and PCL blocks are overlapped, a single value is provided, and the corresponding enthalpies are an estimation calculated according to block content

Table A.6.4. Crystallinity values (%) of the samples calculated from DSC heating scans taking into account the mass fractions of each of the blocks and using $X_c=(\Delta H_m/ \Delta H_{m,100\%})\cdot 100$ and enthalpy of fusion of 100% crystalline polymers ($\Delta H_{m,100\%}$) is taken from literature: 293 J/g for PE[1], 139 J/g for PCL[2] and 214 J/g for PEO[3]

	$X_{c,\,PEO}$ (%)	$X_{c,\,PCL}$ (%)	$X_{c,\,PE}$ (%)
$PE^{7.1}$	-	-	75.7
$PE_{32}{}^{7.1}$ *-b-* $PEO_{68}{}^{15.1}$	84.8	-	7.1
$PE_{22}{}^{7.1}$ *-b-* $PEO_{46}{}^{15.1}$ *-b-* $PCL_{32}{}^{10.4}$ (T1)	39.3*	60.4*	4.5
$PE^{9.5}$	-	-	54.7
$PE_{52}{}^{9.5}$ *-b-* $PEO_{48}{}^{8.8}$	86.2	-	26.9
$PE_{37}{}^{9.5}$ *-b-* $PEO_{34}{}^{8.8}$ *-b-* $PCL_{29}{}^{7.6}$ (T2)	31.3*	48.1*	43.5

*PEO and PCL crystallinity values in the triblock terpolymers are an estimation according to block content since the melting peaks of the blocks are overlapped and melting enthalpies cannot be distinguished properly

Table A.6.5. WAXS indexation for all the blocks studied in the samples[5, 6]

Blocks	(hkl) planes	q values (nm^{-1})
PLLA	(010)	10.3
PLLA	(110)/(200)	12.0
PLLA	(113)/(203)	13.5
PEO	(120)	13.8
PE	(110)	15.4
PCL	(110)	15.5
PLLA	(210)	15.7
PEO	(032)/(112)/(132)/(212)	16.4
PCL	(200)	16.7
PE	(200)	16.9

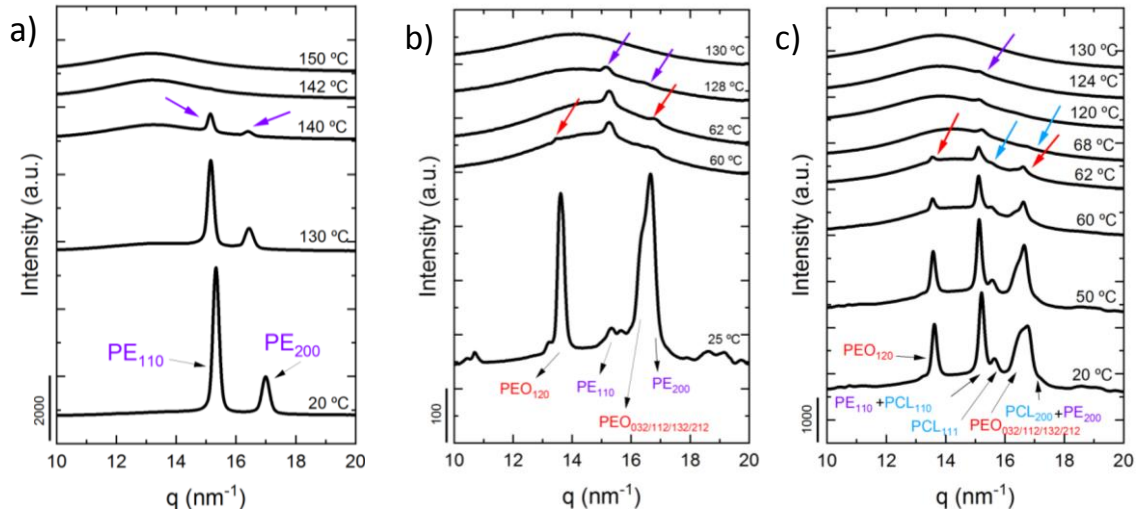

Figure A.6.1. WAXS patterns taken during subsequent heating at 20 °C/min for a) $PE^{7.1}$, b) $PE_{32}{}^{7.1}$ -*b*- $PEO_{68}{}^{15.1}$ and c) $PE_{22}{}^{7.1}$ -*b*- $PEO_{46}{}^{15.1}$ -*b*- $PCL_{32}{}^{10.4}$ (T1) at different temperatures with arrows indicating transitions for each block (violet for PE, blue for PCL and red for PEO) and the corresponding (hkl) planes of the blocks

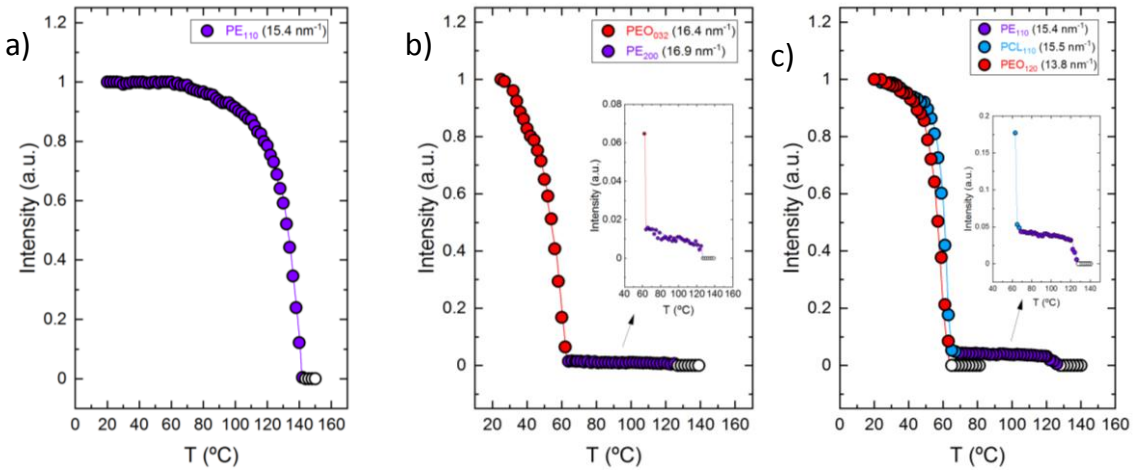

Figure A.6.2. Normalized WAXS intensities as a function of temperature calculated from heating WAXS data in Figure A.6.1 for a) $PE^{7.1}$, b) $PE_{32}{}^{7.1}$ -*b*- $PEO_{68}{}^{15.1}$ and c) $PE_{22}{}^{7.1}$ -*b*- $PEO_{46}{}^{15.1}$ -*b*- $PCL_{32}{}^{10.4}$ (T1). Colored data points and lines (violet for PE, blue for PCL and red for PEO) are employed to follow the crystallization of each block. Empty data points represent the molten state of the corresponding block in the samples

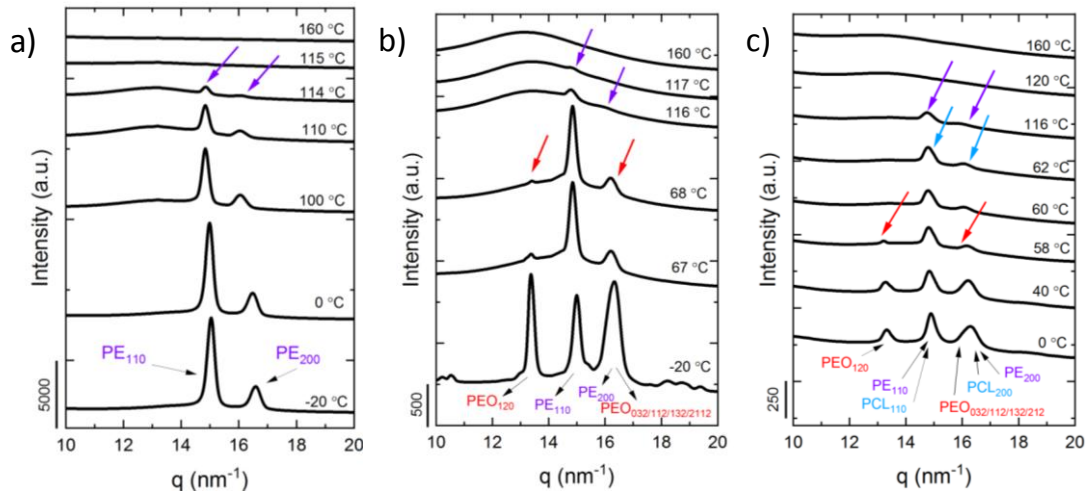

Figure A.6.3. WAXS patterns taken during subsequent heating at 20 °C/min for a) $PE^{9.5}$, b) $PE_{52}{}^{9.5}$ -*b*- $PEO_{48}{}^{8.8}$ and c) $PE_{37}{}^{9.5}$ -*b*- $PEO_{34}{}^{8.8}$ -*b*- $PCL_{29}{}^{7.6}$ (T2) at different temperatures with arrows indicating transitions for each block (violet for PE, blue for PCL and red for PEO) and the corresponding (hkl) planes of the blocks

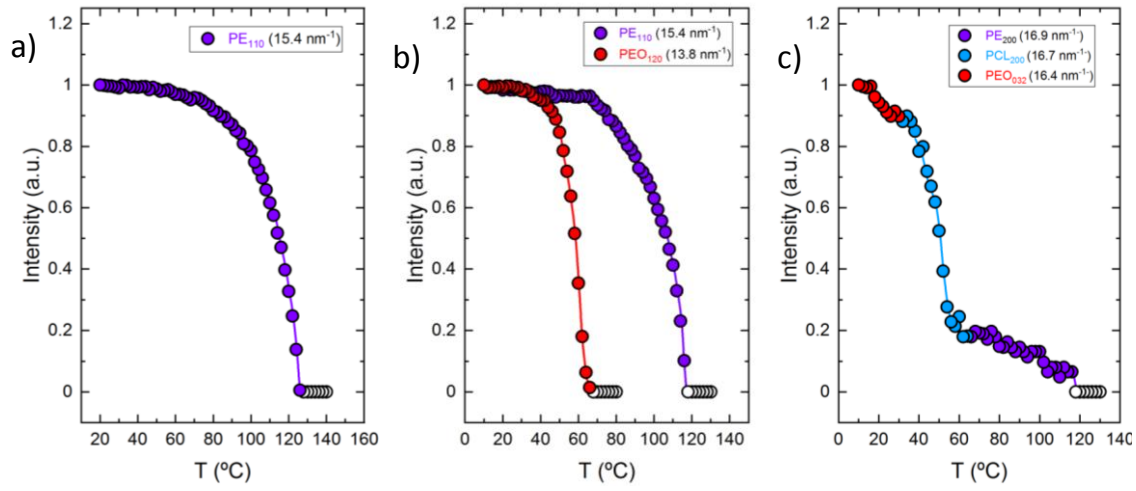

Figure A.6.4. Normalized WAXS intensities as a function of temperature calculated from heating WAXS data in Figure A.6.3 for a) $PE^{9.5}$, b) $PE_{52}{}^{9.5}$ -*b*- $PEO_{48}{}^{8.8}$ and c) $PE_{37}{}^{9.5}$ -*b*- $PEO_{34}{}^{8.8}$ -*b*- $PCL_{29}{}^{7.6}$ (T2). Colored data points and lines (violet for PE, blue for PCL, red for PEO) are employed to follow the crystallization of each block. Empty data points represent the molten state.

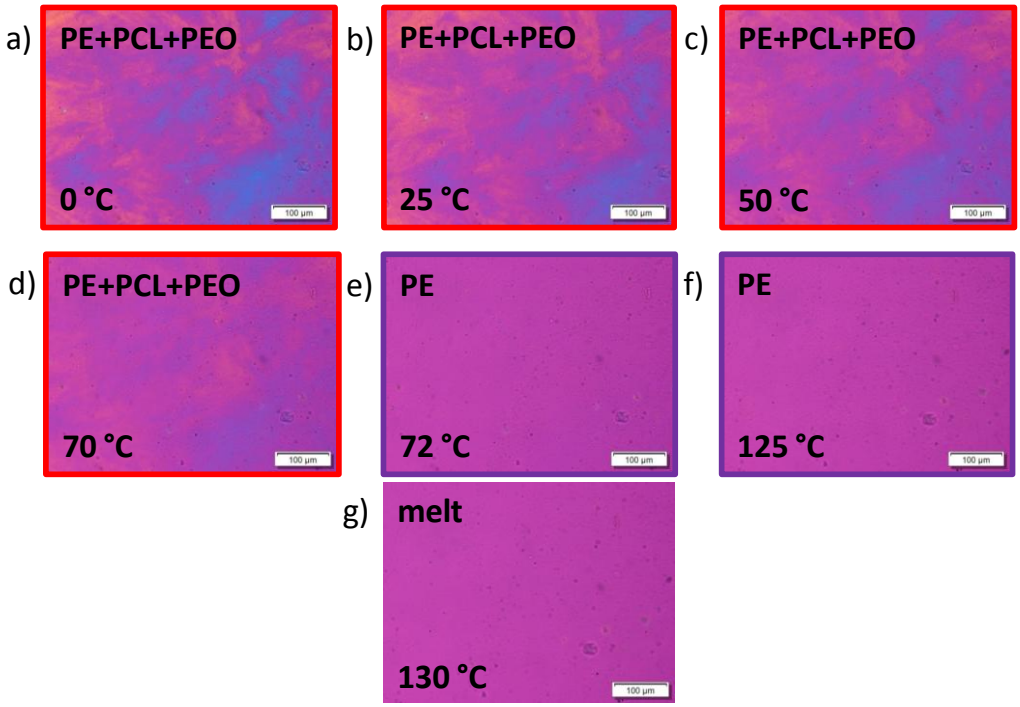

Figure A.6.5. PLOM subsequent heating micrographs from 0 ºC to the melt at 20 °C/min for the triblock $PE_{22}^{7.1}$ -*b*- $PEO_{46}^{15.1}$ -*b*- $PCL_{32}^{10.4}$ (T1) for the indicated temperatures with their crystallized blocks, with colored boxes indicating the crystallization of each of the blocks (violet for PE, blue for PCL and red for PEO)

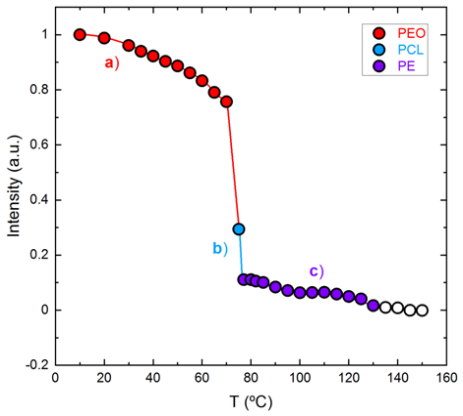

Figure A.6.6. PLOM intensity measurements from micrographs of Figure A.6.5 as a function of temperature indicating melting of the a) PEO block, b) PCL block, and c) PE block for the triblock terpolymer $PE_{22}^{7.1}$ -*b*- $PEO_{46}^{15.1}$ -*b*- $PCL_{32}^{10.4}$ (T1) with colored data points and lines (red for PEO, blue for PCL and violet for PE) to follow crystallization of each block. Empty data points represent the molten state of the sample

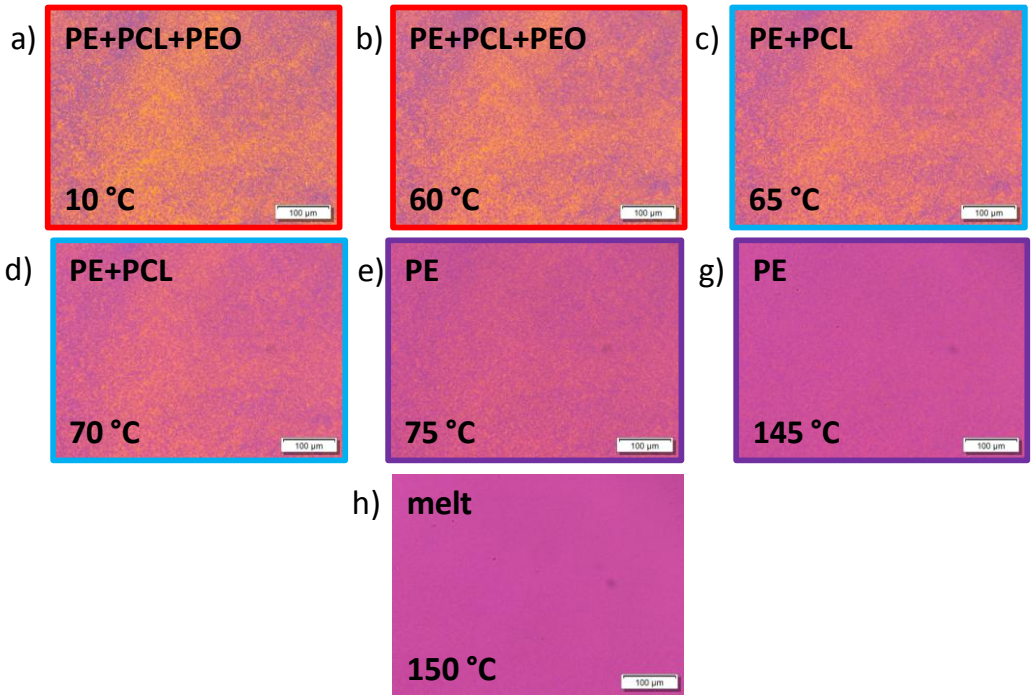

Figure A.6.7. PLOM subsequent heating micrographs from 10 ºC to the melt at 20 °C/min for the triblock $PE_{37}^{9.5}$ -*b*- $PEO_{34}^{8.8}$ -*b*- $PCL_{29}^{7.6}$ (T2) for the indicated temperatures, with colored boxes indicating the crystallization of each of the blocks (violet for PE, blue for PCL and red for PEO) and the crystallized blocks in each of the micrographs

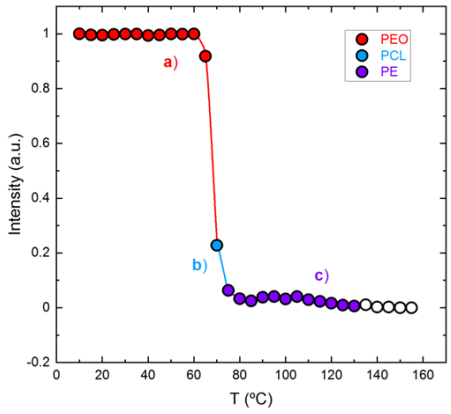

Figure A.6.8. PLOM intensity measurements from micrographs of Figure A.6.7 as a function of temperature indicating melting of the a) PEO block, b) PCL block, and c) PE block for the triblock terpolymer $PE_{37}^{9.5}$ -*b*- $PEO_{34}^{8.8}$ -*b*- $PCL_{29}^{7.6}$ (T2) with colored data points and lines (red for PEO, blue for PCL and violet for PE) to follow crystallization of each block. Empty data points represent the molten state of the sample

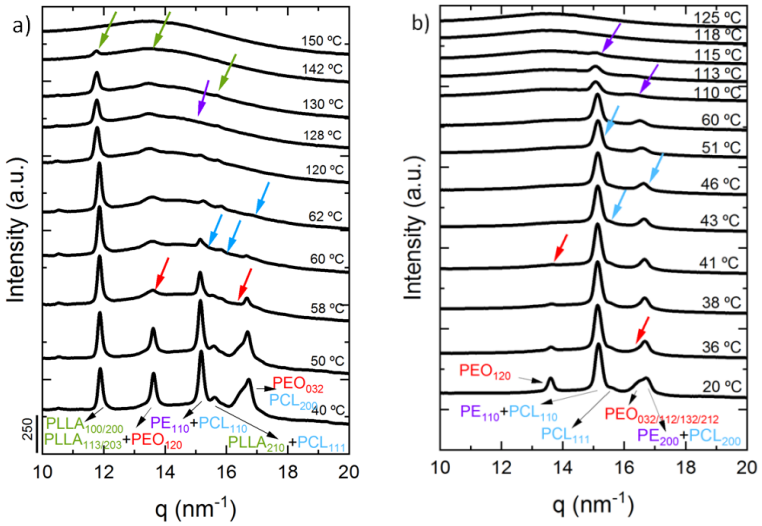

Figure A.6.9. WAXS patterns taken during subsequent heating at 20 °C/min for a) $PE_{18}^{7.1}$-*b*-$PEO_{37}^{15.1}$-*b*-$PCL_{26}^{10.4}$-*b*-$PLLA_{19}^{7.6}$, b) $PE_{29}^{9.5}$-*b*-$PEO_{26}^{8.8}$-*b*-$PCL_{23}^{7.6}$-*b*-$PLLA_{22}^{7.3}$, at different temperatures with arrows and (hkl) planes indicating transitions of the block (violet for PE, green for PLLA, blue for PCL, red for PEO)

Table A.6.6. Thermal DSC cooling properties of the tetrablock quarterpolymers Q1) $PE_{18}^{7.1}$-*b*-$PEO_{37}^{15.1}$-*b*-$PCL_{26}^{10.4}$-*b*-$PLLA_{19}^{7.6}$; Q2) $PE_{29}^{9.5}$-*b*-$PEO_{26}^{8.8}$-*b*-$PCL_{23}^{7.6}$-*b*-$PLLA_{22}^{7.3}$ (the PLLA block does not crystallize)

	T_c, PEO (ºC)	T_c, PCL (ºC)	T_c, PE (ºC)	T_c, PLLA (ºC)	ΔH_c, PEO (J/g)	ΔH_c, PCL (J/g)	ΔH_c, PE (J/g)	ΔH_c, PLLA (J/g)
Q1	36.4	43.8	75.1	81.2	33.5	23.6	3.6	1.7
Q2	25.5		100.5	-	25.7	22.7	46.8	-

Table A.6.7. Thermal DSC heating properties of the tetrablock quarterpolymers Q1) $PE_{18}^{7.1}$-*b*-$PEO_{37}^{15.1}$-*b*-$PCL_{26}^{10.4}$-*b*-$PLLA_{19}^{7.6}$; Q2) $PE_{29}^{9.5}$-*b*-$PEO_{26}^{8.8}$-*b*-$PCL_{23}^{7.6}$-*b*-$PLLA_{22}^{7.3}$ (the PLLA block does not crystallize)

	T_m, PEO (ºC)	T_m, PCL (ºC)	T_m, PE (ºC)	T_m, PLLA (ºC)	ΔH_m, PEO (J/g)	ΔH_m, PCL (J/g)	ΔH_m, PE (J/g)	ΔH_m, PLLA (J/g)
Q1	56.0	60.8	122.8	132.5	37.5	26.4	2.3	1.9
Q2	50.7		114.7	-	28.2	24.9	42.4	-

Table A.6.8. Crystallinity values (%) of the samples calculated from DSC cooling and heating data according to the mass fractions of each of the blocks, using $X_c=(\Delta H_m/\ \Delta H_{m,100\%})\cdot 100$ and $(\Delta H_{m,100\%})$ of polymers taken from literature: 293 J/g for PE[1], 139 J/g for PCL[2], 214 J/g for PEO[3] and 93 J/g for PLLA[4]

		$X_{c,\ PEO}$ (%)	$X_{c,\ PCL}$ (%)	$X_{c,\ PE}$ (%)	$X_{c,\ PLLA}$ (%)
Q1	Cooling	65	42	6	9
	Heating	41	70	4	11
Q2	Cooling	46	71	55	-
	Heating	51	78	50	-

*Tetrablock quarterpolymers: Q1) $PE_{18}^{7.1}$ -*b* -$PEO_{37}^{15.1}$ -*b*- $PCL_{26}^{10.4}$ -*b*- $PLLA_{19}^{7.6}$; Q2) $PE_{29}^{9.5}$ -*b*- $PEO_{26}^{8.8}$ -*b*- $PCL_{23}^{7.6}$ -*b*- $PLLA_{22}^{7.3}$

*As cooling and heating DSC transitions of the blocks PE/PLLA and PEO/PCL overlap, an estimation of the crystallinity values according to block content is reported. The PLLA block in Q2 does not crystallize

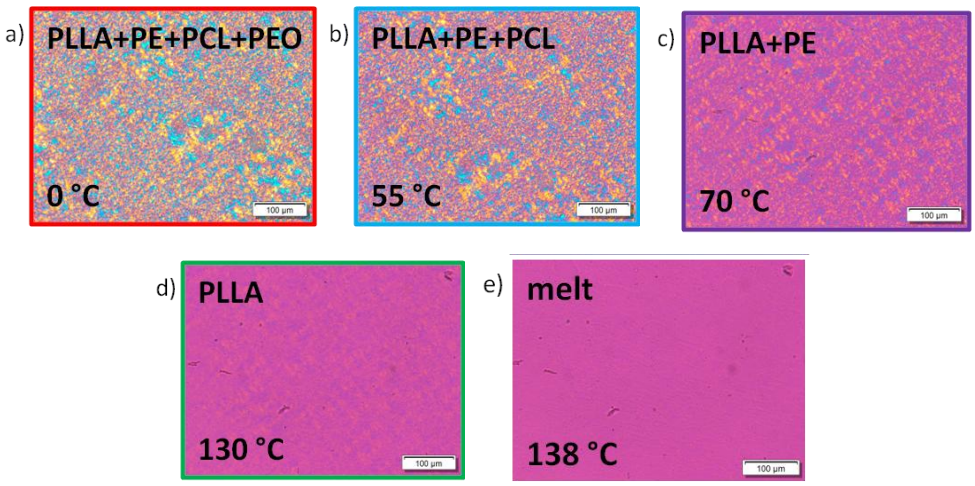

Figure A.6.10. PLOM subsequent heating micrographs from 0 ºC to the melt at 20 °C/min for the tetrablock quarterpolymer $PE_{18}^{7.1}$ -*b* -$PEO_{37}^{15.1}$ -*b*- $PCL_{26}^{10.4}$ -*b*- $PLLA_{19}^{7.6}$ (Q1) with colored boxes indicating the crystallization of each of the blocks (violet for PE, green for PLLA, blue for PCL and red for PEO): a) PLLA, PE, PCL and PEO at 0 ºC, b) PLLA, PE and PCL at 55 ºC, c) PLLA and PE at 70 ºC, d) PLLA at 130 ºC, and e) the molten state at 138 ºC

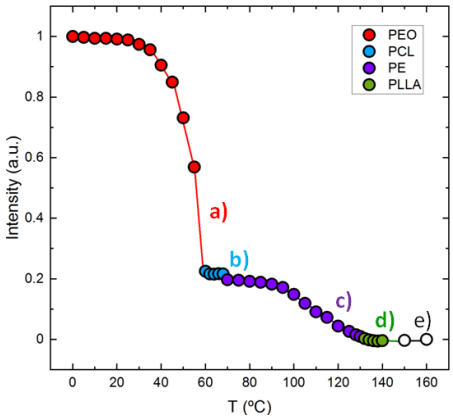

Figure A.6.11. PLOM intensity measurements from micrographs of Figure A.6.10 as a function of temperature indicating melting of the a) PEO block, b) PCL block, c) PE block, d) PLLA block and e) melting for the tetrablock quarterpolymer $PE_{18}^{7.1}$ –*b* –$PEO_{37}^{15.1}$ –*b*- $PCL_{26}^{10.4}$ –*b*- $PLLA_{19}^{7.6}$ (Q1) with colored data points and lines (red for PEO, blue for PCL, violet for PE and green for PLLA) to follow crystallization of each block. Empty data points represent the molten state of the sample

References

1. Ren, M.; Tang, Y.; Gao, D.; Ren, Y.; Yao, X.; Shi, H.; Zhang, T.; Wu, C., Recrystallization of biaxially oriented polyethylene film from partially melted state within crystallite networks. *Polymer* **2020,** *191*, 122291.

2. Izquierdo, R. G.-G., N.; Rodríguez, M. T.; Cáceres, E.; García, S. J.; Gómez Ribelles, J. M.; Monleón, M.; Monllau, J. C.; Suay, J., Biodegradable PCL scaffolds with an interconnected spherical pore network for tissue engineering. *Journal of Biomedical Materials Research* **2007**, 25-35.

3. Ebers, L. S.; Auvergne, R.; Boutevin, B.; Laborie, M. P., Impact of PEO structure and formulation on the properties of a lignin/PEO blend. *Industrial Crops and Products* **2020,** *143*, 111883.

4. Shamsah, A. H.; Cartmell, S. H.; Richardson, S. M.; Bosworth, L. A., Material characterization of PCL: PLLA electrospun fibers following six months degradation in vitro. *Polymers* **2020,** *12*, 700.

5. Palacios, J. K.; Mugica, A.; Zubitur, M.; Iturrospe, A.; Arbe, A.; Liu, G.; Wang, D.; Zhao, J.; Hadjichristidis, N.; Müller, A. J., Sequential crystallization and

morphology of triple crystalline biodegradable PEO-*b*-PCL-*b*-PLLA triblock terpolymers. *Royal Society of Chemistry Adv.* **2016,** *6*, 4739.

6. Castillo, R. V.; Müller, A. J.; Lin, M. C.; Chen, H. L.; Jeng, U. S.; Hillmyer, M. A., Confined crystallization and morphology of melt segregated PLLA-*b*-PE and PLDA-*b*-PE diblock copolymers. *Macromolecules* **2012,** *45*, 4254-4261.

7.3 Publications derived from this thesis

1. Matxinandiarena, E.; Múgica, A.; Zubitur, M.; Yus, C.; Sebastián, V.; Irusta, S.; Loaeza, A. D.; Santana, O.; Maspoch, M. L.; Puig, C.; Müller, A. J., The effect of titanium dioxide surface modification on the dispersion, morphology and mechanical properties of recycled PP/PET/TiO_2 PBNANOs. *Polymers* **2019**, *11* (10), 1692

2. Matxinandiarena, E.; Múgica, A.; Zubitur, M.; Zhang, B.; Ladelta, V.; Zapsas, G.; Hadjichristidis, N.; Müller, A. j., The effect of the cooling rate on the morphology and crystallization of triple crystalline PE-*b*-PEO-*b*-PLLA and PE-*b*-PCL-*b*-PLLA triblock terpolymers. *ACS Applied Polymer Materials* **2020**, *2*, 4952-4963

3. Matxinandiarena, E.; Múgica, A.; Tercjak, A.; Ladelta, V.; Zapsas, G.; Hadjichristidis, N.; Cavallo, D.; Flores, A.; Müller, A.J., Sequential crystallization and multicrystalline morphology in PE-*b*-PEO-*b*-PCL-*b*-PLLA tetrablock quarterpolymers. *Macromolecules* **2021**, *54*, (15), 7244-7257

4. Matxinandiarena, E.; Múgica, A.; Zubitur, M.; Ladelta, V.; Zapsas, G.; Cavallo, D.; Hadjichristidis, N.; Müller, A.J.; Crystallization and morphology of triple crystalline PE-*b*-PEO-*b*-PCL triblock terpolymers. *Polymers* **2021**, *13* (18), 3133

Summary

The aim of this doctoral thesis is the analysis and comparison of multiphase polymeric systems with at least two crystallizable phases. An in-depth comprehension of the crystalline behavior and morphology is essential in order to design and develop new materials with enhanced properties.

The first part of this research focuses on double crystalline PET/HDPE polymer blends with titanium dioxide nanoparticles and compatibilizing agents. The chosen blend composition to study such effects was 70 PET/30 HDPE after the analysis of the whole composition range. This sample shows sea-island morphology, in which the matrix corresponds to PET (70%) and the dispersed droplets are HDPE (30%). The particle size of the dispersed phase was reduced by adding nanoparticles due to their preferential location at the interphase, which forms a physical barrier that avoids coalescence.

In addition, due to the presence of TiO_2 nanoparticles in PET waste (opaque PET bottles), recycled 80rPP/20rPET/TiO_2 polymer blend nanocomposites (PBNANOs) were prepared using three different TiO_2 nanoparticles: hydrophilic (hphi), hydrophobic (hpho), and hydrophobically modified (hphoM). The hydrophilic/hydrophobic balance controls the nanoparticle location, and TEM results show a decrease in droplet size when nanoparticles are located at the interphase. The most effective nanoparticles were the hydrophobically modified (hphoM) ones, although large loadings are needed (12%) to completely cover the droplet surface and improve mechanical properties. In addition, a good correlation is found between the crystallization rate of PET (determined by DSC) and nanoparticle location, because of the nucleating effect of the nanoparticles in the PET phase.

The second part of the work studies multicrystalline block copolymers. The addition of a third and fourth crystalline block to a double crystalline diblock copolymer makes the analysis more challenging, but novel PE-*b*-PEO-*b*-PLLA and PE-*b*-PCL-*b*-PLLA tricrystalline triblock terpolymers and PE-*b*-PEO-*b*-PCL-*b*-PLLA tetracrystalline tetrablock quarterpolymers of different molecular weight and compositions (and their corresponding PE-*b*-PEO-*b*-PCL triblock terpolymers,

PE-*b*-PEO diblock copolymers and PE homopolymers) were synthesized, with three and four potentially crystallizable blocks.

Regarding PE-*b*-PEO-*b*-PLLA and PE-*b*-PCL-*b*-PLLA tricrystalline triblock terpolymers, DSC cooling ramps from the melt at 20 and 1 °C/min and simultaneously performed in situ SAXS/WAXS and PLOM measurements at identical conditions, allows to identify the superstructural morphology and the crystallization sequence unequivocally. The effect of the cooling rate is demonstrated since using 20 ºC/min as cooling rate, the crystallization sequence starts with the PE block, continues with the PLLA block, and ends with the PEO or PCL block depending on the triblock terpolymer. The faster crystallization kinetics of the PE block is responsible for this crystallization sequence. On the contrary, when employing 1 ºC/min as cooling rate, the PLLA block crystallize first and only for the terpolymer with the highest amount of PLLA. Thus, cooling conditions determine the final morphology and properties of these materials.

Furthermore, this research continues with the study of the crystallization behaviour of PE-*b*-PEO-*b*-PCL tricrystalline triblock terpolymers (T1: $PE_{22}^{7.1}$-*b*-$PEO_{46}^{15.1}$-*b*-$PCL_{32}^{10.4}$ and T2: $PE_{37}^{9.5}$-*b*-$PEO_{34}^{8.8}$-*b*-$PCL_{29}^{7.6}$) and PE-*b*-PEO-*b*-PCL-*b*-PLLA tetracrystalline tetrablock quarterpolymers (Q1: $PE_{18}^{7.1}$ -*b* -$PEO_{37}^{15.1}$ -*b*- $PCL_{26}^{10.4}$ -*b*- $PLLA_{19}^{7.6}$ and Q2: $PE_{29}^{9.5}$ -*b*- $PEO_{26}^{8.8}$ -*b*- $PCL_{23}^{7.6}$ -*b*- $PLLA_{22}^{7.3}$). Superscripts give number average molecular weights in kg/mol and subscripts composition in wt. %. Their precursors have also been studied for comparison purposes.

The triple crystalline nature of the PE-*b*-PEO-*b*-PCL triblock terpolymers was demonstrated by DSC, SAXS/WAXS, and PLOM techniques using the same conditions, and the crystallization at 20 ºC/min starts with the PE block, continues with the PCL block, and ends with the PEO block. Although the crystallization of the PCL and PEO block overlap, WAXS and PLOM experiments allow identifying both transitions. According to SAXS, both T1 and T2 are weakly phase segregated in the melt. PLOM experiments show that triblock terpolymers have a non-

spherulitic or microspherulitic morphology, while their precursors show a spherulitic morphology.

The crystallization behavior of novel PE-*b*-PEO-*b*-PCL-*b*-PLLA tetracrystalline tetrablock quarterpolymers was firstly investigated. SAXS indicated that Q1 is melt miscible, while Q2 is weakly segregated in the melt but breaks out during crystallization. The crystallization sequence was determined by DSC and WAXS: PLLA first, then PE, then PCL, and finally PEO in the case of the Q1 quarterpolymer, as in Q2, the PLLA block is not able to crystallize due to its low isotacticity. WAXS and PLOM intensity measurements are good tools to independently identify the crystallization transitions of the PEO and PCL blocks on one hand and the PE and PLLA block on the other one, as their crystallization temperatures overlap. In the quarterpolymer Q1, four types of different lamellae coexist because it self-assembles into tetracrystalline banded spherulites. Nanoindentation measurements were performed in order to analyze the impact of the nanostructural features on the mechanical properties. These experiments show that the storage modulus and hardness of the Q1 quarterpolymer are different from those of the PE and PLLA blocks. The low crystallinity of the PE and PLLA block is mainly responsible for this behaviour. The quarterpolymer Q2 shows lower mechanical properties that Q1, possibly due to the thinner PE crystal lamellae according to its lower melting point.

Resumen

El objetivo de esta tesis doctoral es el análisis y la comparación de sistemas poliméricos multifásicos con al menos dos fases cristalizables. Un estudio profundo del comportamiento cristalino y la morfología es esencial para diseñar y desarrollar nuevos materiales con propiedades mejoradas.

La primera parte de esta investigación se centra en el estudio de mezclas de polímeros PET/HDPE doblemente cristalinas con nanopartículas de dióxido de titanio y agentes compatibilizantes. La muestra escogida, tras el análisis de varias composiciones, fue la 70 PET/30 HDPE. La muestra presenta una morfología "sea-island", en la que la matriz corresponde a PET (70%) y la fase dispersa en forma de gotas corresponde a HDPE (30%). El tamaño de partícula de la fase dispersa se reduce al añadir las nanopartículas de titanio dióxido, dado que se ubican principalmente en la interfase, formando una barrera física que evita la coalescencia.

Además, debido a la reciente presencia de las nanopartículas de TiO_2 en los residuos de PET (botellas de PET opacas), se han preparado nanocompuestos 80rPP/20rPET/TiO_2 con materiales reciclados, empleando para ello tres tipos de nanopartículas TiO_2 diferentes: hidrofílicas (hphi), hidrofóbicas (hpho) y hidrofóbicamente modificadas (hphoM). El equilibrio hidrofílico/hidrofóbico controla la ubicación de las nanopartículas, y los resultados de TEM muestran una disminución del tamaño de las gotas de la fase dispersa cuando dichas nanopartículas se ubican en la interfase. La nanopartícula más eficaz resulta ser la hidrofóbicamente modificada (hphoM), aunque se necesitan grandes cargas (12%) para cubrir completamente la superficie de la gota y así mejorar las propiedades mecánicas. Además, hay una buena correlación entre el grado de cristalinidad del PET (determinada por DSC) y la ubicación de las nanopartículas, debido al efecto nucleante de las nanopartículas en la fase de PET.

La segunda parte del trabajo consiste en el estudio de copolímeros de bloques multicristalinos. La adición de un tercer y cuarto bloque cristalino hace que el análisis sea más desafiante con respecto a copolímeros dibloque doblemente cristalinos, pero nuevos terpolímeros tribloque tricristalinos de PE-*b*-PEO-*b*-PLLA

y PE-*b*-PCL-*b*-PLLA y tetrapolímeros tetrabloque tetracristalinos PE-*b*-PEO-*b*-PCL-*b*-PLLA de diferentes pesos moleculares y composiciones (y sus correspondientes terpolímeros tribloque PE-*b*-PEO-*b*-PCL, copolímeros dibloque PE-*b*-PEO y homopolímeros PE), con tres y cuatro bloques potencialmente cristalizables se lograron sintetizar y estudiar.

Con respecto a los terpolímeros tribloque tricristalinos PE-*b*-PEO-*b*-PLLA y PE-*b*-PCL-*b*-PLLA, se ha llevado a cabo un enfriamiento desde el fundido en DSC a 20 y 1 ° C/min, a la vez que se realizan mediciones in situ de SAXS/WAXS y PLOM en idénticas condiciones. Esto permite identificar inequívocamente la morfología superestructural y la secuencia de cristalización de cada uno de los materiales. Se ha estudiado el efecto de la velocidad de enfriamiento, ya que a 20 ºC/min, la secuencia de cristalización comienza con el bloque de PE, continúa con el bloque de PLLA y termina con el bloque de PEO o PCL dependiendo del terpolímero tribloque en cuestión. La rápida cinética de cristalización del bloque de PE es responsable de esta secuencia de cristalización. En cambio, al emplear 1 ºC/min como velocidad de enfriamiento, el bloque de PLLA cristaliza primero y solo para el terpolímero con mayor cantidad de PLLA. Por tanto, las condiciones de enfriamiento determinarán la morfología y las propiedades finales de estos materiales.

Esta investigación continúa con el estudio de la cristalización de terpolímeros tribloque tricristalinos PE-*b*-PEO-*b*-PCL (T1: $PE_{22}^{7.1}$-*b*-$PEO_{46}^{15.1}$-*b*-$PCL_{32}^{10.4}$ y T2: $PE_{37}^{9.5}$-*b*-$PEO_{34}^{8.8}$-*b*-$PCL_{29}^{7.6}$) y PE-*b*-PEO-*b*-PCL-*b*-PLLA tetrapolímeros tetrabloque tetracristalinos (Q1: $PE_{18}^{7.1}$ -*b* -$PEO_{37}^{15.1}$ -*b*- $PCL_{26}^{10.4}$ -*b*- $PLLA_{19}^{7.6}$ y Q2: $PE_{29}^{9.5}$ -*b*- $PEO_{26}^{8.8}$ -*b*- $PCL_{23}^{7.6}$ -*b*- $PLLA_{22}^{7.3}$). Los superíndices se refieren a los pesos moleculares en kg/mol y los subíndices a la composición en peso. Los precursores también se han estudiado con fines comparativos.

La naturaleza triplemente cristalina de los terpolímeros tribloque PE-*b*-PEO-*b*-PCL se demostró mediante técnicas DSC, SAXS/WAXS y PLOM utilizando las mismas condiciones. La cristalización a 20 ºC/min comienza con el bloque de PE, continúa con el bloque de PCL y termina con el bloque de PEO.

Aunque la cristalización de los bloques de PCL y PEO se superponen, los experimentos WAXS y PLOM permiten identificar ambas transiciones por separado. Según los experimentos SAXS, tanto T1 como T2 están débilmente segregados en el fundido. Los experimentos de PLOM muestran que los terpolímeros tribloque tienen una morfología no-esferulítica o microesferulítica, mientras que sus precursores muestran una morfología esferulítica.

Siguiendo con el estudio, se investigó la cristalización de los nuevos tetrapolímeros tetrabloque tetracristalinos de PE-*b*-PEO-*b*-PCL-*b*-PLLA. Resultados de SAXS indican que Q1 es miscible en el estado fundido, mientras que Q2 está débilmente segregado en el fundido, aunque esta segregación se rompe durante la cristalización. La secuencia de cristalización se determina mediante DSC y WAXS: el PLLA primero, luego el PE, luego la PCL y finalmente el PEO en el caso del tetrapolímero Q1, ya que en el caso de Q2, el bloque de PLLA no es capaz de cristalizar debido a su baja isotacticidad. Las mediciones de intensidad de WAXS y PLOM son buenas herramientas para identificar de forma independiente las cristalizaciones de los bloques de PEO y de PCL por un lado, y el bloque de PE y de PLLA por el otro, ya que sus temperaturas de cristalización se superponen. En el tetrapolímero Q1 coexisten cuatro tipos de lamelas diferentes, dado que se autoensamblan en esferulitas tetracristalina. Además, se realizaron mediciones de nanoindentación para analizar el impacto que tienen las características nanoestructurales en las propiedades mecánicas. Estos experimentos muestran que el módulo de almacenamiento y la dureza del tetrapolímero Q1 son diferentes a los de los bloques de PE y de PLLA. La baja cristalinidad del bloque de PE y de PLLA es la principal responsable de este comportamiento. El tetrapolímero Q2 muestra propiedades mecánicas más bajas que Q1, posiblemente debido a la formación de lamelas de PE más delgadas según su punto de fusión más bajo.